Gran Sasso Science Institute
Scuola Internazionale Superiore di Studi Avanzati

Improvement of Performances and Background Studies in GERDA Phase II

PhD thesis

submitted April 20th, 2017

PhD Candidate

Valerio D'Andrea

Advisors

dr.ssa Carla Maria Cattadori
INFN Milano Bicocca

dr. Luciano Pandola
INFN Laboratori Nazionali del Sud

Tutors

dr. Francesco Salamida
Università degli Studi dell'Aquila

dr. Stefano Riboldi
Università degli Studi di Milano e INFN Milano

Gran Sasso Science Institute

Ciclo XXIX – A.A 2013-2016

If you're not failing every now and again,
it's a sign you're not doing anything very innovative.

Woody Allen

I have done a terrible thing.
I invented a particle that cannot be detected.

Wolfgang Ernst Pauli

Contents

Introduction

The GErmanium Detector Array (GERDA) experiment, located at the Laboratori Nazionali del Gran Sasso (LNGS) of INFN, searches for the neutrinoless double beta ($0\nu\beta\beta$) decay of ^{76}Ge, a process that implies the violation of the lepton number conservation as predicted to occur in extensions of the Standard Model (SM) of particle physics.

High Purity Germanium (HPGe) detectors enriched to 87% in the double beta emitter ^{76}Ge are deployed being both source and detectors of the $0\nu\beta\beta$ decay. The experiment was planned in two stages. Phase I had been running from November 2011 to May 2013 using 18 kg of enriched semi-coaxial HPGe detectors from previous experiments. Since 2013 the GERDA setup has been upgraded to perform its next step in the $0\nu\beta\beta$ searches, aiming to reach a sensitivity to the $0\nu\beta\beta$ decay half-life larger than 10^{26} yr in about 3 years of physics data taking. This is achieved operating a total detector mass of about 35 kg of ^{76}Ge and with a background reduction of factor ten with respect to the Phase I.

The major upgrade of Phase II is the deployment of 30 new enriched BEGe detectors so as to both double the target mass of ^{76}Ge and reduce the background by a superior pulse shape discrimination (PSD).

GERDA Phase II data taking started in December 2015. After 6 months a first data release with 10.8 kg·yr of exposure was performed, showing that the design background has been achieved and setting a new limit on the $0\nu\beta\beta$ decay half life of ^{76}Ge of $5.3 \cdot 10^{25}$ yr (90% C.L.).

My thesis work can be divided in two main sections: a significant part moved in the framework of the upgrade to Phase II and, after the start of the data taking, the focus moved to the study of the new physics data and the Phase II $0\nu\beta\beta$ decay sensitivity.

In particular, during the upgrade phase, I worked on test and integration with Ge detectors of the new front-end electronics and on the analysis of the tests and commissioning data. In addition I worked on the development of an optimized digital signal processing for the events energy reconstruction. The goal was to exploit the superior energy resolution and the powerful PSD of the new BEGe detectors.

The second part of this thesis focuses on the study of the background spectrum and related sources and on the statistical analysis to assess the GERDA Phase II $0\nu\beta\beta$ decay sensitivity in different background scenarios.

The thesis is structured as follow. In chapter 1 an overview on the neutrino physics and $0\nu\beta\beta$ decay is given. The state of art on the $0\nu\beta\beta$ search and the future prospects are also presented. Chapter 2 focuses on the GERDA experiment: the description of the experimental setup, the main results from Phase I, the upgrade program and the first results from Phase II are described.

The main original content of the thesis is presented in the following chapters.

Chapter 3 describes the work performed with the front-end electronics for GERDA Phase II: the proposed design, the integration tests, the results and the final configuration are reviewed. The development of the new digital shaping filter and the results from its application to the new Phase II data are presented in chapter 4.

The study of the Phase II background spectrum is shown in chapter 5: the main visible structures, the α and γ contaminations are studied in detail.

Finally, chapter 6 describes the study of the GERDA sensitivity on the neutrinoless double beta decay of ^{76}Ge. A new time-dependent background model has been developed and applied to Monte Carlo realizations of Phase II datasets, under the hypothesis of not-constant background, that follows from the analysis of the α contamination.

In chapter 7 are summarized the main results of the thesis.

Appendix A reports the final GERDA Phase II detector configuration and the energy resolution obtained in the Phase II global calibration. The description of the method to evaluate the cross-talk between the 40 channels in Phase II and the table with all cross-talk values are presented in appendix B. The results reported in the appendices, that have been provided within the present thesis, are implemented in the GERDA official analysis and in the recent publications [1, 2].

Chapter 1

Neutrinoless double beta decay

The observation of the neutrinoless double beta ($0\nu\beta\beta$) decay would have important consequences in particle physics and other fields, including cosmology. It would prove that lepton number is not conserved and that the neutrino has a Majorana mass term. In addition, it represents a powerful method to determine the absolute neutrino mass.

The importance of the topic has stimulated the development of several experiments to search for $0\nu\beta\beta$ decay on a number of isotopes which undergo double beta decay.

In this chapter a theoretical introduction on neutrino and neutrinoless double beta decay is presented. The state of art concerning the neutrino physics and its mass is reported in Sec. 1.1 with a brief historical introduction. In Sec. 1.2 is presented the theory behind the double beta decays, in particular regarding the $0\nu\beta\beta$ process and the formula of the decay rate, with the basis of the calculation of the phase space factor and the nuclear matrix element. Finally, the status of the experimental search and the future prospects on double beta decays are given in Sec. 1.3.

1.1 Present knowledge on neutrinos

In 1930 Wolfgang Pauli postulated a very light, neutral particle with spin 1/2 to explain the continuous energy spectrum of electrons in β decays [3]. This particle was later called neutrino (indicated with ν) by Enrico Fermi in 1933 to avoid a naming conflict with the newly discovered neutron. The neutrino discovery took 26 years until 1956 when Frederick Reines and Clyde L. Cowan performed a nuclear reactor experiment observing electron anti-neutrinos [4, 5]. As foreseen by Pauli, the measured cross section was extraordinary small and well in agreement with the prediction of $6.3 \cdot 10^{-44}$ cm^2.

In 1933 Enrico Fermi developed the first theory for the weak interactions [6]: a 4-fermion vertex was introduced to describe weak decays and weak interactions (later it became clear that this theory is an approximation of the complete electroweak theory).

In 1937 E. Majorana introduced a new quantization for the fermionic field [7], as an alternative to the Dirac formalism (see Sec. 1.1.2).

A further step in the understanding of neutrino physics was represented by the introduction, in 1953, of the concept of total lepton number by E. J. Konipinski and H. M. Mahmoud for the explanation of the missing observation of some decays [8]. A few years later, B. Pontecorvo suggested the use of separate lepton numbers for electrons and muons in order to explain the non-observation of $\mu \to e + \gamma$ [9].

Goldhaber measured the helicity of the neutrino in 1957 [10], showing that neutrinos are only left-handed and anti-neutrinos right-handed. This experiment was in agreement with the Wu experiment which had showed parity violation in weak interaction just one year earlier [11]. Additionally, β decay experiments at the time showed that the neutrino mass is smaller than 0.5 keV [12]. With these properties, neutrinos are included in the Standard Model (SM) as part of the electroweak theory which was developed by Glashow, Salam and Weinberg in 1961 [13].

1.1.1 Neutrino oscillations

The idea of neutrino mixing, analogous to the quark sector, was introduced by Maki, Nakagawa and Sakata in 1962 [14], but the first connection to possible neutrino flavor oscillations was introduced seven years later by Gribov and Pontecorvo [15]: the neutrino flavor oscillation, similar to the quark flavor oscillation with the Cabibbo-Kobayashi-Maskawa (CKM) matrix, is possible only if neutrinos have a non-zero mass.

The basic assumption for neutrino oscillation is that the weak flavor eigenstates are not identical to the mass eigenstates. The flavor and mass eigenstates are a superposition of each other which can be described as:

$$\nu_{lL} = \sum_i U_{li} \nu_{iL} \tag{1.1}$$

where $l = e, \mu, \tau$ are the lepton flavors, $i = 1, 2, 3$ are the mass eigenstates and L indicates the left-handed component of the neutrino field. U is the Pontecorvo-Maki-Nakagawa-Sakata (PMNS) matrix that can be parametrized as [16]:

$$U = \begin{pmatrix} c_{12}c_{13} & s_{12}c_{13} & s_{13}e^{-i\delta} \\ -s_{12}c_{23} - c_{12}s_{23}s_{13}e^{i\delta} & c_{12}c_{23} - s_{12}s_{23}s_{13}e^{i\delta} & s_{23}c_{13} \\ s_{12}s_{23} - c_{12}c_{23}s_{13}e^{i\delta} & -c_{12}s_{23} - s_{12}c_{23}s_{13}e^{i\delta} & c_{23}c_{13} \end{pmatrix} \times \\ \times \begin{pmatrix} 1 & 0 & 0 \\ 0 & e^{i\frac{\alpha_{21}}{2}} & 0 \\ 0 & 0 & e^{i\frac{\alpha_{31}}{2}} \end{pmatrix} \tag{1.2}$$

where $c_{ij} = \cos\theta_{ij}$, $s_{ij} = \sin\theta_{ij}$ (θ_{ij} are the mixing angles), δ Dirac is the charge conjugation parity (CP) violation phase and α_{21}, α_{31} are the two Majorana CP violation phases, present only if neutrinos are Majorana particles. The observable oscillation, however, does not depend on the Majorana phases.

The neutrino oscillation probabilities depend on the neutrino energy E, the distance between source and detector L and the elements of the PMNS matrix.

The transition probability that a neutrino created with flavor l is detected with a flavor l' is:

$$P_{l\to l'} = \delta_{ll'} - 4\sum_{i>k} Re(U^*_{li}U_{l'i}U_{lk}U^*_{l'k})\sin^2\left(\frac{\Delta m^2_{ki}L}{4E}\right) + \\ + 2\sum_{i>k} Im(U^*_{li}U_{l'i}U_{lk}U^*_{l'k})\sin^2\left(\frac{\Delta m^2_{ki}L}{2E}\right) \quad (1.3)$$

where $\Delta m^2_{ki} = m^2_k - m^2_i$ is the squared mass difference between the mass eigenstates k and i. In order to determine the unknown Δm^2_{ki} an experiment has to know precisely E and L of the neutrinos.

The experiments with solar, atmospheric, reactor and accelerator neutrinos have proved the existence of neutrino oscillations. Disappearance of the solar ν_e, reactor $\bar{\nu}_e$ and of atmospheric ν_μ and $\bar{\nu}_\mu$ due to the oscillations have been observed respectively, in the solar neutrino [17, 18, 19, 20, 21, 22], KamLAND [23] and Super-Kamiokande [24] experiments.

Strong evidences for ν_μ disappearance due to oscillations were obtained also in the long-baseline accelerator neutrino experiments K2K [25] and in the MINOS [26] and T2K [27] long baseline experiments. Evidences for ν_τ appearance due to $\nu_\mu \to \nu_\tau$ oscillations were published by the Super-Kamiokande [28] and OPERA [29] collaborations.

In 2011 the T2K [30] an the MINOS [31] collaborations also obtained data consistent with $\nu_\mu \to \nu_e$ oscillations, confirmed in 2013 [32]. Subsequently, the Double Chooz Collaboration reported [33] indications for disappearance of reactor $\bar{\nu}_e$ at $L \sim 1.1$ km. Strong evidences for reactor $\bar{\nu}_e$ disappearance at $L \sim 1.65$ km and $L \sim 1.38$ km and were obtained in the Daya Bay [34], RENO [35] and Double Chooz [36] experiments.

The most recent measured oscillation parameters are shown in Tab. 1.1: the two Majorana CP violation phases cannot be measured with these experiments, since the flavour neutrino oscillation probabilities of Eq. (1.3) do not depend on them.

Table 1.1: The best-fit values of the 3-neutrino oscillation parameters, derived from a global fit of the current neutrino oscillation data (from [37]). Are reported both the values for NH and IH. $\Delta m^2 = m^2_3 - (m^2_1 + m^2_2)/2$.

Parameter	hierarchy	best fit value $\pm 1\sigma$
Δm^2_{21} [10^{-5} eV^2]	NH or IH	$7.37^{+0.17}_{-0.16}$
$\lvert\Delta m^2\rvert$ [10^{-3} eV^2]	NH	$2.50^{+0.04}_{-0.04}$
	IH	$2.46^{+0.05}_{-0.04}$
$\sin^2\theta_{12}$ [10^{-1}]	NH or IH	$2.97^{+0.17}_{-0.16}$
$\sin^2\theta_{13}$ [10^{-2}]	NH	$2.14^{+0.11}_{-0.09}$
	IH	$2.18^{+0.09}_{-0.12}$
$\sin^2\theta_{23}$ [10^{-1}]	NH	$4.37^{+0.23}_{-0.20}$
	IH	$5.69^{+0.28}_{-1.41}$
δ/π	NH	$1.35^{+0.29}_{-0.22}$
	IH	$1.32^{+0.35}_{-0.25}$

Experiments measuring oscillations are only sensitive to the mass squared differences Δm^2_{ij} and not to the absolute mass scale. In Tab. 1.1 are reported the value of Δm^2_{21} and the absolute value of $\Delta m^2 = m_3^2 - (m_1^2 + m_2^2)/2$, the sign of Δm^2 determines the spectrum of the neutrino mass eigenstates. In addition $\Delta m^2_{21} \ll \Delta m^2$, creating a possible hierarchy.

Until now the mass of the lightest mass state is not known, depending on its value the neutrino mass spectrum (in literature also called hierarchy) can take different forms:

- normal hierarchy (NH): $m_1 \ll m_2 < m_3$, $\Delta m^2 > 0$;
- inverted hierarchy (IH): $m_3 \ll m_1 < m_2$, $\Delta m^2 < 0$;
- quasi-degenerate (QD) mass spectrum: $m_1 \sim m_2 \sim m_3$, $m_i^2 \gg \Delta m^2$.

The determination of the neutrino mass hierarchy is a central and challenging research topic in particle physics. Dedicated experiments are the atmospheric neutrinos Cherenkov detectors PINGU [38] and the magnetized detectors INO [39].

The mass of the electron anti-neutrino can be directly probed in precise measurements of the β decay spectrum close to the end-point by measuring the spectral distortion by a small but finite neutrino rest mass. The current best limit are from the Mainz and Troitsk experiments with a mean upper limit of $m_\beta < 2$ eV [40, 41]. The KATRIN experiment [42], with an expected ten-times improved sensitivity, is currently in the commissioning phase.

1.1.2 Dirac and Majorana mass

A neutrino field ν follows the Dirac equation [43, 44] because it is a spin 1/2 fermion:

$$(i\gamma^\mu \partial_\mu - m_D)\nu = 0 \tag{1.4}$$

with the Lagrangian:

$$\mathcal{L} = \bar{\nu}(i\gamma^\mu \partial_\mu - m_D)\nu \tag{1.5}$$

where m_D is the Dirac mass for the neutrino field. The mass term of Eq. (1.5) can be written as:

$$\mathcal{L}_D = -m_D \bar{\nu}\nu = -m_D(\bar{\nu}_R \nu_L + \bar{\nu}_L \nu_R) \tag{1.6}$$

where ν_L (ν_R) is the left (right)-handed field. The Dirac mass is thus created by the coupling of the chiral fields.

In the case of electrons (or other charged fermions) the mass is created as indicated by Eq. (1.6). For the neutrino, there is no evidence about the existence of the right-handed field ν_R and therefore about the Dirac mass: this means that for the neutrino either $m_D = 0$ or there is ν_R.

This is the starting point of the problem of neutrino mass.

Another possibility to write the neutrino mass has been introduced by Ettore Majorana in the 1937 [7]. He tried to describe the massive ν using only the left-handed field (the one observed), rewriting ν_R as function of ν_L using the charge conjugation operator.

Majorana requires the condition:

$$\nu_R = C\bar{\nu}_L^T = \nu_L^C \tag{1.7}$$

and the neutrino field becomes:

$$\nu = \nu_L + \nu_R = \nu_L + \nu_L^C \tag{1.8}$$

that means $\nu^C = \nu$ or that neutrino and anti-neutrino are the same particle.

Using the Eq. 1.7 it is possible to rewrite the Dirac equation using only left-handed neutrino (the same is true for the right-handed) and is also possible add a new mass term in the Lagrangian with only ν_L:

$$\mathcal{L}_M = -\frac{1}{2} m_L (\bar{\nu}_L \nu_L^C + \bar{\nu}_L^C \nu_L) \tag{1.9}$$

this is the Majorana mass term for left-handed neutrino (it exists an analogous term for ν_R introducing the mass m_R).

To summarize there are at least two scenarios:

- if ν_R exists it is possible to have both mass terms (Dirac and Majorana);
- if ν_R does not exist and neutrino is only left-handed we cannot have a Dirac mass m_D but only a Majorana mass that violates the lepton number conservation by 2 units.

See-saw mechanism The most general Lagrangian to describe to neutrino mass, including both Dirac and Majorana terms can be written as:

$$\mathcal{L} = -\frac{1}{2} (\bar{\nu}_L^C \nu_R) M \begin{pmatrix} \nu_L \\ \bar{\nu}_R^C \end{pmatrix} + \text{h.c.} \tag{1.10}$$

where the mass matrix M is:

$$M = \begin{pmatrix} m_L & m_D \\ m_D & m_R \end{pmatrix} .$$

From the mass matrix, it is possible to obtain the mass eigenvalues:

$$\det[M - mI] = 0 \ \Rightarrow \tag{1.11}$$

$$m = \frac{1}{2} \left[(m_L + m_R) \pm \sqrt{(m_L - m_R)^2 + 4m_D^2} \right] . \tag{1.12}$$

Choosing $m_L = 0$ and $m_R \gg m_D$ it is possible to obtain the eigenvalues:

$$m_1 \simeq -\frac{m_D^2}{m_R} \tag{1.13}$$

$$m_2 \simeq m_R \left(1 + \frac{m_D^2}{m_R^2} \right) \simeq m_R . \tag{1.14}$$

The eigenstate associates with m_1 is mostly the familiar left-handed light Majorana neutrino, instead to one associates with m_2 is mostly the heavy sterile right-handed partner.

This is the famous See-saw mechanism of type I [45, 46, 47] (if one state goes up the other goes down); it provides an elegant explanation to the question of why the neutrino has a mass so much smaller than the other charged leptons. The assumption $m_L = 0$ is natural, since a Majorana mass term for the left-handed chiral field ν_L breaks the symmetries and the renormalizability of the SM. Taking $m_1 \sim 0.05$ eV and $m_D \sim m_{top} \sim 180$ GeV the result is $m_R \sim 0.3 \times 10^{15}$ GeV.

The experiments studying flavour neutrino oscillations (described in previous section) cannot provide information on the nature of the neutrino mass. The only feasible experiments having the potential of establishing that the massive neutrinos are Majorana particles are at present the experiments searching for $0\nu\beta\beta$ decay.

1.2 The neutrinoless double beta decay

The neutrino mass nature (Dirac or Majorana), the type of neutrino hierarchy and the absolute scale of neutrino masses are open problems. New information can be obtained by searching for the neutrinoless double beta decay.

This section focuses on the double beta decay theory and its importance. Recent detailed reviews on the state of art of the $0\nu\beta\beta$ decay are in Ref. [48, 49, 50].

1.2.1 Double beta decays

The double beta decay, consisting in the transformation of a pair of neutrons into two protons and two electrons as a single process, was first considered by Maria Goeppert-Mayer in 1935 [51]. Two year later the new formalism to describe the neutrino mass of Majorana, Wolfgang Furry considered for the first time the neutrinoless double beta ($0\nu\beta\beta$) decay [52].

The double beta decay is a second order weak nuclear decay process with extremely long half-lives and it corresponds to the transition from a nucleus (A, Z) to $(A, Z + 2)$. It can be experimentally observed in nuclear configurations in which two consecutive single beta decays are energetically forbidden or strongly suppressed. Therefore, candidate isotopes for detecting the $\beta\beta$ decays are even-even nuclei that, due to the nuclear pairing force, are lighter than the nearby odd-odd $(A, Z + 1)$ nucleus, making single beta decay kinematically forbidden.

A double beta process can be described as follows: starting from an initial nuclear state, one nucleon decays into another nucleon producing a pair of leptons (electron and neutrino); this is a virtual transition since the ground state of the parent nucleus has a lower energy than the intermediate state (with a nucleus and 2 leptons); the $\beta\beta$ takes place when there is a second virtual decay with a second pair of leptons. The final state can or cannot conserve lepton number and the result is a two anti-neutrinos or a neutrinoless double beta decay.

The standard model predicts the double beta with 2 anti-neutrinos ($2\nu\beta\beta$)

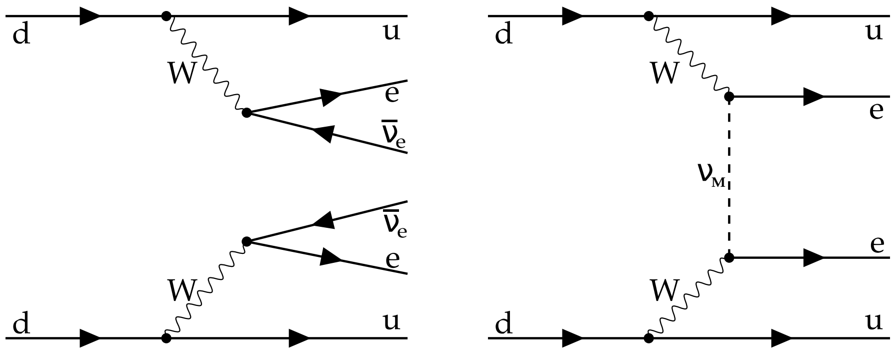

Figure 1.1: Double beta decays. On the left, double beta decay with the emission of 2 anti-neutrinos, lepton number is preserved. On the right, the neutrinoless double beta ($0\nu\beta\beta$) process due to the exchange of massive Majorana neutrino (indicated by ν_M) with lepton number violation.

mode:

$$(Z, A) \to (Z + 2, A) + 2e + 2\bar{\nu}_e$$

which has been observed in a few isotopes (see Sec. 1.3). In Fig. 1.1 on the left the Feynman diagram for the $2\nu\beta\beta$ process is displayed. This process can be described as a second-order perturbative treatment of the SM Hamiltonian, with only left-handed couplings since the transition is allowed by the selection rules of the weak interaction.

The other kind of double beta decay is not predicted by the Standard Model and its final state consists in the emission of only two electrons:

$$(Z, A) \to (Z + 2, A) + 2e \ .$$

This decay violates the leptonic number by 2 units ($\Delta L = 2$), Fig. 1.1 on the right shows a possible Feynman diagram of this process, due to the exchange of massive Majorana neutrinos ν_M.

Other possible mediators of this decay, which differ in the various extensions of the SM, could be right-handed weak currents, super-symmetric particles or massive neutrinos. Independently on the mechanism, the observation of $0\nu\beta\beta$ decay would prove the existence of physics beyond the SM, the non-conservation of total lepton number and that neutrinos have a Majorana mass component.

The last statement is supported by Schechter and Valle [53], that described the transition between $\bar{\nu}_e \to \nu_e$, present in the $0\nu\beta\beta$ decay, as radiative corrections with a black box as shown in Fig. 1.2. Anyway, a recent calculation [54] proved that the contribution to the Majorana mass term of the electron neutrino mass provided by these radiative corrections is of $\sim 10^{-24}$ eV. This implies that other Majorana and/or Dirac mass terms must exist in order to explain the known mass splittings and mixing angles.

Extensions of the standard model accommodate right-handed currents and corresponding couplings between left-handed and right-handed terms. These are included in the framework of the grand unification theories (GUT), like

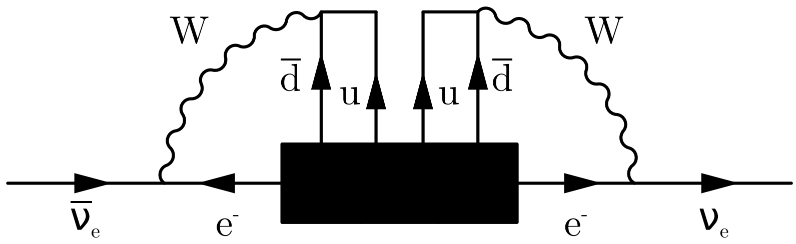

Figure 1.2: Diagram representing the contribution of the "black box" operator to the Majorana mass. Adapted from [54].

for example the simple $SO(10)$ gauge theory [55] and several more complicated scenarios. However, a complete theory able to explain the nature of the neutrino mass and to provide predictions of new phenomena does not exist yet.

1.2.2 Lifetime of neutrinoless double beta decay

In the low energy limit (the energy is much smaller than W bosons mass and the weak interaction is reducible to an effective theory) the interaction of neutrinos can be described by the current-current four fermion interactions. In this approximation the expression for the lifetime of double beta decays can be derived (detailed description can be found in the work of Doi et al. of 1981 [56]).

The general formula for the rate of neutrinoless double beta decay can be factorized into three factors as follows:

$$\left(T^{0\nu}_{1/2}\right)^{-1} = G_{0\nu}|M_{0\nu}|^2\left(\frac{m_{\beta\beta}}{m_e}\right)^2 \tag{1.15}$$

where $T^{0\nu}_{1/2}$ is the half-life of the $0\nu\beta\beta$ processes, $G_{0\nu}$ is the phase space factor (PSF) and $M_{0\nu}$ is the nuclear matrix element (NME).

In the expression of Eq. (1.15) a fundamental quantity appears, the effective Majorana mass $m_{\beta\beta}$ defined by:

$$m_{\beta\beta} = \sum_{i=1}^{3} U^2_{ei} m_i \tag{1.16}$$

where U is the PMNS mixing matrix and m_i are the neutrino mass eigenvalues. This quantity appears in the Eq. (1.15) because the Majorana neutrino propagator enters in the amplitude. It follows that the decay rate is proportional to $m^2_{\beta\beta}$. The key idea is that, by studying the $0\nu\beta\beta$ decay, it is possible to measure its half-life and then estimate $m_{\beta\beta}$.

Given Eq. (1.15), the half-life of $0\nu\beta\beta$ can be obtained by the independent computation of PSF and NME. These two quantities are the main ingredients of $\beta\beta$ studies and in the latest years systematic works allowed to better evaluate both quantities. In the following part of this section the basis of the calculation of them are presented.

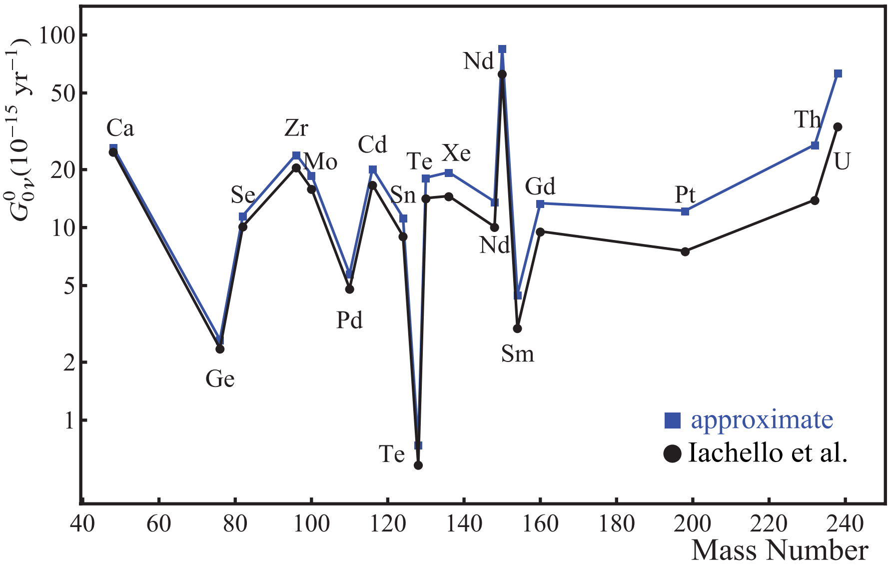

Figure 1.3: Phase space factor for $0^+ \to 0^+$ $0\nu\beta\beta$ decay obtained by Iachello et al. (black) and by previous works (blue) [57].

1.2.3 Phase space factors

The phase space factor contains the available final state density and depends mainly on the Q-value of the decay. The numerical calculation is obtained through the integration of the electron wave functions (for detailed description see [57]).

One of the first theories to calculate the phase space factors $G_{0\nu}$ in double beta decays was developed in the 1981 [56]. In the following years the theory was reformulated by other groups, with calculation for a certain number of $\beta\beta$ nuclei (presented for example in [58]). In these works the results were obtained approximating the electron wave function at the nuclear radius without electron screening.

Recent developments in the numerical evaluation of Dirac wave functions and in the solution of the Thomas-Fermi equation allowed to calculate accurately phase space factors for $2\nu\beta\beta$ and $0\nu\beta\beta$ decays [57].

Starting from the relativistic electrons theory, the radial wave function is evaluated using a robust numerical method. Then is included a correction due to the finite nuclear size, introducing an uniform charge distribution, and the contribution of screening, using the Thomas-Fermi approximation. Finally the result is used for the evaluation of the phase space factor $G_{0\nu}$.

Fig. 1.3 shows the values for $G^0_{0\nu}$ (transition between ground states of the nuclei $0^+ \to 0^+$) obtained in [57] in comparison with previous results that adopted an approximate electron wave function. The difference between the new calculation and the older ones is increasing with Z: for light nuclei ($Z = 20$) is order of a few percent, about 30% for Nd ($Z = 60$) and larger than 90% for U ($Z = 92$).

1.2.4 Nuclear matrix elements

The most critical ingredient in the evaluation of the lifetime of the $0\nu\beta\beta$ decay (Eq. (1.15)) is the nuclear matrix element (NME) $M_{0\nu}$. It depends on the form of the hadronic current of the weak Hamiltonian and on the structure of the initial and final nuclei. It is a difficult task for the double beta decays because the ground and many excited states of open-shell nuclei with complicated nuclear structure have to be considered.

Nuclear matrix elements have been evaluated in a variety of models using the concepts of general nuclear structure, the most important being the interacting shell model (ISM) [59], the quasiparticle random phase approximation (QRPA) [60] and the interacting boson model (IBM) [61, 62].

Given a model one can write the associated hadronic current, write a transition operator and evaluate its matrix elements between initial and final states. This evaluation is in general quite difficult, because in the decay from an even-even nucleus to another even-even nucleus the structure of the intermediate odd-odd nucleus must be known. However for $0\nu\beta\beta$ decay one can use the closure approximation (because of the momentum transfer carried by the neutrino propagator is $q \sim 100$ MeV) and the calculation of the NME becomes the calculation of a 2-body matrix element. The starting point is the transition operator of the process (in this case is mentioned the formulation adopted in Refs. [60, 61]).

The transition operator in momentum space is written as:

$$T(p) = H(p)\frac{m_{\beta\beta}}{m_e} \tag{1.17}$$

where $H(p)$ is the 2-body operator:

$$H(p) = \sum_{m,n} \tau_m^+ \tau_n^+ [-h^F(p) + h^{GT}(p)\vec{\sigma}_m \cdot \vec{\sigma}_n + h^T(p) S_{mn}^p] \tag{1.18}$$

where $h^{F,GT,T}$ are the Fermi (F), Gamow-Teller (GT) and tensor (T) contributions and S_{mn}^p is a tensor operator defined by:

$$S_{mn}^p = 3[(\vec{\sigma}_m \cdot \hat{p})(\vec{\sigma}_n \cdot \hat{p})] - \vec{\sigma}_m \cdot \vec{\sigma}_n \ . \tag{1.19}$$

The terms $h^{F,GT,T}$ of Eq. (1.18) can be factorized as:

$$h^{F,GT,T}(p) = v(p)\tilde{h}^{F,GT,T}(p) \tag{1.20}$$

where $v(p)$ is the neutrino potential and $\tilde{h}^{F,GT,T}(p)$ are form factors that depends on the coupling constants $g_V = 1$ and $g_A = 1.269$ (for a more detailed discussion see [61]).

Considering the decay of a nucleus ${}^A_Z X_N$ into a nucleus ${}^{\ A}_{Z+2}Y_{N-2}$, the nuclear matrix elements between the ground state of the initial nucleus and the final state with angular momentum J_F is:

$$M_{0\nu} = \langle {}^A X, 0_1^+ | H(p) | {}^A Y, J_F \rangle \tag{1.21}$$

in the case of $0\nu\beta\beta$ the final angular momentum cannot be greater than one, the only possibility is final nucleus with $J_F = 0_1^+, 0_2^+$.

To evaluate the nuclear matrix elements normally the Eq. (1.21) is split in many terms following the definition of the transition operator (1.18).

The results for $M_{0\nu}$ depend on the model and approximation schemes adopted for the description of the nucleus and interactions between nucleons; in the following part is briefly described the basis of the principal methods used in literature.

Interacting Shell Model In the interacting shell model (ISM) [59] the calculations are based on the independent particle model that works with the assumption that nucleons are moving independently in a mean field with a strongly attractive spin-orbit term:

$$U(r) = \frac{1}{2}\ \hbar\omega r^2 + D\ \vec{l}^{\,2} + C\ \vec{l}\cdot\vec{s} \tag{1.22}$$

the harmonic oscillator part describes the bound nucleon and the spin-orbit term is added to give the separation of the sub-shell and explain the nuclear magic numbers.

When the number of protons and neutrons departs from magic numbers, it is mandatory to include the residual 2-body nucleon interaction that contains both a kinetic (K) and a potential (V) term:

$$\sum_{i,j} K_{ij} a_i^+ a_j - \sum_{i,k} V_{ijkl}\ a_i^+ a_j^+ a_k a_l\ . \tag{1.23}$$

Given a good residual interaction V_{ijkl} the problem is reduced to diagonalize a matrix in a large basis. In the evaluation of nuclear matrix, a limited valence space is used but all configurations of valence nucleons are included. The ISM model describes well properties of low-lying nuclear states, but there are technical difficulties and only few $0\nu\beta\beta$ decay can be studied with this method.

Quasiparticle Random Phase Approximation The idea of the QRPA model is that the important part of the residual interaction between nucleons is the pairing force, that favors the coupling of neutrons with neutrons and protons with protons and accounts for the tendency to form especially stable configurations with even N and Z (like in $\beta\beta$ nuclei). The result is that the ground state is mainly composed of Cooper-like pairs of neutrons and protons. In QRPA the nucleon pair is introduced using the Bardeen-Cooper-Schrieffer (BCS) theory of superconductivity.

In the QRPA is performed an unitary transformation to change from a particle to a quasiparticle basis. Quasiparticles are generalized fermions which are partly particles (with probability u_j^2) and partly holes (with probability v_j^2); this is just a mathematical construct to account for the pairing force between nucleons.

After the basis transformation, the QRPA evaluates the transition amplitude that connect the 0^+ vacuum of quasiparticles with any J_F excited state, described as harmonic oscillator above the vacuum. The transition amplitude is then modified as needed, since the creation of a particle-hole pair from the BCS vacuum (the so-called forward-going amplitude X) can lead to the same

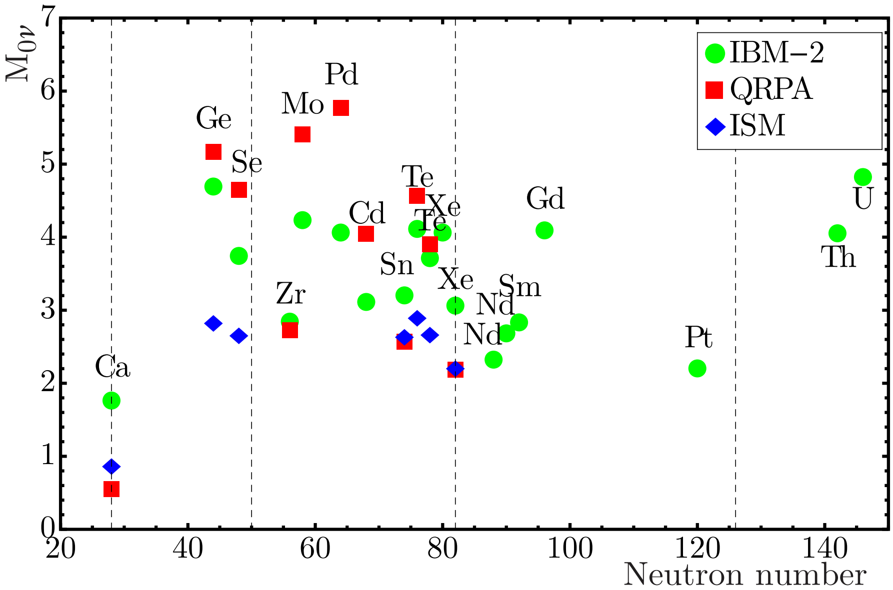

Figure 1.4: Most updated NME calculations for the $0\nu\beta\beta$ with the IBM-2 [62], QRPA [60] and ISM [59] models. Picture from Ref. [62].

final state J_F as the destruction of a particle-hole pair from a 2-particle, 2-hole excitation (the backward-going amplitude Y). The amplitudes X and Y and the corresponding energy eigenvalues ω are determined by solving the QRPA equations of motion for each J_F:

$$\begin{pmatrix} A & B \\ -B & -A \end{pmatrix} \begin{pmatrix} X \\ Y \end{pmatrix} = \omega \begin{pmatrix} X \\ Y \end{pmatrix} \tag{1.24}$$

the terms A and B depend on the interaction matrix elements between quasi-particle configurations; these interaction matrix elements are multiplied by adjustable coupling constants.

Interacting boson model The IBM [61, 62] aims to share both strengths of ISM and QRPA and describes excitation spectra and electromagnetic transitions among collective states up to heavy nuclei.

The IBM adopts the algebra of boson creation and annihilation operators to provide simple Hamiltonians that generate complex and realistic collective spectra. In its original form (referred as IBM-1), the degrees of freedom are N bosons, each can be in six positive parity states: an angular-momentum-zero state (labeled as s) and five angular-momentum-two states (labeled as $d\mu$, with μ the magnetic projection). In the IBM-2, which is used to study $\beta\beta$ decay, there are separate s and d boson states for neutrons and protons. The IBM is an interesting model since has clear connections between the other models.

Fig. 1.4 shows a comparison among the most recent NME calculations of the nuclear matrix elements computed with the most common models ISM, QRPA and IBM-2. It can be seen that the discrepancies can be generally quantified in some tens of percent. As it will be discussed in next section, the main source of uncertainty in the inference does not rely on the NME calculations, but on the determination of the quenching of the axial vector coupling constant g_A.

1.2.5 The quenching problem

The estimation of g_A is an even more delicate topic. A convenient parametrization for the NMEs is the following [63]:

$$M_{0\nu} = g_A^2 \left(M_{GT}^{0\nu} - \left(\frac{g_V}{g_A} \right)^2 M_F^{0\nu} + M_T^{0\nu} \right) \tag{1.25}$$

where g_V and g_A are the vector and axial coupling constants of the nucleon, $M_{GT}^{0\nu}$ is the Gamow-Teller operator matrix element between initial and final states (spin-spin interaction), $M_F^{0\nu}$ is the Fermi contribution (spin independent interaction) and $M_T^{0\nu}$ is the tensor operator matrix element.

The form of Eq. (1.25) emphasizes the role of g_A. In fact in literature the NME is usually redefined as $M_{0\nu} = g_A^2 M_{0\nu}$ taking out the contribution of g_A.

As pointed out in [61], typically the value of g_A for the free neutron is used. In literature, this ranges between 1.25 and 1.27. A problem arises from the comparison between the predicted and measured $2\nu\beta\beta$ decay half-lives of several isotopes, systematically smaller than the estimated ones.

A possible explanation is the "quenching" of g_A induced by either some limitation in the calculation or by the omission of non-nucleonic degrees of freedom. The quenching of g_A is function of the mass number A:

$$g_A^{eff} = g_A \cdot A^\alpha \tag{1.26}$$

where α depends on the model used for the NME calculation and varies between -0.12 and -0.18 ($A = 1$ for free neutrons). Going back to the case of $0\nu\beta\beta$ decay, we can ask if the value of g_A is quenched in the same way as for $2\nu\beta\beta$ decay or not. So far, no commonly accepted answer exists, and the question is topic of debate. What is the correct value of g_A is still an open issue and introduces a considerable uncertainty in the determination of $m_{\beta\beta}$ from the $0\nu\beta\beta$ rate formula of Eq. (1.15) (more detailed description on this topic are in Refs. [48, 50]).

1.3 Search for double beta decays

From the experimental point of view, the search for a $0\nu\beta\beta$ signal consists in the detection of the two emitted electrons. The energy of the recoiling nucleus is negligible and the sum of two electrons energy corresponds to the Q-value of the $\beta\beta$ process ($Q_{\beta\beta}$). Fig. 1.5 shows a schematic view of the two-electrons spectra: a monochromatic peak at $Q_{\beta\beta}$ is expected for the $0\nu\beta\beta$ decay, while the $2\nu\beta\beta$ process has a continuous spectrum with $Q_{\beta\beta}$ as end point.

An important aspect in the search of the $0\nu\beta\beta$ decay is the choice of the isotope. The first requirement is an high $Q_{\beta\beta}$ of the $\beta\beta$ emitter, since it directly influences the background; an ideal choice would be $Q_{\beta\beta}$ larger than 2614.5 keV, which represents the end point of the dominant natural gamma

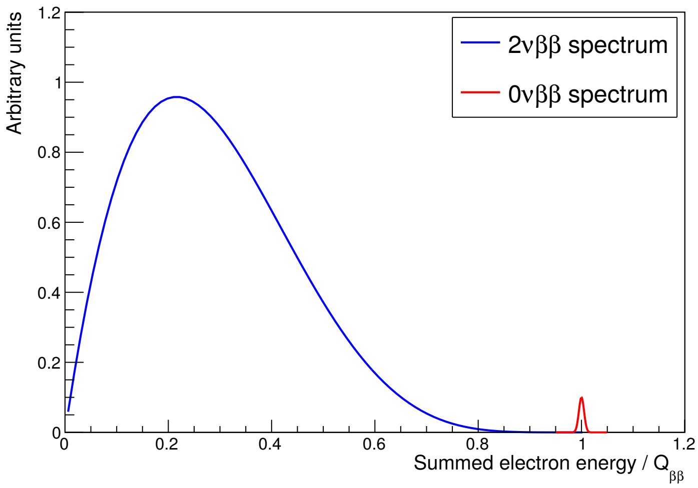

Figure 1.5: Schematic view of the $2\nu\beta\beta$ and the $0\nu\beta\beta$ decay spectra.

radioactivity. Another fundamental requirement is high isotopic abundance of the $\beta\beta$ emitter; the majority of candidate isotopes have a natural isotopic abundance $< 10\%$, the only exception being ^{130}Te with 34.5%.

A recent work [64] compared the available calculations of matrix elements and phase space factors for all $\beta\beta$ candidates. The results on the effective Majorana mass limits as function of a renormalized specific phase space and the squared nuclear matrix element are shown in Fig. 1.6 for selected $\beta\beta$ candidates. A nearly uniform inverse correlation between phase space and the square of the nuclear matrix element has been found. As a consequence, no $\beta\beta$ isotope is clearly favored or disfavored, all have about the same sensitivity to $0\nu\beta\beta$ decay per unit mass.

Among all possible candidate $\beta\beta$ emitters, the isotopes adopted in $0\nu\beta\beta$ experiments are ^{48}Ca, ^{76}Ge, ^{82}Se, ^{96}Zr, ^{100}Mo, ^{116}Cd, ^{130}Te, ^{136}Xe and ^{150}Nd.

1.3.1 Neutrinoless double beta decay sensitivity

The number of signal events expected from $0\nu\beta\beta$ decay (referred as $N^{0\nu}$) in an experiment with mass M after a live-time of T can be written as [65]:

$$N^{0\nu} = \frac{\ln 2 \cdot N_A \cdot M \cdot T \cdot \epsilon \cdot f_{ab}}{m_A \cdot T^{0\nu}_{1/2}} \tag{1.27}$$

where N_A is the Avogadro constant, m_A is the molar mass of the $\beta\beta$ emitter, ϵ is the detection efficiency of $0\nu\beta\beta$ events and f_{ab} is the isotopic abundance.

On the other hand, any $0\nu\beta\beta$ decay experiment has a background, the number of background events can be written as:

$$b = \mathrm{BI} \cdot M \cdot T \cdot \Delta E \tag{1.28}$$

where the background index (BI) is defined as the rate of background events per unity of mass, energy and time; ΔE is the search energy window of the $0\nu\beta\beta$ decay, proportional to the energy resolution of the detector.

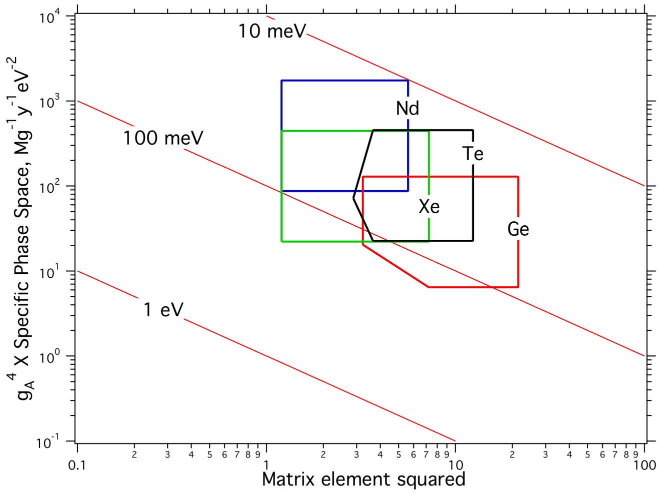

Figure 1.6: Limits on the effective Majorana neutrino mass as function of the specific phase space and the squared matrix elements for the $\beta\beta$ candidates ^{76}Ge, ^{130}Te, ^{136}Xe and ^{150}Nd. The vertical span reflects the range of g_A, the matrix elements are evaluated following all the available theoretical calculations. From [64].

The sensitivity of a given $0\nu\beta\beta$ experiment is expressed by a "detection factor of merit" $S^{0\nu}$, defined as the process half-life corresponding to the maximum signal that could be hidden by the background fluctuations. To obtain an estimation for $S^{0\nu}$ as a function of the experiment parameters, it is sufficient to require that the $0\nu\beta\beta$ signal exceeds the statistical fluctuations of the total detected counts:

$$N^{0\nu} \geq n_\sigma \sqrt{N^{0\nu} + b} \tag{1.29}$$

where n_σ is the confidence level expressed in units of σ. From Eqs. (1.27)–(1.29) can be derived the expression for the $0\nu\beta\beta$ sensitivity [48]:

$$S^{0\nu} = \frac{\ln 2 \cdot N_A \cdot \epsilon \cdot f_{ab}}{m_A} \cdot \frac{1}{n_\sigma} \cdot \sqrt{\frac{M \cdot T}{\mathrm{BI} \cdot \Delta E}} \ . \tag{1.30}$$

This formula emphasizes the role of the essential experimental parameters needed in the search of the $0\nu\beta\beta$ decay:

- detection efficiency ϵ: it depends on the experimental technique; in GERDA, ϵ is factorized into an active volume fraction and individual cut efficiencies;
- isotopic abundance f_{ab}: as already mentioned, the natural isotopic abundance of many $\beta\beta$ emitters is $< 10\%$; often is performed an isotopic enrichment to increase the abundance, which also increases the costs of the experiment;
- target mass M: the increase in target mass typically comes with a similar increase in cost;

- experimental live-time T;
- background index BI: it depends on the experimental technique and on radio-purity of material; the BI can be improved by additional cuts and techniques to discriminate signal and background events (as in GERDA);
- energy resolution: crucial parameter also to minimize the background produced by the $2\nu\beta\beta$ decay (see Fig. 1.5).

Of particular interest is the case in which BI is so low that the expected number of background events (Eq. (1.28)) is less than one count ($b \lesssim 1$) within a given exposure: this is called "background free" condition. Next generation experiments aim to this condition. As will be shown in chapter 2, the first Phase II data showed that GERDA will be the first background free experiment in the $0\nu\beta\beta$ field, since will remain in this condition up to its design exposure.

In this case the number of the background events can be considered as a constant and hence the expression of the $0\nu\beta\beta$ sensitivity of Eq. (1.30) is not more valid; now is given by [48]:

$$S^{0\nu} = \frac{\ln 2 \cdot N_A \cdot \epsilon \cdot f_{ab}}{m_A} \cdot \frac{M \cdot T}{N_s} \tag{1.31}$$

where N_s is the number of observed events in the region of interest. The advantage of the formula of Eq. (1.31) is that the sensitivity $S^{0\nu}$ grows linearly with the experimental mass and time, instead of by square root like Eq. (1.30).

1.3.2 History of the double beta experiments

Starting from the middle of the XX century, several experiments studied the $\beta\beta$ decays. In all cases the most advanced methods and detectors at that time were adopted, aiming to a background reduction more and more strict. In this section are presented the most important experiments; more on the long history of $\beta\beta$ search can be found in Refs. [66, 67].

The first experiment on the search for the $2\nu\beta\beta$ decay was performed in 1948 by Fireman with the isotope ^{124}Sn using Geiger counters; he obtained a positive result with an half-life of $T^{2\nu}_{1/2} = 4$–$9 \cdot 10^{15}$ yr [68]. This result was not confirmed later in more sensitive experiments performed in following years, the best bound for the $2\nu\beta\beta$ decay of ^{124}Sn was $T^{2\nu}_{1/2} > 2 \cdot 10^{17}$ yr [69].

The $2\nu\beta\beta$ decay was discovered for the first time in a geochemical experiment: Inghram e Reynolds in 1950 with the isotope ^{130}Te detected a signal with $T^{2\nu}_{1/2} = 1.4 \cdot 10^{21}$ yr [70]; the result initially was not considered seriously because the half-life was orders of magnitude higher than previous results. It was considered correct only after 15–20 yr.

Around the 1960 it became clear the importance of studying the $0\nu\beta\beta$ decay. Many experiments started to make an effort giving limits on the half-life of this process. A sensitivity of the order of 10^{21} yr was reached for the ^{76}Ge isotope, using a Ge(Li) detector [71], and for ^{48}Ca and ^{82}Se, with two experiments based on a streamer chamber in a magnetic field plus plastic scintillators [72, 73].

Between the 1960s and the 1970s, several research groups carried out geochemical experiments observing the $2\nu\beta\beta$ decay in ^{130}Te [74], ^{82}Se [75] and ^{128}Te [76].

In the 1980s [77] the activity on the $0\nu\beta\beta$ decay search increased strongly, in particular numerous measurements were performed with ^{76}Ge using High Purity Germanium (HPGe) detectors obtaining limits on the $0\nu\beta\beta$ half-life of 10^{22}–10^{23} yr. In the 1991 the new limit of $T^{0\nu}_{1/2} > 1.2 \cdot 10^{24}$ yr was obtained with ~ 7.2 kg of Ge detectors [78]. Two large experiments with HPGe detectors made of germanium enriched in ^{76}Ge ($^{\mathrm{enr}}$Ge) were constructed in the following years: Heidelberg-Moscow (HdM) [79, 80] and the International Germanium Experiment (Igex) [81, 82], that obtained a limit of $1.9 \cdot 10^{25}$ yr and $1.6 \cdot 10^{25}$ yr (90% confidence level (C.L.)), respectively.

A stringent limit on $0\nu\beta\beta$ decay was also obtained for the ^{136}Xe by the Gotthard experiment with a time projection chamber with 3.3 kg of xenon enriched in ^{136}Xe to 62%, the limit of $T^{0\nu}_{1/2} > 4.4 \cdot 10^{23}$ yr was obtained [83]. In the same period the Milano group operated a ^{136}Xe multiwire chamber at Laboratori Nazionali del Gran Sasso (LNGS) [84].

In this period was also observed the first $2\nu\beta\beta$ decay of ^{82}Se in a direct counter experiment with a time projection chamber [85]. The measurements of the $2\nu\beta\beta$ half-life was performed also for other isotopes with ELEGANT V [86] and the NEMO-2 detector [87, 88, 89].

In 2001, after the publication of the HdM experiment final results [80], part of the collaboration published a claim to have observed the $0\nu\beta\beta$ decay for the ^{76}Ge [90], reporting an half-life of $T^{0\nu}_{1/2} = 1.19^{+0.37}_{-0.23} \cdot 10^{25}$ yr [91]. Later, pulse shape discrimination was used to strengthen the claim [92]. This claim aroused a number of replies and was strongly criticized by many physicists [93], the situation was clarified only in 2013 by the results from the first phase of the Gerda experiment [94] that strongly disfavored the $0\nu\beta\beta$ observation (see Sec. 2.2).

1.3.3 Present status of the double beta search

The status of the $\beta\beta$ decays search is in continuous evolution: many experiments are running, under construction or proposed. The $2\nu\beta\beta$ decay have been observed in 12 isotopes (^{48}Ca, ^{76}Ge, ^{82}Se, ^{96}Zr, ^{100}Mo, ^{116}Cd, ^{128}Te, ^{130}Te, ^{136}Xe, ^{150}Nd, ^{238}U and ^{130}Ba). The updated half-lives are reported in Tab. 1.2.

Lower limits for the $0\nu\beta\beta$ half-life were established in last years by Gerda, NEMO-3 [107], EXO-200 [108], KamLAND-Zen [109], CUORE [110] and AURORA [100]. Since the work of the present thesis is performed in the framework of the Gerda experiment, the entire chapter 2 is dedicated to the description of its experimental setup and results. The other $0\nu\beta\beta$ experiments are briefly described in the following text.

The NEMO-3 detector [107] had been operating in the Modane Underground Laboratory from 2003 to 2010. It uses a tracking calorimeter technique in order to investigate double beta decay processes for different $\beta\beta$ isotopes: thin foils made out of seven $\beta\beta$ emitters are located in a drift chamber with

Table 1.2: Present $2\nu\beta\beta$ decay half-life results with respective experiments. The first error is statistical and the second is systematic.

isotope	$T_{1/2}^{2\nu}$ [yr]	experiment
^{48}Ca	$(6.4^{+0.7+1.2}_{-0.6-0.9}) \cdot 10^{19}$	NEMO-3 (2016)[95]
^{76}Ge	$(1.926 \pm 0.094) \cdot 10^{21}$	GERDA (2015) [96]
^{82}Se	$(9.6 \pm 0.3 \pm 1.0) \cdot 10^{19}$	NEMO-3 (2005) [97]
^{96}Zr	$(2.35 \pm 0.14 \pm 0.19) \cdot 10^{19}$	NEMO-3 (2010) [98]
^{100}Mo	$(7.11 \pm 0.02 \pm 0.54) \cdot 10^{18}$	NEMO-3 (2005) [97]
^{116}Cd	$(2.74 \pm 0.04 \pm 0.18) \cdot 10^{19}$	NEMO-3 (2016) [99]
^{116}Cd	$(2.62 \pm 0.14) \cdot 10^{19}$	AURORA (2016) [100]
^{128}Te	$(2.0 \pm 0.3) \cdot 10^{24}$	geochemical (1991-2008) [101]
^{130}Te	$(7.0 \pm 0.9 \pm 1.1) \cdot 10^{20}$	NEMO-3 (2011) [102]
^{130}Te	$(8.2 \pm 0.2 \pm 0.6) \cdot 10^{20}$	CUORE-0 (2016) [103]
^{136}Xe	$(2.38 \pm 0.02 \pm 0.14) \cdot 10^{21}$	KamLAND-Zen (2012) [104]
^{136}Xe	$(2.165 \pm 0.016 \pm 0.059) \cdot 10^{21}$	EXO-200 (2013) [105]
^{150}Nd	$(9.34 \pm 0.22^{+0.62}_{-0.60}) \cdot 10^{18}$	NEMO-3 (2016) [106]
^{238}U	$(2.0 \pm 0.6) \cdot 10^{21}$	radiochemical (1991) [101]
^{130}Ba	$\sim 10^{21}$	geochemical (1996-2009) [101]

a magnetic field. Outside of the drift region there is a calorimeter made of large blocks of plastic scintillator coupled to low radioactivity photomultipliers (PMTs). The tracking detector is used to identify electron tracks and can measure the delay time of any tracks up to 700 μs after the initial event. Recent published limits (at 90% C.L.) for the $0\nu\beta\beta$ half-life are $T^{0\nu}_{1/2} > 1.1 \cdot 10^{24}$ yr for ^{100}Mo [111], $T^{0\nu}_{1/2} > 2.0 \cdot 10^{22}$ yr for ^{48}Ca [95], $T^{0\nu}_{1/2} > 2.0 \cdot 10^{22}$ yr for ^{150}Nd [106] and $T^{0\nu}_{1/2} > 1.0 \cdot 10^{23}$ yr for ^{100}Cd [99].

The EXO-200 experiment [108] operates a cylindrical liquid xenon time projection chamber of 40 cm diameter and 40 cm length, enriched to 80.6% in ^{136}Xe. It is installed at the Waste Isolation Pilot Plant near Carlsbad, New Mexico. The energy resolution of around 3.5% (FWHM) is achieved by measuring both the ionization and scintillation signals. In 2014, after two years of data taking, EXO-200 set an half-life limit for the $0\nu\beta\beta$ decay of ^{136}Xe of $T^{0\nu}_{1/2} > 1.1 \cdot 10^{25}$ yr (90% C.L.) (with a sensitivity of $1.9 \cdot 10^{25}$ yr) [108].

KamLAND-Zen is a $\beta\beta$ decay experiment which exploits the existing detection infrastructure and radio-purity of KamLAND [112]. The detector consists of a spherical inner balloon located at the center of 13 tons of Xe-loaded liquid scintillator with about 320–380 kg of ^{136}Xe. The energy resolution is 9.5% (FWHM). A first experimental phase, started in 2011, was limited by the presence of an unexpected background peak from ^{110m}Ag. After a scintillator purification campaign that produced a significant background reduction, in December 2013 the second phase started. Combining the data from the two phases, the collaboration published a new lower limit for the $0\nu\beta\beta$ decay of ^{136}Xe of $T^{0\nu}_{1/2} > 1.07 \cdot 10^{26}$ yr (90% C.L.) (with a sensitivity of $5.6 \cdot 10^{25}$ yr) [109].

CUORE [113], continuation of CUORICINO [114], is a ^{130}Te experiment with TeO_2 cryogenic bolometers. The experiment is now in the final stages of construction at LNGS and consists of 19 towers containing 52 TeO_2 crystals

Table 1.3: Recent experimental lower limits on the $0\nu\beta\beta$ decay half-life for light Majorana neutrino exchange and upper limit ranges on $m_{\beta\beta}$ (both at 90% C.L.) with respective experiments. The evaluation of $m_{\beta\beta}$ is taking into account the uncertainties on the NME and PSF calculations.

isotope	$T_{1/2}^{0\nu}$ [yr]	$m_{\beta\beta}$ [eV]	experiment
^{48}Ca	$> 2.0 \cdot 10^{22}$	< 6–26	NEMO-3 [95]
^{76}Ge	$> 5.3 \cdot 10^{25}$	< 0.15–0.33	GERDA [1, 2]
^{100}Mo	$> 1.1 \cdot 10^{24}$	< 0.33–0.62	NEMO-3 [111]
^{116}Cd	$> 1.9 \cdot 10^{23}$	< 1.2–1.8	AURORA [100]
^{130}Te	$> 4.0 \cdot 10^{24}$	< 0.27–0.76	CUORE-0 [110]
^{136}Xe	$> 1.1 \cdot 10^{26}$	< 0.061–0.165	KamLAND-Zen [109]
^{150}Nd	$> 2.0 \cdot 10^{22}$	< 1.6–5.3	NEMO-3 [106]

each (in total $\sim$ 200 kg of ^{130}Te). After a commissioning phase is expected to start in 2017. A first CUORE tower was already operational (referred as CUORE-0 [110]), achieving a detector energy resolution of 5.1 ± 0.3 keV (FWHM) and a background level in the region of interest of $(5.8 \pm 0.6) \cdot 10^{-2}$ cts/(keV·kg·yr). Combining CUORE-0 and CUORICINO data a limit for the $0\nu\beta\beta$ decay of ^{130}Te of $T_{1/2}^{0\nu} > 4.0 \cdot 10^{24}$ yr (90% C.L.) was published [110]. The goal of the CUORE experiment is reach a sensitivity of $T_{1/2}^{0\nu} \gtrsim 10^{26}$ yr.

The AURORA experiment [100], in progress at LNGS, is investigating on $\beta\beta$ decays of ^{116}Cd with 1.162 kg cadmium tungstate crystal scintillators enriched in ^{116}Cd to 82%. Recently AURORA set a new limit for the $0\nu\beta\beta$ of ^{116}Cd of $T_{1/2}^{0\nu} > 1.9 \cdot 10^{23}$ yr (90% C.L.) [100].

Tab. 1.3 summarizes the most recent results on $0\nu\beta\beta$ decay, including half-life lower limits and upper limit ranges on the effective Majorana neutrino mass $m_{\beta\beta}$, evaluated using Eq. (1.15) with the commonly PSF and NME calculations (see Sec. 1.2.2) and assuming axial coupling constant $g_A = 1.269$.

The current situation on the $0\nu\beta\beta$ search is graphically shown in Fig. 1.7: the most stringent limits on $m_{\beta\beta}$ for ^{76}Ge, ^{100}Mo, ^{130}Te and ^{136}Xe are superimposed to the predictions of $m_{\beta\beta}$ from oscillations as a function of the lightest neutrino mass in case of normal (in red) and inverted (in green) hierarchy. Up to now the most stringent upper limit on $m_{\beta\beta}$ is established by the recent KamLAND-Zen result [109], value that anyway still not enters into the IH region. Besides the hope of discovering a $0\nu\beta\beta$ signal, the goal of near future experiments is the investigation of this region.

1.3.4 Future double beta experiments

In addition to the above mentioned Gerda, CUORE, KamLAND-Zen and EXO-200, many experimental double beta groups are extensively working to increase the sensitivity on the $0\nu\beta\beta$ search. Some of them are described in this section.

Majorana [115] uses similar germanium diodes like Gerda ($\sim$ 27 kg of ^{76}Ge) in vacuum in a compact cryostat made out of electro-formed copper. A new world wide collaboration, including Gerda and Majorana, has formed under the name of Legend. It aims to a ton-scale future experiment by

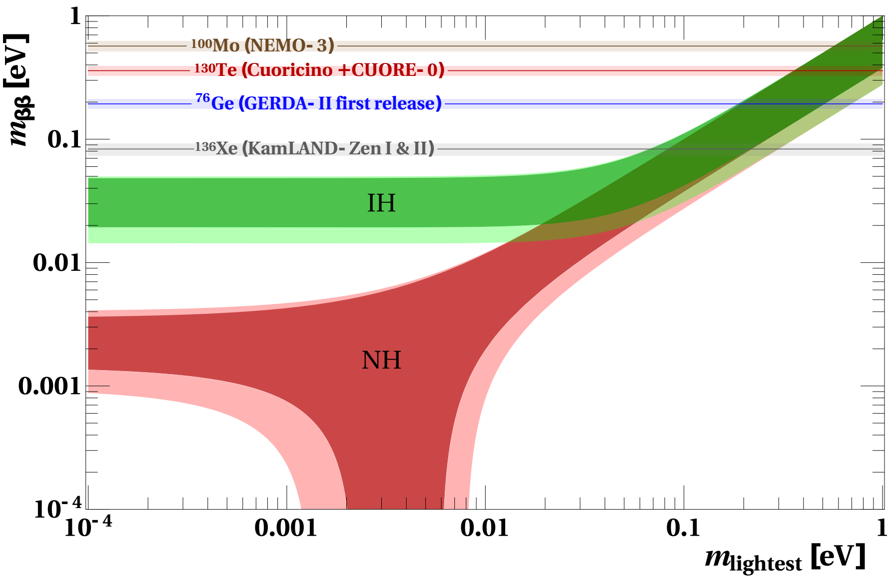

Figure 1.7: Predictions on $m_{\beta\beta}$ from oscillations as a function of $m_{lightest}$ with the relative 3σ regions for NH and IH in red and green respectively. The horizontal bands show the experimental limits for the isotopes ^{76}Ge [1, 2], ^{100}Mo [111], ^{130}Te [110] and ^{136}Xe [109]. Picture from [48].

selecting the best techniques, the goal is reach a $0\nu\beta\beta$ sensitivity up to 10^{28} yr corresponding to $m_{\beta\beta} < 10$–20 meV.

nEXO [116] is an expansion of EXO-200 by using a low background and 2.3% energy resolution. The expected half-life sensitivity for ^{136}Xe is around 10^{28} yr ($m_{\beta\beta} < 6$–15 meV) by using 5 ton of ^{136}Xe isotopes for 5 yr.

SuperNEMO [117] is a planned continuation of NEMO-3 with much improved performance (in reconstruction efficiency, energy resolution and background) that aims to study the IH region with 100 kg of ^{82}Se isotopes. The expected sensitivity on the $0\nu\beta\beta$ decay is around 10^{26} yr. A SuperNEMO demonstrator with 7 kg of ^{82}Se is in preparation.

CUPID (CUORE Upgrade with Particle Identification) [118] is a proposed ton-scale bolometer experiment that aims to reach a sensitivity for $m_{\beta\beta}$ of the order of 10 meV. The collaboration is starting with 40 crystals of Li_2MoO_4 (6 kg of ^{100}Mo).

SNO+ [119] is a large liquid scintillator-based experiment located underground at SNOLAB, Sudbury, Canada. Designed as a multipurpose neutrino experiment, the primary goal of SNO+ is a search for the $0\nu\beta\beta$ of ^{130}Te. In the first phase, foreseen for 2017, the detector will be loaded with 0.3% natural tellurium ($\sim$ 800 kg of ^{130}Te), with an expected effective Majorana neutrino mass sensitivity in the region of 55–133 meV.

Other double beta prospects with respective references are here listed: NEXT [120], LUCIFER [121], AMoRE [122], COBRA [123], LUMINEU [124], MOON [125], CANDLES [126].

1.4 Conclusions

The neutrinoless double beta ($0\nu\beta\beta$) decay is the best way to test lepton number violation and the nature of the neutrino (Majorana or Dirac type). The search of this process is up to now one of the leading fields in particle physics that is involving both theoretical and experimental groups.

In recent years progress has been done in the calculation of the expected $0\nu\beta\beta$ half-life: precise evaluation of the phase space integrals and nuclear matrix elements with different nuclear models. The critical point of determining the uncertainties is the quenching of the axial current.

From experimental point of view, some experiments (e.g. KamLAND-Zen, GERDA) are reaching $0\nu\beta\beta$ sensitivity of the order of $\gtrsim 10^{26}$ yr. Many other experiments are already running or planned. The common future goal is investigate the inverted hierarchy region and a bound for the effective Majorana neutrino mass of $\lesssim$ meV.

Chapter 2

The GERDA experiment

The GErmanium Detector Array (GERDA) [127, 128] is one of the leading experiments searching for the neutrinoless double beta decay. The recent results [2] presented at the NEUTRINO 2016 conference set a new limit for the $0\nu\beta\beta$ decay half-life of ^{76}Ge and also showed that GERDA will be the first background free experiment of the field [1].

The experiment was proposed in March 2004 [129] with the new concept of operating an array of HPGe detectors in a large volume of liquid argon [130]. GERDA is located at the Laboratori Nazionali del Gran Sasso and started its operation in November 2011. The first physics data taking, denoted as Phase I, was carried out until June 2013 with the purpose to test the HDM claim of a $0\nu\beta\beta$ signal [91]: a limit of $T^{0\nu}_{1/2} > 2.1 \cdot 10^{25}$ yr (90% C.L.) was found [94] with an exposure of 21.6 kg·yr and a background index of 10^{-2} cts/(keV·kg·yr) at $Q_{\beta\beta} = 2039$ keV; from statistical test, the compatibility of the Phase I results with the claim is 2%.

In 2013, at the completion of Phase I, the setup upgrade was started. After a commissioning phase, since December 2015 the Phase II physics data taking is ongoing. The goal is an improvement of the $0\nu\beta\beta$ half-life sensitivity to $\gtrsim 10^{26}$ yr with an exposure of about 100 kg·yr by reducing the background level of an order of magnitude with respect to Phase I.

The present chapter is organized as follow: the description of the general GERDA experimental setup is presented in Sec. 2.1; in Sec. 2.2 the physics results from Phase I are discussed; then Sec. 2.3 describes the upgrade to Phase II with particular consideration for the new Broad Energy Germanium (BEGe) detectors deployed in GERDA. Finally the commissioning runs, the final setup (Sec. 2.4) and the first results from Phase II (Sec. 2.5) are presented.

2.1 Experimental setup

GERDA is located in the Hall A of the underground Laboratori Nazionali del Gran Sasso (LNGS) [131] of INFN, one of the largest underground facility worldwide. Fig. 2.1 shows a view of the laboratory and an external picture of GERDA. A rock overburden of about 3500 m water equivalent removes the hadronic components of cosmic ray showers and reduces the muon flux by six orders of magnitude to 1.2 $\mu/(\mathrm{m}^2{\cdot}\mathrm{h})$.

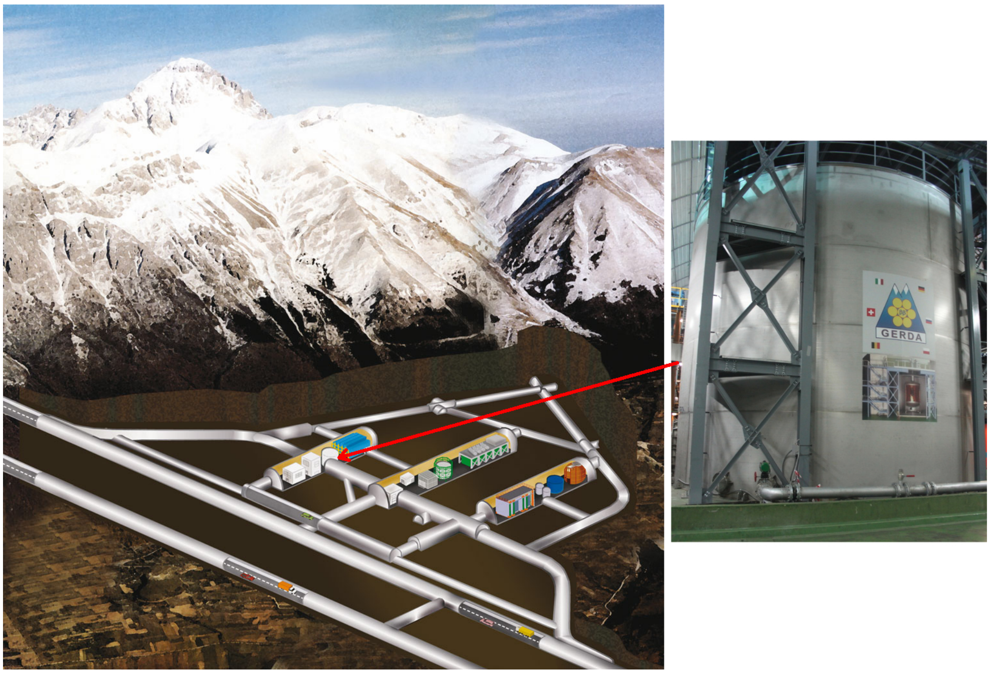

Figure 2.1: Map of the Laboratori Nazionali del Gran Sasso [131] of INFN, three main halls provides the installation of the experiments. GERDA is located in the north wing of the Hall A, occupying an area of $10.5 \times 10.4\ \mathrm{m}^2$.

The GERDA setup, illustrated in Fig. 2.2, is designed to minimize the main background sources which affected the previous generation experiments. The shielding concept follows a layers approach.

HPGe detectors, made from germanium with the ^{76}Ge isotope fraction enriched to 87% (^{enr}Ge), are exposed acting both as sources and detection media. The detectors are mounted in low mass ultra-pure holders and are directly inserted in 64 m^3 of liquid argon (LAr), acting as cooling medium and shield against external background radiation.

The argon cryostat is complemented by a water tank with 10 m diameter which further shields from neutron and γ backgrounds. It is instrumented with PMTs to veto the cosmic muons by detecting Čerenkov radiation. The muon veto hermeticity is provided by plastic scintillators installed on the top of the structure.

Above the water tank is a clean room with a glove box to handle the germanium detectors and assembly them into strings.

2.1.1 HPGe detectors

The GERDA detector array is composed of strings of two HPGe detectors types (the working principles of these detectors are described in Sec. 3.1): semi-coaxial detectors refurbished from previous experiments and newly produced BEGe detectors (described in Sec. 2.3).

The major fraction of the Phase I exposure was collected by ^{enr}Ge semi-coaxial detectors from the HDM [79] (five detectors named ANG1–5) and IGEX

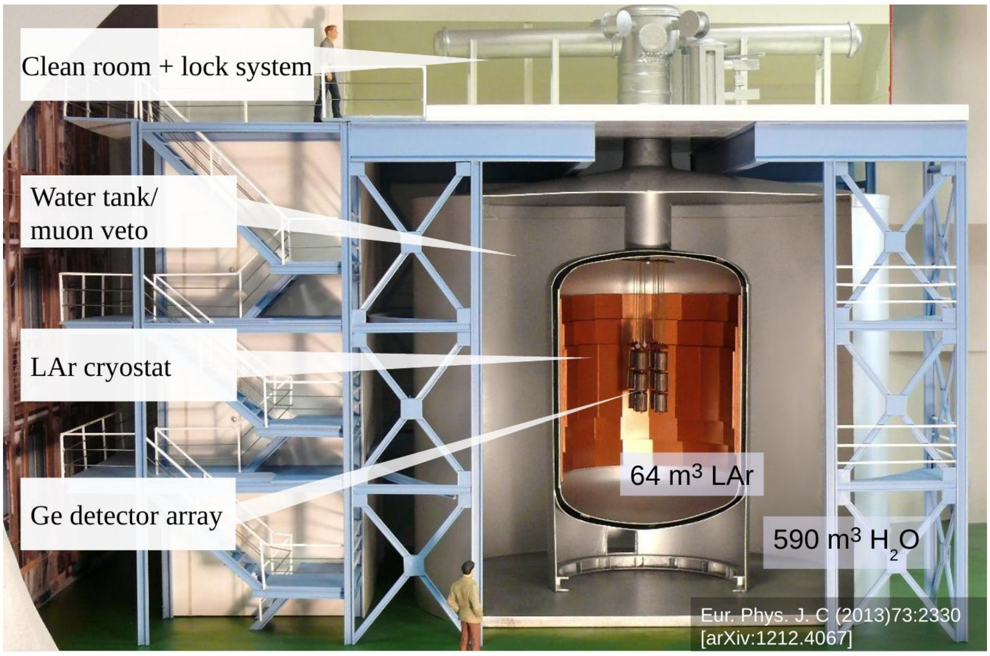

Figure 2.2: View of the GERDA experiment [127]. The germanium detector array is inserted in the LAr cryostat with an internal copper shield, all is surrounded by a water tank housing the Cherenkov muon veto.

[81] (three detectors named RG1–3) experiments. Five newly produced ^{enr}Ge BEGe detectors were also deployed at the end of Phase I. Three coaxial detectors with natural germanium (^{nat}Ge) isotopic abundance from the Genius Test Facility (GTF) project [132, 133] were also installed.

In Phase I, each string was surrounded with a 60 μm thin copper foil called mini-shroud (MS) to prevent ^{42}K migration to the detector surface. The detectors were mounted into low mass Cu holders allowing a modular assembly of multiple detectors into strings. The electrical contact to the detectors was realized with copper screws and calibrated pressure. Fig. 2.3 shows some picture of a Phase I string assembly inside the glove box.

The detector configuration and the improvements developed for Phase II are described in Sec. 2.3.

2.1.2 Data acquisition and data flow

The germanium detectors are read out with a front-end electronics that satisfy several requirements due to the non standard working conditions of GERDA. Part of the work of this thesis concerns the development and test of the new electronics for Phase II, described in chapter 3.

The signal from the detectors are digitized by a Flash Analog to Digital Converter (FADC) in a binary raw data format, that are then converted to standardized format based on the MAJORANA-GERDA Data Objects (MGDO) [134], a software library jointly developed by GERDA and MAJORANA, providing general-purpose interfaces and analysis tools to support the digital pro-

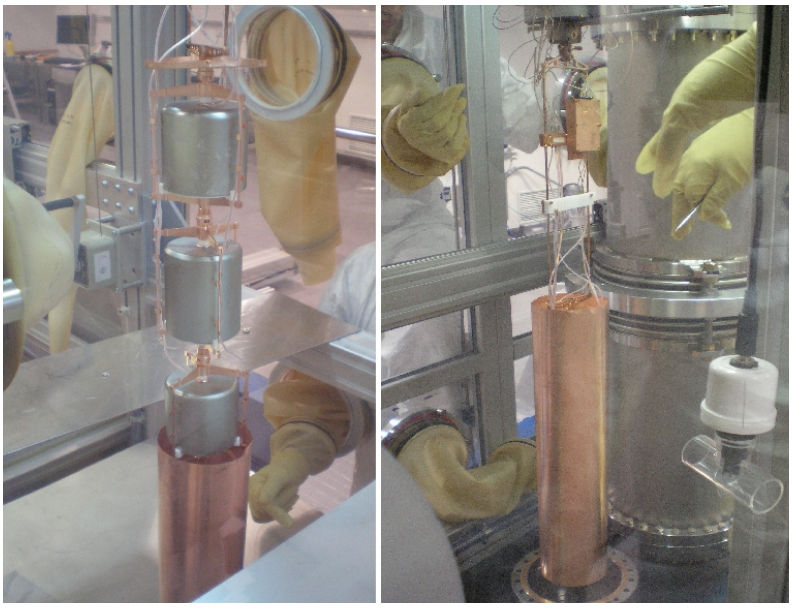

Figure 2.3: Phase I detector string mounting in glove box. Each detector string was surrounded by a thin copper Mini-Shroud.

cessing of experimental or simulated signals.

The MGDO data objects are stored as ROOT [135] files, by the conversion of raw data; the FADC provides a coarse energy estimation of the event. Those events with a FADC energy within ±25 keV from $Q_{\beta\beta}$ are blinded; they remain saved in the backup of the raw data until all the analysis criteria are finalized.

The event reconstruction is performed with Gelatio (GErda LAyouT for Input/Output) [136], a software framework that contains independent modules that are applied to the input ROOT file in order to extract several informations (e.g. energy, baseline, rise time, amplitude of the current signal). A description of the analysis modules is presented in Ref. [137].

The new procedure to extract the energy from each waveform developed for Gerda Phase II is part of this thesis and is widely described in chapter 4.

2.2 Gerda Phase I results

From November 2011 to May 2013 a global exposure of 21.6 kg·yr has been collected. Data blinding was implemented for the first time in a $0\nu\beta\beta$ experiment data analysis protocol. Events with energies close to $Q_{\beta\beta}$ were not processed. After the fine energy calibration, the pulse shape discrimination (PSD) criteria [138] and the background model [139] were finalized, the blinded events were revealed except for ± 5 keV (± 4 keV) around $Q_{\beta\beta}$ for the coaxial (BEGe) detectors; only at the very end the $Q_{\beta\beta}$ region was unblinded and analyzed.

The Gerda background model [139] predicts a flat energy distribution between 1930 and 2190 keV from Compton events of γ rays of ^{208}Tl and ^{214}Bi decays, degraded α events and β rays from ^{42}K and ^{214}Bi.

In the range $Q_{\beta\beta}$ ± 5 keV seven events are observed before the PSD, to be

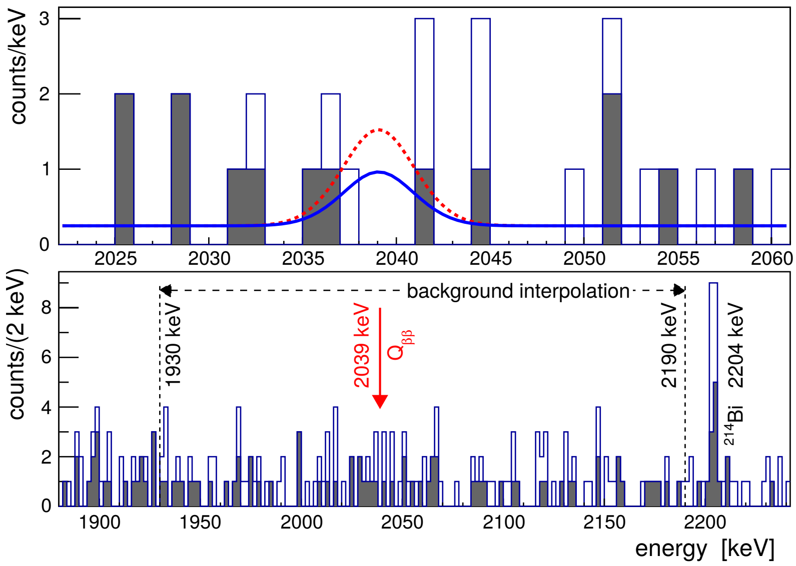

Figure 2.4: Combined energy spectrum from all ^{enr}Ge detectors without (with) PSD is shown by open (filled) histogram. The lower panel shows the region used for the background evaluation. In the upper panel, the spectrum zoomed to $Q_{\beta\beta}$ is superimposed with the expectations (with PSD selection) based on the $0\nu\beta\beta$ claim [91] (red dashed) and with the 90 % upper limit from [94].

compared to 5.1 ± 0.5 expected background counts. Three out of the six events from the semi-coaxial detectors are classified as single site event (SSE) by the artificial neural network (ANN) method [138], consistent with the expectation. The event in the BEGe dataset is rejected by the A/E cut (the powerful PSD method for the BEGe detectors that uses the ratio between the amplitude of the current pulse A and the total energy E, described more in detail in Sec. 2.3.1), hence no events remain within $Q_{\beta\beta} \pm \sigma_E$ after PSD.

The combined energy spectrum around $Q_{\beta\beta}$, without (empty) and with (filled) the PSD selection, is shown in Fig. 2.4.

To derive the signal strength $N^{0\nu}$ and a frequentist coverage interval, a profile likelihood fit was performed [94, 140]. The fitted function consists of a constant term for the background and a Gaussian peak for the signal with mean at $Q_{\beta\beta}$ and standard deviation σ_E according to the expected resolution.

The best fit value is $N^{0\nu} = 0$ that means no signal events above the background. The derived half-life limit on $0\nu\beta\beta$ decay is:

$$T_{1/2}^{0\nu} > 2.1 \cdot 10^{25}\text{yr (90\% C.L.)} \tag{2.1}$$

including the systematic uncertainty.

GERDA Phase I data show no indication of a peak at $Q_{\beta\beta}$ and the claim for the observation of $0\nu\beta\beta$ [90, 91] decay in ^{76}Ge is not supported.

This result is consistent with the limits by HDM and IGEX experiments and extending the profile likelihood fit including the data sets of those experiments the best fit yields is still $N^{0\nu} = 0$ and a new limit for the $0\nu\beta\beta$ decay is established:

$$T_{1/2}^{0\nu} > 3.0 \cdot 10^{25}\text{yr (90\% C.L.)} \tag{2.2}$$

In addition to the new limit on the $0\nu\beta\beta$, the Phase I data allowed to establish the new value for the two neutrino accompanied $\beta\beta$ decay ($T_{1/2}^{2\nu} = 1.926 \pm 0.094 \cdot 10^{21}$ yr), to search for neutrinoless $\beta\beta$ decay processes accompanied with Majoron emission (no signals were found and lower limits of the order of 10^{23} yr were set) [141] and to study the two neutrino $\beta\beta$ decay of ^{76}Ge to excited states of ^{76}Se [96] (no signal observed and new bounds determined for three transition, two orders of magnitude larger than those reported previously).

2.3 Upgrade to Phase II

The GERDA Phase II goal is the tenfold reduction of the Phase I background; this can only be achieved with an optimized experimental design. After several years of R&D, a version of the Broad Energy Germanium (BEGe) detector from Canberra with a thick entrance window has been selected. The advantages of using the BEGe detectors are their superior rejection of background with a simple and powerful analysis and their optimal energy resolution due to a very low detector capacitance.

In addition an active suppression of background by detecting the LAr scintillation light is introduced.

Fig. 2.5 shows the core of the Phase II GERDA setup: the Ge detector array, whose mass is doubled compared to Phase I, is at the center of a vetoed LAr volume.

The design allows to assemble both the detector array and the surrounding LAr veto system in the closed lock under dry nitrogen atmosphere and to lower both systems together into the cryostat.

2.3.1 BEGe detectors

The BEGe detectors for Phase II (5 of them already used in Phase I) are a modified model BE5030 available from Canberra Semiconductor (Olen) [143, 144]. A schematic view of a BEGe detector is shown in Fig. 2.6.

The detector is made of p-type HPGe with the Li^- drifted n^+ contact (0.7 mm specified thickness) covering the whole outer surface, including most of the bottom part. The small p^+ contact is located in the middle of the bottom side. The working principles of the germanium detectors are presented in Sec. 3.1.

The raw material for the BEGe diodes enriched in ^{76}Ge has been produced in form of 53.3 kg of $^{\text{enr}}\text{GeO}_2$ from ECP (Zelonogorsk, Russia) with the ^{76}Ge isotope enriched to $\sim 88\%$. The reduction and purification of the GeO_2 was achieved with an efficiency of 94% yielding 35.5 kg $^{\text{enr}}$Ge(6N) for crystal production at Canberra (Oak Ridge), a total of 9 crystals could be pulled. The crystals were cut into 30 slices and sent to Canberra (Olen) where they were transformed into working BEGe detectors with a total mass of 20.0 kg.

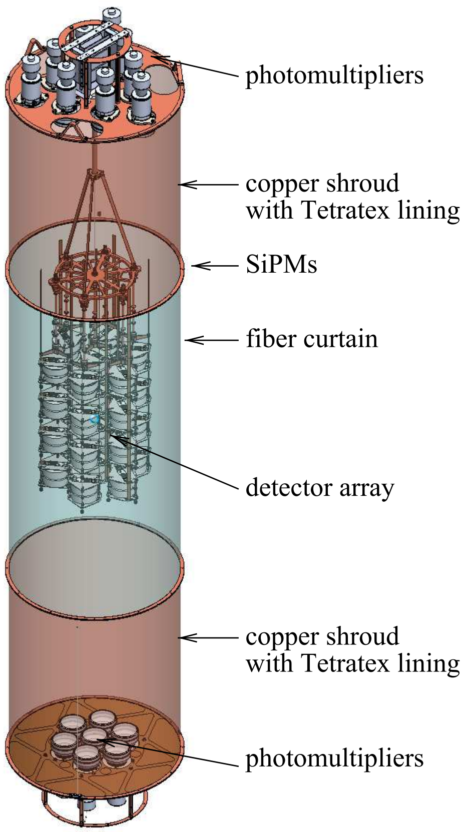

Figure 2.5: Phase II assembly of detector array and LAr veto system as it is immersed into the GERDA cryostat [142].

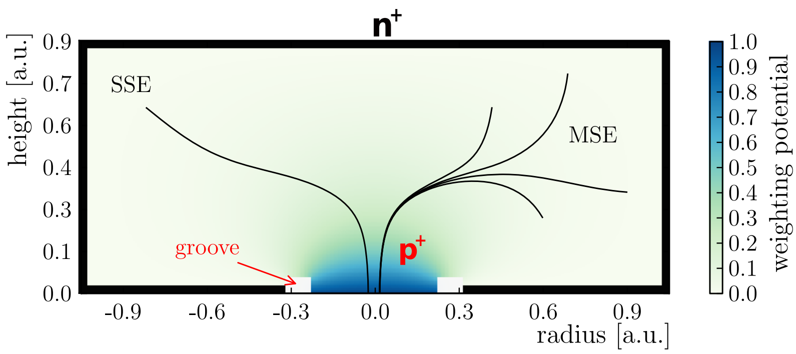

Figure 2.6: Scheme of a BEGe detector. The p^+ electrode is separated from the n^+ electrode by a groove covered by an insulating passivation layer. The weighting potential is strongest close to the p^+ electrode as indicated by the color. Examples of a SSE and a MSE events are illustrated by means of the hole trajectories of the individual energy depositions. Adapted from [143].

All detectors have been characterized in the HADES underground facility close to Olen; the relevant operational parameters including active volumes, dead layers and pulse shape performances have been defined. 29 out of 30 detectors (the only exception is GD02D) work according to specifications reaching full depletion with bias voltages below 5 kV and an energy resolution at 1.3 MeV of < 1.9 keV of FWHM when operated in a standard vacuum cryostat and standard Canberra Ge detector front-end electronics. In a final step, Al pads for wire bonding were evaporated on the p^+ and n^+ substrates of each crystal.

During all production steps, the exposure of the enriched material to the cosmic radiation has been reduced significantly by shielded transport and underground storage of the material.

The two main advantages of these detectors are their optimal energy resolution, due to the very low input capacitance ($\sim$ pF), and the powerful pulse shape discrimination. This thanks to the particular shape and configuration of the p^+ and n^+ contacts that produce a highly non-uniform electrical field (discussed in the following).

Pulse shape discrimination with BEGe detectors In the BEGe detectors the dimensionless weighting potential is strong close to the p^+ electrode, as is shown in Fig. 2.6 by the color code. A ionization inside the detector creates electrons and holes which drift due to the applied potential and the field created by the space charge of the depleted diode (see Sec. 3.1 for more details on Ge detectors). The time dependent induced current $I(t)$ on the p^+ electrode is given by the Shockley-Ramo theorem [145] as:

$$I(t) = q \cdot \vec{v}(\vec{r}(t)) \cdot \nabla\Phi(\vec{r}(t)) \tag{2.3}$$

where q is the drifting charge, $\vec{v}(\vec{r}(t))$ the drift velocity at position $\vec{r}(t)$ and Φ is weighting potential when the detector is reverse biased. The holes drift to the p^+ electrode along the central BEGe region, independently of the starting point; following Eq. (2.3), $I(t)$ has a peak at the end of the drift where $\nabla\Phi$ is largest. This means that the maximum A of $I(t)$ is directly proportional to the deposited energy E. The contribute from electrons is negligible since they drift through volumes with low $\nabla\Phi$. The result is that the A/E ratio is constant for all SSEs except for ionizations in a small volume close to the p^+ electrode

In contrast, for MSEs the energy is released in several depositions, hence the A/E of the summed signal is reduced. Fig. 2.7 shows the comparison of the charge and current pulses produced by a single site (in black) and a multi-site (in blue) event with the same energy.

For ionizations close to the n^+ contact (e.g. surface β events) the diffusion time is comparable to the drift time and hence A/E is also reduced. For p^+ surface events electrons drift through the volume with largest $\nabla\Phi$, in this case the A/E ratio is larger than for SSE. Detailed description of the BEGe behaviour depending on ionization type can be found in Refs. [146, 147].

A $0\nu\beta\beta$ signal is characterized by the absorption of two emitted β particles within a small volume of few mm^3, interpreted as SSE. On the contrary γ events

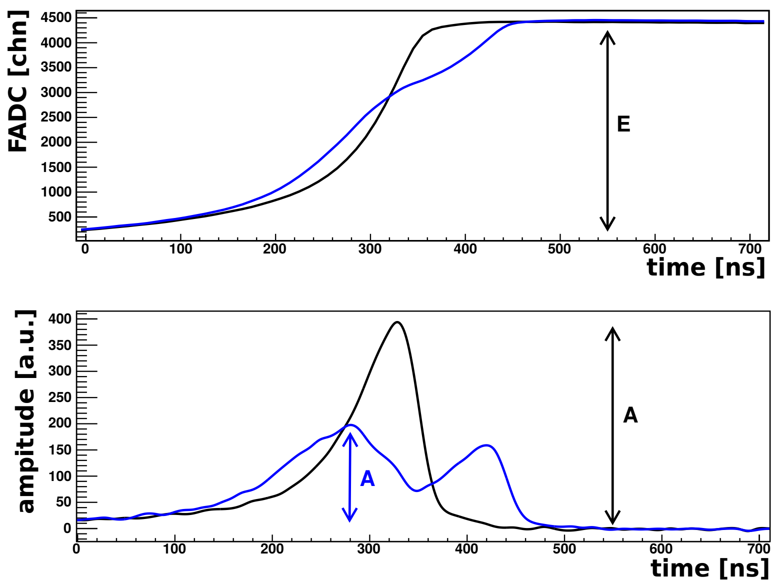

Figure 2.7: Comparison of the signal generated by a MSE (blue lines) and by a SSE (black lines). Upper and lower panels show the charge and current pulses respectively. The MSE is a superposition of two smaller pulses, the maximum of current pulses A is very different, while the energy is the same.

with similar energy can undergo multiple Compton scattering leading to MSE. Based on this pulse shape differences, background events can be efficiently identified and suppressed through the A/E ratio.

The pulse shape discrimination (PSD) power of the BEGe detectors is studied in GERDA with ^{228}Th calibration sources. The double escape peak (DEP) of the ^{228}Th 2614.5 keV photon, that shows up at 1592.5 keV, is mostly populated by SSE like the $0\nu\beta\beta$ decay. On the other hand, full energy peak (FEP), single escape peak (SEP) and Compton continua events are usually MSE. A low side A/E cut which keeps the 90% of the DEP events is set, then the survival fractions of the FEP, SEP and Compton events is studied. A high side A/E cut is needed to reject surface events occurring close to the p$^+$ electrode.

The A/E distributions of DEP events exhibits a Gaussian peak, in order to obtain a good PSD efficiency, a FWHM of $\sim 1\%$ is required.

The detailed PSD procedure adopted for BEGe detectors is described in [138, 148], the PSD efficiency obtained in the first Phase II release is presented in Sec. 2.5.

2.3.2 Liquid argon instrumentation

Fig. 2.5 shows the LAr veto instrumentation: 9 top and 7 bottom PMTs [149, 150] collect light from a LAr volume of 220 cm height and 49 diameter surrounding the Ge detector array. A curtain of wavelength shifting fibers, coupled to silicon photomultipliers (SiPMs) [151, 152], encloses the middle 100 cm length of this volume and can collect light also outside the diameter of the enclosed cylinder. Hence the diameter of the vetoed LAr volume at the Ge detector array level is enlarged.

The upper and lower parts of the vetoed volume, 60 cm in height each, consist of thin-walled (0.1 mm) copper cylinders lined by wavelength shifting reflector foils (Tetratex + TPB), while the fiber curtain is made of 1×1 mm wavelength shifting fibers coated with TPB and coupled in groups of nine to 3×3 SiPM arrays.

Pointing with their diagonals to the central axis, the total of 810 fibers covers almost 80% of the circumference.

2.3.3 Detector assembly

To provide a further background reduction a new holder for detectors, new contacts and new read-out electronics were implemented for Phase II. The development of the new electronics is active part of the present thesis and is described in detail in chapter 3.

Since the model of the GERDA Phase I background [139] showed that a large fraction of the background is originated from sources close to the Ge detectors, in Phase II most of the material close to the Ge detector array were replaced by material of higher radio-purity and reduced mass, Fig. 2.8 shows the design of the new detector holder. The Phase I spring-loaded detector contacts have been replaced by wire bonded ones. Moreover the new holder is made by a plate of 40 g of mono-crystalline silicon which is intrinsically radio-pure. The silicon plate provides also the fixation of both the signal and the high voltage (HV) contacts to the front-end electronics.

2.4 Phase II commissioning and final configuration

After several integration tests conducted in the Germanium Detector Laboratory (GDL) and in the main GERDA cryostat between the 2013 and the 2015, where germanium detectors were tested with the new instrumentations, the commissioning of the Phase II started in summer 2015. During this period I worked as active member of the GERDA Integration Team, in particular on the integration and test of the new front-end electronics with the detectors (see Chap. 3), on the preparation and maintenance of the cabling to read out the signals from Ge detectors and on the installation of the HV filters.

The preparation of a complete detector array is a delicate operation consisting in several sequential steps: first of all the detectors are mounted in the holders (two BEGes in a pair holder, see Fig. 2.8, or one coaxial in a single holder) and connected to the HV and signal cables through wire bonding; then the string is assembled with eight BEGe or three coaxial detectors per string and installed in the lock through a copper bar. Fig. 2.9 shows some step of a BEGe string assembly performed in the nitrogen flushed glove box.

The first commissioning run was performed in July 2015, 28 detectors (23 BEGe and 5 coaxial) were mounted in 5 strings. Some detector showed problems connected with the design of the new electronics front-end (see Sec. 3.4) and other detectors showed high leakage current and did not reached the oper-

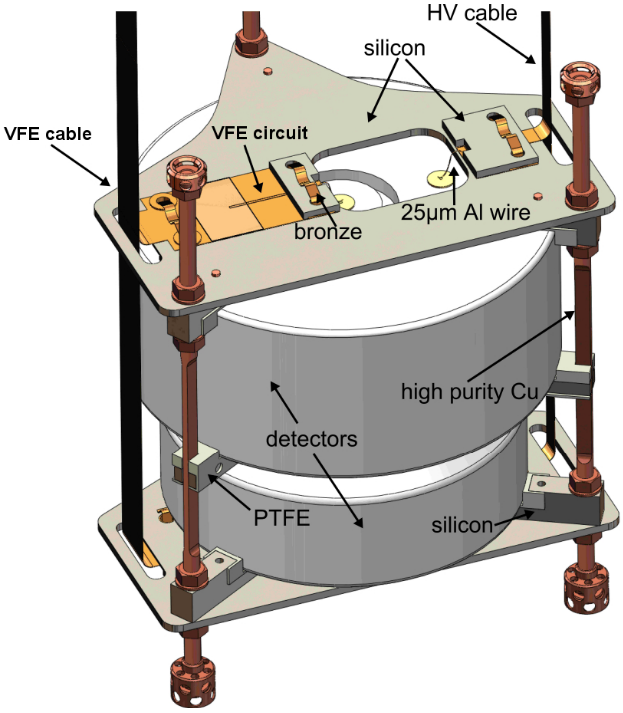

Figure 2.8: Schematic view of the new Phase II holder for a pair of BEGe detectors.

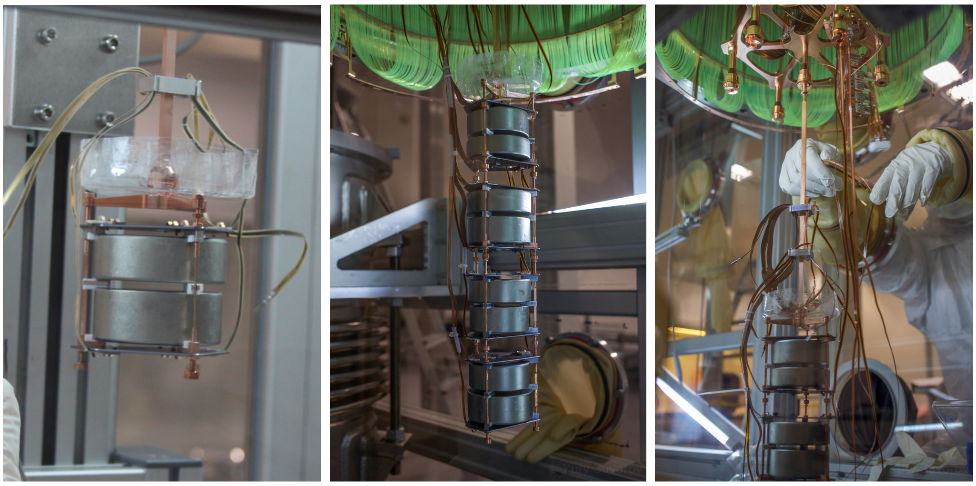

(a) (b) (c)

Figure 2.9: Steps of a BEGe string assembly: (a) mounting of a pair of BEGe detector in an holder, (b) complete string with eight detectors and (c) view of the Cu structure holding the string and the electronics front-end inside the lock.

ational voltage. In total only 15 detectors were working properly with a total mass of 12.3 kg (the performance obtained during the commissioning regarding energy resolution and discrimination power are presented in Sec. 3.5). After this run, detectors with excessive leakage current were sent to Canberra for repair.

Due to an incident during the string immersion, the second commissioning was performed in September 2015 only with only 12 detectors (8 BEGe and 4 coaxial) arranged in 3 strings. Still few detectors show an high leakage current, but the ratio of the working detectors increased with respect to the first run (see Sec. 3.5 for results).

The third commissioning run was performed in November 2015 with a total of 28 detectors (22 BEGe and 6 coaxial). In this case all the detectors worked properly, only two of them showed electronic instabilities. The achievement of this run put the basis to build the complete GERDA array.

During the commissioning runs many detectors were sent to Canberra, they underwent the groove passivation to reduce the problems of the leakage current. In addition it became clear that several BEGe detectors with excessive leakage current were facing upward, this arrangement it seems to increase the particles floating in the LAr deposit in the groove triggering the reverse current. The back-to-back detector mounting assembly (see Fig. 2.8) were modified to have the groove looking downward. As a consequence of the taken actions the fraction of detectors showing reverse current significantly decreased.

The final installation of the GERDA Phase II detectors took place in December 2015 after the detectors were reprocessed by Canberra. On December 20th, 2015 the Phase II configuration with all the detectors mounted in the array was achieved and the data taking has been started.

Fig. 2.10 shows a picture of the full array just before the immersion in LAr: seven ^{enr}Ge plus three natural coaxials and thirty ^{enr}Ge BEGe detectors for a total of 40 detectors accounting for 35.6 kg of ^{enr}Ge and 7.6 kg of ^{nat}Ge are organized in seven strings.

A schematic view of the detector arrangement and the list of the detector names is reported in App. A. The BEGe detectors (20 kg of ^{enr}Ge) are organized in three strings of eight and one string of six detectors, the coaxial detectors (15.6 kg of ^{enr}Ge) are organized in three strings of three detectors, plus one coaxial in a BEGe string. Each detector string is surrounded by a nylon mini shroud [153], preventing the ^{42}K ions from being drifted and diffused at the detector surfaces (see Sec. 5.3.3 for more details on the mini shroud).

After the immersion of the array all 40 detectors are working, most of them are at operational voltage showing a leakage current < 100 pA, three BEGe and one coaxial detectors are showing a value of leakage current $\gtrsim 100$ pA and needed a decrease of the bias voltage.

2.5 First results of GERDA Phase II

After six months of data acquisition, the first Phase II data were released and new results on the $0\nu\beta\beta$ decay were extracted [1] combining the datasets from Phase I (also including an extra period with respect to published results [94])

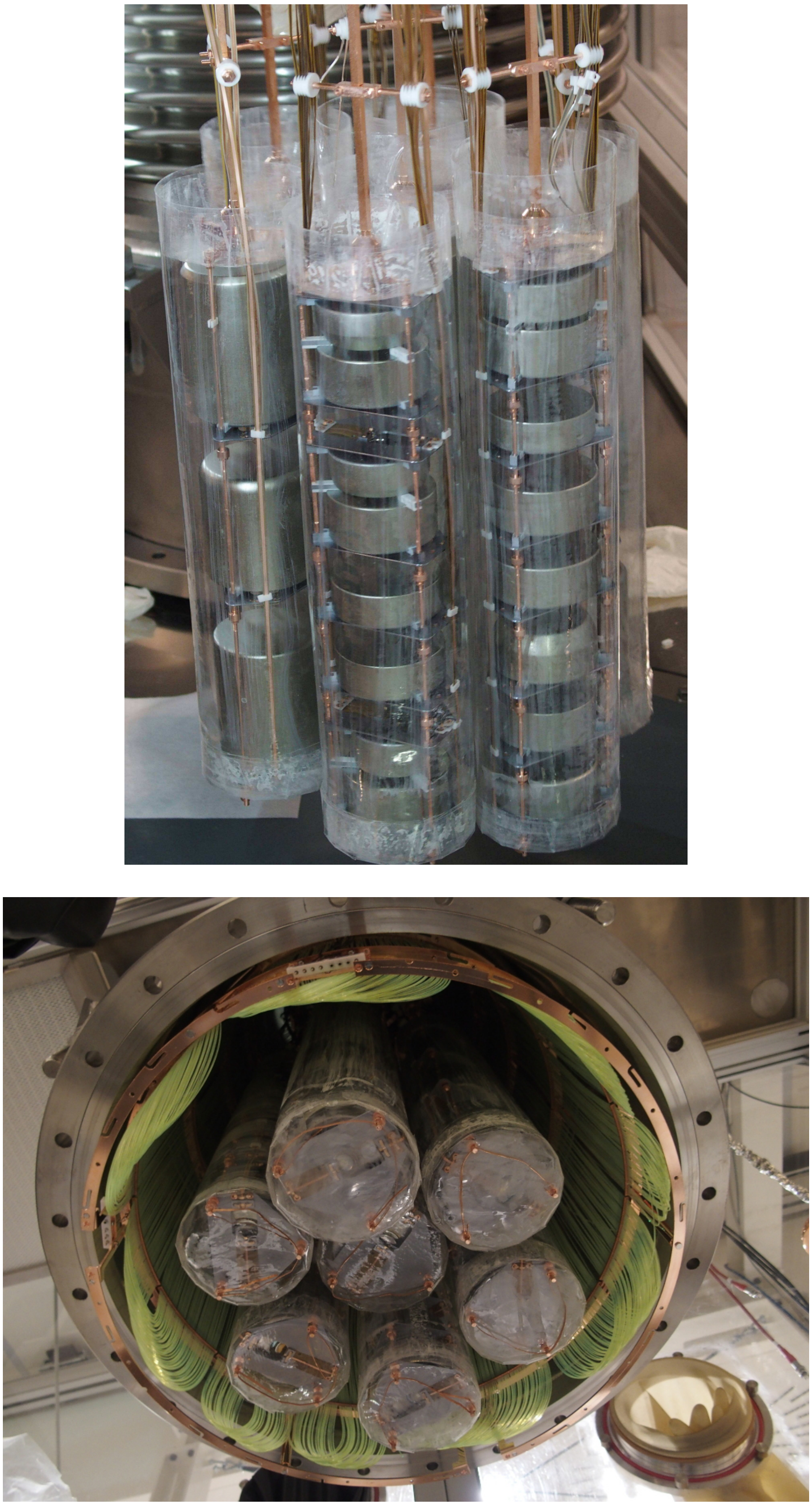

Figure 2.10: Full GERDA Phase II detector array mounted on December 2015. In the top picture, one string of coaxial and two of BEGe detectors are visible, the bottom one shows also the fiber curtain with the SiPMs.

and the new data acquired from December 2015 until June 2016, corresponding to an exposure of 10.8 kg·yr of $^{\mathrm{enr}}$Ge (5.0 kg·yr from $^{\mathrm{enr}}$Ge coaxial and 5.8 kg·yr from BEGe detectors).

During the Phase II data taking an energy region of 50 keV around $Q_{\beta\beta}$ was blinded as in Phase I. The average duty cycle is 82%, mostly due to calibrations and hardware adjustments. Only data recorded in stable conditions are used for physics analysis, corresponding to $\sim 85\%$ of the total data. In addition a set of quality cuts provide the rejection of the signals originated from electrical discharges in the high voltage line or bursts of noise [154].

The energy deposited in the Ge detectors is reconstructed offline with a digital filter developed in this thesis and described in detail in chapter 4. The procedures to determine the energy scale and the energy resolution at $Q_{\beta\beta}$ are also presented.

The cross-talk between the 40 Phase II channels has been evaluated during the thesis work, the adopted procedure and the results are reported in App. B. The average cross-talk is -0.15% and -0.41% in BEGe and coaxial strings respectively. Excluding few cases, typical values between detectors in different strings are $> -0.1\%$.

The events are rejected as background if a muon trigger occur within 10 μs, referred as muon veto (MV), or signals are detected simultaneously in multiple detectors, the anti-coincidence (AC) cut. Then, as described in Sec. 2.3, a further background suppression detecting the LAr scintillation light and through the pulse shape discrimination is applied to the events.

An event is rejected by the LAr veto if a PMT or a SiPM record a signal of amplitude above 50% of the expectation for a single photo-electron within 5 μs from the germanium trigger. Accidental coincidences between the LAr veto system and the detectors create a dead time of $(2.3 \pm 0.1)\%$.

As already discussed in Sec. 2.3.1, the PSD for BEGe detectors is based on the ratio of the peak amplitude of the current signal A and the total energy E [148]. Low values of A/E are typical for multi-site events and high values for surface events. The average survival probability of a $0\nu\beta\beta$ event is $(87 \pm 2)\%$, estimated from ^{208}Tl DEP events.

For the coaxial detectors the PSD is based on two neural networks to discriminate multi-site and degraded α events. The first one is identical to the one used in Phase I [138, 155] and shows a $0\nu\beta\beta$ survival fraction of $(85 \pm 5)\%$. The second neural network algorithm is applied for the first time and identifies surface events on the p$^+$ contact, in this case the survival probability of a $0\nu\beta\beta$ event is $(93 \pm 1)\%$. The combined PSD efficiency for coaxial detectors is $(79 \pm 5)\%$.

Fig. 2.11 shows the Phase II spectra separately for coaxial (a) and BEGe (b) detectors. The prominent features of the spectra and the visible γ peaks are part of the studies of the present thesis and are discussed in chapter 5. The light Grey spectra in Fig. 2.11 show the effect of the LAr veto (i.e. a factor ~ 5 reduction at K lines and ~ 2 in the range 1940–2140 keV), then the background is further reduced by applying the pulse shape discrimination cut (red spectra).

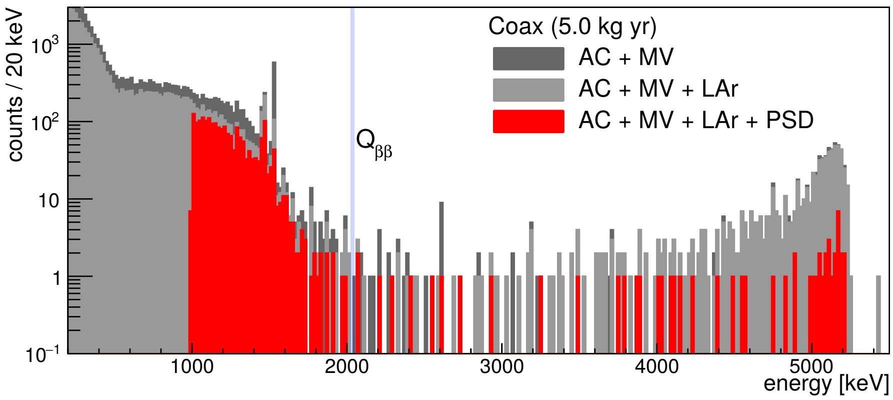

(a) $^{\rm enr}$Ge coaxial detectors.

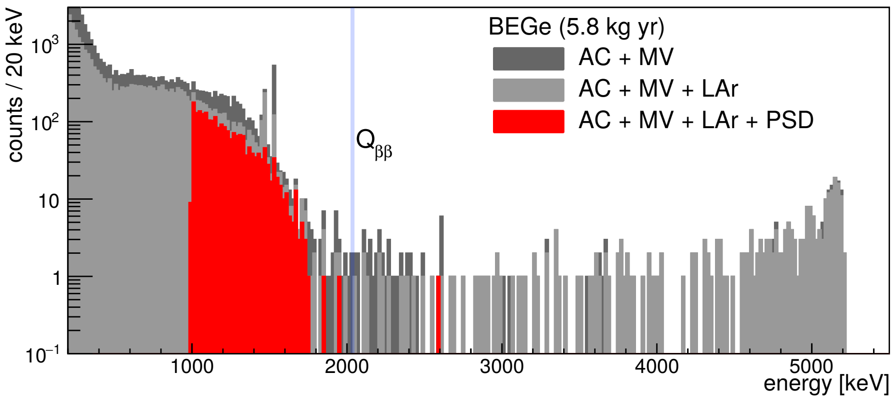

(b) BEGe detectors.

Figure 2.11: Full energy spectrum of first Phase II release for $^{\rm enr}$Ge coaxial (a) and BEGe (b) detectors. The dark-gray spectra are obtained after anti-coincidence (AC) and muon veto (MV) cuts, the light-gray ones include the liquid argon veto (LAr), in red are reported the final spectra after the pulse shape discrimination (PSD).

$0\nu\beta\beta$ **analysis** The blinded events in the $Q_{\beta\beta}$ region were processed after fixing all data selection criteria and analysis parameters. Tab. 2.1 lists the relevant parameters for the datasets used in the new $0\nu\beta\beta$ analysis: three datasets from Phase I already used in previous publication [94], the additional Phase I exposure (called "Phase I extra") and the new Phase II data (labeled as "Phase IIa").

The analysis range is from 1930 to 2190 keV without the intervals (2104 ± 5) keV and (2119 ± 5) keV of known γ-lines predicted by the background model [139]. For the coaxial detectors four events survive the cuts, corresponding to a background index of $3.5^{+2.1}_{-1.5} \cdot 10^{-3}$ cts/(keV·kg·yr), a reduction by a factor of three compared to Phase I (see Tab. 2.1). Thanks to the better PSD performance, only one event remains in the BEGe data which corresponds to BI $= 0.7^{+1.1}_{-0.5} \cdot 10^{-3}$ cts/(keV·kg·yr). These results show that the challenging background goal of Phase II has been achieved.

Fig. 2.12 shows the final spectra in the blinded region: Phase I data (23.6

Table 2.1: List of datasets used in the new $0\nu\beta\beta$ analysis [1]: exposures (for total mass), energy resolutions in FWHM, efficiencies (including enrichment, active mass, reconstruction efficiencies and dead times) and background indices (BI) in the analysis window.

dataset	exposure [kg·yr]	FWHM [keV]	efficiency	BI [cts/(keV·kg·yr)]
Phase I golden	17.9	4.3 (1)	0.57 (3)	$11 \pm 2 \cdot 10^{-3}$
Phase I silver	1.3	4.3 (1)	0.57 (3)	$30 \pm 10 \cdot 10^{-3}$
Phase I BEGe	2.4	2.7 (2)	0.66 (2)	$5^{+4}_{-3} \cdot 10^{-3}$
Phase I extra	1.9	4.2 (2)	0.57 (3)	$5^{+4}_{-3} \cdot 10^{-3}$
Phase IIa coax	5.0	4.0 (2)	0.51 (7)	$3.5^{+2.1}_{-1.5} \cdot 10^{-3}$
Phase IIa BEGe	5.8	3.0 (2)	0.60 (2)	$0.7^{+1.1}_{-0.5} \cdot 10^{-3}$

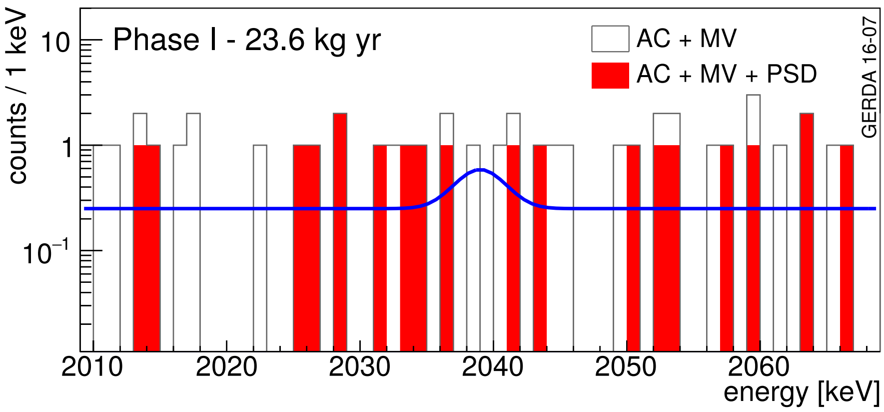

(a) $^{\mathrm{enr}}$Ge coaxial Detector.

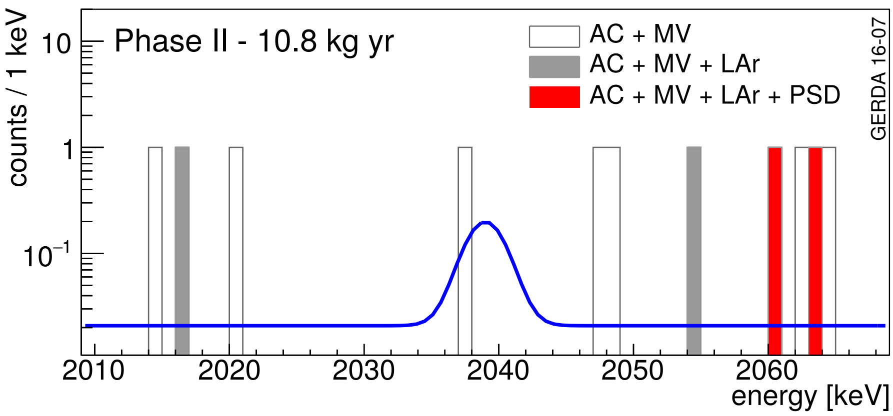

(b) BEGe detectors.

Figure 2.12: Zoom on the region around $Q_{\beta\beta}$. Left: Phase I data, right: first Phase II data. The abbreviations are the same of Fig. 2.11. The blue lines show fitted background level and 90% C.L. limit on $0\nu\beta\beta$ decay.

kg·yr) and new Phase II data (10.8 kg·yr). At $Q_{\beta\beta} \pm 30$ keV only two events survives all the cuts (Fig. 2.12(b)): the closest is at 20 keV from $Q_{\beta\beta}$.

Both a Frequentist and a Bayesian analysis based on an unbinned extended likelihood function were performed combining Phase I data and the new data (more detail on these statistical methods are discussed in Sec. 6.1). The fit function for every dataset is a flat distribution for the background (one free parameter per set) and for a possible signal a Gaussian centered at $Q_{\beta\beta}$ with a width according to the corresponding resolution listed in Tab. 2.1.

In the Frequentist analysis the best fit yielded no $0\nu\beta\beta$ signal, setting a 90% C.L. limit on the ^{76}Ge $0\nu\beta\beta$ decay half-life:

$$T^{0\nu}_{1/2} > 5.3 \cdot 10^{25} \text{ yr} . \tag{2.4}$$

The result is close to the median sensitivity of $4.0 \cdot 10^{25}$ yr (90% C.L.).

The Bayesian fit for a prior flat in $1/T$ yields a limit of $T^{0\nu}_{1/2} > 3.5 \cdot 10^{25}$ yr (90% credible interval (C.I.)). The sensitivity assuming no signal is $3.1 \cdot 10^{25}$ yr (90% C.I.).

The first data from Phase II showed the quality of the GERDA design and the effectiveness of background suppression techniques, consisting in the powerful pulse shape discrimination of BEGe detectors and the detection of the argon scintillation light. GERDA is the first background free experiment in the field, since it will remain in the background free condition up to its design exposure. Therefore the sensitivity grows approximately linearly with exposure. In three years of data taking the background level will lead to a sensitivity for the $0\nu\beta\beta$ decay up to 10^{26} yr.

Chapter 3

Germanium detectors readout electronics in GERDA

The requirement of both ultra-low background and cryogenic operation are stringent conditions for the design and manufacturing of the GERDA readout electronics. In the framework of the setup upgrade to the second experimental phase, a not minor fraction of this thesis work focused on the development, test and integration of the front-end electronics to read signals from germanium detectors.

In Sec. 3.1 a brief introduction on the working principles and the common configurations of germanium detectors are presented. Then the core of the chapter is described. Sec. 3.2 reviews the typical readout of a germanium detector. In Sec. 3.3 the solution adopted in Phase I is presented: the trade off between minimizing the background and maximizing the energy resolution defined the location of the front-end electronics. In order to optimize the detector performances, a new front-end electronics design has been proposed for Phase II that is reviewed in detail in Sec. 3.4. The tests performed during the Phase II commissioning, the results and the final front-end electronics configuration are summarized in Sec. 3.5.

3.1 Germanium detectors

Germanium detectors are ionization detectors largely adopted in γ spectrometry. They are characterized by an excellent energy resolution, a response proportional to the absorbed energy and a good full-energy peak efficiency.

They can detect:

- photons, by photoelectric effect (transferring the energy to an electron), Compton scattering (scattering with loosely bound electrons) and pair production (if the energy is larger than the e^+–e^- pair mass of 1022 keV);
- electrons and positrons, via ionization (scattering with other electrons in the material) or Bremsstrahlung (scattering in the strong Coulomb field of a nucleus);

- α particles, via inelastic collision with atomic electrons (described by the Bethe-Bloch formula).

Germanium is a semiconductor material having a fully occupied valence band, as for the insulators, but with band-gap of the order of 1 eV only (while in insulators is $\sim$ 10 eV) so that the thermal excitation is enough to move electrons to the conduction band, creating the so called leakage current. When a semiconductor is used as particle detector, the leakage current induces noise in the signal, which can be reduced by operating the detector at cryogenic temperature.

In real semiconductors some impurities, affecting the band levels and the conductivity, are always present. To take advantage of the semiconductor properties, the impurities are inserted in controlled way in order to introduce band levels: this operation is called doping. In the case of germanium with four valence electrons, the n-type doping consists in the introduction of an atom with five valence electrons, producing an electron in excess and the atom is called donor; the p-type doping is when an atom with valence three is present, a hole is generated and the atom is called acceptor. For germanium, the n-type (or n^+) junction is normally obtained via lithium deposition and drift for a thickness of about 0.5–2 mm, while the p-type (p^+) junction is done via boron implantation for a thickness of few dozens nm.

The semiconductor detectors are based on a p-n junction, creating an electrostatic system named diode. In the junction, the free electrons and holes present in the n-type and p-type region diffuse into the opposite materials, hence generating a region depleted of free charge carriers. This region is called depletion zone and is used as the active volume of a semiconductor detector in which particle interaction creates electron-hole pairs that can be collected. Normally the depletion zone is very small, it can be significantly extended by applying a bias voltage of the order of a few kV: a positive voltage applied to the n-type side further depletes electrons, a negative voltage to the p-type side depletes holes. The voltage required to achieve full depletion of the crystal is the depletion voltage.

When a particle enters the depletion region, it releases energy creating electron-hole pairs, the produced charge Q is proportional to the released energy E:

$$Q = \frac{E \cdot e}{\eta} \tag{3.1}$$

where $e = 1.6 \cdot 10^{-19}$ C is the elementary charge, η is the average energy required to create an electron-hole pair. In Ge ($\eta = 2.96$ eV) a released energy of $E = 1$ MeV produces a charge of $Q = 54$ fC.

Moreover, the leakage current increases with the applied voltage, with strong consequences on the electronic noise. For these two reasons it is necessary to minimize the impurities of the semiconductor. One of the most extensively employed types of detectors are the High Purity Germanium (HPGe), where the impurities concentration is $\sim 10^{-13}$ atoms/Ge.

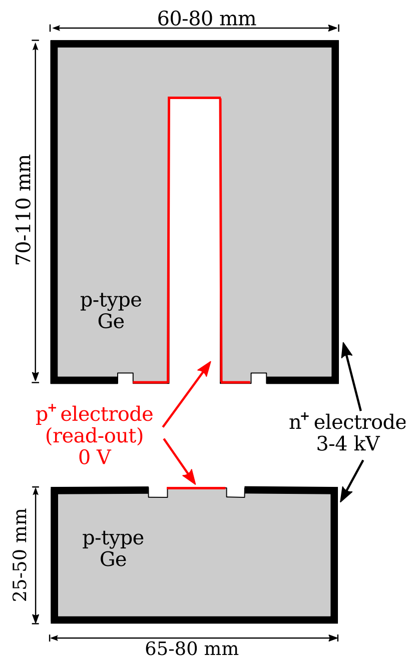

Figure 3.1: Schematic view of a semi-coaxial HPGe detector (top) and a BEGe detector (bottom) with their different surfaces and dead layers.

3.1.1 Configurations of Ge detectors

High Purity Germanium detectors are produced in various configurations. In the planar geometry the p^+ and n^+ contacts are on the basis of a cylindric crystal, in a p-type detector the HV is applied to the n^+ contact and the signal is read out on the p^+.

A largely used geometry is the coaxial one: it consists of a cylinder with a central bore hole. In p-type detectors the n^+ contact, a Li-diffused thick dead layer, is present in all the detector surface, except the bore hole where the p^+ contact is obtained via boron implantation. The n^+ and p^+ contacts are separated by a groove, which is typically passivated. The dimensions of a semi-coaxial detector can range from $\sim$ 4 cm to $\sim$ 10 cm in both diameter and height, while the bore hole diameter is $\sim$ 1 cm. The most common HPGe coaxial detector commercially available is the semi-coaxial (or close-ended) type, where the bore hole has not the same height of the cylinder.

Another type of germanium detector, relevant in GERDA, is the Broad Energy Germanium (BEGe) detector, installed in GERDA Phase II and described in Sec. 2.3. Fig. 3.1 shows a schematic view of the semi-coaxial and the BEGe detector.

To determine the drift velocity of the charged particles in the detectors, is needed the study of the electric field, solving the Poisson equation $\nabla^2\varphi = -\rho/\varepsilon$ (where $\rho = -eN$, N is the impurities concentration). In the coaxial geometry the field can be expressed as [156]:

$$E(r) = \frac{\rho}{2\varepsilon}r - \frac{V + (\frac{\rho}{4\varepsilon})(r_2^2 - r_1^2)}{r\ln(r_2/r_1)} \tag{3.2}$$

where r_1 and r_2 are the internal and external radius of the coaxial detector, V is the applied voltage and ρ the impurities density.

The detector capacitance is a crucial parameter, the energy resolution depends on it (as will be presented in the following). In HPGe coaxial detectors the capacitance per unit length is $C_{det} = 2\pi\varepsilon/\ln(r_2/r_1)$, reducing r_1 it can be minimized, usually $C_{det} \sim 30$ pF.

When a cloud of electron-hole pairs is created, they are attracted to the opposite electrodes due to the presence of the electric field. The time dependent charge $Q(t)$ and the induced current $I(t)$ on the p$^+$ electrode are given by the Shockley-Ramo theorem [145] as:

$$Q(t) = -Q \cdot [\Phi(\vec{r_h}(t)) - \Phi(\vec{r_e}(t))] \tag{3.3}$$

$$I(t) = Q \cdot [\vec{v_h}(\vec{r_h}(t)) \cdot \nabla\Phi(\vec{r_h}(t)) - \vec{v_e}(\vec{r_e}(t)) \cdot \nabla\Phi(\vec{r_e}(t))] \tag{3.4}$$

where Q is the total charge generated by the incoming particle, $v_{\vec{h(e)}}(r_{\vec{h(e)}}(t))$ the drift velocity at position $r_{\vec{h(e)}}(t)$ for the holes (electrons) at time T and Φ is the weighting potential.

The weighting potential can be calculated solving the Poisson equation; for an arbitrary detector geometry it is possible only with numerical methods. For BEGe detectors a computation of the signal pulses can be found in Ref. [147].

3.2 Signal readout with germanium detectors

The front-end electronics for a germanium detector operating as a fully depleted reverse-biased diode is a charge sensitive preamplifier (CSP). Its primary function is to extract the signal from the detector preserving the intrinsic signal-to-noise ratio while transforming a charge into a voltage signal.

The classical CSP consists of a Junction Field-Effect Transistor (JFET) as input device and a subsequent amplifier, both coupled to an RC feedback circuit. The capacitor integrates the charge generating a steep change in voltage at the output. The resistor, connected in parallel to the capacitor, is needed to restore the voltage to its baseline value.

The CSP output signal is characterized by a fast step with a rise time of 10–100 ns and an exponential tail that can be written as [157]:

$$V_o(t) = \begin{cases} -\frac{Q}{C_F} \cdot \frac{1-e^{-t/\tau_F}}{t_0/\tau_F} & 0 \le t < t_0 \\ -\frac{Q}{C_F} \cdot \frac{(e^{t_0/\tau_F}-1)}{t_0/\tau_F} e^{-t/\tau_F} & t \ge t_0 \end{cases} \tag{3.5}$$

where Q is the charge released in the detector, t_0 is the duration of the signal, C_F and R_F are the feedback capacitor and resistor, $\tau_F = C_F \cdot R_F$ is the time constant of the circuit. Since generally $t_0 \ll \tau_F$, Eq. (3.5) can be simplified as:

$$V_o(t) = -\frac{Q}{C_F} \cdot e^{-t/\tau_F} \ . \tag{3.6}$$

For germanium detectors operated in standard conditions in a cryostat, the input JFET and the feedback components of the CSP are located as close as possible to the detector in order to reduce the electronic noise, the rest of the circuit is located at room temperature at a small distance, within 0.5 m.

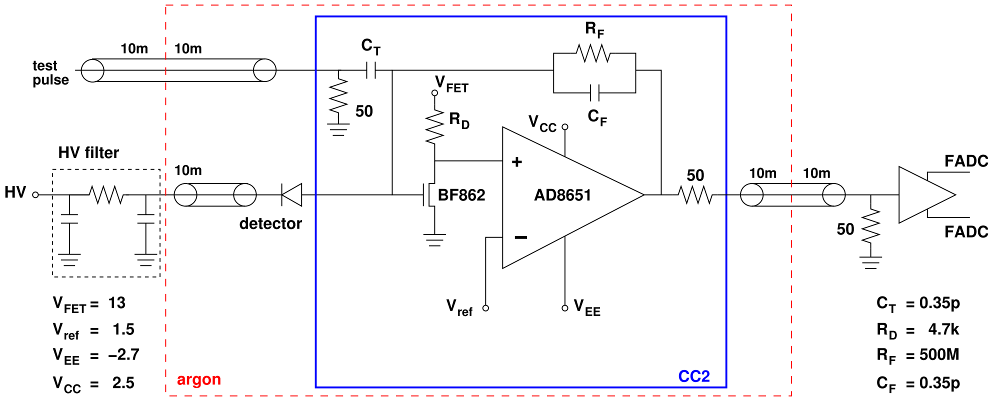

Figure 3.2: The scheme of the Phase I front-end circuit including grounding and cable lengths. The parts within the dotted box are on the CC2 CSP. The red dashed line shows the limits of the argon volume. The resistor values are given at room temperature. From [127].

In GERDA this scheme cannot be implemented as the distance from the detectors to the room temperature exceeds 10 m. The signal propagation time to close the feedback loop would consequently be longer than 100 ns. This would limit the bandwidth or lead to oscillations and the pulse shape information would be largely lost. Hence in the GERDA setup the CSP is entirely working at cryogenic temperatures.

3.3 Front-end electronics for Phase I

A few circuits have been designed and tested as the front-end electronics of the GERDA experiment, e.g. the "PZ0" CSP [158, 159]. After several tests, the preamplifier chosen for the Phase I was the "CC2" CSP [160], a low-noise hybrid CSP, based on 2 main active components: the BF862 n-channel JFET (NXP Semiconductors) as input stage and a subsequent CMOS AD8651 (Analog Devices) operational amplifier. Both components are used in commercial packages.

Specific design attention has been dedicated to both the circuit schematic (visible in Fig. 3.2) and the Printed Circuit Board (PCB) layout in order to achieve high immunity to the electrical disturbances conducted by the low voltage power supply cables. In the final scheme, the CC2 is a PCB printed on an high-purity Cuflon® substrate (delivered by Poliflon [161]), 3 channels are integrated on a single layer (see Fig. 3.3(a)).

The CC2 is located inside a copper box that provides electromagnetic shielding. The input wires connecting to the detectors are copper strips with PTFE tube insulators. All copper strips are fixed along the detector supports to avoid microphonics. Fig. 3.3(b) shows the CC2 circuit connected to a Phase I coaxial detector string.

The CC2 with the component values given in Fig. 3.2, has: dynamic range of at least 10 MeV, power consumption of less than 45 mW/channel, cross talk between channels of less than 0.1%, rise time of typically 55 ns and decay time

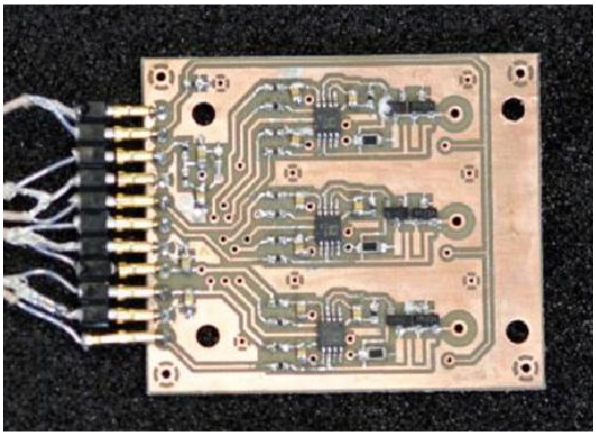

(a) CC2 CSP

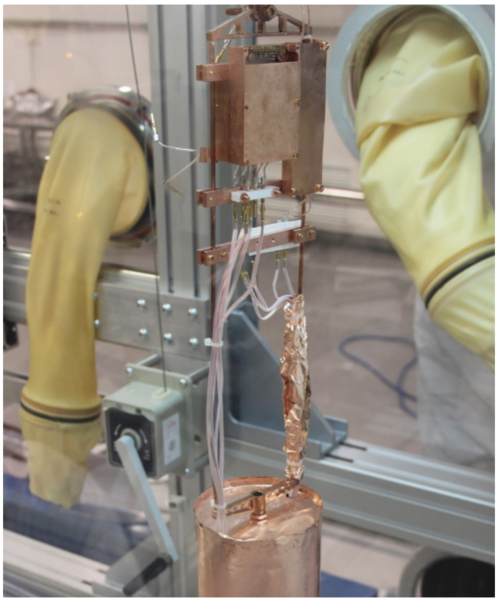

(b) Phase I detector string

Figure 3.3: (a) The CC2 CSP manufactured on a Cuflon® PCB with radio-pure components, also input and output connectors are visible. (b) Phase I BEGe detectors string coupled with the three channels CC2 preamplifier inside a copper box about 30 cm above the string.

of 180 μs. For a 600 g coaxial detector the energy resolution achieved was 1.96 keV at the 1274 keV γ-line of ^{22}Na (that correspond to $\sim$ 0.15%).

A pulser signal is sent periodically to the test pulse input of the CC2. The voltage step at the capacitor C_T injects a fixed charge at the input of the CC2 and thus allows a monitoring of the entire readout chain during data taking.

3.4 New Phase II front-end electronics

The front-end configuration for GERDA Phase II aimed at both the reduction of the radioactivity budget from the CSP and the improvement of the performance in terms of noise, bandwidth and energy resolution.

To achieve these requirements the split of the CSP in two sections was attempted: the very front-end (VFE) section, mounted close to the detector and consisting of the input JFET and feedback components, and a main amplifying section with the rest of the circuit.

In this context two new CSP have been proposed and tested: the GeFRO CSP [162, 163], an extremely radio-pure and innovative solution with the VFE alone in the cryostat and the amplifying circuit at room temperature, and a revised Phase I front-end electronics, the CC3 CSP [164, 165].

In the GeFRO the output of a slow feedback loop, optimized for the maximum achievable closed-loop bandwidth, and a feedback diode (instead of the RC devices) was providing the energy information, while a fast open loop output provides the complementary information at high frequency.

After several tests performed from 2011 to 2013, the CC3 has been selected as new front-end device for Phase II, since it was showing better performance in terms of energy resolution and stability. The GeFRO behavior was strongly dependent on the input signal rate: with a rate order of few 100 Hz, relevant for calibrations, the energy resolution was degraded as the circuit suffered of gain variations (a detailed description is reported in [166]).

The CC3 has the same conceptual scheme of the CC2, with the big difference of the attempt to separate the CSP in two stages: the VFE section designed to be positioned very close to the detector with extremely radio-pure components, and the rest of the CC3, about 1 m far away. Fig. 3.4 shows the scheme of the new circuit: the green box includes the VFE section, the blue box includes the main section. Both will be reviewed in detail in the following.

3.4.1 Very front-end section

One of the main challenges in the development of the new front-end electronics for Phase II was to accomplish the stringent radio-purity requirement for the realization: a total activity per detector of $\sim$ μBq in the most relevant isotopes ^{228}Th and ^{226}Ra.

After several implementations the final design of the VFE stage is a flex cable made on a Pyralux® substrate (by Tecnomec [167], 3 mils of thickness and up to 1 m long); at the detector side the electronic components are located and contacted, at the other side the connections to the second stage are printed. The flex cable is designed as a coplanar waveguide of $\sim$ 50 Ω impedance. It

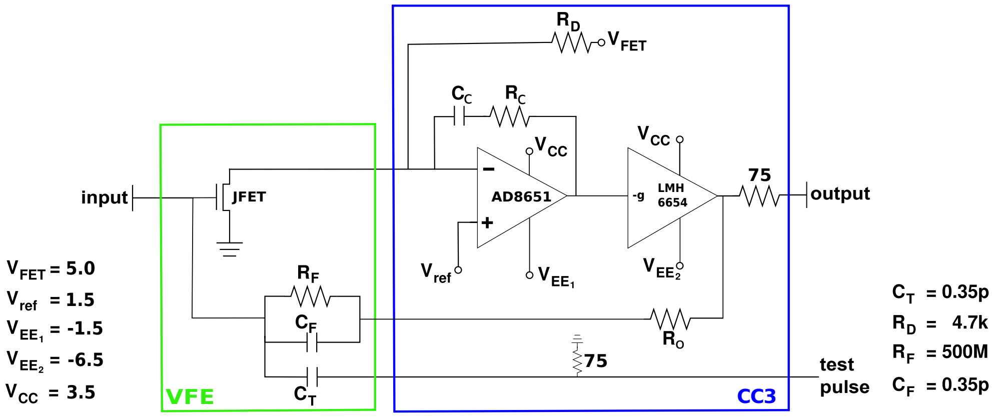

Figure 3.4: Scheme of GERDA Phase II front-end electronics: the CC3 CSP. The green box includes the VFE section, containing input JFET, feedback components and test capacitor, the blue box includes the main section of the CSP, where 2 operational amplifiers and passive components are placed.

drives three signals (the thin Cu traces visible in Fig. 3.5(a)): the input test, the JFET output signal and the feedback signal. The flexibility allowed to route the cables along the detector string avoiding connection at the detector level.

Fig. 3.5(a) shows a picture of the VFE circuit. The JFET SF291 (by Semefab [168]) replaces the BF862 of Phase I. The latter is not a good candidate as it is commercially available only in the standard package, hence is not fitting the radio-purity requirements. The SF291 features are comparable to the BF862's and it is available in die. Its measured activity is < 4.5 μBq of ^{228}Th and 1.3 ± 0.4 μBq of ^{226}Ra [169]. The feedback and test capacitors (of 0.35 pF nominal value) are the strays of custom designed copper traces. The feedback resistor (still not mounted in Fig. 3.5(a)) is a 500 MΩ in 0402 SMD size with a specific activity of 0.2 ± 0.1 μBq of ^{228}Th and 0.7 ± 0.1 μBq of ^{226}Ra [170].

A picture of the assembly of 2 BEGe detectors, made of extremely radio-pure materials (copper, silicon and teflon) is shown in Fig. 3.5(c). The silicon plate provides the fixation of the VFE cable through bronze springs and an aluminum bonding wire connects the detector to the cable.

The radioactivity requirements impose the use of a die JFET electrically connected through bonding wires. Critical issues in the realization of the VFE are the JFET die-attach and electrical contact on the substrate:

- the JFET die-attach requires an adequate glue with low radio-activity and cryogenic. As the original SF291 had the gate contact on its back, a conductive glue was required. A gold eutectic bonding onto Si chips properly shaped was attempted; this solution was poorly stable at low temperatures and was abandoned when the Semefab provided the front contacted JFET; the die-attach was then realized with the Stycast® 2850FT, a two component glue with a low coefficient of thermal expansion and that provides an excellent insulation;

- the JFET wire bonding operations have been made critical by the flexi-

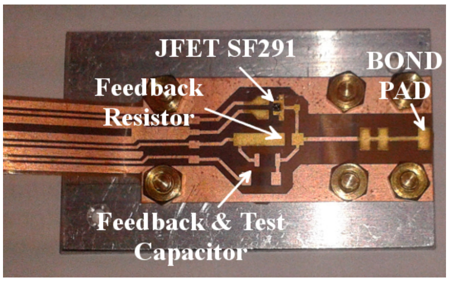

(a) VFE section circuit: JFET SF291, capacitors designed with copper traces, feedback resistor (still not installed) and bond pad to connect the detector.

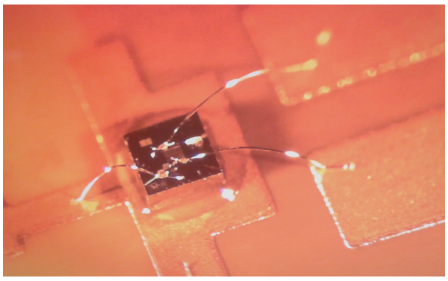

(b) Zoom of a JFET SF291 bonded with the TPT machine at LNGS.

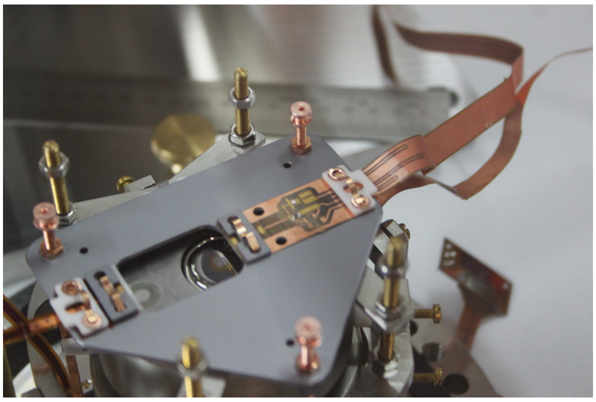

(c) View of a BEGe detectors holder that provides also support for the VFE cable.

Figure 3.5: VFE section of the CC3 preamplifier.

bility of the Pyralux® substrate due to its little thickness (2–3 mils) and by the small size of the JFET SF291 (0.9×0.9 mm, 300 μm of thickness) and of the bond pads (between 70 μm and 100 μm).

The JFET connections were performed on the semi-automatic bonder machine from TPT [171] (model HB 10) placed in a glove box of the GDL laboratory at LNGS. After a training period, needed to familiarize with the not easy working conditions and to find the optimal bonding parameters, several VFE cables have been prepared, an example is shown in Fig. 3.5(b).

3.4.2 Second stage of the CC3 CSP

The second stage of the CC3 is designed to improve the performances of the front-end electronics with respect to previous CSP and to account for the negative effects introduced by the VFE flex cables on the CSP feedback loop.

Fig. 3.6 shows the final version of the CC3 CSP, manufactured with radiopure materials on a 0.8 mm thick Cuflon® substrate and integrating 4 channels on the same PCB. The figure shows also the connections to the VFE sections through 4 interconnecting PCBs and to the 10 m coaxial cables bundle that provide the power supply of the circuit, the injection of the test pulse and drive the output signals out of the cryostat. The total activity of the final version is < 50 μBq per channel.

The scheme of the CC3 (Fig. 3.4) shows that two operational amplifiers are installed in the main section (only one was mounted on the CC2, Fig. 3.2). The new low noise amplifier LMH6654 (Texas Instruments [172]) in SiGe technology, not available when CC2 was designed, is inserted in the new front-end electronics in order to improve the bandwidth of the CSP.

The geometry of the VFE flex cables is intrinsically introducing a stray capacitance of about 80 pF/m in the feedback loop; to reduce the negative effect produced on the JFET output signal a compensative capacitor (called C_C in Fig. 3.4) is placed in the CSP, whose value depends on the length of the VFE cable connected to the specific CC3 channel (in the range 0–10 pF [170]). It is possible to remove this effect at the cost of limiting the bandwidth.

3.4.3 Performance of the CC3 CSP

The front-end electronics developed for Gerda Phase II has been tested in several steps. First tests with prototype versions of the CC3 CSP took place in the INFN laboratory at the Milano Bicocca University, where the CSP has been coupled to an encapsulated BEGe detector depleted in ^{76}Ge. These tests allowed to fully characterize the circuit and its performances.

Then several tests took place in the GDL laboratory at LNGS, here the CC3 was coupled to two bare BEGe detectors (also depleted in ^{76}Ge) reproducing a setup very close to the final Gerda working conditions. The results showed very good performance in terms of stability, energy resolution, bandwidth and dynamic range. As an example the results obtained in the GDL test of June 2014 with the depleted BEGe detector “1/D” will be reported (results from [173]): in more than one day of data acquisition the baseline was stable within

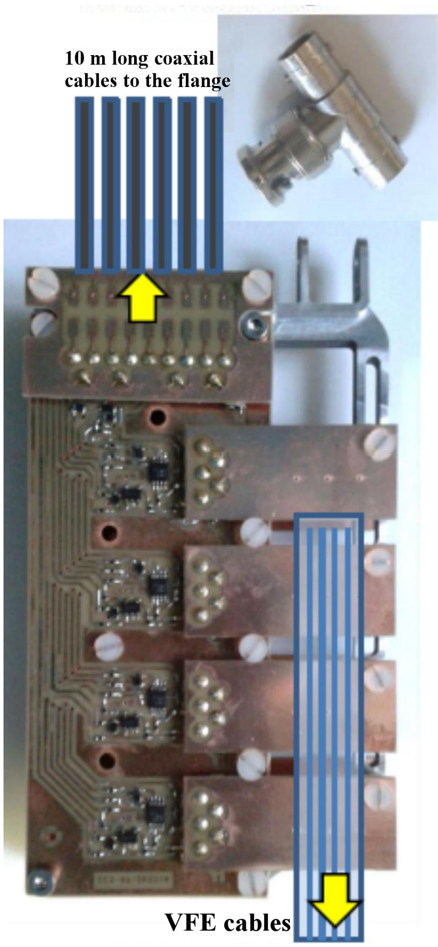

Figure 3.6: Final version of the 4 channels CC3 CSP, manufactured with radio-pure materials on a 0,8 mm thick Cuflon® substrate. Adapted from [170].

1%, the energy resolution in terms of FWHM was 2.62 ± 0.01 keV at the 2614.5 keV peak ($\sim 0.1\%$), the rise time for pulser events was ~ 100 ns and the FWHM for the A/E ratio of the DEP was 1.2%. All values are within the requirements, the energy resolution is at the level of the one obtained by Canberra working in a standard configuration and the pulse shape features (rise time and A/E resolution) allow to exploit the efficient PSD of the BEGe detectors.

Starting from August 2014 the CC3 CSP was adopted in the GERDA cryostat in several detector integration tests, needed to install and integrate all the final Phase II hardware elements: detector holders, readout electronics, detectors and LAr veto. These tests pointed out a critical issue concerning the VFE components: during the procedure of the detector strings assembly in the glove box there was a not negligible probability to break the bonding wires of the die JFET and, in addition, in some cases the JFET was burned out through electrostatic discharges produced during the handling inside the glove box (highly flushed with argon gas).

In the following months many attempts to solve this problem were done, trying to strengthen the bonding connection between JFET and the VFE cable by improving the bond quality and, on the other side, trying to avoid the production of electrostatic discharges by grounding the JFET termination during the string assembly. Also a try to protect the JFET through potting with araldite after the bonding has been performed [174]. Unfortunately all the attempts did not solve completely the problem and the JFET mortality remained too high to be acceptable. In order to achieve a reliable front-end electronics for the GERDA setup, the CC3 CSP has been revised and a backup solution following the Phase I scheme, described in the next section, has been applied.

3.5 Final front-end electronics design

The commissioning of Phase II started in the summer 2015 when all the instrumentation to build the detector array was ready. Before achieving the final Phase II configuration with 40 detectors three attempts had been performed with different detector number and setup configuration (see Sec. 2.4 for more details on the Phase II commissioning).

Due to the problems described in the previous section, the VFE components are no longer installed on the cable head, close to the detector, but are mounted on a PCB near the CC3 main section, reproducing a CSP similar to the one used in Phase I. The CC3 CSP general scheme of Fig. 3.4 is still valid since only the location of the VFE section is different and this requires only few minor changes concerning value and type of the components of the main amplifying stage.

In Tab. 3.1 the specifications of the two CSPs tested during the upgrade to GERDA Phase II are reported: the original version of the CC3 with VFE components mounted close to the detector on the cable head (indicated with CC3*) and the Phase I like version of the CC3 (CC3**). For comparison the specifications of the CC2, adopted in Phase I, are also reported.

Table 3.1: Charge sensitive preamplifiers adopted or tested for Phase II, in comparison with the Phase I CSP, CC2. The specifications and a brief Summary of each circuit are reported. CC3* is referring to the version with VFE components mounted close to the detector, CC3** is the Phase I like version, adopted in the final Phase II configuration.

CSP	gain [mV/MeV]	dynamic range [MeV]	power consumption [mW/chn]	rise time [ns]	
CC2	150	10	45	55	adopted in Phase I
CC3*	150	> 15	60–70	60–80	tested in 2011-2015; mechanical problems and not reliable
CC3**	150	> 15	60–70	20–40	adopted in Phase II

Fig. 3.7 (left) shows the final CC3 CSP with the interconnecting VFE-PCBs: the JFET can be now the well-known encapsulated BF862 (also used in Phase I), feedback resistor and capacitors are unchanged. Fig. 3.7 (right) shows a schematic of the signal cable connections to CC3: a single trace flexible strip (instead of coplanar waveguide used in the previous design) coming from the detector is inserted in the space between a gold leaf and a copper peace inside a PTFE structure, then fixed with a screw.

The final VFE location has both pros and cons with respect to the original Phase II electronics. The increased distance between detectors and VFE section is positive with respect to the total activity budget, as no electronic components are close to the detector. The only contribution to the radioactivity budget comes from the single trace signal and HV cables whose mass is of few grams (0.4 g/m the signal and 2.7 g/m for the HV cable). In the final Phase II configuration achieved in December 2015, different ribbon cables were installed for the signal and HV contact: the HV contacts are in 10 mils Cuflon® (from Haefele [176]) or in 3 mils Pyralux® (from Tecnomec [167]); the signal contacts are 3 mils both for Pyralux® and Cuflon®. The Cu trace is 18 μm thick for all ribbon contacts. The measured activity of these cables is reported in Tab. 5.1, their contribution to the background is discussed more in detail in Chap. 5.

The installation of the VFE components close to the main section of the CC3 CSP not only allows to use an encapsulated and soldered JFET, but also removes the stray capacitance of the VFE cable allowing to increase the bandwidth. To take advantage of this, the amplification of the second operational amplifier (the LMH6654) has been increased reflecting in a reduction of the waveform rise time of a factor of ~ 3 improving the PSD performances.

On the other hand the new front-end design introduces also negative effects. When the input JFET is close to the detector the input referred noise is minimized, while here we have an input connection from 40 to 80 cm long, hence a degradation of the signal-to-noise ratio is expected.

The Phase II commissioning runs tested the performances of the detectors and their readout (CC3 with close VFE) in terms of resolution and PSD.

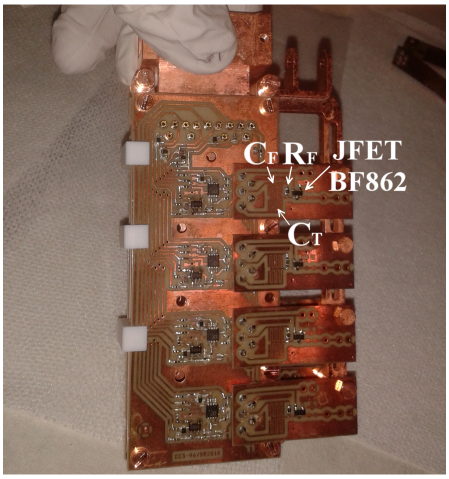

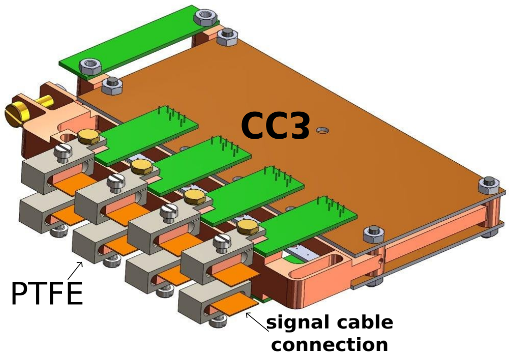

Figure 3.7: Phase I like front-end electronics. Left: picture of the 4 channels CC3 CSP manufactured on Cuflon® substrate and with interconnecting PCBs where the VFE components (input JFET, feedback components and test capacitor) are placed. Right: schematic view of the copper frame with two CC3, showing the new system to provide the connection of the signal cables from detectors [175].

Table 3.2: Performances obtained in the GDL test of June 2014 with the depleted BEGe detector "1/D" [173] and in the three commissioning runs of Phase II [177, 178], in terms of average energy resolution in calibration at the 2.6 MeV peak for BEGe and coaxial detectors and resolution of the A/E ratio of DEP events for BEGe detectors.

test	$\mathrm{FWHM}_{2.6\mathrm{MeV}}$ BEGe	Coax	$\mathrm{FWHM}_{A/E}$ [%]
GDL test	2.62 ± 0.01	/	1.2
1st commissioning	$3.3^{+1.3}_{-0.3}$	$4.2^{+0.4}_{-0.3}$	2.0–4.2
2nd commissioning	3.1 ± 0.2	4.0 ± 0.1	1.7–2.8
3rd commissioning	$3.0^{+0.2}_{-0.5}$	$4.0^{+0.2}_{-0.4}$	1.5–3.4

3.5.1 Results from Phase II commissioning

In the first commissioning of July 2015 (see Sec. 2.4 for more detail on the setup) the average energy resolution achieved in 3 calibration runs at the 2614.5 keV peak (values from [177]) is $3.3^{+1.3}_{-0.3}$ keV FWHM for the BEGe detectors and $4.2^{+0.4}_{-0.3}$ keV for the coaxial detectors. As expected the energy resolution is worse than for VFE close to the detectors but still acceptable. About the PSD, the resolution range of the A/E parameter of the DEP for the BEGe detectors is 2.0–4.2% (from [178]). The 100 MHz signals are strongly affected by high-frequency noise superimposed to the waveforms that in turn affects significantly the discrimination power. The results are listed in Tab. 3.2, in comparison with a GDL test of June 2014.

Before starting the new run a devoted work session to find and mitigate the high-frequency noise sources was performed. They were mostly generated by the HV power supply and, both improving the grounding connections and modifying the HV filter schematic, a significantly noise reduction was achieved [179].

In the 5 calibration runs performed in more than one month of data acquisition of the second commissioning (September 2015) the average energy resolution (FWHM at the 2614.5 keV peak) [177] was 3.1 ± 0.2 keV for BEGe detectors and 4.0 ± 0.1 keV for coaxial detectors, i.e. compatible with previous results. On the other hand, an improvement was visible in the PSD side thanks to the mitigation of the high-frequency disturbances: selecting the events from the DEP the resolution of the A/E for the BEGe detectors ranges between 1.7% and 2.8% [178], not as good as in the GDL tests but acceptable to discriminate background events (see Tab. 3.2).

The last commissioning (November 2015) was performed after a further attempt to reduce the disturbances and noise sources, in this case no significant improvement was achieved and the performances were at the same level of the second run both in energy and A/E resolution (the results are listed in Tab. 3.2). Some residual unexpected noise was still superimposed to the waveforms, the origin is probably connected to the long contacts from the detector to the JFET. In Sec. 4.5 a detailed study of the noise observed during the Phase II data taking is presented.

3.6 Conclusions

A new charge sensitive preamplifier has been developed during the upgrade to Gerda Phase II (the CC3 [164]). The initial design foresaw a separation of the CSP in two stages: the VFE section, including JFET and feedback components positioned very close to the detector, and the rest of the circuit, about 1 m away. The integration tests performed between 2013 and 2015 showed some problem in the reliability of the VFE, hence the latter has been moved and located close the amplifier (40–80 cm from the detector as in Phase I) where an encapsulated JFET could be used.

The results obtained in the commissioning indicate that the modified version of the Phase II front-end electronics, as expected, is performing worse than the original design, both in terms of energy resolution ($\sim 10\%$) and pulse shape discrimination (measured with the resolution of the A/E parameter).

On the other hand the solution is quite robust and reliable, unlike in the original Phase II scheme, and the major advantage is the strong reduction of the radioactivity budget from the readout electronics.

Including also the need to start the Phase II data acquisition as soon as possible, this scheme has been adopted as it is an acceptable compromise between all the stringent requirements. Fig. 3.8 shows the final installation of the front-end electronics for Phase II: six copper frames, with two modified version of CC3 preamplifiers each, are mounted above the array location on the copper structure that holds up the seven Ge detectors strings.

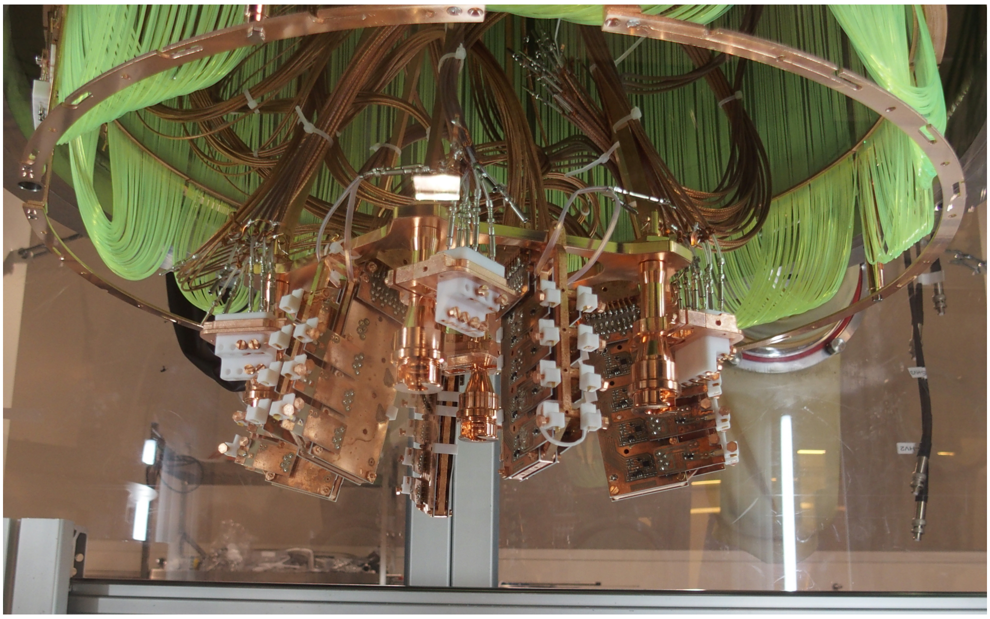

Figure 3.8: Final design of the front-end electronics mounted in the GERDA lock, six copper frames with two CC3s are installed on the Cu structure. The signal cable coming from the detectors are connected with the PCBs after the string assembly.

Chapter 4

Energy reconstruction in GERDA Phase II

Most radiation detectors require signal processing so that both energy or time profile of the interacting radiation can be properly extracted, this is the case of germanium detectors.

In Ge detectors the preamplifier output signal is either shaped and then processed by an analog to digital converter or directly digitized by a FADC and then shaped offline with a dedicated algorithm. The latter is named Digital Signal Processing (DSP), the advantages with respect to the analog process are the large (in principle infinite) number of shaping filters that can be applied and that the recorded data remain available for further reprocessing, while in the analog processing the original pulse shape is lost.

In GERDA the energy is evaluated by DSP. In this chapter the development of a novel filtering technique is described; it was first already applied to the data from Phase I with a significative improvement in the energy resolution [180, 181, 182].

In Sec. 4.1 the possible sources of the electronic noise and the factors that determine the energy resolution of a Ge detector readout are discussed. Then in Sec. 4.2 the GERDA Phase I DSP is reviewed. The development of the new shaping filter, the Zero Area Cusp-like (ZAC), is presented in Sec. 4.3. The new filter has been applied in recent GERDA Phase II data: the implementation details and the detector performances achieved with the ZAC filter are discussed in Sec. 4.4. Finally, in Sec. 4.5 the actual noise affecting the GERDA germanium readout is discussed and related to the array configuration and the front-end electronics design.

4.1 Noise sources and energy resolution in germanium detectors

4.1.1 Noise sources in a Ge detector readout system

A germanium detector and its readout can be modeled as in Fig. 4.1. The detector is considered a noiseless source of a δ-like charge pulse with capacitance C_{det}. The trace recorded by the FADC can be modeled as the output

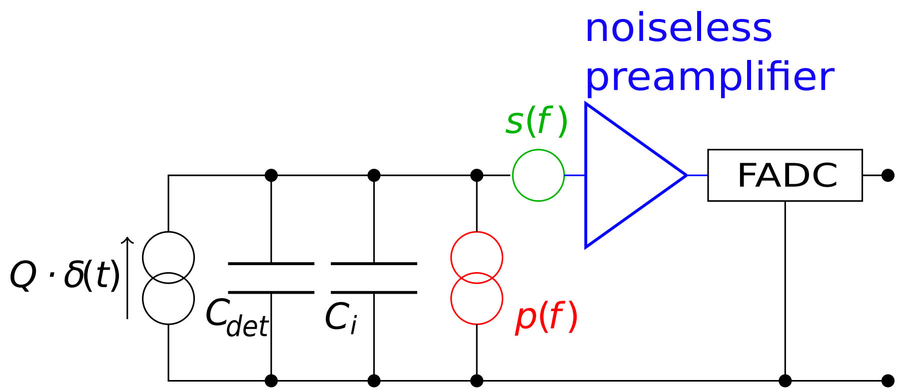

Figure 4.1: Signal and main noise sources in a germanium detector readout system. Picture adapted from [180].

of a noiseless preamplifier connected to the detector, a series voltage generator with spectral density $s(f)$ (green in Fig. 4.1) and a parallel current generator with spectral density $p(f)$ (red in Fig. 4.1). C_i is the preamplifier input capacitance.

The amplitude of the electronic noise is usually expressed in terms of the Equivalent Noise Charge (ENC), defined as the input-referred amount of charge that may theoretically be uniquely responsible for the actual output-referred measurement noise; measured in electrons input charge.

The intrinsic ENC with shaping time τ_s is given as [183]:

$$\mathrm{ENC}^2 = \alpha \frac{1}{\tau_s} \frac{2k_B T}{g_m} C_{tot}^2 + \beta A_f C_{tot}^2 + \gamma \left(e I_{tot} + \frac{k_B T}{R_F} \right) \tau_s \qquad (4.1)$$

where $C_{tot} = C_{det} + C_F + C_i$ is the total capacitance, R_F and C_F are the feedback resistor and capacitor, $I_{tot} = I_{det} + I_{gate}$ is total current (sum of the detector leakage current I_{det} and the gate current I_{gate}), g_m is the JFET transconductance ($\sim$ 10 mA/V in GERDA), k_B is the Boltzmann constant and T the operating temperature (87.3 K for LAr). The constants α, β and γ depend on the adopted signal shaping filter (i.e. for a Gaussian filter $\alpha = 0.89$, $\beta = 1$ and $\gamma = 1.77$, for an infinite cusp $\alpha = 1$, $\beta = 0.64$ and $\gamma = 1$) [183].

The first term of Eq. (4.1) is the series noise and is proportional to the square of total capacitance C_{tot}. Assuming that the shaping time is $\tau_s = 10\ \mu$s, $\alpha = 1$ and $C_i = 10$ pF, the contribution of the series noise is $\sim$ 100 e^2 for detectors with $C_{det} \sim 1$ pF (BEGe detectors) and $\sim$ 1500 e^2 for detectors with $C_{det} \sim 30$ pF (coaxial detectors).

The second term of Eq. (4.1) represents the $1/f$ noise of the JFET with amplitude A_f and is also proportional to C_{tot}^2; its value depends on the specific setup and is in the range of 10^2–10^4 e^2. Both the series and the $1/f$ noise scale with C_{tot}^2 and this explains why the BEGe detectors have better energy resolution than the coaxial ones.

The third term of Eq. (4.1) is the parallel noise generated by the total current I_{tot} and the thermal noise of the feedback resistor R_F. Considering that I_{gate} is typically below 1 pA and assuming that $I_{det} = 10$–100 pA and $R_F = 500$ MΩ, the parallel noise is $\sim$ 2000 e^2.

The parallel noise is proportional to τ_s and the series noise to its inverse while the $1/f$ noise is independent of τ_s. Therefore, the optimal shaping time is the one which minimizes the sum of the series and parallel noises. More detailed descriptions of the noise origin and its treatment in germanium detectors can be found in [183, 184].

4.1.2 Energy resolution

The energy resolution of a Ge detector depends on several factors: the electronic noise, the charge production process in the detector volume and the detector charge collection and integration.

The electronic noise is described in the previous section and is independent from the energy. In terms of Full Width at Half Maximum (FWHM) can be written as:

$$\mathrm{FWHM}_{el} = 2.355 \ \frac{\eta}{e} \ \mathrm{ENC} \tag{4.2}$$

where η is the average energy necessary to generate an electron-hole pair ($\eta =$ 2.96 eV in Ge) and ENC is given by Eq. (4.1). With the example values used in the previous section (and assuming the $1/f$ contribution of 1000 e^2), this term contributes with about 0.5 (0.7) keV for BEGe (coaxial) detectors to the total FWHM, imposing a lower limit to the achievable resolution.

A second contribution to the energy resolution is given by the charge production process in the detector volume and is due to the fluctuation of the number of electron-hole created by the particle interaction. The contribution to the FWHM is:

$$\mathrm{FWHM}_p = 2.355 \ \sqrt{\eta \ F \ E} \tag{4.3}$$

where F is the Fano factor ($F = 0.13$ for Ge [185]); this term is increasing with the energy, its contribution to the total FWHM at the 2614.5 keV peak is ~ 2 keV.

The last contribution to the FWHM is given by the charge collection of the detector and by the charge integration properties of the shaping filter. This term, negligible for fully depleted working detectors, is normally expressed by the empirical formula:

$$\mathrm{FWHM}_c = 2.355 \ c \ E \tag{4.4}$$

where c is a parameter related to the quality of the charge collection and integration.

The three terms of Eqs. (4.2), (4.3) and (4.4) have independent origins, hence they can be summed in quadrature to give the overall FWHM:

$$\mathrm{FWHM}(E) = 2.355\sqrt{\frac{\eta^2}{e^2} \ \mathrm{ENC}^2 + \eta \ F \ E + c^2 \ E^2} \ . \tag{4.5}$$

4.2 Signal processing for GERDA Phase I

In GERDA the signals are digitized with 14 bits precision ($2^{14} = 16384$ samples are recorded) and 100 MHz sampling frequency. To improve the data transfer rate, for energy reconstruction only, the traces are rebinned summing up 4

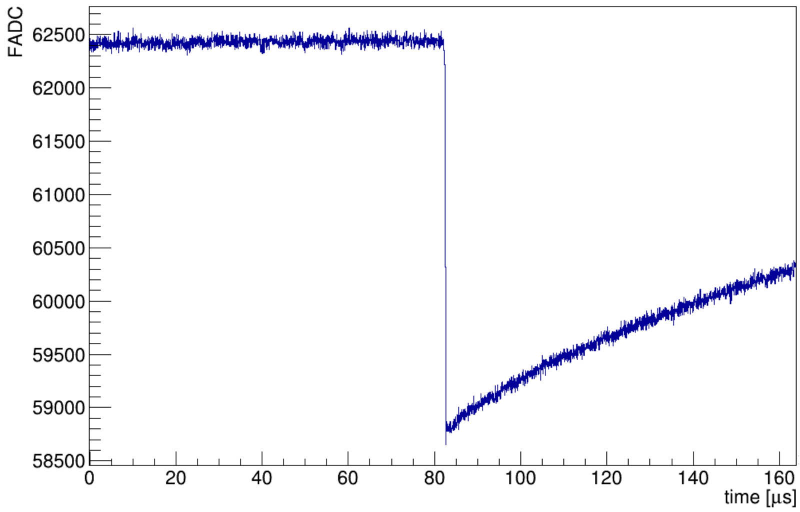

Figure 4.2: Typical GERDA waveform. A ~ 80 μs baseline is recorded before each signal, the fast signal (~ 100 ns) is followed by an exponential decay tail of $\tau \sim 150$ μs due to the discharge of the feedback capacitor.

consecutive bins. In this way, the waveforms contain 4096 bins of 40 ns width. Fig. 4.2 shows the typical acquired waveform: a ~ 80 μs long baseline is recorded before each signal, then the charge signal rises up (fall down in the figure) in ~ 100 ns followed by a $\tau \sim 150$ μs long exponential tail due to the discharge of the feedback capacitor, as described in Eq. (3.5).

Since Phase I, in GERDA is implemented an offline energy reconstruction: the digitized charge pulses are recorded and then analyzed with the software tool GELATIO [136]. The standard energy reconstruction algorithm, used in Phase I and for reference purposes also in Phase II, is a digital pseudo-Gaussian filter, consisting of different steps:

- first the signal is reversed and the baseline is subtracted;
- then the signal ($x_0[t]$) is differentiated with time constant $L = 5$ μs:

$$x_0[t] \rightarrow x_1[t] = x_0[t] - x_0[t-L] \tag{4.6}$$

  this corresponds to a CR analog circuit;
- finally a series of 25 Moving Average (MA) of 5 μs length are applied:

$$x_i[t] \rightarrow x_{i+1}[t] = \frac{1}{L}\sum_{t'=t-L}^{t} x_i[t'] \quad i = 1 \ldots 25 \tag{4.7}$$

  this corresponds to $(\mathrm{RC})^{25}$ analog shaping.

The main steps of the algorithm are illustrated in Fig. 4.3, the final signal has a shape close to a Gaussian function, the energy is given by the height of

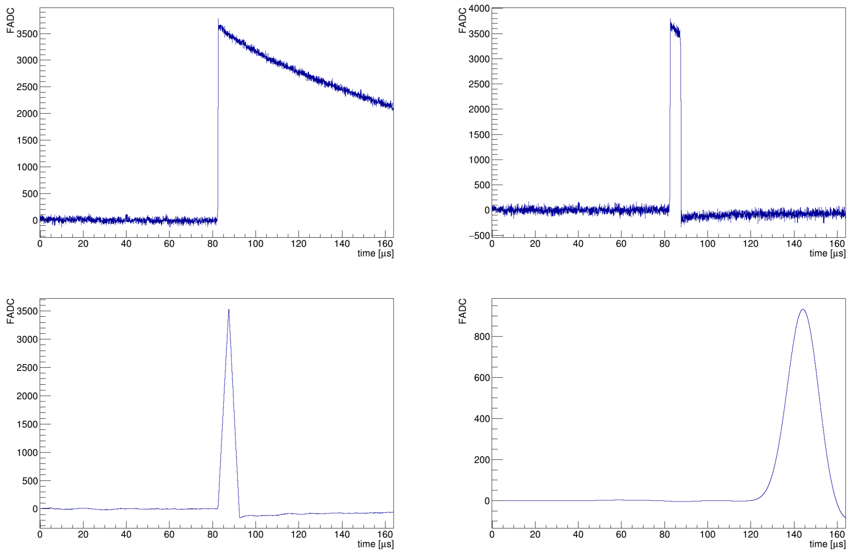

Figure 4.3: GERDA Phase I energy reconstruction procedure. Top left: typical waveform after inversion and baseline subtraction. Top right: waveform after the differentiation operation described in Eq. (4.6). Bottom: signal after one (left) and 25 (right) MA operations (see Eq. (4.7)).

the output signal. The choice of a 5 μs shaping time and of 25 MA iterations allows a good filtering of the high-frequency noise.

This algorithm is stable and relatively fast, but is limited by several factors. This pseudo-Gaussian shaping is a high-pass filter followed by $n = 25$ low-pass filters. The resolution obtained with the pseudo-Gaussian shaping is very close to the optimal when the low frequency noise is negligible [183]. This is not the case for GERDA where the charge sensitive preamplifier (CSP) is placed at a distance of 40–80 cm from the detectors due to the low background requirements.

Another negative aspect, is that the adopted pseudo-Gaussian shaping is the same for all detectors, although the signal formation properties and the noise conditions are individual. An improvement in energy resolution can therefore be obtained by tuning the parameters of the shaping filter individually for each detector.

4.3 Optimum filter for energy estimate: ZAC filter

Several methods have been developed to achieve the optimum digital shaping for a given experimental setup [183, 184, 186, 187, 114]. During the upgrade to Phase II many of them were applied to data from integration tests [166]. Also a tentative to develop the optimal Wiener filtering [188] has been implemented: the computation time needed is longer than other adopted methods, since it is calculated in the frequency domain, and the shape is similar to the innovative filter subject of this chapter, directly created in the time domain. For these reasons the Wiener filter was abandoned.

It can be proven [186] that in case of series and parallel noise only and with infinitely long waveforms the optimum shaping filter for energy estimation of a δ-like signal is an infinite cusp when sides have the form $\exp(t/\tau)$ where τ is the reciprocal of the corner frequency, the frequency at which the contribution of the series and parallel noise of the referred input becomes equal. In real case, with waveforms of finite length, a modified cusp is obtained building the two sides with sinh-curves.

As pointed out in the previous section, in GERDA $1/f$ low-frequency noise is a significant component due to the detector to front-end distance. In this case the energy resolution is optimized using filters with total area equal to zero [189]. In addition, the low-frequency baseline fluctuations (e.g. due to microphonics) are well subtracted by filters with parabolic shape [190].

Following these arguments an optimized shaping filter for the GERDA setup can be achieved with a Finite Impulse Response (FIR) cusp-like filter with zero total area. This can be obtained by subtracting two parabolas from the sides of the cusp filter keeping the area under the parabolas equal to that underlying the cusp.

The Ge detector output current is not a pure δ-function, but has a width of approximately 1 μs. If a cusp filter is used, this leads to the effect of a ballistic deficit [191, 192] and consequently to the presence of low-energy tails in the spectral peaks.

This can be avoided by inserting a flat-top in the central part of the cusp with a width equal to almost the maximum length of the charge collection in the diode. The resulting filter is a Zero-Area finite-length Cusp-like (ZAC) filter with central flat-top, implemented as:

$$\mathrm{ZAC}(t) = \begin{cases} \sinh\left(\frac{t}{\tau_s}\right) + A\left[\left(t-\frac{L}{2}\right)^2 - \left(\frac{L}{2}\right)^2\right] & \text{for } 0 < t < L \\ \sinh\left(\frac{L}{\tau_s}\right) & \text{for } L < t < L+FT \\ \sinh\left(\frac{2L+FT-t}{\tau_s}\right) + A\left[\left(\frac{3}{2}L+FT-t\right)^2 - \left(\frac{L}{2}\right)^2\right] & \\ & \text{for } L+FT < t < 2L+FT \end{cases} \tag{4.8}$$

where τ_s is the cusp parameter that has to role of the shaping time, L is the length of one cusp side, FT is the flat-top length and the constant A is chosen such that the total integral is zero. The ZAC filter is realized numerically following Eq. (4.8) with the substitution $t \to \Delta t \cdot i$ (where $\Delta t = 40$ ns is the sampling time, i is sampling index) therefore $\mathrm{ZAC}(t) \to \mathrm{ZAC}[i]$ for $i = 1, ..., N_{zac}(= 2L + FT)$.

Fig. 4.4 shows an example of the ZAC filter construction: a cusp-like filter (green dashed line) and two negative parabolas (blue dashed line) are summed up to obtain the final filter (red full line).

Since the filter has to be applied to a current pulse, a deconvolution of the preamplifier response function, i.e. an exponential curve with decay time $\tau_F = R_F C_F$, is needed on the charge waveform (Fig. 4.2). This is achieved through convolution with a filter consisting of two elements $f_\tau = [1, -\exp(-\Delta t/\tau_F)]$. Given that the convolution is commutative, for convenience the ZAC filter is immediately convoluted with the inverse preamplifier response function f_τ

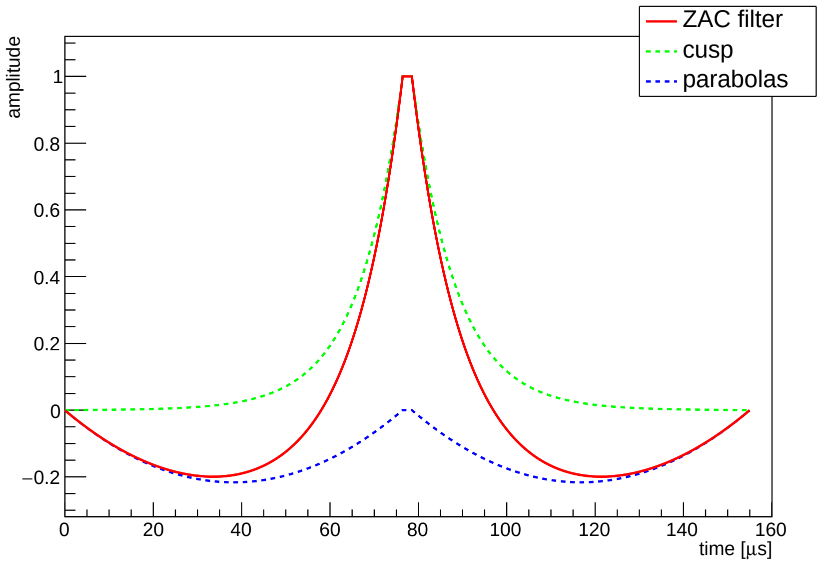

Figure 4.4: ZAC filter construction: finite-length cusp (green dashed line) and two negative parabolas (blue dashed line) are summed to obtain the ZAC filter (red full line).

obtaining:

$$\mathrm{ZAC}_{dec}[i] = \mathrm{ZAC}[i] \cdot (-e^{-\Delta t/\tau_F}) + \mathrm{ZAC}[i+1] \cdot 1 \tag{4.9}$$

for $i = 1, ..., N_{zac} - 1$. An example of the result of this operation is shown in Fig. 4.5. The resulting filter ZAC_{dec} is then convoluted with the charge pulse, namely the preamplifier output signal x:

$$y[i] = \sum_{k=i}^{i+N_{zac}-2} x[k] \cdot \mathrm{ZAC}_{dec}[i + N_{zac} - 1 - k] \tag{4.10}$$

for $i = 1, ..., N - N_{zac} + 2$, where N is the number of x samples ($N = 2^{14}/4 = 4096$). The energy is then calculated as the maximum of the convoluted signal y.

4.4 Application of the ZAC filter to Phase II data

The ZAC filter, developed to optimize the energy resolution of GERDA detectors, has been already applied to the Phase I data [180] obtaining a significative improvement in the range of 5–23% for both BEGe and coaxial detectors with respect to standard filtering.

The work of this thesis is addressed to the application of the ZAC filter to the new data from Phase II collected starting from December 2015. In this section the strategy used to implement it and the performances achieved are described.

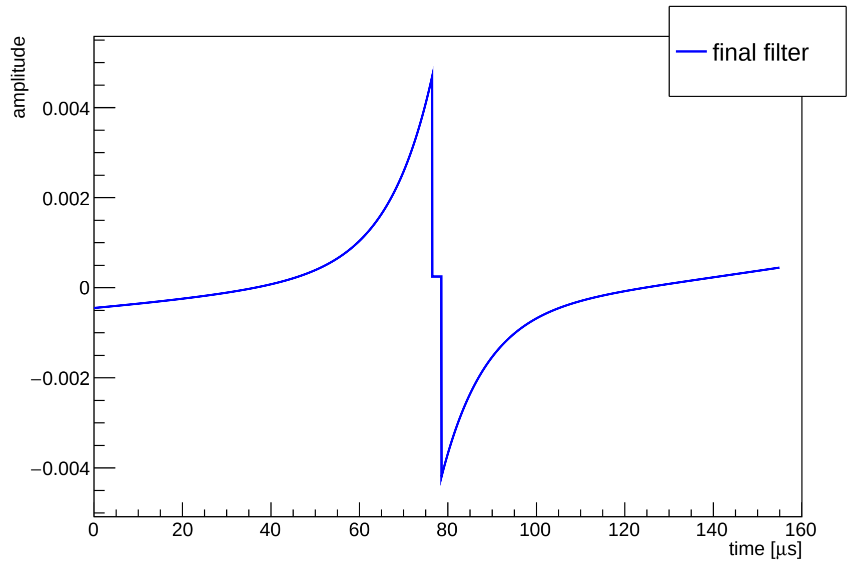

Figure 4.5: ZAC filter after the convolution with the inverse preamplifier response function. This filter is then convoluted with the output waveform.

4.4.1 ZAC filter optimization strategy

Eqs. (4.8) and (4.9) show that the final shaping filter (Fig. 4.5) depends on four parameters: L, FT and τ_s describe the ZAC filter and τ_F the preamplifier discharge time. In order to obtain the best energy resolution, the parameters are tuned separately for each detector.

The optimization strategy developed in this thesis (and used on Phase II data) is slightly different with respect to Phase I [180]. Because of the increased number of detectors (40 versus 11), an effort in the reduction of the computation time needed to run the ZAC optimization is performed. Moreover the new setup configuration shows a different trend of the energy resolution as function of the ZAC filter parameters.

Before filtering the charge waveforms, some quality cuts are applied in order to reject those events which are non-physical or not properly formed. In particular only pulses with a trigger position between 79.5 and 82.5 μs and a rise time in the range 0.2–3 μs are selected.

The ZAC optimization flow is as in Phase I: the energy spectrum obtained in ^{228}Th calibration runs is reconstructed only in the region of the 2614.5 keV peak with different ZAC parameters. Then this peak is fitted and the FWHM is extracted. The set of parameters that maximize the energy resolution is adopted to reconstruct the entire spectrum.

The ^{208}Tl peak is fitted with the function [193]:

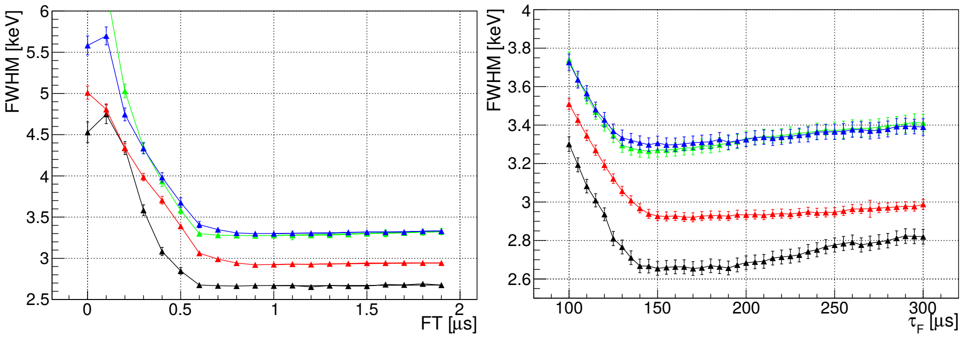

(a) Flat top optimization.

(b) τ_F optimization.

Figure 4.6: ZAC optimization graphs: FWHM of the 2614.5 keV peak in a Phase II calibration run as function of the FT (a) and the τ_F (b) parameters. The 4 colors correspond to different BEGe detectors of the GERDA setup.

$$f(x) = A_1 \cdot \exp\left(-\frac{(x-\mu)^2}{2\sigma^2}\right) + \\ + \frac{A_2}{2} \cdot \exp\left(\frac{x-\mu}{A_3}\right) \cdot \operatorname{erfc}\left(\frac{x-\mu}{\sqrt{2}\sigma} + \frac{\sigma}{\sqrt{2}A_3}\right) + \\ + A_4 + \frac{A_5}{2} \cdot \operatorname{erfc}\left(\frac{E-\mu}{\sqrt{2}\sigma}\right) \quad (4.11)$$

corresponding to a Gaussian peak with a low-energy tail (second line) sitting on flat background and on a step-like function (last line). The FWHM is obtained from the resulting fit function as $2.355 \cdot \sigma$.

Hence the ZAC optimization is the study of the energy resolution dependence on the four parameters. It will be presented in the following by the analysis of the FWHM as function of each parameter.

The length of the filter L is chosen as long as possible following the arguments in [186]; no significant variation of the FWHM is visible with L in the range 140–163 μs. The value adopted to produce all the ZAC filters is $L = 155$ μs (as the example in Fig. 4.4).

The flat top FT is related to the detector charge collection time, typically between 0.5 and 1.0 μs. In order to find the optimal FT for each detector, it was varied in the range 0–2 μs with steps of 0.1 μs. Fig. 4.6(a) shows an example of the FT optimization graph for four detectors in a Phase II calibration run: as expected the FWHM is decreasing until FT is 0.6–0.8 μs in all cases, then it is nearly constant. This is because the energy resolution improves until the FT collects all the charge released in the detector; any further increase is no effective. Following this argument and thanks to the very low detector leakage currents, the flat top is fixed to 1 μs for all the detectors and it is not scanned during the optimization.

The exponential decay time of the preamplifier output τ_F can be calculated once the feedback components ($\tau_F = R_F \cdot C_F = 500$ M$\Omega \cdot 0.3$ pF $= 150$ μs) are known. Due to the presence of long front-end cables, which translates into parasitic capacitance, a signal deformation could arise and the search of the optimal τ_F could be needed. Fig. 4.6(b) shows the FWHM values at the 2614.5 keV peak as function of τ_F in the range from 100 to 300 μs. In all the cases the best energy resolution is obtained with $\tau_F \simeq 150$ μs, corresponding to the circuital value. This fact encouraged to fix also this parameter during the ZAC optimization ($\tau_F = 150$ μs), reducing significantly the computation time and still ensuring an optimal filtering.

The situation is different for the τ_s parameter that is the filter shaping time and its value depends on the actual electronic noise, as described in Secs. 4.1.1 and 4.3. The optimal τ_s is individually searched in 1 μs steps for each detector in each calibration run in the range 1–30 μs. Fig. 4.7 shows some examples of optimization graphs for this parameter: in red, green and blue the FWHMs obtained in 3 calibration runs of Phase II taken during March 2016 are reported.

The energy resolution is optimized by very different τ_s values, depending on the detector and also on the specific calibration run. In particular three typical situations can be distinguished:

- detectors with very good energy resolution (FWHM $\sim$ 2.6 keV for BEGe detectors) have the minimum FWHM with shaping time $\tau_s \sim 10$ μs; Fig. 4.7(a) shows the FWHM vs τ_s graph for the BEGe detector GD91A;

- a second type of graph is obtained when the energy resolution is worse than expected (FWHM > 3 keV for BEGe detectors), here a minimum FWHM cannot be clearly observed and the best shaping time is $\tau_s >$ 15 μs, as showed in Fig. 4.7(b) with the example of the GD35A detector;

- finally, when the detector is showing a leakage current of $\gtrsim$ 100 pA the parallel noise dominates, as described in Sec. 4.1.1, and the FWHM minimum is very pronounced at $\tau_s \sim 4$ μs; an example of the optimization graph for the detector GD91B is reported in Fig. 4.7(c).

The behaviour of the ZAC optimization graphs is strongly related to the specific noise spectrum, this topic is detailed discussed in Sec. 4.5 where a study of the possible noise sources is presented.

To summarize, the new ZAC optimization developed for GERDA Phase II is performed running the shaping time τ_s from 1 to 30 μs and fixing the flat top to 1 μs and the preamplifier decay time to 150 μs. This strategy leads to an optimal energy resolution for all Ge detectors with a minimal computation time of few hours per calibration run. In Phase I instead a brute force approach was adopted, running all the parameters in a wide range to find the minimum FWHM.

4.4.2 Performances and stability in calibration data

The ZAC filter was used to produce the energy spectra in the GERDA Phase II first release [1, 2], corresponding to 6 months of data acquisition from December 20th, 2015 to June 1st, 2016. In this section the detector performance of this period are reviewed.

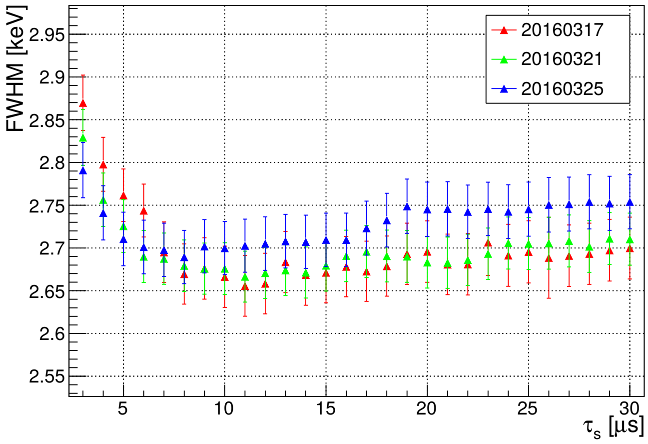

(a) τ_s optimization for GD91A.

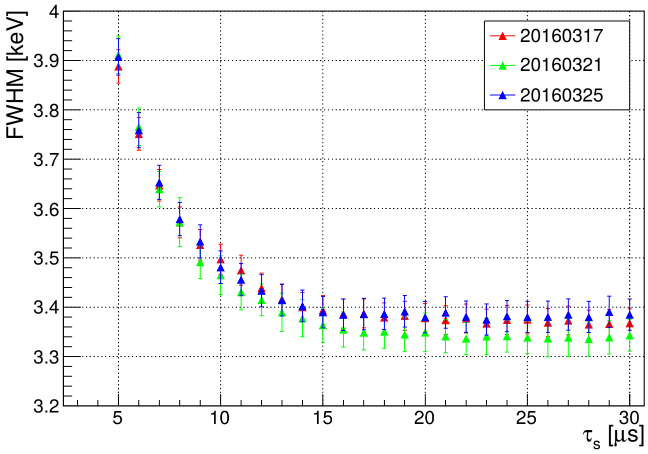

(b) τ_s optimization for GD35A.

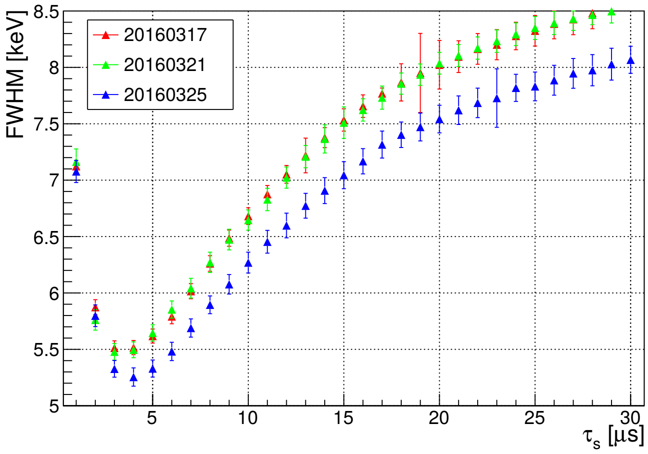

(c) τ_s optimization for GD91B.

Figure 4.7: ZAC optimization graphs: FWHM of the 2614.5 keV peak as function of the shaping time τ_s in 3 calibration runs of Phase II. Top: highly performing detector; middle: poorly performing detector affected by series and $1/f$ noise; bottom: poorly performing detector affected by leakage current.

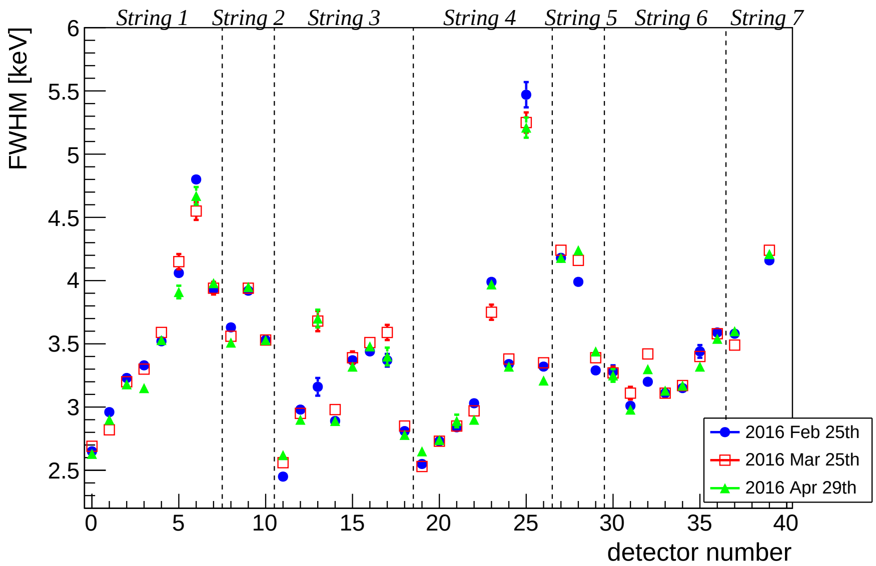

Figure 4.8: Energy resolution in terms of FWHM at 2614.5 keV obtained for three calibration runs during the first months of GERDA Phase II, are included all BEGe and coaxial detectors. From [194].

During the data acquisition the Ge detector array is weekly irradiated by three ^{228}Th sources; the calibration was performed in total 31 times during this six months. The ZAC filter has been optimized in each of them following the recipe described in the previous section.

The performance of the 40 detectors in terms of energy resolution at the 2614.5 keV peak obtained with optimal ZAC filter is shown in Fig. 4.8. The figure shows the FWHMs in three Phase II calibrations for all BEGe, ^{enr}Ge and ^{nat}Ge coaxial detectors, the horizontal axis gives the detector progressive number and the top legend reports the string number. Strings 1, 3 and 4 contain only BEGe detectors, string 2 and 5 only ^{enr}Ge coaxial detectors, string 6 contains six BEGe and one ^{nat}Ge coaxial detector (number 36), string 7 contains the three ^{nat}Ge coaxial detectors (one of them, number 38, is not working properly and its FWHM value is not reported). The detector configuration of Phase II is reported in App. A.

Fig. 4.8 reveals that the energy resolution for the BEGe detectors correlates to the position in the string: in most cases the best FWHM values are achieved for the top detectors, then the resolution degrades with the position. This can be connected to the fact that the detector number within the string scales with the length of the signal contact. For the coaxial detectors the same trend is not found; this is probably due to their larger intrinsic capacitance. However this trend is not completely understood, a possible explanation and its connection with the electronic noise is presented in Sec. 4.5.

Excluding two BEGe detectors with known problems, i.e. GD02D (number 6) having imperfections in the crystal impurity distribution and GD91B (number 25) that is driving a leakage current of $\gtrsim$ 100 pA, the Phase II en-

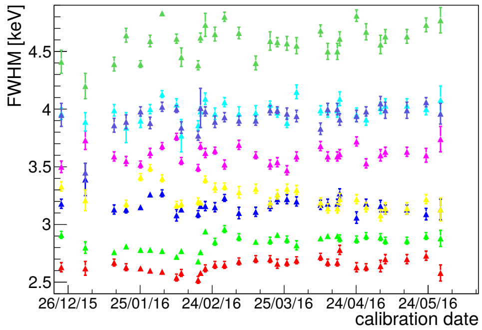

(a) FWHM stability in string 1.

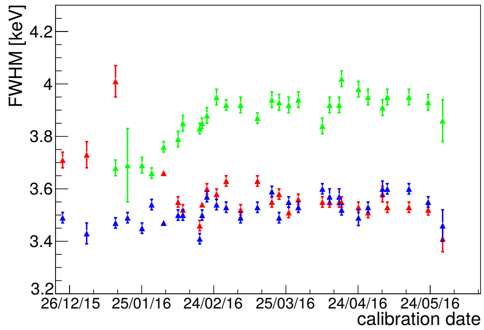

(b) FWHM stability in string 2.

Figure 4.9: FWHM at 2614.5 keV obtained in all the 31 calibration runs for a BEGe (a) and a ^{enr}Ge coaxial (b) detector string.

ergy resolution is in the range from 2.5 keV to about 4.0 keV for the BEGe detectors and from 3.2 keV to 4.2 keV for the coaxial detectors. The average FWHM evaluated for the three considered calibrations is of $3.18^{+0.44}_{-0.37}$ keV, 3.73 ± 0.22 keV and 3.87 ± 0.15 keV respectively for BEGe, ^{enr}Ge coaxial and ^{nat}Ge coaxial detectors.

With respect to the pseudo-Gaussian shaping (the method adopted in Phase I and described in Sec. 4.2, here used as reference), the ZAC filter leads to an average energy improvement of 0.20 keV that corresponds to 6.2% for BEGe detectors and 0.37 keV (9.6%) for coaxial detectors.

The FWHM values obtained in the three considered calibration runs and reported in Fig. 4.8 describe the situation of the entire Phase II data taking. The same plot for the energy resolution has been created also with the super-calibration data (that is including all the 31 calibrations) and is presented in App. A, together with a table of the FWHM for the 40 detectors: the values are all compatible with Fig. 4.8. As described in Sec. 4.4.4, the super-calibration results are used to extract the FWHM at $Q_{\beta\beta}$.

The performances of the Ge detectors remain quite stable during the entire data acquisition. Fig. 4.9 shows the FWHM at 2614.5 keV obtained in all the 31 calibration runs for the string 1 containing eight BEGe detectors and the string 2 containing three ^{enr}Ge coaxial detectors. The FWHM for BEGe detectors (Fig. 4.9(a)) is stable within 5–10% in all the cases and, excluding the first period where the detector marked in red is not working properly, the energy resolution for coaxial detectors is stable within 5% (Fig. 4.9(b)).

4.4.3 Energy calibration

After the ZAC optimization, the energy spectra are calibrated in order to determine the energy scale for the physics data. This operation is performed through a dedicated ROOT [135] based software that for each detector first searches and finds the central position in the uncalibrated spectrum of the peaks produced by the ^{228}Th sources and then gives the calibration curve as output (a description of the calibration software is presented in [195]).

Fig. 4.10 shows an example of ^{228}Th spectrum acquired during a Phase II

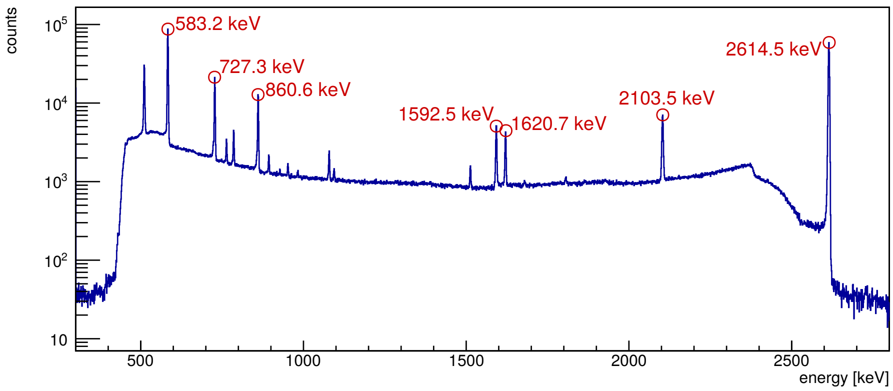

Figure 4.10: Example of ^{228}Th calibration spectrum: the prominent lines are searched in the calibration software to determine the conversion between FADC channels and energy in keV.

calibration run, summing the contribution of all detectors. In order to reduce the disk space usage, in calibration the hardware trigger threshold is set to $\sim$ 400 keV. Since the major contribution to the physics spectrum below 500 keV is from the ^{39}Ar β continuum (for more details see Chap. 5) there is no need to have a very precise calibration at low energy in GERDA.

The peaks used for the energy calibration are the main γ lines in the ^{228}Th decay chain, in particular: the full energy peaks (FEPs) at 583.2, 860.6 and 2614.5 keV, the double escape peak (DEP) at 1592.5 keV and the single escape peak (SEP) at 2103.5 keV from ^{208}Tl, and the FEPs at 727.3 and 1620.7 keV from ^{212}Bi.

The software starts searching for the 2614.5 keV line that is fitted with the function of Eq. (4.11). Then, using a raw calibration realized with the position of the first line, the other lines are identified and fitted with a Gaussian function on a flat constant, to take into account the continuum spectrum. The seven peak positions are then extracted from the fits and a linear calibration curve is produced for each detector:

$$E = a + b \cdot E_{fadc} \tag{4.12}$$

where E is the calibrated energy (in keV) and E_{fadc} is the uncalibrated one, a and b are the calibration parameters. Fig. 4.11(a) shows an example of the linear curve for the BEGe detector GD91A in a calibration of March 2016.

In order to investigate the linearity of the system, a quadratic calibration curve is also produced for each spectra:

$$E = a + b \cdot E_{fadc} + c \cdot E_{fadc}^2 \tag{4.13}$$

with respect to Eq. (4.12) there is a third parameter c.

An example of results from calibration is reported in Tab. 4.1: the first column shows the nominal value of the peaks from [196], then the second and the third columns report the values of the fitted calibration curve in correspondence of the peak positions, respectively for the linear and the quadratic case.

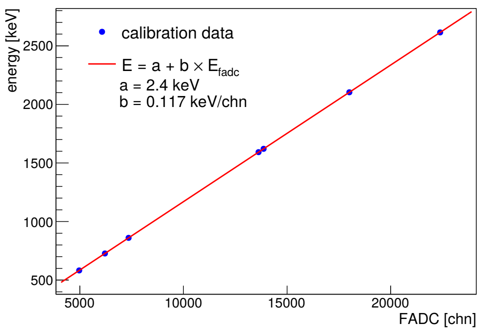

(a) Linear calibration curve.

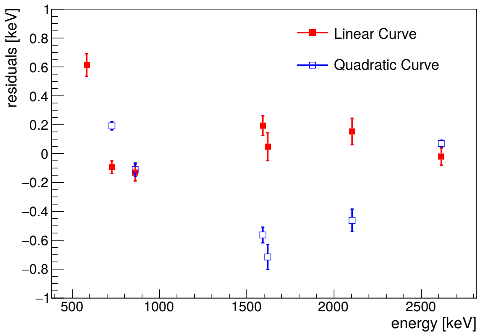

(b) Residuals of the peak positions.

Figure 4.11: Energy calibration for the BEGe detector GD91A in the run of March 17th, 2016: (a) linear calibration curve and (b) residuals of the peak positions for linear and quadratic curves (b). Value from Tab. 4.1.

Table 4.1: Calibration results for the BEGe detector GD91A in the run of March 17th, 2016: nominal value [196] and peak position using a linear and a quadratic calibration curve.

E_{nom}	E_{linear}	$E_{quadratic}$
2614.51	2614.53 ± 0.06	2614.44 ± 0.02
2103.51	2103.36 ± 0.09	2103.97 ± 0.02
1620.74	1620.69 ± 0.09	1621.45 ± 0.01
1592.51	592.32 ± 0.07	593.08 ± 0.01
860.564	860.70 ± 0.05	860.68 ± 0.01
727.33	727.42 ± 0.04	727.14 ± 0.01
583.187	582.57 ± 0.09	581.96 ± 0.01

In addition, the residuals from the two fits are calculated and plotted as function of the energy:

$$\Delta E = E_{nom} - E_{fit} \tag{4.14}$$

where E_{fit} is the value from the calibration curve and E_{nom} is the nominal peak value. Fig. 4.11(b) shows the plot of the residuals of the values listed in Tab. 4.1 corresponding, as before, to the GD91A detector.

Both Fig. 4.11(b) and Tab. 4.1 show that values from the linear calibration (red) are closer to the nominal ones with respect to the quadratic (blue), supporting the system linearity (detailed description in [195]).

In the analyzed calibration data there is no need for a quadratic description of the energy scale. Hence for all the detectors in the Phase II data production the energy reconstruction is performed through linear calibration curves.

Once the energy scale is determined from a calibration run, it is applied to the physics energy spectra acquired in the time between two consecutive calibrations. Both the optimal ZAC parameters from the minimization of the FWHM (described in Sec. 4.4.1) and the linear calibration curve of Eq. (4.12) are applied to the physics data in a specific validity time window of the calibration run, established by monitoring the detectors stability in terms of baseline, energy and test pulse position.

4.4.4 Energy resolution in physics data

An important parameter to validate the procedures of energy reconstruction and calibration is the energy resolution in the physics data, extracted from the fit of the γ-lines at 1461 keV and 1525 keV from ^{40}K and ^{42}K respectively. Thanks to the low background, these two lines, as later reported in chapter 5, are the only with sufficient statistics for the extraction of a reliable FWHM.

The K lines resolution is used also for the determination of the energy resolution at $Q_{\beta\beta}$, crucial value in the search of the $0\nu\beta\beta$ decay. The procedure to extract the FWHM at $Q_{\beta\beta}$ and the final value adopted in the Phase II analysis [1, 2] is presented in the second part of this section.

The fit of the ^{40}K and ^{42}K γ-lines is performed on three independent datasets, BEGe, $^{\mathrm{enr}}$Ge coaxial and $^{\mathrm{nat}}$Ge coaxial detectors, integrated over the entire time period.

For the three datasets, the energy region between 1440 and 1560 keV is selected and fitted through an extended unbinned maximum likelihood with two Gaussians on a flat background. This method does not depend on binning and works better in low statistics cases. The standard deviation of the two Gaussian functions is fixed to the same value since the energy of the two peaks is close and the same peak width is expected. The extracted value is used to determine the energy resolution in physics data.

Fig. 4.12 shows the plot of the energy spectra reconstructed with the ZAC filter in the selected region. In the same figure the energy resolutions obtained in the fits are also plotted: for the BEGe detectors the resulting FWHM is 2.66 ± 0.08 keV, for the $^{\mathrm{enr}}$Ge coaxial detectors is 3.81 ± 0.12 keV and for the $^{\mathrm{nat}}$Ge coaxial detectors is 3.79 ± 0.14 keV. The corresponding values obtained with the pseudo-Gaussian shaping are 2.75 ± 0.08 keV, 4.03 ± 0.12 keV and

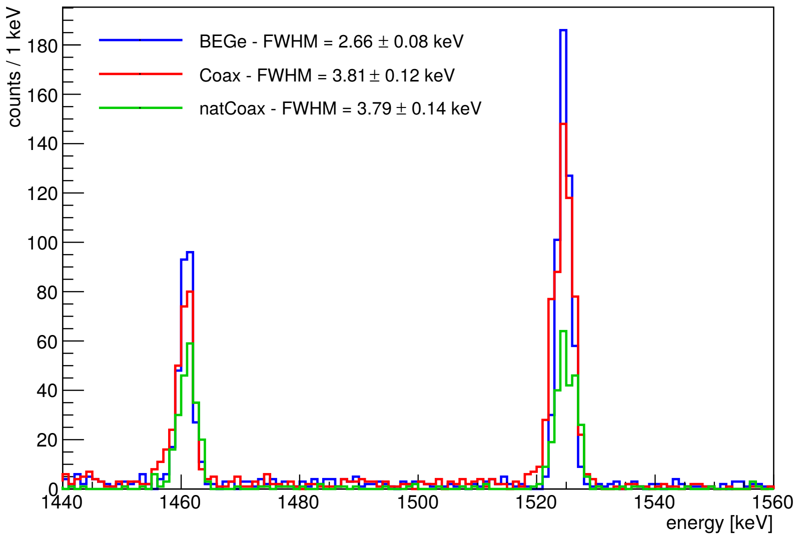

Figure 4.12: ^{40}K and ^{42}K γ-lines of the GERDA Phase II background spectrum reconstructed with the ZAC filter.

3.88 ± 0.14 keV, showing an improvement with the implementation of the new shaping filter.

Energy resolution at $Q_{\beta\beta}$ Since some instability can occur during the physics runs, to determine the energy resolution at $Q_{\beta\beta}$ is performed a comparison between the FWHM obtained on the K peaks and the value expected at the same energy from the calibration data. If the two values are compatible within 1 σ, the FWHM at $Q_{\beta\beta}$ is simply extracted from the resolution curve of the calibration data, otherwise a correction term is computed.

A global calibration, referred as super-calibration, including all the 31 Phase II calibration runs, is used to extract to energy resolution at $Q_{\beta\beta}$ for the BEGe and $^{\mathrm{enr}}$Ge coaxial datasets. The $^{\mathrm{nat}}$Ge coaxial detectors are not included in this analysis since this case is not interesting for the search of the $0\nu\beta\beta$ decay. App. A reports the FWHM obtained in the super-calibration for the 40 detectors.

As described in Sec. 4.4.3, the ^{228}Th calibration peaks are identified and fitted getting the FWHM. Then these values are fitted with the function that describes the energy resolution for Ge detectors (see Sec. 4.1.2), neglecting the charge collection term[1], Eq. (4.5) becomes:

$$\mathrm{FWHM}(E) = \sqrt{c_1 + c_2 \cdot E} \tag{4.15}$$

where c_1 and c_2 are the fit parameters that take into account the electronic noise and the fluctuation of the charge collection process. The DEP and the SEP are not included in this fit since they are wider than the other γ-lines due to Doppler broadening [197], hence the fit of Eq. 4.15 is performed with five points.

[1]this because low energy tails are not observed in the ZAC optimal filtered energy spectra

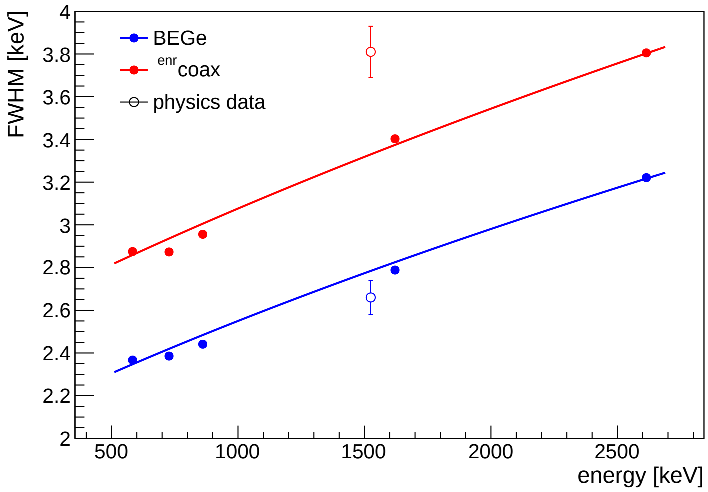

Figure 4.13: Energy resolution obtained in calibration data (filled symbols) and at the K γ-lines from physics data (open symbols).

Table 4.2: Comparison of the energy resolution obtained in calibration and physics data and final $Q_{\beta\beta}$ resolution for BEGe and the ^{enr}coaxial detectors.

	BEGe	^{enr}Coax
$\mathrm{FWHM}^{cal}_{1525}$	2.78 ± 0.01	3.34 ± 0.01
$\mathrm{FWHM}^{phy}_{1525}$	2.66 ± 0.08	3.81 ± 0.12
offset		0.47 ± 0.12
$\mathrm{FWHM}_{Q_{\beta\beta}}$	3.00 ± 0.08	4.03 ± 0.12

Fig. 4.13 shows the resolution curves obtained for the BEGe (blue) and the $^{\mathrm{enr}}$Ge coaxial datasets (red); the filled symbols are the FWHMs of the calibration data, the open ones are from the fit of the K γ-lines from physics data.

The energy resolution at 1525 keV is extracted from the resulting curves and is compared with the values obtained from the background spectrum fit (Fig. 4.12). Tab. 4.2 reports a summary of the FWHM values: the results from the super-calibration are indicated as $\mathrm{FWHM}^{cal}_{1525}$, the ones from physics data as $\mathrm{FWHM}^{phy}_{1525}$.

For the BEGe detectors the resolution comparison shows that in physics data the FWHM is compatible with the value from calibration. In this case the FWHM at $Q_{\beta\beta}$ that is directly extracted from the resolution curve. For the $^{\mathrm{enr}}$Ge coaxial detectors, the FWHM at $Q_{\beta\beta}$ is taken from the resolution curve plus the difference between the FWHM at 1525 keV obtained in the calibration and in the physics data. All the values are reported in Tab. 4.2. In both cases the error on the $\mathrm{FWHM}_{Q_{\beta\beta}}$ is computed summing in quadrature the uncertainties of the two FWHM values.

The energy resolution at $Q_{\beta\beta}$ are then used in the statistical analysis of the $0\nu\beta\beta$ decay search [1, 2] to fix the width of the Gaussian function for the expected signal.

4.5 Noise studies in GERDA Phase II

As already pointed out, a noise investigation in the GERDA setup has been performed [198]. Given the results presented in the previous sections, the purpose of this study is to characterize the actual noise and possibly identify the sources.

In Sec. 3.5 the preamplifier installed in the final Phase II configuration is described: as in Phase I, it is a classical CSP, named CC3 (see Sec. 3.4), where JFET and feedback components are mounted close to it and connected to the detector through Pyralux®/Cuflon® flex contacts 40 to 80 cm long.

Since the commissioning runs (see Secs. 2.4 and 3.5), an additional noise was observed. It was not observed neither in Phase I (CSP and front-end components in the same configuration as in Phase II) nor in Phase II tests with the front-end components close to the detector. This noise causes a degradation of the detector performance both in term of energy resolution and pulse shape discrimination power; for the BEGe detectors the latter is evaluated as the resolution of the A/E parameter (defined in Sec. 2.3) for 1592 keV DEP events.

The same noise is observed in Phase II data. Fig. 4.8 shows how the BEGe energy resolution worsen with the detector position in the string: averaging on all the positions, the FWHM at the 2614.5 keV peak is ~ 3.2 keV, about 20% higher than the optimal value expected for BEGe detectors and actually achieved in top detectors and in the individual detector in GDL tests.

To evaluate the BEGe performance, another relevant parameter is the resolution of the A/E parameter. Fig. 4.14 shows the percentage FWHM of A/E for BEGe detectors (indicated as $\text{FWHM}_{A/E}$), combining three ^{228}Th Phase II calibration runs. It shows the same trend of Fig. 4.8: the $\text{FWHM}_{A/E}$ also scales with the position of the detector in the string and best values ($\sim 1.5\%$) are obtained for the top detectors (i.e. close to the front-end). Moreover, for the PSD parameter resolution of Fig. 4.14 the degradation is quantitatively larger with respect to the energy resolution following the BEGe position: many bottom detectors show a $\text{FWHM}_{A/E}$ around 3%, doubled with respect to the best values achieved for top detectors.

This shows that the noise in Phase II impacts on the BEGe performance in terms of PSD, hence to distinguish $0\nu\beta\beta$ decay events from the background. This, in addition to the energy resolution deterioration, seems connected to the detector to front-end distance hence to the length of the signal cable.

The purpose of the study presented in this section is to better understand the noise figure and the detector performances, and try to identify the source of the extra noise.

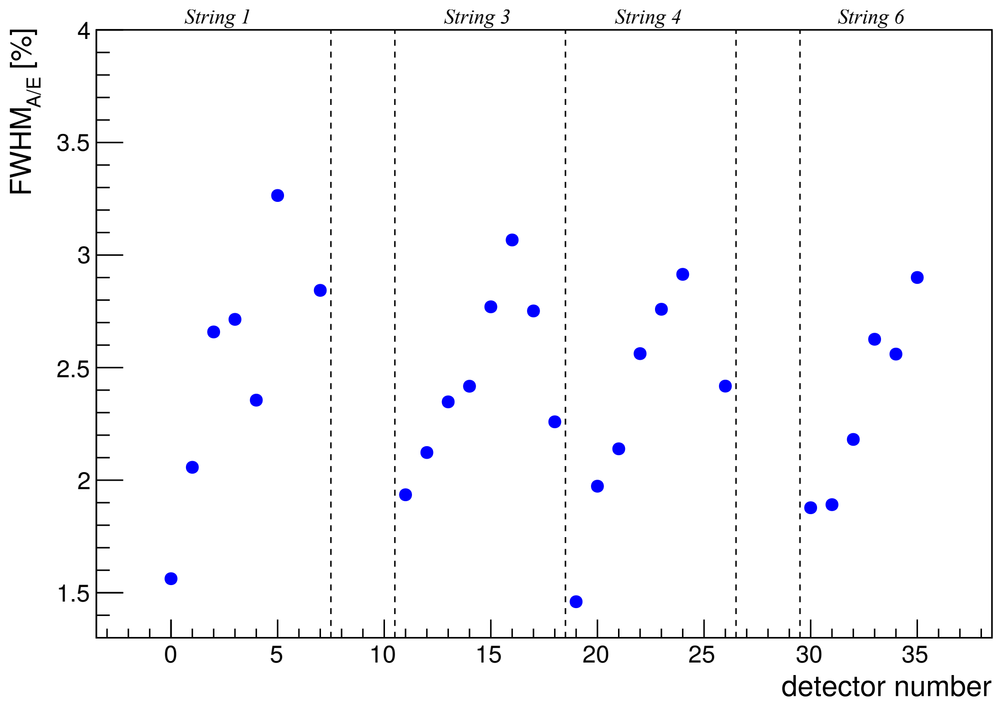

Figure 4.14: Percentage FWHM of the A/E parameter of DEP events for BEGe detectors in Phase II. The detectors GD02D (number 6) and GD91B (number 25) are not considered for this analysis. Values from [199].

4.5.1 Spectral power density study

The starting point of the noise study is the analysis in the frequency domain of the baseline signals. A ROOT [135] software including MGDO [134] libraries has been developed to analyze the long baseline traces of 160 μs (acquired during the physics runs), perform the Fast Fourier Trasform (FFT) and then calculate the power spectral density.

Fig. 4.15 shows typical frequency spectra for the BEGe detectors of the string 1 (a) and the ^{enr}Ge coaxial detectors of the string 2 (b) in Phase II, the different colors correspond to the detectors of the strings. This situation is reached after several work sessions, performed during the commissioning, to identify and mitigate the noise sources. In particular (as also described in Sec. 3.5) an improvement on the noise situation was obtained reinforcing the grounding connections on the HV filters of Ge detectors and photomultipliers [200].

Both spectra of Fig. 4.15 exhibit a white noise continuum that decreases with the frequency and some noise pickup between 3 and 7 MHz and above 9 MHz, much more intense in the coaxial detectors. The BEGe frequency plot (Fig. 4.15(a)) shows an evident trend of the noise power at frequencies < 4 MHz with the detector position in the string; the same trend is less evident in the coaxial string (Fig. 4.15(b)).

The trend observed in the BEGe power spectral density corresponds to the degradation of the energy resolution, described in Sec. 4.4.2 and visible in

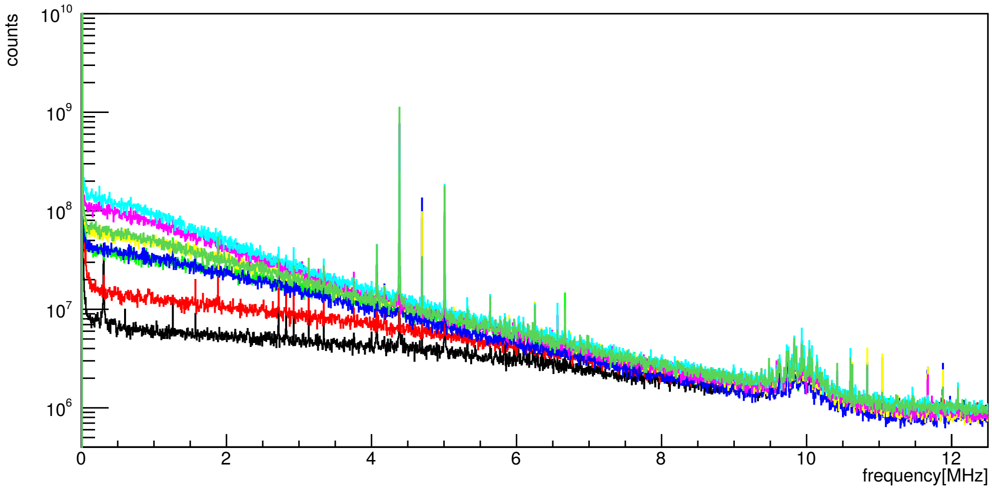

(a) BEGe detectors of string 1.

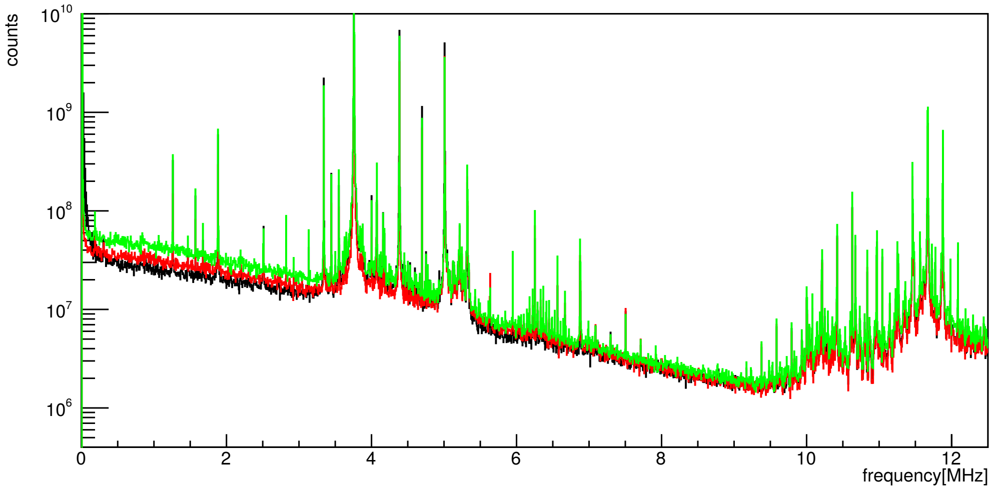

(b) ^{enr}Ge coaxial detectors of string 2.

Figure 4.15: Power spectral density calculated through the FFT of the output waveforms for the string 1 (a) and the string 2 (b). The different colors correspond to the detector of the strings.

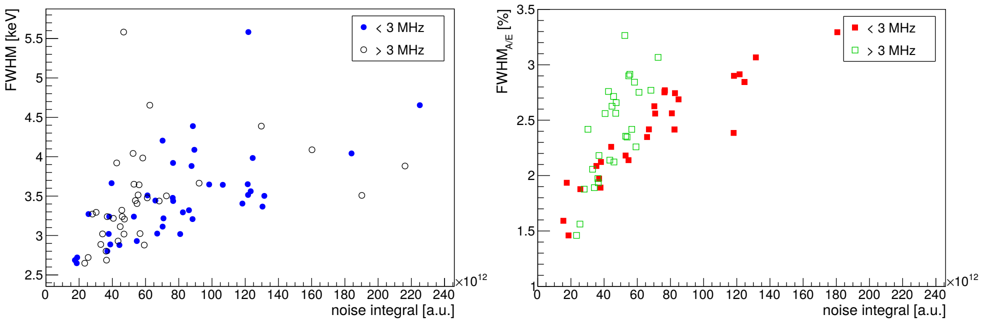

(a) Energy resolution. (b) A/E resolution.

Figure 4.16: Energy (a) and A/E (b) resolutions as function of the noise integral at low ($<$ 3 MHz) and high ($>$ 3 MHz) frequencies for the Phase II detectors.

Fig. 4.8, and of the A/E resolution, as showed Fig. 4.14. To quantify the noise, the integral of the frequency spectra in the region up to 3 MHz (referred as low frequencies) and in the region above 3 MHz (high frequencies) is performed.

Fig. 4.16 shows the plot of the FWHM at the 2614.5 keV peak in the Phase II super-calibration (see App. A) and the FWHM of the A/E parameter (values of Fig. 4.14) as function of the noise integral at low and high frequencies. The different colors and symbols indicate the two frequency regions, each point corresponds to one Phase II detector (in the case of the A/E resolution only BEGe detectors are considered).

Both the plots of Fig. 4.16 show a correlation between the resolution and the noise integral at low and high frequencies. The A/E correlation is much more evident (Fig. 4.16(b)): the increase of the noise reflects in a significative broadening of the A/E peak of DEP events.

This is explained by the different frequencies relevant for the energy and the A/E ratio (in particular the current amplitude A). In the energy reconstruction the ZAC shaping provides an optimal reduction of noise, filtering low and high frequency noise. Different story for the amplitude of the current pulse A, in this case is not possible filter the high frequency noise because the structures important for the PSD would be also removed, losing in discrimination power. Attempts to improve the filtering of the current signal have been performed but no conclusive results were obtained [182, 201]. The crucial point is that the PSD performance of the BEGe detectors are strongly sensible to the high frequency noise figure, more than the energy resolution.

4.5.2 Fit of the energy resolution

The analysis of the energy resolution of the Ge detectors as function of the filter shaping time τ_s (see Secs. 4.1.1 and 4.1.2) indicated a trend of the BEGe detectors with the position in the strings: top BEGe detectors show a very good resolution ($\sim$ 2.6 keV at the 2614.5 keV peak) and an optimization graph (Fig. 4.7(a)) with a low level of both series and parallel noise; going down in the BEGe strings the FWHM worsen and the ZAC optimization graph (Fig. 4.7(b)) shows an increase of series and $1/f$ noise; finally, when the detectors are driving leakage current there is a third kind of graph (Fig. 4.7(c)), clearly dominated by the parallel noise induced by this current. These statements follow by the electronic noise formula described in Eq. (4.1): the contribution of the series and the parallel noise are dominant at low and high values of the shaping time τ_s respectively; while the contribution of the $1/f$ noise is constant with τ_s.

The frequency spectra and the particular trend observed in the energy resolution motivated to better investigate the noise situation. On February 24th, 2016 a pulser-only data acquisition has been performed and used to study the electronic noise as function of the ZAC shaping time and the string position. The goal is qualify and quantify the electronic noise sources and possibly identify the source of the extra noise causing the energy and A/E resolutions deterioration.

The pulser energy is reconstructed with the ZAC filter using different values of the shaping time τ_s, the FWHM is extracted with a Gaussian fit and then converted in terms of ENC following Eq. (4.2). The resulting ENC^2 as function of τ_s is finally fitted with Eq. (4.1):

$$\mathrm{ENC}^2 = \alpha \frac{1}{\tau_s} \frac{2k_B T}{g_m} C_{tot}^2 + \beta A_f C_{tot}^2 + \gamma \left(eI_{tot} + \frac{k_B T}{R_F} \right) \tau_s$$

the constants α, β and γ are fixed to the value for a finite cusp-like filter from [183], the value of the JFET transconductance is independently measured $g_m =$ 10 mA/V and the feedback resistor is $R_F = 500$ MΩ; the total capacitance is written as:

$$C_{tot} = C_{det} + C_i + C_F + C_{stray} \tag{4.16}$$

including an additional stray capacitance produced by the signal cable; the total current is $I_{tot} = I_{det} + I_{gate}$ and the assumption of $I_{det} = I_{tot}/2$ is adopted, i.e. $I_{gate} = I_{det}$.

The parameters extracted from the fit are the total capacitance C_{tot}, the amplitude of the $1/f$ noise A_f and the intensity of the total current I_{tot}.

Fig. 4.17 shows examples of pulser ENC^2 plotted as function of the ZAC shaping time for the BEGe detectors GD91A and GD00D, in blue is reported the fit function and the results are in the legend.

Comparing the fit from the different detectors it appears that in some cases the parameters are not well defined, in particular the parallel noise contribution due to the low values of the detector and gate current.

However an interesting situation seems to appear: the stray capacitance C_{stray}, calculated with Eq. (4.16), is increasing with the BEGe position in the string and may be the responsible of the observed excess noise. Fig. 4.18 shows the extracted C_{stray} for the 40 detectors: the values in BEGe detectors are between 10 and 80 pF with a trend similar to the one observed in the energy (Fig. 4.8) and the A/E (Fig. 4.14) resolution. The origin of this stray capacitance could be in the capacitive couplings of the long signal front-end contacts that run overlapped along the BEGe detector string, the front-end contacts length scales with the position in the string and could explain the increase of C_{stray}, but such high values are difficult to explain.

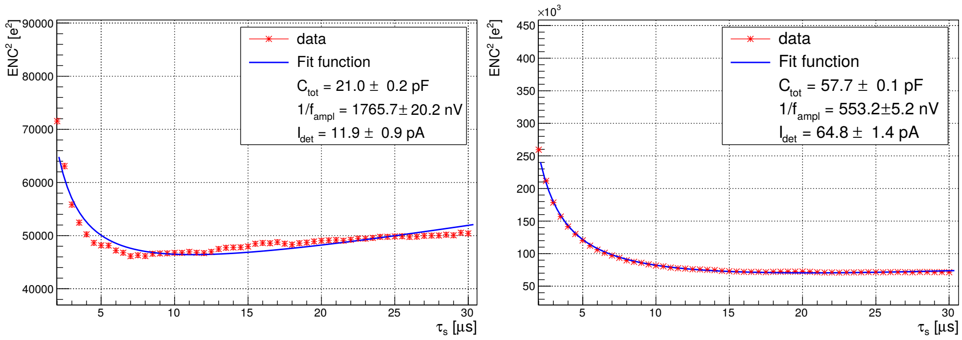

(a) Detector GD91A.

(b) Detector GD00D.

Figure 4.17: Pulser ENC^2 as function of the ZAC shaping time for the BEGe detector GD91A. The fit function (in blue) is Eq. (4.1), the resulting parameters are reported in the legend.

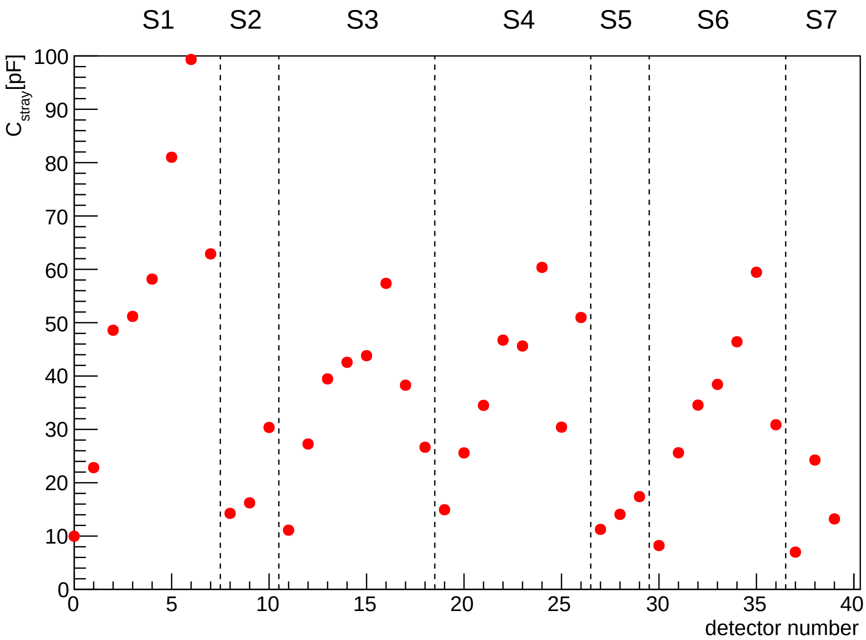

Figure 4.18: Stray capacitance C_{stray} as function of the detector number from the fit of the ENC^2.

Also in the coaxial detectors the C_{stray} extracted from the fit increases with the position (in particular string 2 and 5 in Fig. 4.18), showing values between 5 and 30 pF. On the contrary this trend was not found in the coaxial detector resolution (Fig. 4.8): apart from individual detector peculiarities, this may be related to the different ratios of parasitic and intrinsic detector capacitance. BEGe detectors have $C_{det} \sim$ pF, while coaxial detectors $C_{det} \sim 10$ pF: hence the stray capacitance accounts for a larger fraction of their intrinsic capacitance. This hypothesis has to be verified.

The use of signal cables with length between 40 and 80 cm (responsible of this C_{stray}) is a consequence of the final front-end electronics solution adopted in Phase II. As described in chapter 3, in the original Phase II design the JFET and the feedback components were mounted in the proximity of the detector, in order to avoid the signal-to-noise ratio degradation that has been instead observed in the Phase II data. On the other hand the final solution shows several advantages with respect to the original design (see Sec. 3.5), like the good reliability and the lower contribution to the radioactivity budget.

Anyway the situation is not clear and further work is needed on this side; for this a GERDA prototype setup has been constructed in the Max Planck Laboratory of Heidelberg in order to better investigate on the noise sources of the GERDA setup.

4.6 Conclusions

A new digital signal processing, applied successfully in GERDA Phase I [180], has been used on the new Phase II data showing an improvement with respect to the standard filter both in calibration and in physics data.

The performance of the Phase II detectors in terms of FWHM at the 2614.5 keV in the calibrations show an average resolution of $3.18^{+0.44}_{-0.37}$ keV, 3.73 ± 0.22 keV and 3.87 ± 0.15 keV respectively for BEGe, ^{enr}Ge coaxial and ^{nat}Ge coaxial detectors. The energy resolution at $Q_{\beta\beta}$ integrated over 6 months is 3.00 ± 0.08 keV (4.03 ± 0.12 keV) for BEGe (^{enr}Ge coaxial) detectors, values adopted in the first Phase II release [1].

In addition the study of the energy resolution as function of the position of the BEGe detectors in the strings show a peculiar trend that can be related to the detector to front-end distance, as expected from the design of the front-end electronics installed in Phase II. A similar trend is observed also in the resolution of the A/E parameter for DEP events. The amount of the extra noise is instead larger than expected.

The noise studies confirmed the strong correlation between the performance of Ge detectors and the measured noise figure, both in terms of energy resolution and PSD. A possible source of the extra-noise has been identified: the stray capacitance of the signal contacts that increases with the distance from detector to the front-end, hence connected with the Phase II front-end design.

This fundamental extra noise is at present a limit for the PSD of the BEGe detectors. The GERDA future developments deploying larger mass of ^{76}Ge will need longer strings, hence a clear picture on the extra noise from capacitive coupling of the detector surfaces and contact cables will be crucial, mostly in case of front-end components located at CSP side.

Chapter 5

Study of the GERDA Phase II background spectrum

The second part of this thesis is devoted to the study of the new physics data from GERDA Phase II. In particular in this chapter a detailed analysis of the background spectrum and the background sources is presented.

The screening measurements of the material adopted in the construction of the Phase II array and the background observed in Phase I [139, 202] gave indications on the structure expected in the new spectrum: contaminations from ^{238}U and ^{238}Th chains and from ^{40}K, in addition to the structures produced by the unstable Ar isotopes present in the 64 m^3 liquid argon bath.

The $0\nu\beta\beta$ decay analysis is performed in GERDA after the application of LAr veto and PSD: these cuts provide a strong reduction of the background, in particular in the $Q_{\beta\beta}$ region, where an ultra-low background has been already observed in the first Phase II data [1]. Anyway, a study of the background before these cuts is crucial to determine the residual contaminations and to understand how the background can be further reduced in future experiments.

After the description of general information on the Phase II data, Sec. 5.1 reports the main results from the screening measurements and the full background spectrum collected in the first months of Phase II for the three datasets (BEGe, ^{enr}Ge coaxial and ^{nat}Ge coaxial detectors). Then in Sec. 5.2 a study of the observed α spectrum, the distribution per detector and the trend of the α events as function of time are presented and discussed. The study of the γ-lines is presented in Sec. 5.3, where the visible peaks in the spectrum are analyzed.

Part of this study is published in [203].

5.1 Phase II data, contaminations and background spectrum

The physics data of GERDA Phase II collected from December 20th, 2015 and until October 30th, 2016 are used in this background study. The data from June 1st, 2016 are unpublished and corrently blinded in the region around the $Q_{\beta\beta}$.

Table 5.1: γ-ray screening measurements for the relevant components of Phase II. The activity of ^{40}K, ^{226}Ra (from ^{214}Bi) and ^{228}Th (from ^{208}Tl) is reported. The values are from [153, 207, 208, 209].

component	amount	units	^{40}K	^{226}Ra	^{228}Th
Pyralux® cables	41 pc	μBq/pc	34 ± 12	3 ± 1	4 ± 1
Cuflon® signal cables	29 pc	μBq/pc	100 ± 50	25 ± 5	< 11
Cuflon® HV cables	10 pc	μBq/pc	300 ± 80	22 ± 5	< 22
Si plate	~ 1 kg	μBq/kg	2600 ± 1400	< 350	< 480
nylon-shroud	7 pc	μBq/pc	130 ± 40	3 ± 1	2 ± 1
LAr veto fibers	~ 0.85 kg	μBq/kg	460 ± 90	42 ± 3	58 ± 1

As already mentioned in Sec. 2.1, the output waveforms from the Ge detectors are digitized and converted in ROOT files and then processed with the Gelatio framework [136]. In order to reject non-physical events, various quality cuts are applied to the data: the trigger position is required to be between 77.5 and 82.5 μs, the rise time in the range 0.1–4 μs and also a limitation on the slope of the baseline is applied in order to remove pile-up events (signal superimposed to the exponential decay tail of the previous one). The study of the quality cuts is in Ref. [154].

Data are reconstructed with the ZAC shaping filter and then calibrated following the procedure described in Sec. 4.3. The information extracted by each calibration run are applied to the physics data in a validity time defined according the hardware operations on the setup (ordinary and extraordinary maintenance).

In total 253.4 days of live time have been acquired: 130.7 days until June 1st, 2016 (that has been used for the first Phase II data release [1, 2]) and additional 122.7 days acquired in the following months until the end of October 2016. The duty cycle in the entire data acquisition is 86.5%.

The data from each detector are validated through the monitoring of the test pulse position and gain stability (see [204, 205]). The analyzed data correspond to an exposure of 11.1 kg·yr, 9.3 kg·yr and 3.8 kg·yr respectively for BEGe, ^{enr}Ge and ^{nat}Ge coaxial detectors.

5.1.1 Contaminations expected from screening results

The Gerda hardware components have been tested for their radio-purity prior the installation, with a gamma ray spectroscopy using HPGe screening facilities (in particular the GeMPI [206] facility located at the LNGS underground laboratory) or with mass spectrometry through Inductively Coupled Plasma Mass Spectrometers (ICP-MS).

The main expected contaminations, according to screening results, are from materials located close to the detector array. Firstly, the contribution of the LAr volume surrounding the Ge strings, in particular the long-lived isotopes ^{39}Ar and ^{42}Ar. The other relevant components with their activity budget of ^{40}K, ^{226}Ra and ^{228}Th are listed in Tab. 5.1.

The signal and HV cables contribute to the background spectrum. As discussed in Sec. 3.5, in Phase II array are installed Pyralux® cables (11 signal +

30 HV) with thickness of 3 mils, Cuflon® signal cables (29 pieces, 3 mils thick) and Cuflon® HV cables (10 pieces, 10 mils thick), all with length between 40 and 80 cm. The activity budget from cables are listed in Tab. 5.1: they show the larger contamination of ^{40}K, with a total activity of $\simeq 7.3$ mBq, and ^{226}Ra, with $\simeq 1.1$ mBq; in both cases the strongest contribution is coming from the Cuflon® cables.

Contributions are expected also from the detector holders. They consist in one Si plate of 1.5 mm and three Cu bars as vertical fixture per detector (as shown in Figs. 2.8 and 3.5(c)), plus a Cu star and a Cu bar on top detectors needed to hold up the string (visible in Fig. 2.9(c)). The Cu contribution is negligible. The specific activities of the Si plate are reported in Tab. 5.1: it contributes to the total ^{40}K budget with $\simeq 2.6$ mBq.

Other components located close to the array are the mini shrouds that surround each string. They are made of nylon with tetraphenyl butadienne (TPB) coating and consist of three parts (lateral, bottom and top surfaces) with thickness of 0.125 mm [153]. The contaminations are listed in Tab. 5.1: the seven mini-shrouds mounted in the Phase II array contribute to the total budget of ^{40}K (with $\simeq 0.9$ mBq), ^{226}Ra (with $\simeq 21$ μBq) and ^{228}Th (with $\simeq 14$ μBq).

In addition a minor contribution is expected also from the LAr instrumentation, in particular from the wavelength shifting fibers [151, 152] located ~ 10 cm far to the external strings. The activity budgets evaluated through the ICPMS measurement of the fibers [209] are listed in Tab. 5.1.

5.1.2 Phase II background spectrum

Fig. 5.1 shows the background spectra of Phase II before pulse shape discrimination and LAr veto cuts for the three types of detectors (BEGe in blue, $^{\text{enr}}$Ge coaxial in red and $^{\text{nat}}$Ge coaxial in green), normalized by their exposure. The events in an energy window of 50 keV centered at $Q_{\beta\beta}$ (2039 keV) are not available for this study: a blinded $0\nu\beta\beta$ decay analysis is performed and this region will be open only after fixing the analysis procedure.

The spectra of Fig. 5.1 show the expected prominent structures:

- the low energy region up to 500 keV is dominated by the long-lived ^{39}Ar isotope, whose expected activity in LAr is 1.01 ± 0.08 Bq/kg [210]; ^{39}Ar is a β-emitter with $T_{1/2} = 269$ yr and Q $= 565$ keV;
- the spectrum of the $2\nu\beta\beta$ decay is dominating the energy region from 600 to 1400 keV and it is extending up to $Q_{\beta\beta}$. This structure is not visible in the $^{\text{nat}}$Ge coaxial spectrum; the half-life of the $2\nu\beta\beta$ decay of the ^{76}Ge was measured in Phase I and is $(1.926 \pm 0.094) \cdot 10^{21}$ yr [141];
- at 1461 keV and 1525 keV the γ-lines from ^{40}K and ^{42}K respectively are visible. They are the most intense lines of the Gerda spectrum, hence adopted to determine the energy resolution in the physics data (see Sec. 4.4.4); more details on these two isotopes are reported in Sec. 5.3;
- γ-lines from ^{214}Bi and ^{208}Tl are also visible, they occur in the radioactive decay chain of ^{226}Ra and ^{228}Th. Both isotopes decay by β^- with Q-value

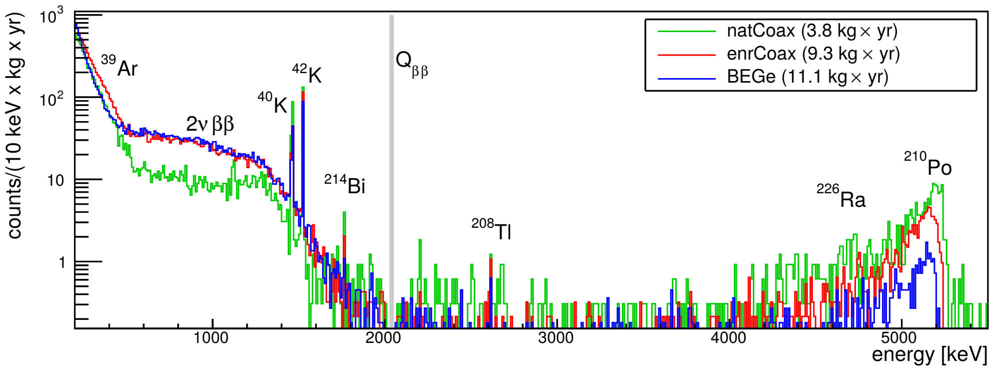

(a) Phase II energy spectra in the region 200 keV - 5.5 MeV

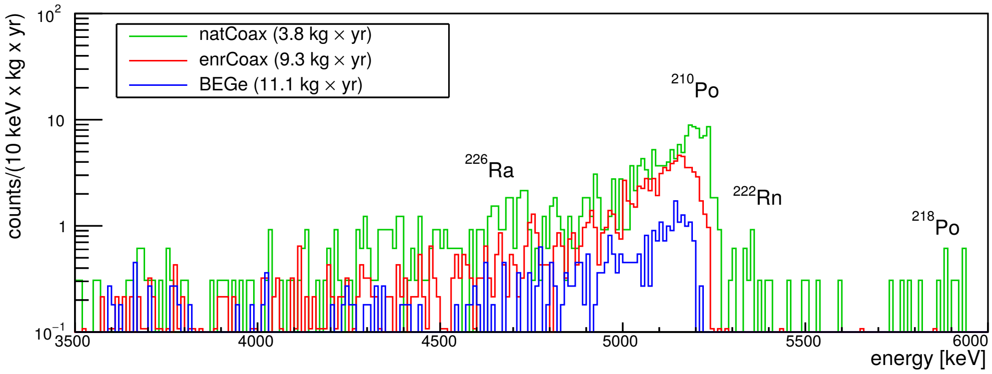

(b) Phase II high energy spectra

Figure 5.1: Normalized GERDA Phase II spectra, before pulse shape discrimination and LAr veto, for BEGe (blue), $^{\mathrm{enr}}$Ge coaxial (red) and $^{\mathrm{nat}}$Ge coaxial (green) detectors. The prominent features and the $Q_{\beta\beta}$ region (where the $0\nu\beta\beta$ decay is expected) are indicated.

at 3.27 and 5.00 MeV respectively, producing several γ lines also in the $Q_{\beta\beta}$ region; the analysis is reported in Sec. 5.3;

- the high energy region (Fig. 5.1(b)) shows a prominent α structure from ^{210}Po in all three datasets: a peak at Q-value and a tail on its left side extending to lower energies is visible. In addition the ^{nat}Ge coaxial spectrum shows also other α contaminations; the analysis of the α structures is reported in Sec. 5.2.

In the following sections a detailed analysis of the observed α and γ contaminations is presented.

5.2 Alpha-induced background

The high-energy spectra of Fig. 5.1(b) shows a strong contribution from ^{210}Po, an α-emitting isotope with $Q = 5.41$ MeV and $T_{1/2} = 138.4$ days. Other peak structures with lower intensities are observed in the ^{nat}Ge spectrum (green in Fig. 5.1(b)) around 4.7 MeV, 5.4 MeV and 5.9 MeV, that indicate a contribution from the successive α decays in ^{226}Ra decay chain: ^{226}Ra with $Q = 4.87$ MeV and $T_{1/2} = 1600$ yr, ^{222}Rn with $Q = 5.59$ MeV and $T_{1/2} = 3.8$ days and ^{218}Po with $Q = 6.11$ MeV and $T_{1/2} = 3.1$ min [196].

α particles with energies between 4 and 9 MeV have a short range in germanium and LAr of the order of 10 μm. For this reason only decays occurring on or in the close proximity of the detectors p$^+$ contact surface can contribute to the background spectrum. The p$^+$ dead layer is ~ 1 μm, while the n$^+$ electrode ~ 1 mm thick shields from α [127, 143].

The α structures of Fig. 5.1(b) have a peak with a maximum at energy lower than the corresponding Q-value (e.g. the peak of the ^{210}Po is at ~ 5.25 MeV while $Q = 5.41$ MeV) and a tail towards lower energy. Simulations of α decays from ^{210}Po and ^{226}Ra sub-decay chain in Phase I [139] show that this effect is due to the detector dead layer thickness: thicker dead layer reflects in a shift of the maximum peak at lower energies. The ^{210}Po α structure for BEGe detectors is slightly shifted with respect to the coaxial detectors, accounting for a thicker p$^+$ dead layer (1 μm).

Fig. 5.1(b) also shows that the two spectra from coaxial detectors (in red and in green) have a stronger α contamination with respect to the BEGe detectors (in blue). This can be related to their larger p$^+$ contact surface (around factor of ten) due to the bore hole and some radio-purity variability of the implantation process at time of detector production.

Nevertheless the study of the distribution of the α events among the detectors is not completely in agreement with this statement: Fig. 5.2 shows the detector count rate per unit of surface and time, of events with energy between 3.5 and 5.3 MeV. An evident trend is not observed since there is a large variation of the rate in the 40 detectors.

The strongest contaminations are in one ^{enr}Ge and one ^{nat}Ge coaxial detector, that show a rate larger than 2 cts/(cm^2·yr). They correspond to ANG4 (number 29) and GTF45 (number 39), that are mounted in the lowermost side of the relative string (see App. A). A high α count rate ($\gtrsim 1$ cts/(cm^2·yr)) is

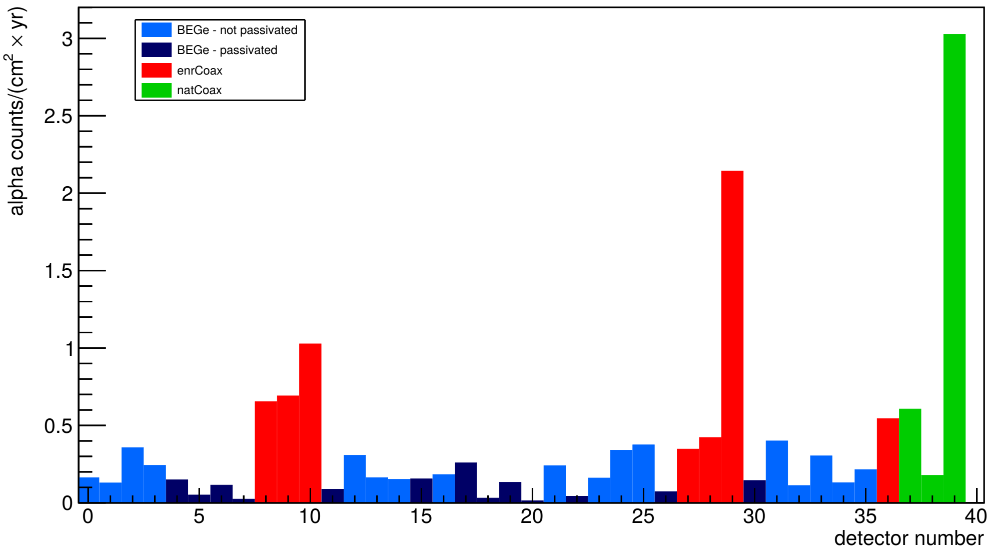

Figure 5.2: α detector count rate per unit of surface and year for BEGe (not passivated in light blue and passivated in dark blue), ^{enr}Ge coaxial (red) and ^{nat}Ge coaxial (green) detectors.

observed also in the bottom ^{enr}Ge coaxial detector of string 2 (ANG3, number 10).

The BEGe detectors (light and dark blue in Fig. 5.2) have a count rate between ~ 0.05 cts/(cm^2·yr) and ~ 0.4 cts/(cm^2·yr), showing in some case a value comparable with two ^{enr}Ge coaxial detectors (number 27 and 28). This is not in agreement with an α contamination from the p$^+$ contact surface only: a similar rate for detectors with compatible dimensions would be expected. Another α source is therefore plausible, but the origin is not understood so far.

A possible explanation for the variation of the α count rate in the BEGe detectors is the presence of a passivation layer on the groove in the detectors that showed an high leakage current during the commissioning runs (see Sec. 2.4). Fig. 5.2 reports with different blue tones the not passivated (light) and passivated (dark) BEGe detectors: the majority of the cases with a very low α count rate ($\lesssim 0.1$ cts/(kg·yr)) corresponds to passivated ones. The average α rate for passivated and non-passivated BEGe detectors is of 0.10 cts/(cm^2·yr) and 0.24 cts/(cm^2·yr) respectively. This result gives an indication that passivated detectors have smaller rate: the passivation with thickness of ~ 100 nm may act as further dead layer shielding the α events. Anyway the explanation is not conclusive and is under investigation.

5.2.1 Alpha count rate variation in time

An analysis of the time distribution of the event count rate above 3.5 MeV is performed to confirm the origin of the α spectrum from ^{210}Po, given that the half-life of this isotope is of the order of the present Phase II life time.

If only ^{210}Po is present as a contamination, the α count rate should decrease with an half-life of 138.4 days, while contaminations coming from the ^{226}Ra decay chain in secular equilibrium would cause an event rate constant in time, since the half-life in this case is much longer than the life time of the experiment.

The event rate distributions as function of the time is fitted with an exponential decreasing rate plus a constant rate:

$$f(t) = a + b \cdot \exp\left(-\log(2)\frac{t}{T_{1/2}}\right) \tag{5.1}$$

with $T_{1/2}$ fixed to the ^{210}Po half life of 138.4 days, a and b are the fit parameters. The χ^2 method with a ROOT software has been implemented to perform the fit. In addition to Eq. (5.1), a fit with an exponential rate only is also performed and the resulting χ^2 values in the two models have been compared.

The counts in the energy region between 3500 and 5300 keV are selected for the three kinds of detectors in time intervals of $\Delta t = 10$ days. A correction that takes into account the live time fraction of each interval has to be applied to the counts, following:

$$\text{counts}[t_i] = \text{counts}[t_i]/\text{live-time}[t_i] \tag{5.2}$$

where the live time is calculated through the number of pulser events in the interval i:

$$\text{live-time}[t_i] = \frac{\text{pulser}[t_i]}{\text{maxPulser}[t_i]} \tag{5.3}$$

and

$$\text{maxPulser}[t_i] = \frac{\Delta t}{pulserRate} \cdot \text{activeDetectors}[t_i]\ . \tag{5.4}$$

Fig. 5.3 shows the time distributions of the normalized α count rate for BEGe, $^{\text{enr}}$Ge coaxial and $^{\text{nat}}$Ge coaxial detectors fitted with the function of Eq. (5.1), the fit results are reported in the legends. In this analysis the data from the first month of the acquisition (first two points in Fig. 5.3) are not considered since a stronger ^{222}Rn contamination, due to the array mounting operations, is visible.

The case with higher statistics of the $^{\text{enr}}$Ge coaxial detectors (Fig. 5.3(b)) shows a χ^2/ndf value close the to unity (1.02) and the model of Eq. (5.1) is clearly preferred with respect to a simply exponential fit ($\Delta\chi^2 = 3.8$). The other two datasets of BEGe and $^{\text{nat}}$Ge coaxial detectors (Figs. 5.3(a) and 5.3(c)) have a lower statistics and the fits show higher χ^2/ndf values of 1.37 and 1.62 respectively, however preferring this fit to the model without the constant rate (with $\Delta\chi^2 = 6.7$ for the BEGe and $\Delta\chi^2 = 12.7$ for the $^{\text{nat}}$Ge coaxial case).

The observed α count rate clearly shows that the majority of the events comes from a ^{210}Po contamination on the detector surfaces as was also observed in Gerda Phase I [139]. On the other hand, the time analysis shows that adding a small constant rate to the fit function the agreement with the observed data improves, reflecting in the presence of a minor contamination from the ^{226}Ra decay chain. The new background simulations of Phase II [211, 212] is

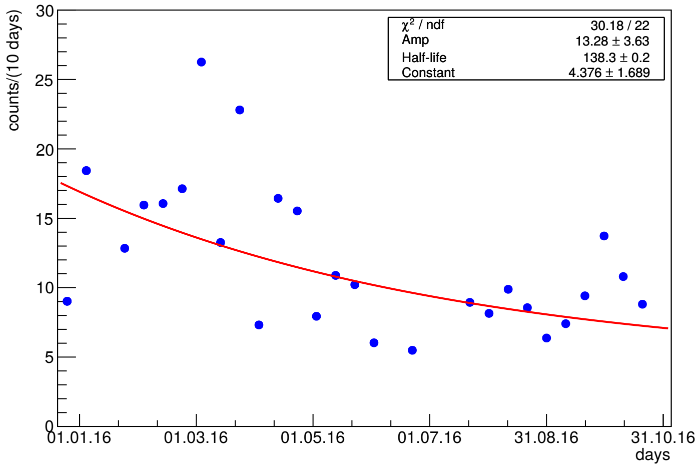

(a) BEGe detectors.

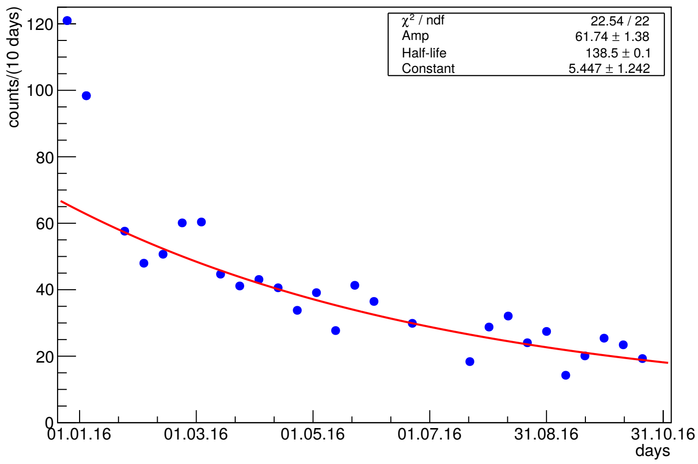

(b) ^{enr}Ge coaxial detectors.

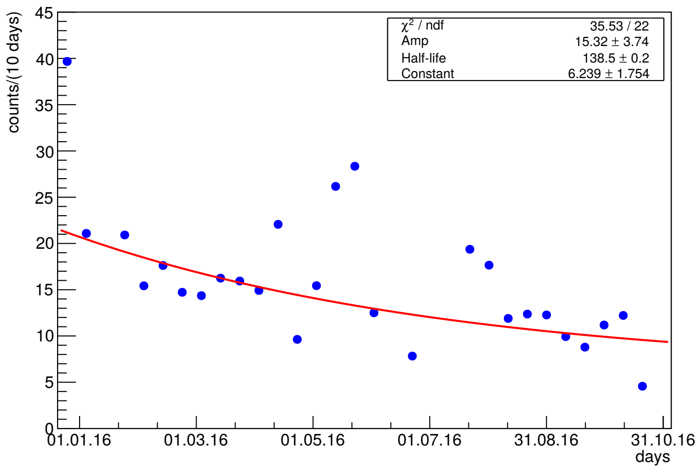

(c) ^{nat}Ge coaxial detectors

Figure 5.3: α count rate normalized to the live time fraction as function of the time for the three kinds of Phase II detectors.

also reporting that a model with a small contribution of the ^{226}Ra daughters in LAr is preferred, as expected from the LAr screening measurements [127].

The results of the α analysis provided the motivation to perform a study of the $0\nu\beta\beta$ decay sensitivity of Phase II including a time dependent background model. This is described in chapter 6.

5.3 Gamma-contaminations

The background spectrum of Fig. 5.1(a) shows the presence of γ-lines that originate from the contaminations of the materials surrounding the detector array (see Tab. 5.1). In this section a systematic analysis of the observed γ-peaks is presented, the goal is to better understand the location of the contaminations and to give indication for the full background modeling.

Additional information on the γ-lines can be found studying the spectrum in (anti-)coincidence with the LAr veto: this study is anyway preliminary since the detection efficiency of the LAr instrumentation for contaminations located in different position is not known precisely until now and results would generate only more confusion.

5.3.1 Count rate evaluation

The count rate at each γ-line is evaluated by fitting binned spectra in a region of 20 keV around the peak, with a model consisting in a gaussian function centered in the expected peak position energy on a flat background. The probability of the model and its parameters are given from Bayes theorem as:

$$P(\lambda|N) = \frac{P(N|\lambda)P_0(\lambda)}{\int P(N|\lambda)P_0(\lambda)d\lambda} \tag{5.5}$$

where λ are the model parameters and N the experimental data; $P(N|\lambda)$ is the likelihood function and $P_0(\lambda)$ the prior probability of the parameters. Taking into account the Poissonian nature of the processes that generates the events in the peak region, the likelihood can be written as:

$$P(N|\lambda) = \prod_{j=1}^{N^{bins}} \frac{(\nu_b^j + \nu_s^j)^{N_j} \cdot e^{-(\nu_b^j+\nu_s^j)}}{(N_j)!} \tag{5.6}$$

where N^{bins} is the number of bins, N_j is the observed number of counts and ν_b^j and ν_s^j are the expected background and signal counts in the bin j; the latter are defined as:

$$\nu_b^j = \int_{E_j}^{E_{j+1}} \frac{\lambda_b}{20\text{ keV}} \cdot dx = \frac{\lambda_b}{20\text{ keV}} \cdot (E_{j+1} - E_j) \tag{5.7}$$

$$\nu_s^j = \int_{E_j}^{E_{j+1}} \frac{\lambda_s}{\sigma\sqrt{2\pi}} \cdot exp\left(-\frac{(x-\mu)^2}{2\sigma^2}\right) dx \tag{5.8}$$

where λ_b and λ_s are the expected total background and signal counts in the fit window of 20 keV and the $\{E_j\}$ are the left edges of the bins; μ and σ are the mean and the standard deviation of the gaussian function.

For all the model parameters λ_b, λ_s, σ and μ are used flat priors. Strong constraints are adopted for the peak positions μ (1 keV of interval around the nominal peak value) and the gaussian width σ (extrapolated by the super-calibration at the relevant energy, see Sec. 4.3).

The parameter of interest λ_s, the expected number of counts, is extracted by marginalizing the global posterior probability distribution of Eq. (5.5). The mode and the 68% probability smallest interval are reported to quote the expected counts for each γ-line. When the mode of the distribution is close to zero and the smallest interval starts from zero, the 90% quantile of the distribution is reported as an upper limit. The signal rates reported in this thesis are calculated normalizing the results obtained for λ_s by the exposure of the considered dataset, the rate is indicated as r_s.

The analysis was carried out using the Bayesian Analysis Toolkit (BAT) [213].

The γ-line rates of all considered isotopes are listed in Tab. 5.2 for the BEGe, ^{enr}Ge coaxial and ^{nat}Ge coaxial datasets; as reference in the table are inserted also the Phase I results taken from Refs. [139, 214].

Table 5.2: Count rate of indicated γ-lines for BEGe, ^{enr}Ge coaxial and ^{nat}Ge coaxial detectors. The mode and smallest 68% interval or 90% quantile are reported. For comparison the Phase I results taken from [139, 214] are shown. The dataset exposures, energy and branching ratios [196] of the γ-lines is also reported.

			Phase II			**Phase I**	
			BEGe	**^{enr}Coax**	**^{nat}Coax**	**BEGe**	**^{enr}Coax**
			11.1 kg·yr	**9.3 kg·yr**	**3.8 kg·yr**	**2.4 kg·yr**	**19.2 kg·yr**
	energy keV	BR %	rate cts/(kg·yr)	rate cts/(kg·yr)	rate cts/(kg·yr)	rate cts/(kg·yr)	rate cts/(kg·yr)
^{42}**K**	1524.7	17.6	$86.1^{+2.4}_{-3.3}$	$111.8^{+4.0}_{-3.2}$	$125.0^{+5.6}_{-5.9}$	$46.6^{+4.6}_{-4.9}$	$60.6^{+2.0}_{-1.8}$
^{40}**K**	1460.8	10.6	$51.6^{+2.1}_{-2.5}$	$53.2^{+3.5}_{-1.7}$	$109.8^{+4.8}_{-6.1}$	$12.7^{+3.2}_{-3.1}$	$14.1^{+1.1}_{-1.2}$
^{214}**Pb**	351.9	35.6	$8.4^{+1.3}_{-1.9}$	$4.5^{+2.7}_{-0.3}$	$8.9^{+3.5}_{-4.9}$	$13.5^{+9.2}_{-7.9}$	$9.6^{+4.3}_{-5.3}$
^{214}**Bi**	609.3	45.5	$6.6^{+1.7}_{-1.3}$	$4.5^{+1.7}_{-1.4}$	$7.4^{+2.1}_{-2.3}$	$12.0^{+6.2}_{-5.3}$	$8.1^{+2.2}_{-2.5}$
	1120.3	14.9	$1.6^{+1.0}_{-1.0}$	$3.5^{+1.2}_{-1.3}$	$4.3^{+2.0}_{-1.8}$	$6.7^{+4.0}_{-4.2}$	< 2.9
	1764.5	15.3	$0.6^{+0.4}_{-0.3}$	$1.6^{+0.6}_{-0.3}$	$3.0^{+1.0}_{-0.9}$	< 2.5	3.2 ± 0.5
	2204.2	4.9	< 0.5	$0.3^{+0.3}_{-0.1}$	$1.1^{+0.9}_{-0.5}$	$1.0^{+0.8}_{-0.7}$	0.9 ± 0.3
^{234m}**Pa**	1001.0	0.8	$2.4^{+1.0}_{-1.3}$	$2.0^{+1.2}_{-1.4}$	< 3.2		
^{208}**Tl**	583.2	85.0	$4.9^{+1.1}_{-1.3}$	< 3.9	< 3.2	< 11.0	$4.0^{+2.2}_{-2.1}$
	2614.5	99.8	$0.6^{+0.3}_{-0.2}$	$1.1^{+0.4}_{-0.4}$	$0.9^{+0.6}_{-0.5}$	$0.6^{+0.7}_{-0.5}$	1.5 ± 0.4
^{228}**Ac**	911.2	26.2	< 3.7	< 3.9	< 2.8	< 8.0	$3.1^{+1.8}_{-2.0}$
	969	15.9	< 2.4	< 3.9	< 2.4	< 8.2	$6.7^{+1.8}_{-2.1}$
^{60}**Co**	1173.2	100	$1.8^{+0.9}_{-1.2}$	< 3.2	< 2.3	< 8.6	$2.9^{+1.5}_{-1.4}$
	1332.3	100	$1.4^{+0.6}_{-0.9}$	$1.9^{+1.2}_{-0.8}$	$4.4^{+1.4}_{-1.6}$	< 6.3	< 1.9
^{207}**Bi**	569.7	97.8	< 3.6	< 3.2	$1.8^{+1.7}_{-1.1}$		
	1063.6	74.6	< 1.2	$3.7^{+1.6}_{-1.2}$	< 3.1		
^{108m}**Ag**	433.9	90.1	< 2.7	< 4.9	< 4.7		
	614.3	90.5	< 2.4	$5.1^{+1.1}_{-2.5}$	< 2.2		
	722.9	90.8	< 2.1	< 3.4	< 2.3		
e^{+}**ann**	511.0		$4.1^{+1.2}_{-0.2}$	$6.8^{+1.4}_{-1.4}$	$6.5^{+3.1}_{-1.9}$	$16.5^{+6.4}_{-6.1}$	$10.4^{+2.4}_{-2.6}$
^{85}**Kr**	514.0	0.4	$6.1^{+2.2}_{-1.2}$	$5.8^{+1.1}_{-2.8}$	< 3.7		

As mentioned in Sec. 5.1, the spectra (Fig. 5.1(a)) at small energies are dominated by the ^{39}Ar β continuum. For this reason only γ-lines above 300 keV are considered in the analysis. In next sections is reported the study of several γ-lines: the prominent peaks from ^{42}K and ^{40}K, then the lines occurring in the natural decay chain of ^{238}U and ^{232}Th and finally other potential minor contaminations.

5.3.2 Likelihood-ratio test

The likelihood-ratio test is used to compare the model defined in Eq. 5.6 with a background-only model, in order to investigate on the presence of uncertain contaminations. The likelihood function in the latter case, indicated as $P_b(N|\lambda_b)$, can be defined as $P(N|\lambda)$ with the condition $\lambda_s = 0$ and depends only on one parameter.

The use of the likelihood-ratio as statistical test can be justified by the Neyman-Pearson lemma [215], which states that this test is the most powerful among all others.

The likelihood-ratio can be defined maximizing the likelihood functions of the two models, as follows:

$$\Lambda = \frac{P_b^{max}(N|\lambda_b)}{P^{max}(N|\lambda_b, \lambda_s, \sigma, \mu)} \tag{5.9}$$

where the maximum likelihood P_b^{max} and P^{max} are obtained by the Bayesian fit.

If one model represents a special case of the other (as in this case), the probability distribution of the test statistic $-2\log\Lambda$ is expected to be distributed as the χ^2 with degrees of freedom equal to the difference in the number of parameters between the two models. Here the background only model has one parameter, while the model including also a gaussian signal has four parameters (three for the gaussian, in addition to the constant). Two of them (σ and μ) are practically fixed and the test statistic can be approximate to the χ^2 distribution with $2 - 1 = 1$ degrees of freedom (indicates as $\chi^2(1)$).

In the present work an investigation of uncertain γ-lines has been performed and the likelihood-ratio is used as statistical test: a σ-equivalent significance is calculated from the $\chi^2(1)$ distribution. Depending on the case, different situations can be found:

- if $-2\log\Lambda \gg 1$ the model including a signal is strongly preferred with respect to the simple background model (in this case the significance is larger than 3σ and no further discussion is needed);

- $-2\log\Lambda = 9$ corresponds to 3σ significance, this value is used to quote the “evidence” on the observed peak;

- if $4 < -2\log\Lambda < 9$ it means that the significance is between 2σ and 3σ, in this case the signal is considered as “hint”;

- if $-2\log\Lambda \gtrsim 1$ no conclusion can be set on the observed peak.

Detailed analysis for each isotope is presented in the following.

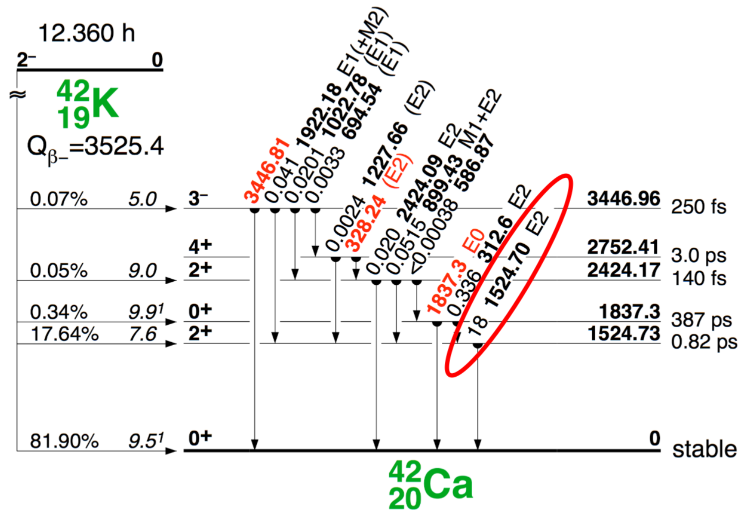

Figure 5.4: Decay scheme of the ^{42}K isotope in the levels of ^{42}Ca.

5.3.3 ^{42}K

The ^{42}K is produced homogeneously in LAr by the β decay of the long-lived ^{42}Ar via cosmogenic activation (Q-value of 599 keV and half-life of 32.9 yr). After the production, the ^{42}K ions are transported in the LAr by electric fields and convective flows. They decay with an half-life of 12.4 hours via β decay with a Q-value of 3525.4 keV to the stable ^{42}Ca. In 18% of the cases, ^{42}K decays to an excited level of ^{42}Ca, which de-excites under emission of a 1524.7 keV photon, explaining the observed line in the energy spectrum. Fig. 5.4 shows the ^{42}K decay scheme.

The presence of ^{42}K is a potential background problem for LAr based experiments, in particular for GERDA since the end point of the β spectrum is above the Q-value of the $0\nu\beta\beta$ decay.

At beginning of Phase I an unexpected ^{42}Ar level, established by the 1525 keV line, was observed. Its concentration depends crucially on the spatial distribution of the electric field and the high voltage of ~ 4 kV applied to Ge detectors leads to an accumulation in their vicinity. To mitigate this effect, a cylindrical 120 μm thick Cu shroud (referred as mini-shroud) was installed around each detector string, reducing significantly the background in the $Q_{\beta\beta}$ region [216]. The ^{42}Ar concentration then measured in Phase I was about a factor 2 higher than the limits available in literature at that time ($< 41\mu$Bq/kg at 90% C.L. [217]), but in agreement with a new study of the ^{42}Ar concentration that reports a specific activity of freshly produced liquid argon of 68^{+17}_{-32} μBq/kg [218].

In Phase II the detector strings are also surrounded by a mini-shroud, but the new setup configuration does not allow to adopt the Phase I solution. This is due to the fact that the Phase II LAr veto works by reading the LAr scintillation light (see Sec. 2.3). A new mini-shroud made of nylon film with very low intrinsic radioactivity and good transparency for the optical photons has been developed [153] and installed in the new Phase II detector array (the seven nylon shrouds surrounding the strings are visible in Fig. 2.10).

The count rate of the γ-line at 1524.7 keV in the new Phase II data is calculated as described in the previous section and the values for the three kinds of detectors are reported in the relative row of Tab. 5.2.

The rate in Phase II is about twice compared to Phase I for both BEGe detectors (with $r_s = 86.1^{+2.4}_{-3.3}$ cts/(kg·yr)) and ^{enr}Ge coaxial detectors (with $r_s = 111.8^{+4.0}_{-3.2}$ cts/(kg·yr)). This may be explained by the use of a different mini-shroud: the transparent non-metallic shrouds of Phase II allow electric field to be dispersed in LAr hence to move ^{42}K ions. In addition, the new setup features unshielded HV cables, while in Phase I coaxial cables with a PTFE tube were installed. This seems to increase the ^{42}K concentration in the proximity of the detectors.

Tab. 5.2 also shows that the rate of the ^{42}K γ-line for BEGe detectors is lower than the other detectors of Phase II (visible also in Phase I rates). This is explained by the smaller size of this kind of detectors with respect to the coaxial ones, that decreases the probability to full absorb the 1524.7 keV photon. The different detector geometry also yields differences in the rate of other γ-lines.

In addition to the presented count rates, for the ^{42}K γ-line is performed also a study of the distribution of the contamination per detector, per string and per position in the Phase II array.

Fig. 5.5 shows the distribution of the counts in the 1524.7 keV line normalized by the exposure in the different cases. The rate in single detectors (Fig. 5.5(a)) is highly variable and shows that in many cases the largest values are in top detectors and low values in central detectors. This trend appears evident in the plot of the rate as function of the position for both BEGe and coaxial detectors (Figs. 5.5(c) and 5.5(d)). This can be related to the statement presented also before: the unshielded HV cables are attracting ^{42}K ions, affecting top detectors more than the others. In addition bottom and top detectors see more LAr volume with respect to the central detectors. The distribution of the 1524.7 keV rate per string (Fig. 5.5(b)) shows higher values for the coaxial strings (2, 5 and 7) with respect to the BEGe strings (as observed also in the value of Tab. 5.2), which is related to the different detector geometry.

5.3.4 ^{40}K

The γ-line at 1460.8 keV derives from the ^{40}K isotope, that decays with an half-life of $1.3 \cdot 10^9$ yr via β decay and electron capture. The Q-values are with 1311.1 keV and 1504.9 keV, well below $Q_{\beta\beta}$. It is expected in small concentration in the material surrounding the detectors (as listed in Tab. 5.1), in particular in the cables and in the detector holders.

The count rate of ^{40}K is reported in the second row of Tab. 5.2. The Phase II values are: $51.6^{+2.1}_{-2.5}$, $53.2^{+3.5}_{-1.7}$ and $109.8^{+4.8}_{-6.1}$ cts/(kg·yr) respectively for BEGe, ^{enr}Ge coaxial and ^{nat}Ge coaxial detectors.

These rates are higher with respect to Phase I by a factor of ~ 4, probably related to the increased number of cables and detector holders and by the introduction of the LAr instrumentation. In addition the rate of the ^{nat}Ge

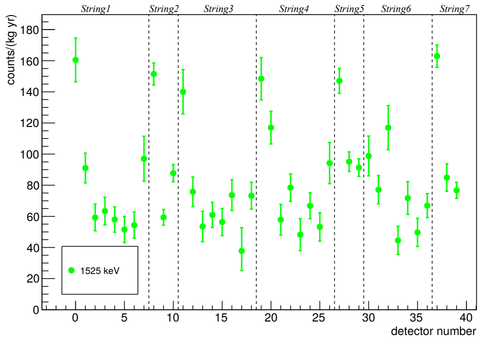

(a) Counts per detector.

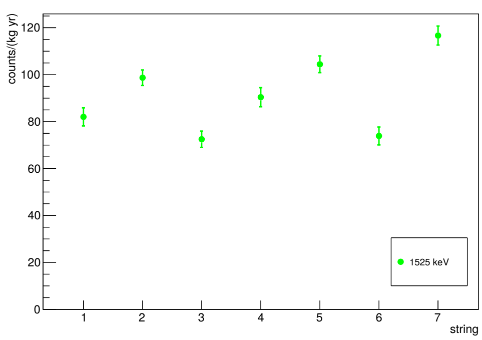

(b) Counts per string.

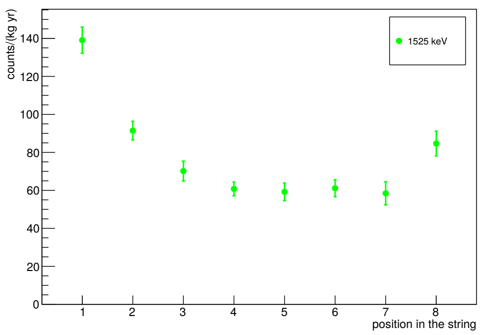

(c) Counts per position in BEGes.

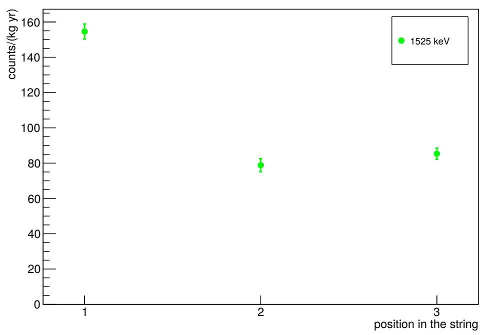

(d) Counts per position in coaxials.

Figure 5.5: Counts rate of the ^{42}K γ-line per detector (a), per string (b), per position in BEGe detectors (c) and in coaxial detectors (d).

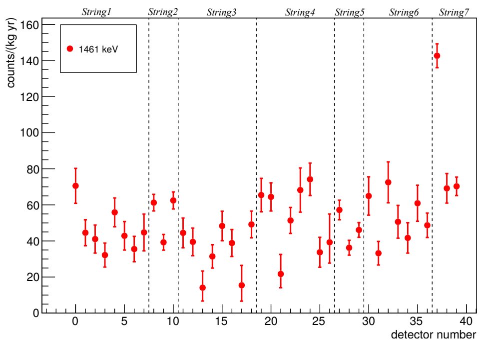

(a) Counts per detector.

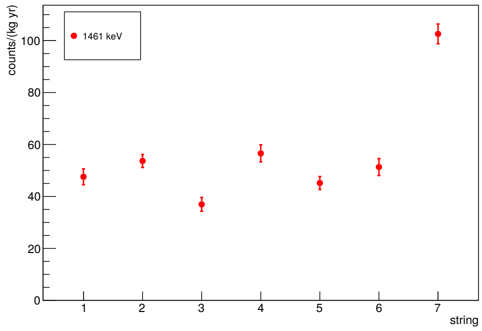

(b) Counts per string.

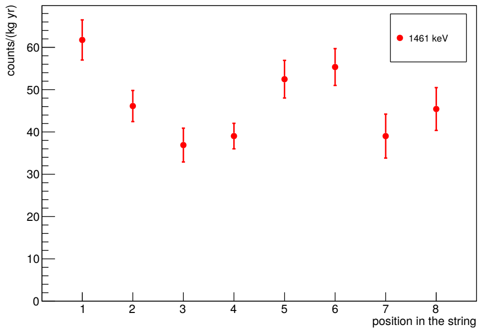

(c) Counts per position in BEGes.

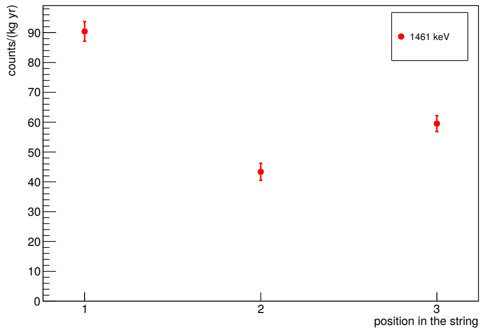

(d) Counts per position in coaxials.

Figure 5.6: Counts rate of the ^{40}K γ-line per detector (a), per string (b), per position in BEGe detectors (c) and in coaxial detectors (d).

coaxial detectors is factor of two greater than the other two datasets, also hinting to the presence of contaminations inside the detector array: the ^{nat}Ge coaxial detectors are in fact mounted in the central string and have a larger amount of material in the close proximity (e.g. the cables of all strings).

As for the ^{42}K γ-line, also for the 1460.8 keV line is performed a study of the distribution of the events in the different detectors, strings and positions. Fig. 5.6 shows the count rate in the various cases.

The single detector distribution (Fig. 5.6(a)) shows a variation of the rates between 10 and 80 cts/(kg·yr), with the exception of the ^{nat}Ge coaxial detector GTF112 (number 37) that reports a value significantly higher ($\sim$ 140 cts/(kg·yr)). This detector is mounted in the top position of the central string: an higher rate can be expected by the fact that all the 80 detector cables pass in its proximity. Anyway the observed big difference cannot arise only from the cables and other ^{40}K contributions may be present, as follow from the comparison between data and simulations performed in [208]. A clear trend is not observed in the 1460.8 keV rate of the other detectors.

Fig. 5.6(b) shows the count rate of the ^{40}K γ-line per string: the GTF112 detector contamination dominates the string 7 value, the other strings show a variation in the range 40–60 cts/(kg·yr) not related with known reasons.

The count rate per detector position (Figs. 5.6(c) and 5.6(d)) is reporting an higher value in the top detectors for both BEGe and coaxial, connected with

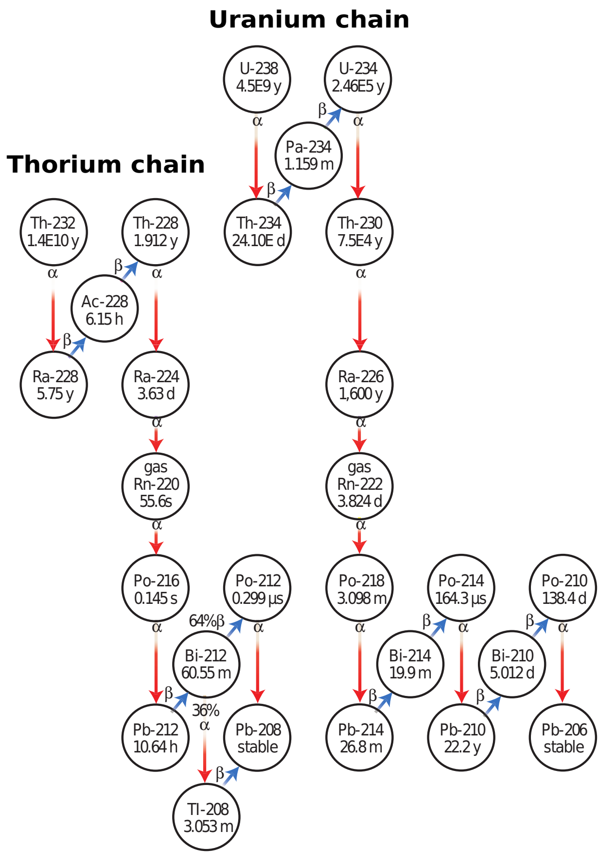

Figure 5.7: ^{238}U and ^{232}Th decay chains. Adapted from [219].

the mentioned cables contamination. In addition the rate as function of the BEGe position reports a strange values for the positions 5 e 6, not explained with the expected sources of the ^{40}K contamination. More investigation is needed on this side with the contribution of the simulations.

5.3.5 ^{238}U chain

The ^{238}U chain, shown in Fig. 5.7, can be broken at ^{226}Ra ($T_{1/2}$ = 1600 yr) and at ^{210}Pb ($T_{1/2} = 22.3$ yr).

The screening measurements of Phase II indicate that the ^{226}Ra contamination is present in the vicinity of the detector array (see Tab. 5.1). Additionally this is also expected on the detector p^{+} surface and in its close surrounding resulting from ^{226}Ra on the detector surfaces [139]. This contamination reflects in the presence of several γ-lines from ^{214}Bi and ^{214}Pb in the background spectra. Contribution also from the upper part of the ^{238}U chain is therefore possible, as this isotope is expected in any natural material and surrounding. Its contamination will be investigated through the 1001 keV γ-line from ^{234m}Pa, not observed in Phase I [139].

^{214}Bi and ^{214}Pb The ^{214}Pb isotope decays by β^{-} emission ($Q = 1019$ keV) to excited levels and ground state level of ^{214}Bi. Only low energy photons are emitted, the three most abundant γ-lines are at 242 keV (7.3%), 295.2 keV (18.4%), and 351.9 keV (35.6%). In this work only the 351.9 keV line is considered since the ^{39}Ar continuum does not allow to study the lower energy lines. The rate from this line is reported in Tab. 5.2 for the three datasets of Phase II in comparison with Phase I values.

The ^{214}Bi disintegrates by β^- decay to the ^{214}Po levels with $Q = 3270$ keV. The dominant γ-lines from ^{214}Bi are more in number and higher in energy than the ^{214}Pb. Fig. 5.8 shows the simplified ^{214}Bi decay scheme reporting only the main γ-lines. The range of useful energies is from about 600 keV to about 2.5 MeV. The most probable line is at 609.3 keV (45.5%), then there is a γ-line at 1120.3 keV (14.9%), one at 1764.5 keV (15.3%) and one at 2204.2 keV (4.9%). The others have individual branching ratios lower than 5% and are not studied here.

The rates of the mentioned four γ-lines from ^{214}Bi are listed in Tab. 5.2. The study of the ^{214}Bi is crucial in the GERDA background since part of the contribution in the $Q_{\beta\beta}$ region is expected from its γ emissions, together with the mentioned α events (see Sec. 5.2) and β spectrum from ^{42}K (see Sec. 5.3.3) and also other γs from ^{208}Tl presented in the next section.

The results obtained in Phase II for the ^{214}Pb and ^{214}Bi show that the ^{226}Ra contamination is lower with respect to Phase I: both rates of the 351.9 keV and the 609.3 keV lines are a factor of $\lesssim 2$ lower in Phase II for the BEGe and $^{\text{enr}}$Ge coaxial datasets. The values are anyway compatible within the errors in most cases.

The comparison of these two lines in Tab. 5.2 (351.9 keV from ^{214}Pb and 609.3 keV from ^{214}Bi) in Phase II datasets show higher rate for BEGe detectors, this may be related with the different ratio between the amount of materials in their vicinity and the detector volumes: any detector has a Si plate plus two cables, this affect more the BEGe than the coaxial detectors since their smaller size. On the contrary, high energy γ peaks from ^{214}Bi (1120 keV, 1765 keV and 2204 keV) have a lower rate in BEGe detectors with respect to coaxial ones. Also this is expected from the different geometry: the probability to full absorb photon decreases with the energy faster in small sized detectors (BEGe).

Fig. 5.9 shows the fit of the 609 keV line for the three datasets, performed with two gaussians plus a constant to take into account the concentration at ~ 614 keV visible in the $^{\text{enr}}$Ge coaxial datasets. This may be an indication of ^{108m}Ag contamination, discussed in Sec. 5.3.7

An interesting study can be performed with the ^{214}Bi through the ratio of the observed γ-lines in the same dataset. The values obtained in experimental data can be compared with the results from the simulation of ^{226}Ra sources in expected positions. This study may allow to better understand the location of the contaminations.

Tab. 5.3 reports the ratios between the 609 keV and the 1120 keV lines and between the 1120 keV and the 1764 keV lines for the three Phase II datasets: the ratios from the experimental data of Tab. 5.2 are reported in the first row, then are shown the results from the ^{226}Ra source simulations in the detector holders, in the cables, in the mini-shrouds and in the fibers of the LAr instrumentation (the measured contaminations are in Tab. 5.1). The simulations are from

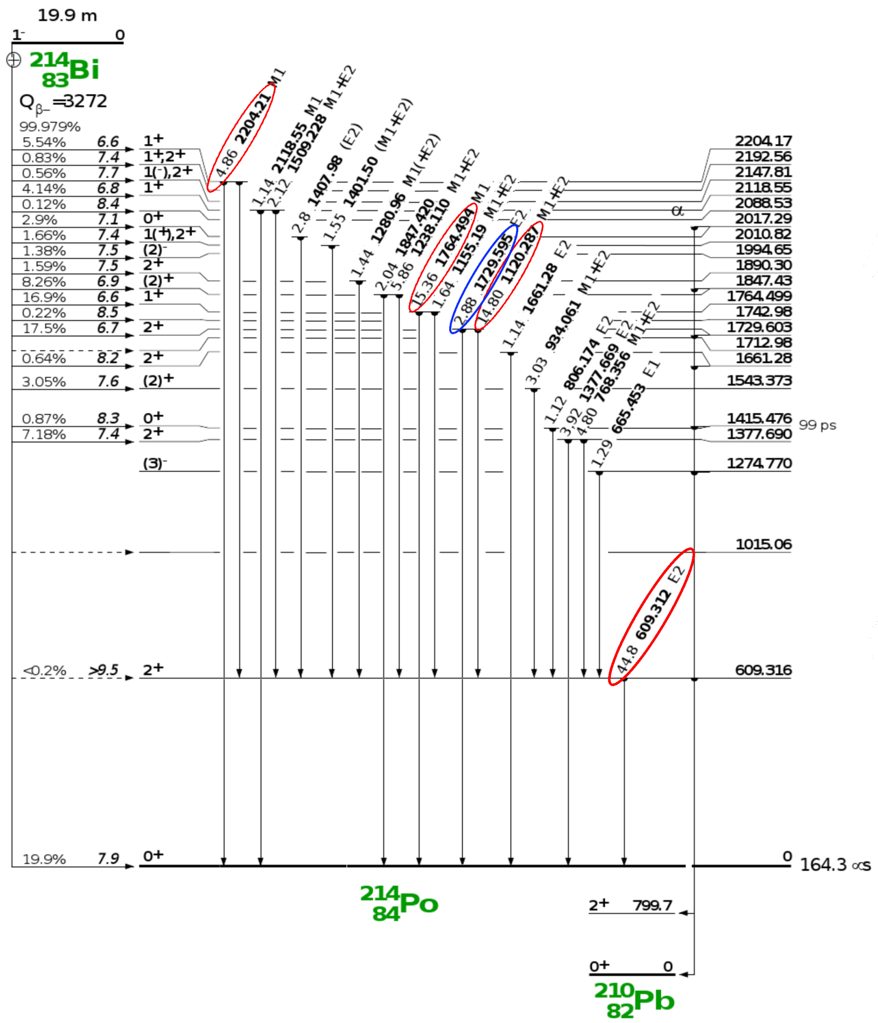

Figure 5.8: Simplified decay scheme of the ^{214}Bi isotope to the levels of ^{214}Po. Only γ-lines with branching ratio larger than 1% are reported. The lines considered for this analysis are indicated with a red sign; in blue is marked the 1729.6 keV line, discussed in the following.

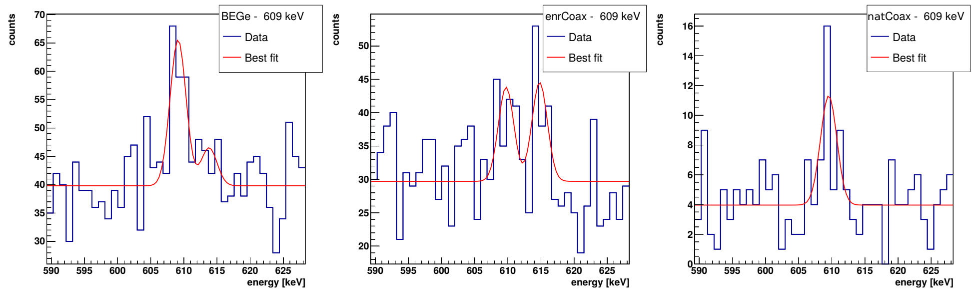

(a) BEGe (b) ^{enr}Ge coaxial (c) ^{nat}Ge coaxial

Figure 5.9: Bayesian fit [213] of the 609 keV line from ^{214}Bi for the three datasets. The ^{enr}Ge coaxial case shows a concentration at $\sim$ 614 keV, hint of ^{108m}Ag contamination; to study also this peak, the fit is performed with two gaussian plus a constant.

Ref. [208].

The table shows how the ratios from simulations are similar when the source is in the materials located in the close proximity of the detectors (holders, cables and mini-shrouds). On the contrary the simulation in fibers produce two visible effects in all the datasets, the ratio 609/1120 decreases and the ratio 1120/1764 increases:

- the first is due to the fact that the low energy line (609.3 keV) is more attenuated by the surrounding LAr, when increasing the distance source-detectors;
- the variation of the 1120/1764 ratio is connected with a summation effect: the 1120.3 keV photon is produced by the transition from the excited level at 1729.6 keV to the first excited level at 609.3 keV of ^{214}Po, then going to the ground state with the emission of a 609.3 keV photon (see the decay scheme in Fig. 5.8); there is a probability to detect the two γ emitted in cascade and hence to see a 1729.6 keV line (sum of 609.3 and 1120.3) in the spectrum: the probability decreases with distance, adding counts to single lines and therefore increasing the ratio 1120/1764.

In some case of Tab. 5.3 the ratio from data are not compatible with any of the different simulations, this may be related to the fact that the simulations are not taking into account some effect due to the ^{214}Bi contamination location and/or geometry (i.e. the 1120/1764 ratio is always less than one in the simulations, while the data shows higher values). However the comparison can be useful to have indications for future studies.

For BEGe detectors, since the rates are in many cases lower than coaxial, the values from data reported in Tab. 5.3 suffer of big errors and the comparison between data and simulations is not feasible. The ^{enr}Ge and ^{nat}Ge coaxial datasets indicates that the simulation in the fibers is more close to the measured ratio, leading anyway to a not definitive conclusion and opening to the possibility of the presence of other ^{226}Ra contaminations outside to the Ge array.

Table 5.3: Ratio of the ^{214}Bi γ-lines. The values from data are obtained from the γ-rates listed in Tab. 5.2, the others are from ^{214}Bi simulations (marked with *) in the different materials where the ^{226}Ra contamination is expected, from [208].

		609/1120	**1120/1764**
BEGe	data	4.2 ± 2.7	2.7 ± 2.1
	holders*	5.09	0.65
	cables*	4.77	0.73
	mini-shroud*	4.53	0.75
	fibers*	3.26	0.99
^{enr}**Coax**	data	1.2 ± 0.6	2.2 ± 0.9
	holders*	4.25	0.56
	cables*	3.99	0.65
	mini-shroud*	4.04	0.67
	fibers*	2.95	0.92
^{nat}**Coax**	data	1.6 ± 0.8	1.4 ± 0.8
	holders*	4.10	0.47
	cables*	3.75	0.56
	mini-shroud*	3.92	0.57
	fibers*	2.16	0.81

^{234m}Pa The ^{234m}Pa isotope decays by β^- emissions to ^{234}U levels (with $Q^- = 2.27$ MeV), to the ground state with 97.6% and excited states with γ-emissions. The most intense γ is at 1001.0 keV with branching ratio of 0.8%. To investigate on the presence of the early ^{238}U chain this line is studied and the rates are reported in Tab. 5.2. In Phase I this line was not observed. This contamination is a potential problem for GERDA since the Q-value of the β decay is above the $Q_{\beta\beta}$.

An excess is observed for the 1001 keV line (see Tab. 5.2) in BEGe and $^{\rm enr}$Ge coaxial detectors with a rate of $2.4^{+1.0}_{-1.3}$ and $2.0^{+1.2}_{-1.4}$ cts/(kg·yr) respectively. The likelihood-ratio test (see Sec. 5.3.2) gives values for the test statistic $-2\log\Lambda$ of 4.4 (3.0), corresponding to 2.1 (1.8) of σ equivalent for the BEGe ($^{\rm enr}$Ge coaxial) dataset. The resulting combined significance, assuming that the two datasets are independent, is 3σ. This results can be considered as hint for the presence of ^{234m}Pa contamination.

Despite the absence of the $2\nu\beta\beta$ spectrum, the $^{\rm nat}$Ge coaxial detectors do not show the line and an upper limit is set in this case (< 3.2 cts/(kg·yr)). Since the natural string is mounted in the central part of the array, this may be an indication of ^{238}U source external to the Ge array. Anyway the statistics does not allow to give solid statements, more exposure is needed to proceed.

5.3.6 ^{232}Th chain

The ^{232}Th chain can be broken at ^{228}Ra ($T_{1/2} = 5.75$ yr) and at ^{228}Th ($T_{1/2} = 1.91$ yr), as is shown in Fig. 5.7. The presence of ^{228}Th is expected from screening measurements of the relevant materials surrounding the Ge detectors (see Tab. 5.1). ^{232}Th contamination may be anyway expected and its search is performed through the study of the γ-lines from ^{228}Ac.

^{208}Tl From the ^{228}Th sub-decay chain, the main γ-lines of the ^{208}Tl are studied, the other γ-lines (e.g. from ^{212}Bi) are not taken into account since the branching ratios are lower.

The ^{208}Tl isotope decays by β^- emission ($Q = 5$ MeV) to various excited levels of ^{208}Pb and can induce background in the $Q_{\beta\beta}$ region via γ ray interaction. The characteristic γ-line at 2614.5 keV can be clearly identified in the spectra of Fig. 5.1(a) in the three datasets. In addition is searched also for the 583.2 keV line (85%). The rates obtained from the Bayesian fit for the Phase II and Phase I datasets are reported in Tab. 5.2.

The low energy peak (583.2 keV) in Phase II data is visible only in the BEGe detectors with a rate of $4.9^{+1.1}_{-1.3}$ cts/(kg·yr) (corresponding to a significance of 3.7 σ-equivalent). Upper limits are set for the two coaxial datasets. This fact can be related to the same argument presented for the low energy γ-lines of the ^{226}Ra chain: the BEGe detectors see a larger amount of materials per volume unit than the coaxials due the different size. In Phase I the situation was the opposite but the BEGe exposure was only 2.4 kg·yr.

As mentioned, the 2614.5 keV line is visible in all datasets with a rate around 1 cts/(kg·yr). Here the same situation of the ^{214}Bi high energy line is found: the different detector geometry allows to the coaxial detectors to absorb with an higher probability the high energy photons, reflecting in a lower rate for the BEGe dataset.

^{228}Ac The ^{228}Ac is the naturally occurring decay daughter of ^{232}Th and ^{228}Ra, it decays by β^- emission ($Q = 2124$ MeV) to the ^{228}Th levels. The most probable γ-lines are at 911.2 keV (26.2%) and 969.0 keV (15.9%) that are considered here, in Tab. 5.2 are reported the resulting rates in the relative rows. In all the cases only upper limit are set.

With the present statistics in Phase II there is no evidence of peaks above the background from ^{228}Ac, hence ^{232}Th and ^{228}Ra contaminations are not observed. Different situation compared Phase I where visible γ-lines were found for the ^{enr}Ge coaxial dataset.

5.3.7 Other isotopes

In addition to the peaks from the potassium isotopes and from the natural decay chains, other potential contaminations, that may be produced through different mechanisms, are studied in the Phase II spectra. As described in Sec. 5.3.2, the likelihood-ratio is used to test on the presence of the signal for uncertain peaks.

^{60}Co Potential background sources that can lead to a background at $Q_{\beta\beta}$ of ^{76}Ge are the long-lived radioisotopes ^{68}Ge and ^{60}Co, produced via cosmogenic activation in the Ge detectors. In GERDA several actions have been performed to minimize activation of germanium [143, 220], anyway a contribution is expected. In addition a background contribution from ^{60}Co is expected due to contamination of materials [139].

In Tab. 5.2 are reported the rate of γ-lines emitted by the ^{60}Co isotope. It decays by β^- to excited levels of ^{60}Co, leading to two photon lines at 1173.2 keV and 1332.5 keV both with 100% probability. The Q-value of the β decay is 2823.9 keV and the half life is 5.3 yr.

At 1332.5 keV an excess is observed in the three datasets of Phase II. The measured count rates is $1.4^{+0.6}_{-0.9}$ cts/(kg·yr) (corresponding to 1.8σ significance), $1.9^{+1.2}_{-0.8}$ cts/(kg·yr) (2.5σ) and $4.4^{+1.4}_{-1.6}$ cts/(kg·yr) (2.9σ) respectively for BEGe, $^{\rm enr}$Ge coaxial and $^{\rm nat}$Ge coaxial detectors. On the contrary, the 1173.2 keV line only in the BEGe detectors shows a positive signal above the background ($1.8^{+0.9}_{-1.2}$ cts/(kg·yr), corresponding to 3.3σ). This result is limited by the available statistics since the two γs occur in cascade and should have almost the same count rate. A better investigation on the ^{60}Co contamination can be performed with larger exposures.

^{207}Bi Another isotope studied in this work is the ^{207}Bi, a long-lived nuclide that disintegrates by electron capture (with an half-life of 32.9 yr and a Q-value of 2397.5 keV) to ^{207}Pb with the emission of γ rays, the main ones being at 569.7 keV (97.8%) and 1063.6 keV (74.6%). These two γ lines from this isotope were observed also in the final spectrum of the HDM experiment [80], here the ^{207}Bi was marked as anthropogenic radio nuclide.

In the Phase II spectra (as listed in Tab. 5.2) a signal for the 1063.6 keV line from ^{207}Bi is observed in the $^{\rm enr}$Ge coaxial detectors: the count rate is $3.7^{+1.6}_{-1.2}$ cts/(kg·yr) and the likelihood-ratio test reports a significance of 2.9σ-equivalent. This gives an hint on the presence of this contamination in these detector type. Anyway the low energy line at 569.7 keV is not visible. Also in this case, more statistics is needed to better investigate on the presence of this isotope.

^{108m}Ag The $^{\rm enr}$Ge coaxial dataset shows a concentration at $\sim$ 614 keV, visible in Fig. 5.9, hint of a ^{108m}Ag contamination. This isotope mostly disintegrates by electron capture to the 1771 keV excited state of ^{108}Pd, followed by the emission of three γ-rays in cascade at 433.9, 614.3 and 722.9 keV.In Phase I the ^{108m}Ag was observed in the coincidence spectrum between two Ge detectors. The same analysis can be performed also in Phase II.

In Tab. 5.2 are reported the count rates of the three γ-lines expected from ^{108m}Ag, a positive indication is observed only in the 614.3 keV line for the $^{\rm enr}$Ge coaxial dataset (peak clearly visible in Fig. 5.9(b)) with $r_s = 5.1^{+1.1}_{-2.5}$ cts/(kg·yr) corresponding to 3.0σ of significance. Not conclusive statements can be set with the current statistics on the presence of this contamination.

511 keV peak and ^{85}Kr The last two count rates reported in Tab. 5.2 are from the 511 keV and the 514 keV γ-lines.

The first is produced by the annihilation positron-electron following the creation of a positron via γ pair production or β^+ decay. The production mechanism of annihilation radiation introduces Doppler broadening [197] therefore has a peak width larger than the other γ-lines. The 511 keV γ-line ("e$^+$ ann" in Tab. 5.2) is visible in all datasets, as shown in Fig. 5.10 with rates of $4.1^{+1.2}_{-0.2}$,

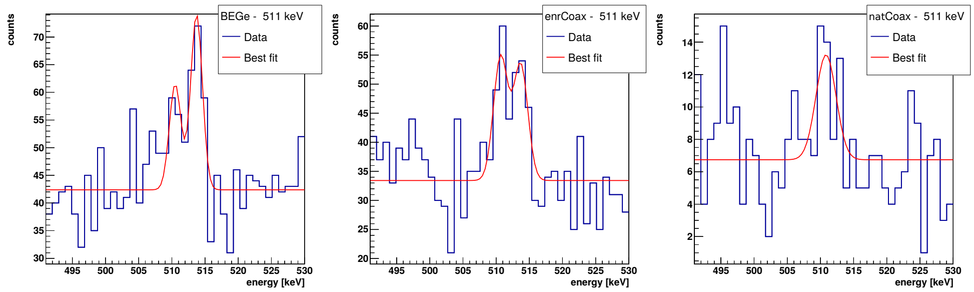

(a) BEGe (b) $^{\mathrm{enr}}$Ge coaxial (c) $^{\mathrm{nat}}$Ge coaxial

Figure 5.10: Bayesian fit [213] of the 511 keV peak and the 514 keV from ^{85}Kr for the three datasets.

$6.8^{+1.4}_{-1.4}$ and $6.5^{+3.1}_{-1.9}$ cts/(kg·yr) respectively for BEGe, $^{\mathrm{enr}}$Ge coaxial and $^{\mathrm{nat}}$Ge coaxial detectors.

In addition is visible a γ-line at 514 keV (not observed in Phase I), in particular in the BEGe (with $6.1^{+2.2}_{-1.2}$ cts/(kg·yr)) and $^{\mathrm{enr}}$Ge coaxial spectra (with $5.8^{+1.1}_{-2.8}$ cts/(kg·yr)). This line, together with the 511 keV, creates double peak structures visible in Fig. 5.10. For this reason the Bayesian fit in this case is performed with two gaussians centered at the two peak positions plus a constant for the background.

The presence of the 514 keV line is an indication of ^{85}Kr contamination, a long-lived anthropogenic isotope that disintegrates by β^- to the ^{85}Rb with $Q = 687$ keV and half-life of 10.7 yr. The low energy spectrum produced by the ^{85}Kr is one of the most serious problems in the xenon based dark matter experiments: several method are implemented to reduce its contamination. In GERDA the ^{85}Kr β spectrum is superimposed to the ^{39}Ar spectrum and it is not a big problem since low energies are not particular interesting in the search of the $0\nu\beta\beta$ decay; anyway, the simulation of new Phase II background model is introducing this contamination as further fit component [221].

5.4 Conclusions

The study of the GERDA Phase II background spectrum showed the presence of the expected structures also visible in the Phase I spectrum. The composition of the observed background and the localization of the various sources are information needed to build the background model and to understand which contributions are expected in the region around the $Q_{\beta\beta}$ value.

The spatial distribution of ^{42}K (from the ^{42}Ar isotope of LAr) is largely influenced by the electric field distribution near the detectors and by the sealing of the mini-shrouds. In Phase II it was shown that the count rate of the 1524.7 keV γ-line is increased with respect to Phase I; this is probably due to the plastic mini-shroud mounted around the strings and the use of unshielded HV cables. If the mini-shrouds are not perfectly sealed, this could be a critical point since the β spectrum of the ^{42}K can produce events in the $Q_{\beta\beta}$ region.

The presence of ^{40}K is also increased with respect to Phase I. This can be related to the larger amount of material in the close proximity of the detectors, in particular the signal and HV cables made in Cuflon® that shows a bigger concentration of ^{40}K.

The contaminations from the natural decay chain of ^{238}U and ^{232}Th, expected from the screening measurements, produce an α structure mostly coming from the ^{210}Po and various γ-lines from ^{214}Bi and ^{208}Tl decays. Both α and γ events from the natural decay chain can potentially induce background events in the region interesting for the study of the $0\nu\beta\beta$ decay. In addition, an indication of the early ^{238}U chain is given by the study of a γ-line from ^{234m}Pa. This contamination, if confirmed, is another potential background for GERDA. The count rate of the γ-lines from ^{214}Bi indicates that this contamination is decreased with respect to Phase I.

Other minor contamination have been also studied: ^{60}Co, ^{207}Bi, ^{108m}Ag and ^{85}Kr. The presence of the listed isotopes has to be confirmed when more statistics will be available. Anyway, the γ-lines from these isotopes are superimposed to the $2\nu\beta\beta$ spectrum, hence an increased exposure may not be enough to improve their significance. The only exception is the ^{85}Kr, visible in BEGe and ^{enr}Ge coaxial detectors. This isotope produces a low energy β spectrum, superimposed with the ^{39}Ar spectrum, far from the $Q_{\beta\beta}$ region.

The studied background spectrum is then further suppressed by the LAr veto and the pulse shape discrimination before performing the $0\nu\beta\beta$ analysis, giving a very low background as result with a BI an order of magnitude lower then Phase I (see Sec. 2.5). Anyway, the work presented in this chapter may become crucial for future GERDA implementations, in order to further reduce the background and increase the sensitivity on the $0\nu\beta\beta$ decay.

Chapter 6

Sensitivity studies with a time-dependent background model in GERDA Phase II

The last part of this thesis deals with the study of the GERDA sensitivity to the neutrinoless double beta decay of ^{76}Ge. The purpose is to assess the $0\nu\beta\beta$ decay sensitivity in different background scenarios following the observed Phase II data and background model.

The first Phase II data release with an exposure of 10.8 kg·yr of ^{enr}Ge, combined with the Phase I data (23.6 kg·yr), set a new limit for the $T^{0\nu}_{1/2}$ (see Sec. 2.5). The achieved BI in the $Q_{\beta\beta}$ region is of $0.7^{+1.1}_{-0.5} \cdot 10^{-3}$ cts/(keV·kg·yr) for BEGe detectors and $3.5^{+2.5}_{-1.5} \cdot 10^{-3}$ cts/(keV·kg·yr) for ^{enr}Ge coaxial detectors. This fulfills the challenging background goal of Phase II. Anyway a further reduction can be expected: the study of the background spectrum (Chap. 5) and the Phase II background model [211, 212] shows that a contribution in the $Q_{\beta\beta}$ region is due to α contaminations, in particular from the ^{210}Po isotope and hence is decreasing in time.

A new background model including a time-dependent component has been developed and applied to simulated Phase II datasets in order to predict the sensitivity in the next future of the GERDA experiment.

A short review on the statistical methods adopted in GERDA is presented in Sec. 6.1, then the new model with a time-dependent component is described in Sec. 6.2. Various simulation of Phase II datasets in different background scenarios, under the hypothesis of not-constant background in the $Q_{\beta\beta}$ region, are produced and analyzed with the new model. The procedure to create them is described in Sec. 6.3. Sec. 6.4 shows the results on the projection of the $0\nu\beta\beta$ decay sensitivity.

6.1 Statistical approaches for the GERDA sensitivity study

The statistical analysis for the search of the $0\nu\beta\beta$ decay in GERDA is performed using both a Frequentist and a Bayesian method based on an unbinned extended likelihood function.

The energy spectrum around $Q_{\beta\beta}$ of each dataset is fitted with a normalized function, sum of a flat distribution for the background and a gaussian distribution centered at $Q_{\beta\beta}$ for a possible $0\nu\beta\beta$ signal.

The parameter of interest for this analysis is the strength of a possible $0\nu\beta\beta$ decay signal, defined as:

$$\mathcal{S} = 1/T^{0\nu}_{1/2} \; . \tag{6.1}$$

The number of the expected $0\nu\beta\beta$ events in the dataset i (indicated as μ_i^S) as function of $\mathcal{S}$ is given by [65]:

$$\mu_i^S = \frac{\ln 2 \cdot N_A \cdot \mathcal{E}_i \cdot \epsilon_i \cdot \mathcal{S}}{m_A} \tag{6.2}$$

where N_A is the Avogadro constant, $m_A = 0.0756$ kg the molar mass of the enriched material, ϵ_i is the efficiency and $\mathcal{E}_i$ the exposure of the dataset i (the equation has been already introduced in Sec. 1.3 with a different parameterization). The efficiency ϵ_i is the product of the ^{76}Ge enrichment fraction ($\sim 87\%$), the active volume fraction of the detectors ($\sim 90\%$), the probability that $0\nu\beta\beta$ events deposit all energy in the active volume ($\sim$ 90–92%) and the efficiency of the analysis cuts (PSD and LAr veto).

The total number of expected background events μ_i^B for a specific dataset i, as a function of the background level BI_i, is:

$$\mu_i^B = \mathrm{BI}_i \cdot \mathcal{E}_i \cdot \Delta E \tag{6.3}$$

where $\Delta E = 240$ keV is the energy region used for the fit, from 1930 keV to 2190 keV excluded the intervals (2104 ± 5) keV and (2119 ± 5) keV from known lines.

The unbinned likelihood function for the dataset i is defined as:

$$\mathcal{L}_i(data_i|\mathcal{S}, \mathrm{BI}_i) = \prod_{j=0}^{N_i^{obs}} f(E_j|\mathcal{S}, \mathrm{BI}_i) \tag{6.4}$$

$$f(E_j|\mathcal{S}, \mathrm{BI}_i) \quad = \quad \frac{1}{\mu_i^B + \mu_i^S} \left[\frac{\mu_i^B}{\Delta E} + \frac{\mu_i^S}{\sigma_i\sqrt{2\pi}} \cdot exp\left(-\frac{(E_j - Q_{\beta\beta})^2}{2\sigma_i^2} \right) \right] \tag{6.5}$$

where j runs over the N_i^{obs} observed events of dataset i, E_j is the energy of the single event and σ_i is fixed to the resolution of the dataset i.

The total likelihood is constructed as product of the $\mathcal{L}_i$ from Eqs. (6.4) and (6.5), weighted with a Poissonian term:

$$\mathcal{L}(data|\mathcal{S}, \mathrm{BI}_i) = \prod_i \frac{\mu_i^{N_i^{obs}} \cdot e^{-\mu_i}}{(N_i^{obs})!} \cdot \mathcal{L}_i(data_i|\mathcal{S}, \mathrm{BI}_i) \tag{6.6}$$

where $\mu_i = \mu_i^B + \mu_i^S$ is total number of expected events in dataset i. The likelihood $\mathcal{L}$ is function of the event energies and has one background parameter

BI_i per dataset, while the signal strength $\mathcal{S}$ is common among the datasets (in Phase I [94] with 3 datasets the likelihood had 4 parameters).

The frequentist analysis uses the Neyman construction of the confidence interval and the two-side profile likelihood as test statistic [16, 222] with the restriction to the physical region $\mathcal{S} = 1/T^{0\nu}_{1/2} \geq 0$: the frequency distribution of the test statistic is generated by Monte Carlo simulations for different assumed $\mathcal{S}$ values. The limit is determined by the largest value of the signal strength $\mathcal{S}$ for which at most 10% of the simulated experiments had a value of the test statistic more unlikely than the one measured in the data (see Phase II results in Sec. 2.5).

In the Bayesian analysis [213, 223] the parameters are extracted by defining the posterior probability density function as:

$$P(\mathcal{S}, \mathrm{BI}_i|\mathrm{data}) = \frac{\mathcal{L}(\mathrm{data}|\mathcal{S}, \mathrm{BI}_i) \cdot P_0(\mathcal{S}) \cdot P_0(\mathrm{BI}_i)}{\int \mathcal{L}(\mathrm{data}|\mathcal{S}, \mathrm{BI}_i) P_0(\mathcal{S}) P_0(\mathrm{BI}_i) d(\mathcal{S}) d\mathrm{BI}_i} \tag{6.7}$$

where $\mathcal{L}$ is from Eq. (6.6), $P_0(\mathcal{S})$ and $P_0(\mathrm{BI}_i)$ are the parameter priors, that in all the cases are chosen flat (in particular the $\mathcal{S} = 1/T^{0\nu}_{1/2}$ prior is limited between 0 and 10^{-24} yr^{-1}). With flat priors the parameter estimation using the posterior probability is equivalent to a maximum likelihood estimation.

To have the probability distribution for each parameter the full posterior of Eq. (6.7) is then marginalized. In the $0\nu\beta\beta$ search, in case of no signal, an upper limit for the sensitivity is calculated as the value that contains the 90% of probability of the marginalized posterior probability for $\mathcal{S}$, indicated as 90% credible interval (C.I.).

In GERDA both the frequentist and Bayesian analysis are performed to quote the limit on the $0\nu\beta\beta$ decay sensitivity [94, 1, 2]. In the study developed in this thesis and presented in the following only the Bayesian approach is adopted; the outcome has in any case general validity.

6.1.1 Sensitivity projection in Phase II

Fig. 6.1 reports the evolution of the 90% C.I. limit on $T^{0\nu}_{1/2}$ as function of the $^{\mathrm{enr}}\mathrm{Ge}$ exposure: the first Phase II data release is used as base for the simulations (more details in Sec. 6.3) and a Bayesian analysis as described in the previous section is adopted.

In the figure the median sensitivity evaluated in 10000 realizations is reported, the regions contain the 68% and the 90% probabilities. Following Fig. 6.1, GERDA Phase II will reach a median sensitivity on the $0\nu\beta\beta$ decay of $15.3 \cdot 10^{25}$ yr after a $^{\mathrm{enr}}\mathrm{Ge}$ exposure of 100 kg·yr.

This result is the reference for the study presented in this chapter: the inclusion of a time-dependent background will be implemented and compared with the constant background case showed in Fig. 6.1, an increase on the median sensitivity would be expected.

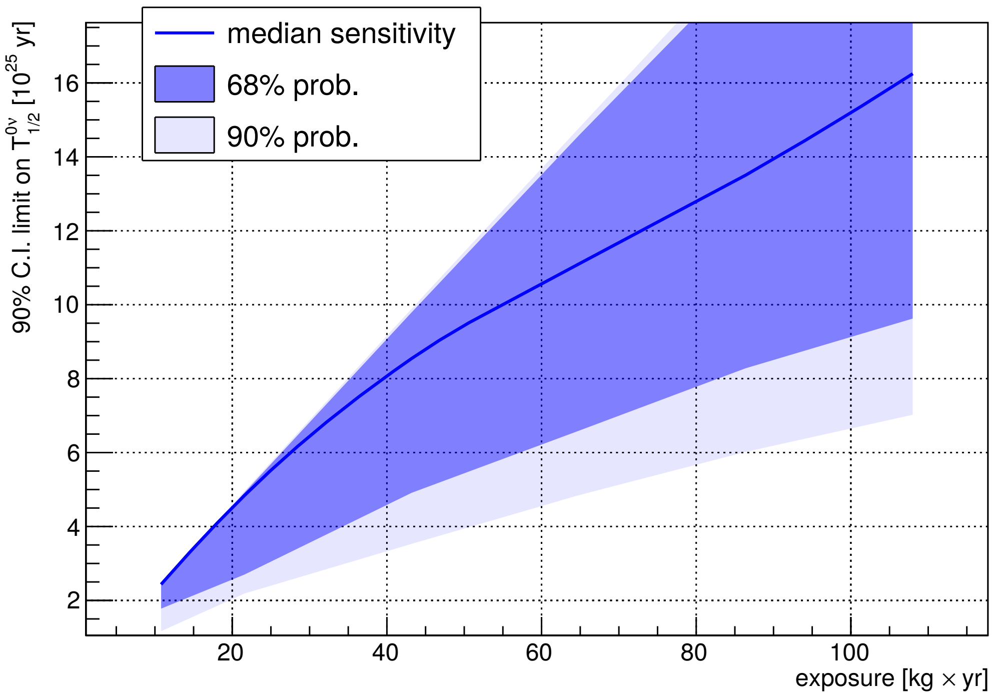

Figure 6.1: Evolution of the $0\nu\beta\beta$ sensitivity as function of the exposure in Phase II projections in simulations of a constant background. The blue line is the median sensitivity, the regions contain the 68% and the 90% of the realizations.

6.2 Background model with a time-dependent component

The study of the Phase II background spectrum (see Chap. 5) and the preliminary background model [211, 212] show that the most important contaminations that can produce events in the $Q_{\beta\beta}$ region are γs from the ^{214}Bi and ^{208}Tl, β from ^{42}K and degraded α from ^{210}Po and ^{226}Ra chain. A rough estimate from the available data gives the same fraction of contribution to the three contributions: 1/3 from β, 1/3 from γ and 1/3 from α events.

On the other hand, the study of the α background (see Sec. 5.2) showed that the majority of the events comes from a ^{210}Po contamination on the detector surfaces, with a minor contribution from the ^{226}Ra decay chain. The α count rate of Phase II as function of the time is compatible with an exponential distribution with a decay time of 138.4 days ($T_{1/2}$ of ^{210}Po) plus a minor constant component (see Fig. 5.3).

Following these arguments, it can be expected a further reduction of the total background level in future Phase II data, since the ^{210}Po contamination is going to decay away.

To take into account the time dependence of the background in the $0\nu\beta\beta$ search, the likelihood function of Eqs. (6.4)-(6.6) has to be redefined.

The background parameter for each dataset BI_i is split in two contributions: a constant component BI_i^c and a time-dependent component BI_i^t. The total number of events still follows Eq. 6.3, the number of constant and time-dependent background events for the dataset i, referred as μ_i^c and μ_i^t respectively, are defined as:

$$\mu_i^c = \mathrm{BI}_i^c \cdot \mathcal{E}_i \cdot \Delta E \tag{6.8}$$

$$\mu_i^t = \mathrm{BI}_i^t \cdot \mathcal{E}_i \cdot \Delta E \tag{6.9}$$

hence the total number of background events can be written as the sum of two contributions $\mu_i^B = \mu_i^c + \mu_i^t$; the definition of the total number of events is the same as before $\mu_i = \mu_i^B + \mu_i^S = \mu_i^c + \mu_i^t + \mu_i^S$.

The new likelihood must depend on the event time, not only on the energy, and, in addition to the flat distribution and the gaussian distribution centered at $Q_{\beta\beta}$, an exponential decaying component has to be added. The likelihood for the dataset i is:

$$\mathcal{L}_i(data_i|\mathcal{S}, \mathrm{BI}_i^c, \mathrm{BI}_i^t) = \prod_{j=1}^{N_i^{obs}} f(E_j, t_j|\mathcal{S}, \mathrm{BI}_i^c, \mathrm{BI}_i^t) \tag{6.10}$$

$$f(E_j, t_j|\mathcal{S}, \mathrm{BI}_i^c, \mathrm{BI}_i^t) = \frac{1}{\mu_i^c + \mu_i^t + \mu_i^S} \times \\ \times \left[\frac{\mu_i^c}{\Delta E \Delta t} + \frac{\mu_i^t}{\Delta E} \frac{e^{-t_j/\tau}}{\tau(1 - e^{-T_{max}/\tau})} + \frac{\mu_i^S}{\Delta t \cdot \sigma_i \sqrt{2\pi}} \cdot exp\left(- \frac{(E_j - Q_{\beta\beta})^2}{2\sigma_i^2} \right) \right] \tag{6.11}$$

where t_j is the time of the event (starting from December 20th, 2015), τ is fixed to the ^{210}Po life-time, Δt is the total time range and T_{max} is the final time. Since the initial time is fixed to $t = 0$ the time range coincides to the final time $\Delta t = T_{max}$ in case of a duty cycle of 100%. The other terms are the same of Eqs. (6.4) and (6.5). The total likelihood function is calculated following Eq. (6.6).

The number of parameters of the time-dependent model is increased with respect to the standard GERDA model: now there are two background parameters per dataset (BI_i^c and BI_i^t) in addition to $\mathcal{S} = 1/T_{1/2}^{0\nu}$.

The new likelihood function of Eqs. (6.10) and (6.11) is used to perform a Bayesian analysis of the Phase II datasets to study the $0\nu\beta\beta$ sensitivity. Flat priors for all parameters $\mathcal{S}$, BI_i^c and BI_i^t are adopted. The fits are performed with BAT [213].

The time-dependent background model is applied to various toy simulations of the GERDA background spectrum with different exposure and live time. To validate the procedure a first analysis is performed on simulated datasets projection of spectra before PSD and LAr veto cuts, then to projections of the final background spectra after all cuts.

6.3 Simulation of Phase II background

The simulated datasets contain a random number of events extracted from the expectation of $0\nu\beta\beta$ and background events. The energy and time of each event are generated following specific criteria.

All simulations are performed with the `TRandom3` ROOT class [224], a pseudo-random number generator based on the Mersenne Twister algorithm [225], with an automatic computation of the seed via a TUUID object [226].

The number of expected background events for each dataset μ_i^B is calculated according to the relative BI_i following Eq. (6.3), then the events in each simulation are generated following the Poisson distribution:

$$P(N_i^{bkg}) = \frac{(\mu_i^B)^{N_i^{bkg}} \cdot e^{-\mu_i^B}}{(N_i^{bkg})!} \tag{6.12}$$

the notation N_i^{bkg} is introduced to indicate the simulated background events for each dataset; this quantity enters in the likelihood function (Eqs. (6.10) and (6.11)) summed to the signal events in $N_i^{obs} = N_i^{bkg} + N_i^{0\nu}$.

The energy of the N_i^{bkg} events is simulated with an uniform distribution between 1930 keV and 2190 keV, excluding the intervals 2104 ± 5 keV and 2119 ± 5 keV, as indicated by the background model.

To generate the event occurrence time, the total number of background events N_i^{bkg} is split in two components: a constant N_i^c and a time-dependent one N_i^t, then the following procedure is adopted.

Simulation of time in background events After six months of data taking in Phase II, the background model predicts that the composition of the background in the energy interval ΔE around $Q_{\beta\beta}$, before applying of the PSD and LAr veto cuts, is equally distributed between α, β and γ contaminations. From the point of view of the simulation this means that 2/3 of the total background events are from β and γ, constant in time, and the rest is from the α contamination. Assuming the latter is entirely from ^{210}Po, it decays in time with $\mathrm{T}_{1/2} = 138$ days.

Hence to generate the background events time this recipe is followed:

- 2/3 of the total counts is generated with an uniform distribution in time, starting from the Phase II initial date (December 20th, 2015) and with an time interval equal to the live time (to simplify the duty cycle is always 100%);
- 1/3 of the total counts is generated with an exponential decaying distribution in time with $\mathrm{T}_{1/2} = 138$ days.

Fig. 6.2 shows an example of simulated background for a dataset with live time of 130.7 days, the expected uniform and exponential components are marked in green and in blue respectively.

Simulation of time in Phase II projections The described recipe for the simulation of the time of background events is valid only for datasets with a live time equal to the Phase II first release (130.7 days). The background model predicted a background composition with the same contribution from α, β and γ on the basis of these data. This means that in the following months a relative reduction of the α component with the time is expected, hence the relative α fraction has to be corrected accordingly.

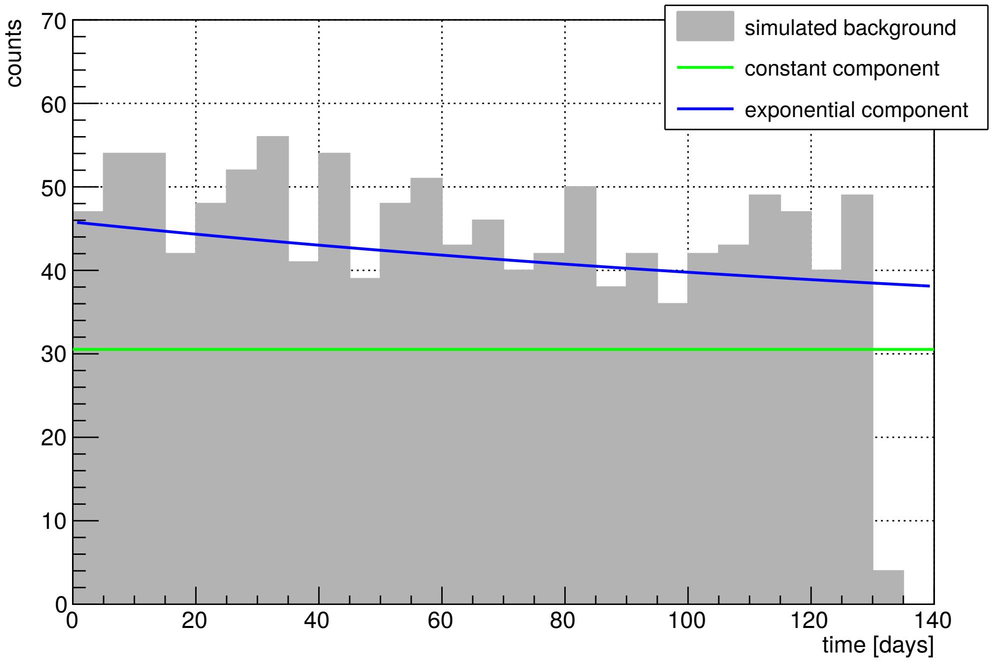

Figure 6.2: Time of the simulated background to reproduce the first Phase II data release with 130.7 days of live time and assuming a duty cycle of 100%. 2/3 of the events are generated with an uniform distribution, 1/3 with exponential distribution in time with $T_{1/2} = 138$ days.

The simulation of the projections of the Phase II datasets is performed by increasing the exposure and the live time by a factor ζ ($\mathcal{E}_i \rightarrow \zeta \cdot \mathcal{E}_i$). Consequently the expected total background events is also increased of ζ:

$$\mu_i^B = \mathrm{BI}_i \cdot \mathcal{E}_i \cdot \Delta E \rightarrow \zeta \cdot \mu_i^B \ . \tag{6.13}$$

then the total simulated counts N_i^{bkg} are generated following Eq. (6.12). The constant background component is obtained in all the cases as:

$$N_i^c = \frac{2}{3} \cdot N_i^{bkg} \ . \tag{6.14}$$

To take into account the decay of the α contamination, the time-dependent component N_i^t is not increased by a constant number (as for N_i^c), a factor depending on the considered time interval is used instead. This is defined as the ratio between the area of the exponential function in the total time interval and in the first six months:

$$\theta = \frac{\int_0^T e^{-t/\tau} dt}{\int_0^{t^*} e^{-t/\tau} dt} = \frac{1 - e^{-T/\tau}}{1 - e^{-t^*/\tau}} \tag{6.15}$$

where t^* is the live time of first six months and $T = \zeta \cdot t^*$ is the live time of the simulated projection; hence:

$$N_i^t = \frac{1}{3} \cdot \theta \cdot \frac{N_i^{bkg}}{\zeta} \tag{6.16}$$

the division by ζ is introduced to remove the increase by this factor contained in N_i^{bkg}. To generalize the formula of the number of background events to a not fixed α component, that until now is 1/3, Eqs. (6.14) and (6.16) can be written as:

$$N_i^c = (1 - \alpha_{frac}) \cdot N_i^{bkg} \tag{6.17}$$

$$N_i^t = \alpha_{frac} \cdot \theta \cdot \frac{N_i^{bkg}}{\zeta} \tag{6.18}$$

where α_{frac} is the initial fraction of α events from ^{210}Po. Also values different from 1/3 are used in the background simulations.

6.4 Phase II sensitivity projection

The Phase II first release performed after 6 months of data taking, with an exposure of 5.8 kg·yr (5.0 kg·yr) for BEGe (^{enr}Ge coaxial) detectors and a live time of 130.7 days, is used as unit of the simulations: 10^4 realizations of various configurations of these datasets are performed, until the total exposure of $\sim$ 100 kg·yr of ^{enr}Ge (as is planned in Phase II) is reached.

The $0\nu\beta\beta$ sensitivity and the background parameters are extracted from the marginalized posterior probability from the Bayesian fit of each realization. To study the $1/T_{1/2}^{0\nu}$ parameter, Monte Carlo repetitions of GERDA are performed without the $0\nu\beta\beta$ signal, then producing the distribution of the 90% C.I. limit. For the background parameters BI_i^c and BI_i^t the distribution of the mode in the marginalized posterior probability is also studied.

6.4.1 Projections of spectra prior PSD and LAr veto cuts

In order to increase the statistics of the Phase II background spectra, a first analysis using the time-dependent background model on simulated datasets is performed on spectra prior the PSD and LAr veto cuts. This analysis is useful to validate the procedure and gives some hint to properly process the final spectra.

All simulations are based on the BEGe and ^{enr}Ge coaxial datasets of the Phase II first release before the cuts: all information of these datasets are reported in Tab. 6.1. The values of the FWHM are calculated as described in Sec. 4.4.4, the efficiency includes the enrichment fraction, the active mass and reconstruction efficiencies.

Table 6.1: Information of the Phase II datasets before the PSD and LAr veto cuts used for the study of the $0\nu\beta\beta$ decay sensitivity.

dataset	live time [days]	exposure [kg·yr]	FWHM [keV]	efficiency $f_{av} \cdot f_{76} \cdot f_{fep}$	BI [cts/(keV·kg·yr)]
BEGe	130.7	5.8	3.0 ± 0.2	0.70	$18.7^{+4.3}_{-3.5} \cdot 10^{-3}$
coaxial	130.7	5.0	4.0 ± 0.2	0.68	$17.4^{+4.6}_{-3.6} \cdot 10^{-3}$

The distribution of the events observed in the two datasets in the interval for the BI evaluation is reported in Fig. 6.3 both in energy and in time.

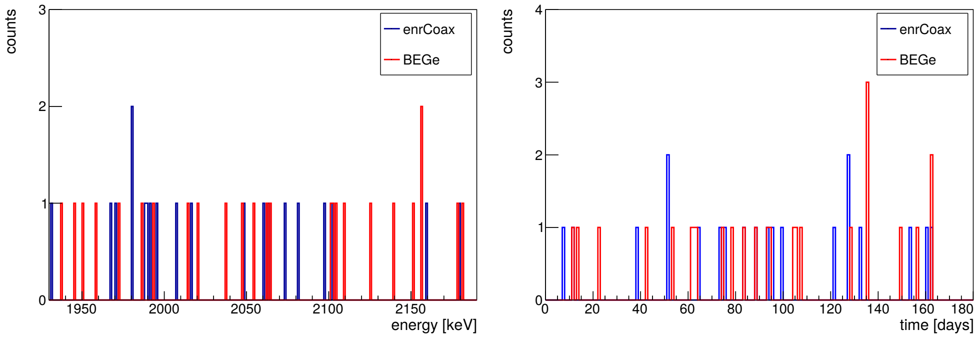

(a) Energy distribution. (b) Time distribution.

Figure 6.3: Distributions of the events in the energy region between 1930 keV and 2190 keV in the first 10.8 kg·yr of exposure in Phase II before the PSD and LAr veto cuts.

The analysis is performed in steps: first the simulations reproduce the datasets of Tab. 6.1, then both the exposure and the live time are increased by a factor of 2, 4 and 6.

Simulation of Phase II datasets Fig. 6.4 shows the distribution of the background parameters BI_i^c and BI_i^t of the time-dependent background model obtained in the Bayesian analysis of 10^4 simulated realizations of the Phase II datasets before the PSD and LAr veto cuts. The reported values in Fig. 6.4 are the mode of the marginalized posterior probability of each parameter.

The constant and time-dependent background parameters (Figs. 6.4(a) and 6.4(b)) show a similar distribution: a large amount of realizations have values near to zero for both BEGe and coaxial datasets, then a broad peak around 0.012 cts/(keV·kg·yr) is visible. This means that the model is not able to disentangle to two background components with such low exposure: it attributes randomly the entire value to one component assuming zero to the other.

The correlation graphs between BI^c and BI^t (Figs. 6.4(c) and 6.4(d)) confirm this statement: the parameters are strongly anti-correlated and the majority of events is concentrated in the two regions with values zero and $\sim$ 0.012 cts/(keV·kg·yr) for both datasets.

Simulation of Phase II datasets increasing exposure and live time Increasing exposure and live time brings to a different situation: the time-dependent model works better, separating the two background components. Fig. 6.5 shows the results of the analysis on the simulated datasets increasing exposure and live time by a factor of six with respect to Tab. 6.1.

The distribution of the constant background parameter BI^c, reported in Fig. 6.5(a), shows a clear peak around 0.013 (0.012) cts/(keV·kg·yr) for the BEGe ($^{\mathrm{enr}}$Ge coaxial) dataset. This is expected since this value corresponds to 2/3 of the total BI (listed in Tab. 6.1). Also in the time-dependent background component BI^t (Fig. 6.5(b)) a peak is visible at lower value. The correlation graphs of Figs. 6.5(c) and 6.5(d) report a clear anti-correlation between BI^c

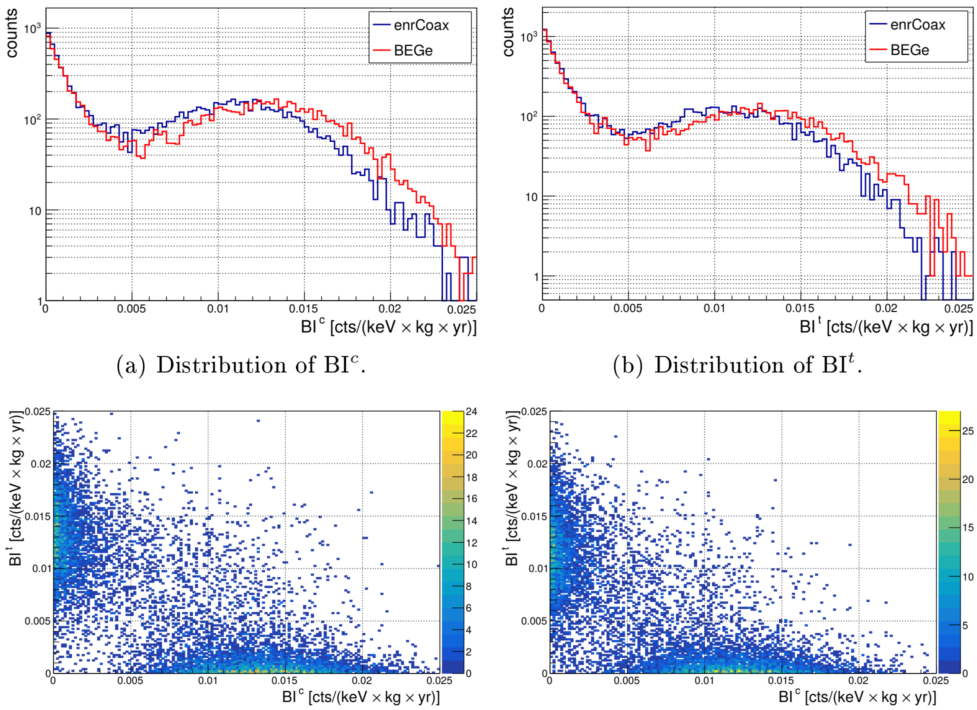

(a) Distribution of BI^c.

(b) Distribution of BI^t.

(c) Correlation in BEGe detectors.

(d) Correlation in $^{\mathrm{enr}}$Ge coaxials.

Figure 6.4: Results from the Bayesian analysis of the simulation of the Phase II background before the PSD and LAr veto cuts.

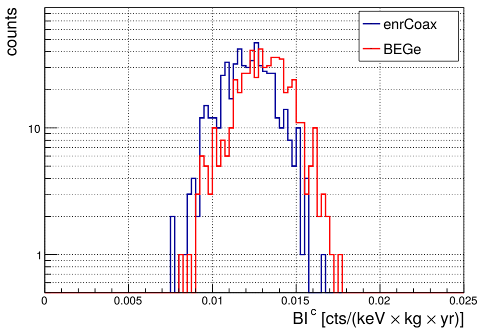

(a) Distribution of BI^c.

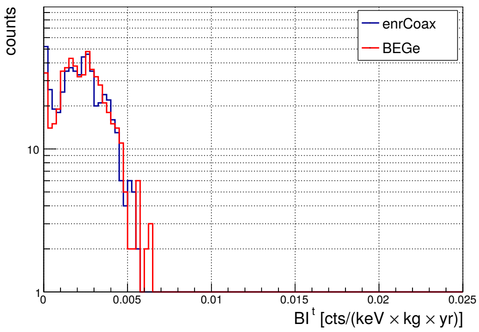

(b) Distribution of BI^t.

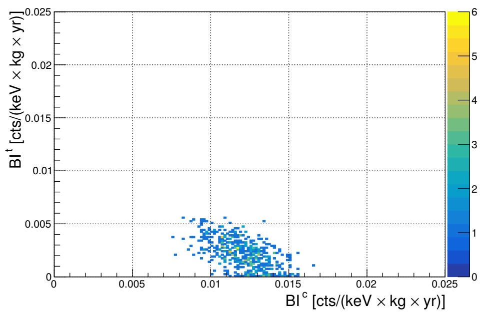

(c) Correlation in ^{enr}Ge coaxials.

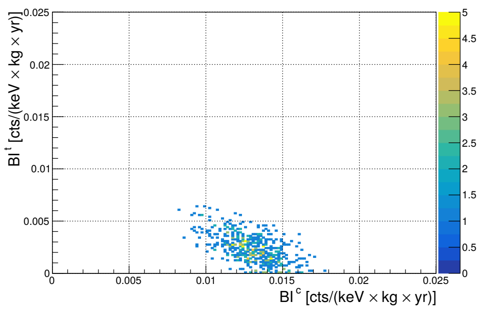

(d) Correlation in BEGe detectors.

Figure 6.5: Results from the Bayesian analysis of the simulation of the Phase II background before the PSD and LAr veto cuts with increased exposure and live-time by a factor of six with respect to Tab. 6.1.

Table 6.2: Relevant parameters of the Phase II datasets after the PSD and LAr veto cuts used for the study of the $0\nu\beta\beta$ decay sensitivity.

dataset	live time [days]	exposure [kg·yr]	FWHM [keV]	efficiency $f_{av} f_{76} f_{fep} f_{psd} f_{lar}$	BI [cts/(keV·kg·yr)]
BEGe	130.7	5.8	3.0 ± 0.2	0.60 ± 0.02	$0.7^{+1.1}_{-0.5} \cdot 10^{-3}$
coaxial	130.7	5.0	4.0 ± 0.2	0.53 ± 0.05	$3.5^{+2.5}_{-1.5} \cdot 10^{-3}$

and BI^t for both datasets, as expected.

The important point is that with this statistics the model is able to disentangle the two components and the results are in agreement with the expectation.

Sensitivity distribution Fig. 6.6 shows the distribution of the 90% C.I. limit on $T^{0\nu}_{1/2}$ in the different simulated datasets: (a) the decaying background with $\alpha_{frac} = 1/3$ and (b) the constant background case. In both figures the four distributions, corresponding to different exposure and live time values, are reported: in red the case of Tab. 6.1 and in blue, green and violet increasing by factor of 2, 4 and 6 respectively. The figure legend reports the median sensitivity for each distribution.

In all cases of Fig. 6.6 there is an end point corresponding to the maximum limit on the $T^{0\nu}_{1/2}$ parameter that can be set with that exposure, with a final peak less visible in the cases with higher exposure. This peak is due to the 90% limit on a Poisson variable, of 2.3 counts, given 0 observed events in the region of interest (ROI) around $Q_{\beta\beta}$. The end point is scaling with the exposure: in the red distributions it is at around $3 \cdot 10^{25}$ yr, then is increasing proportional to the factor ζ.

The comparison of the distributions in the simulation of time-dependent (Fig. 6.6(a)) and constant (Fig. 6.6(b)) background show that they have a very similar behaviour. The median sensitivity further distinguish while the exposure increases. This is an interesting result that encouraged to repeat the same analysis on the Phase II datasets after PSD and LAr veto cuts.

6.4.2 Projections of spectra after PSD and LAr veto cuts

The final analysis on the $0\nu\beta\beta$ decay sensitivity is performed on the spectra after all cuts. As reported in Sec. 2.5, the data from the first Phase II release set a new limit on the $T^{0\nu}_{1/2}$ of ^{76}Ge. The more interesting studies on the $0\nu\beta\beta$ sensitivity are performed through the projection of these datasets. Tab. 6.2 shows the relevant information. The efficiencies here include also the survival fraction of $0\nu\beta\beta$ events after the PSD and LAr veto cuts (values described in Sec. 2.5).

The background indices reported in Tab. 6.2 are calculated on the residual events observed in the two datasets in the window between 1930 keV and 2190 keV. Tab. 6.3 shows time and energy of these events: four events in the $^{\mathrm{enr}}$Ge coaxial and only one event in the BEGe dataset; the big suppression

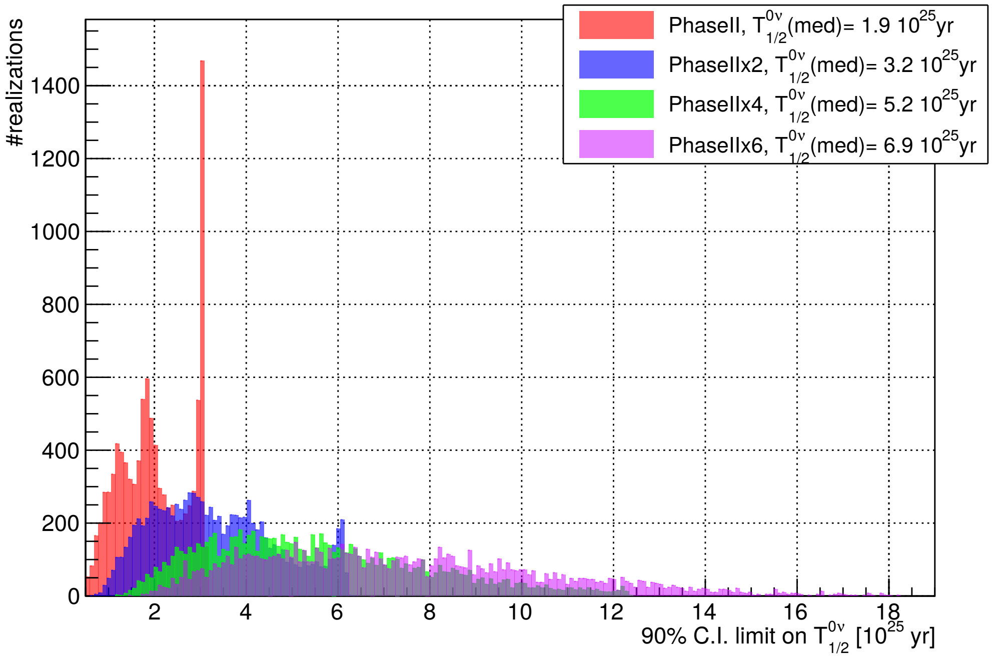

(a) Sensitivity distribution with not constant background.

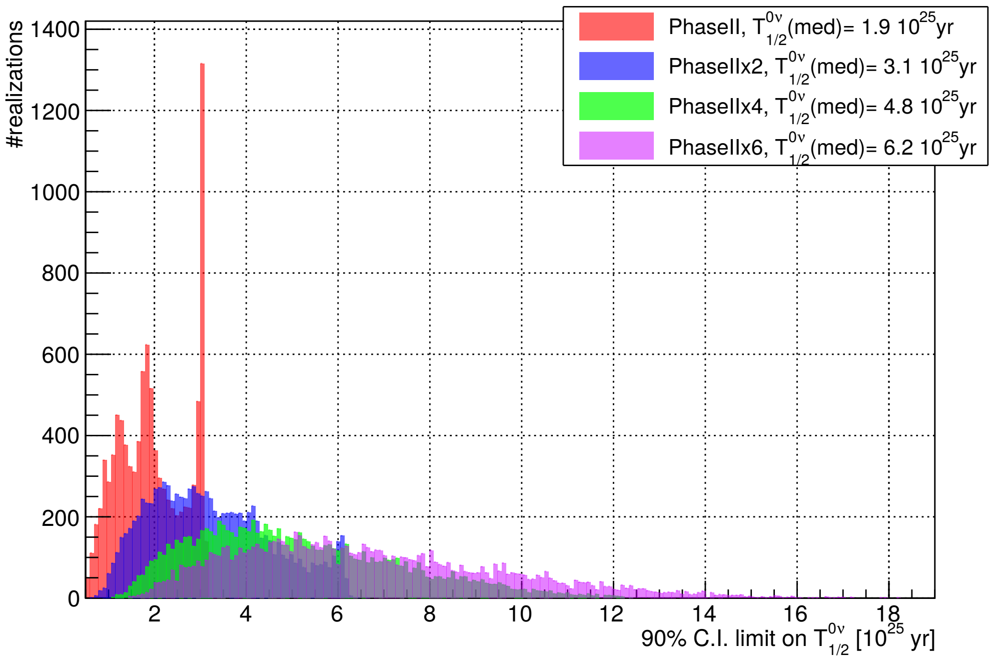

(b) Sensitivity distribution with constant background.

Figure 6.6: Sensitivity distribution in Phase II projections before the PSD and LAr veto cuts.

Table 6.3: Time and energy of the events in the region between 1930 keV and 2190 keV in the first 10.8 kg·yr of exposure in Phase II after the PSD and LAr veto cuts.

dataset	event time	energy [keV]
BEGe	13 Mar 2016 05:40:59	1958.6
coaxial	10 Feb 2016 13:04:08	1995.2
	13 Mar 2016 04:42:33	1968.0
	28 Mar 2016 16:00:18	2063.6
	22 May 2016 11:44:40	2060.5

in the latter case is due to the powerful PSD performances of this kind of detectors.

The results presented in the previous section showed that with an exposure of only 10.8 kg·yr of ^{enr}Ge the time-dependent model is not able to distinguish between the two background components. This is true also in this case, due to the even lower statistics. For this reason a simulation with an exposure of ~ 100 kg·yr is performed without intermediate steps.

Fig. 6.7 shows the distribution of the mode of the background parameters BI_i^c and BI_i^t obtained in 10^4 realizations of datasets of Tab. 6.2, increasing exposure and live time by a factor of ten.

The behaviour is similar to the one observed in Fig. 6.5: the constant background parameter BI^c shows a peak both in BEGe and ^{enr}Ge coaxial detectors at values corresponding to $2/3$ of the total BI. The time-dependent background BI^t is distributed close to zero, this is expected since the α component decreases with the time and its fraction goes to zero when the simulated live time is very large compared the ^{210}Po half life.

Sensitivity distribution The $0\nu\beta\beta$ sensitivity extracted in the analysis of simulations of the final Phase II spectra shows very interesting results.

Fig. 6.8 reports the evolution of the 90% C.I. limit on $T_{1/2}^{0\nu}$ as function of the ^{enr}Ge exposure. In blue is reported the median sensitivity obtained in simulations of a background constant in time, in this case the analysis is performed with the standard likelihood function (see Sec. 6.1) also adopted in the GERDA official analysis.

The red line and the red regions of Fig. 6.8 show the results of the $0\nu\beta\beta$ sensitivity with a time-dependent component in the background, in particular the initial fraction of α from ^{210}Po is set to $1/3$. The line corresponds to the median sensitivity, the two colored regions contain the 68% and the 90% of the realizations. The results are extracted from the Bayesian analysis with the time-dependent model.

The comparison of the two median sensitivity evolution confirms what was observed in the previous section (see Fig. 6.6): with a low exposure (< 30 kg·yr) the two background models show similar sensitivities, then the time-dependent background show higher values. Anyway after ~ 60 kg·yr the gap between the two lines remain almost the same. This can be explained by the fact that after this exposure the α component is gone and only the constant background is

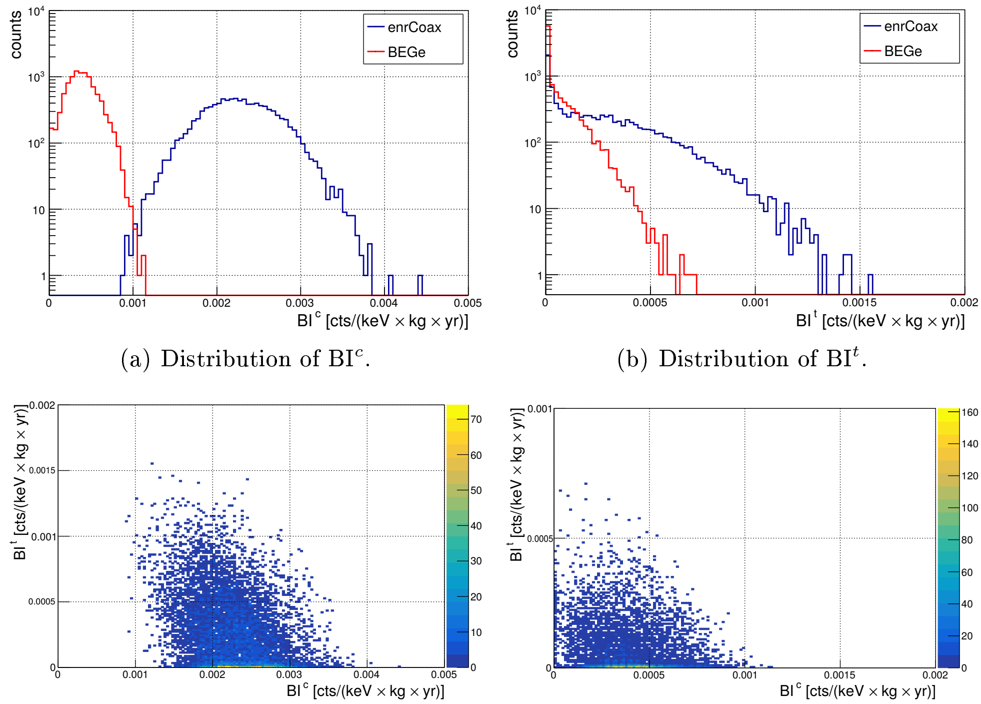

(a) Distribution of BI^c.

(b) Distribution of BI^t.

(c) Correlation in ^{enr}Ge coaxials.

(d) Correlation in BEGe detectors.

Figure 6.7: Results from the Bayesian analysis of the simulation of the Phase II background with increased exposure and live-time.

left, hence there is no way to further improve.

To quantify the gap observed in the median sensitivity in the two background scenarios, the distributions in the case (expected in the Phase II program) are compared in Fig. 6.9. In blue the case of constant background, in red the time-dependent background with $\alpha_{frac} = 1/3$.

The 90% C.I. limit on the $T^{0\nu}_{1/2}$ is in both cases distributed starting from $\sim 10^{25}$ yr and with an end point to $25 \cdot 10^{25}$ yr. A big peak is visible just before the end point, more pronounced than distribution of Fig. 6.6 due to the higher probability to have zero counts. The major difference between the constant and the time-dependent background is the quantity of realizations that yield a sensitivity value in this peak: the red distribution of Fig. 6.9 shows a larger concentration of events around $24 \cdot 10^{25}$ yr than the blue one, this leads to a different median sensitivity of $16.2 \cdot 10^{25}$ yr for the constant background case and $17.6 \cdot 10^{25}$ yr for the time-dependent background.

This is an important result since it shows that the projected median sensitivity for the final Phase II exposure of ~ 100 kg·yr improves of $\sim 8\%$ with respect to a constant background. This under the assumption of background fraction from ^{210}Po αs in the $Q_{\beta\beta}$ region is 1/3. The assumption used until now for the background composition is anyway not strongly supported. The background model of Phase II is in fact based to the spectra before the PSD and LAr veto and is not taking into account the efficiencies of these cuts. The α contamination is strongly suppressed by the PSD, in particular in the BEGe

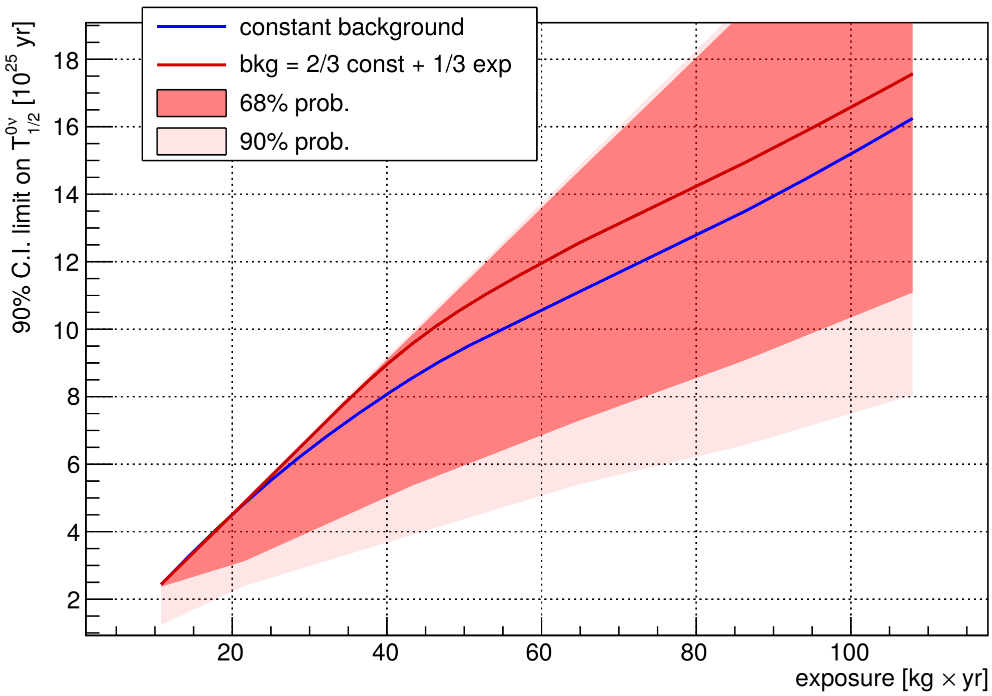

Figure 6.8: Evolution of the $0\nu\beta\beta$ sensitivity as function of the exposure in Phase II projections after PSD and LAr veto cuts in simulations of a constant background (blue) and a time-dependent background with $1/3$ of α component from ^{210}Po. The lines are the median sensitivity, the regions contain the 68% and the 90% of the realizations of the time-dependent case.

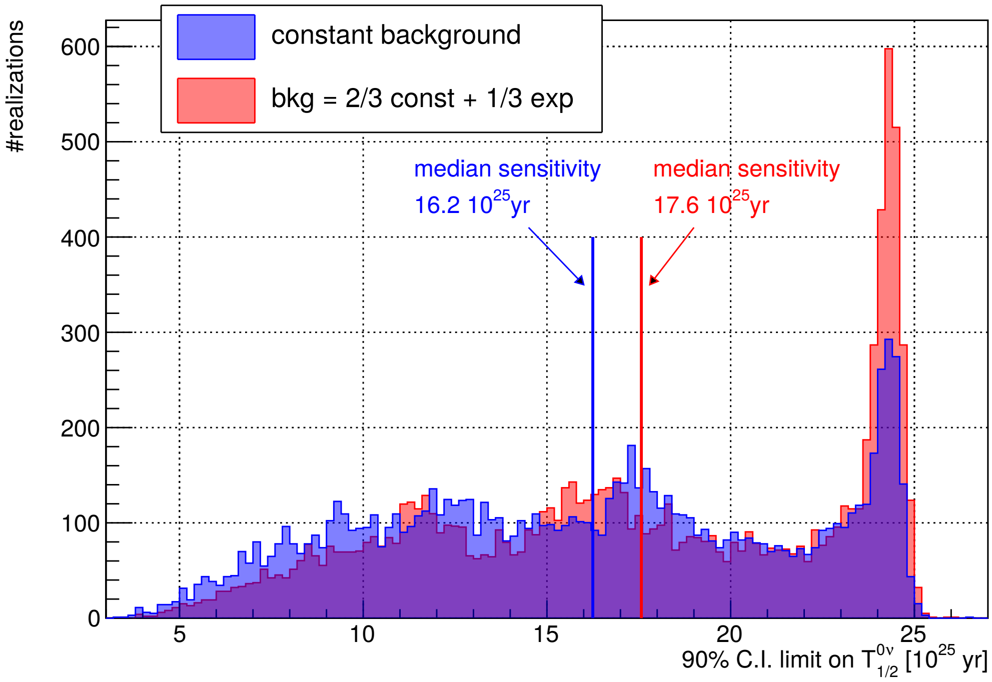

Figure 6.9: Comparison of the $0\nu\beta\beta$ sensitivity distribution with ~ 100 kg·yr in Phase II projections after PSD and LAr veto cuts in simulations of a constant background (blue) and a time-dependent background with 1/3 of α component from ^{210}Po.

detectors where the α structures are no more visible in the final spectrum (see Fig. 2.11). This means that the fraction of 1/3 for α events from ^{210}Po can be considered as an upper limit: also datasets with a different α contamination, following the recipe described in Sec. 6.3, are simulated.

Fig. 6.10 shows the $0\nu\beta\beta$ sensitivity distribution in three different background scenarios, changing the fraction of the time-dependent component in the background simulations of the Phase II projection with ~ 100 kg·yr of exposure. In red, violet and green are reported the cases with α_{frac} of 1/3, 1/4 and 1/5, respectively.

The distributions are very similar but are yielding different values for the median sensitivity (reported in the legend of Fig. 6.10) that is scaling with the fraction of the time-dependent events, as can be expected. In the case with a lower fraction ($\alpha_{frac} = 1/5$) the median sensitivity is $17.0 \cdot 10^{25}$ yr, then is still $\sim 5\%$ higher than the constant background case.

6.5 Conclusions

The preliminary Phase II background model predicts a composition of the events in the $Q_{\beta\beta}$ region equally distributed between α, β and γ contaminations. The study of the α structures observed in the background shows that a strong contribution is coming from the ^{210}Po isotope that decays with an half life of 138.4 days.

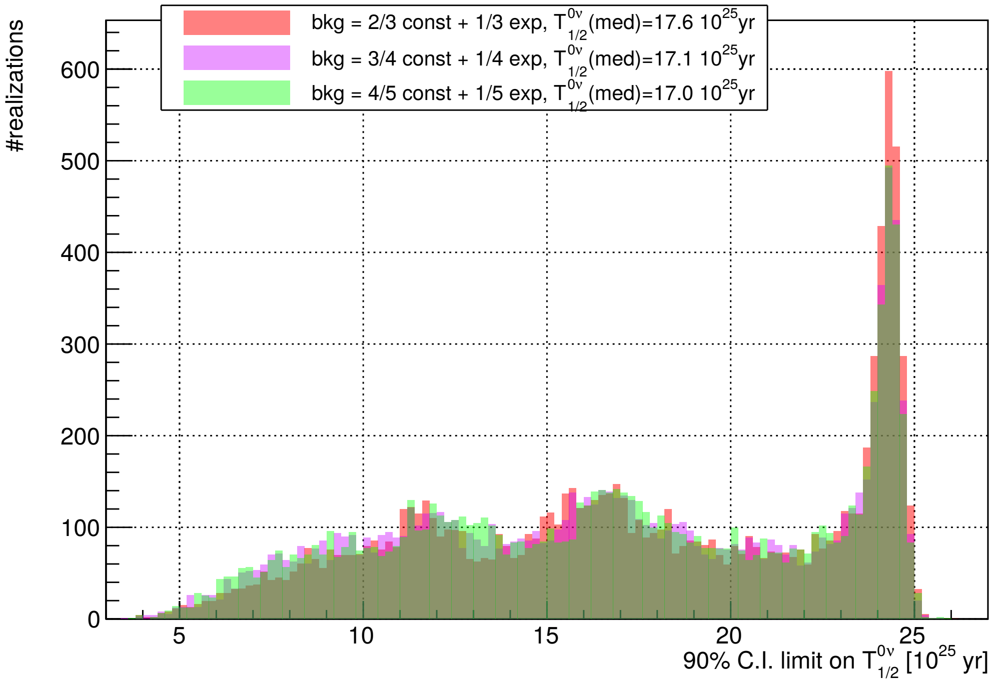

Figure 6.10: $0\nu\beta\beta$ sensitivity distributions in Phase II projections after PSD and LAr veto cuts in simulations of time-dependent background with a different fraction of the α component from ^{210}Po. The background composition and the median sensitivity are reported in the legend.

Simulations of projections of the Phase II datasets with a time-dependent component are generated following these arguments. Then they are analyzed with a Bayesian method in order to extract the prevision on the $T^{0\nu}_{1/2}$ limit that can be expected in the Phase II data taking.

The median sensitivity in different background scenarios with a fraction of α events from the ^{210}Po is improved by 5–8%, due to the fact that the time-dependent background has been considered in the analysis models.

Moreover this work successfully developed and tested a new statistical model, including a time-dependent background component. This model can be in principle applied to various situation.

Chapter 7

Conclusions and Outlook

Since December 2015 the GERDA experiment is taking data with the upgraded apparatus (Phase II) searching for the neutrinoless double beta ($0\nu\beta\beta$) decay of ^{76}Ge. This thesis work was carried out both on the hardware upgrade to Phase II and on the analysis of the new physics data.

The main challenge of $0\nu\beta\beta$ experiments is minimize the background. To achieve it, while preserving the intrinsically excellent Ge detector performances, severe boundary conditions for both the design and the implementation of the front-end electronics are fixed.

Following different approaches, two front-end circuits have been designed and tested. The circuit finally selected is an upgraded version of that adopted in Phase I. To accomplish both requirements, first it was attempted to separate the front-end device from the main amplifying stage locating the first at the detector site and the latter 40 to 80 cm away.

The integration tests performed in the GERDA environment, showed some problem in the reliability of the proposed front-end device: hence a backup solution, with an encapsulated JFET moved back at the amplifying stage (40 to 80 cm from Ge detectors), has been developed and installed during the Phase II commissioning. Because of the increased detector to front-end distance, the new front-end performs slightly worse than the original solution both in energy resolution ($\sim 10\%$) and pulse shape discrimination (PSD) power, nevertheless allowing to achieve high quality physics results. It is both robust and reliable and minimizes the radioactivity budget. For these reasons, it was finally adopted for Phase II.

Another important tool to fully exploit the performances of the GERDA detectors is the digital signal processing. I worked in the development of an optimized shaping filter that produces the best estimate of the energy resolution: the Zero Area Cusp-like (ZAC) filter. This filter, once tuned on the detector properties and their noise figure, was applied to the new Phase II data. An improvement in the energy resolution with respect to the standard semi-gaussian filter, adopted in Phase I, has been obtained: the energy resolution at $Q_{\beta\beta}$ integrated over six months is 3.00 ± 0.08 keV (4.03 ± 0.12 keV) for BEGe ($^{\text{enr}}$Ge coaxial) detectors.

A detailed noise investigation in the GERDA setup has been also performed: both energy resolution and PSD power of the BEGe detectors correlate with the position in the strings and this is in turn strongly correlated to the measured noise figure. The study identified a possible source of the observed extra-noise that degrades the detector performance: the stray capacitance of the signal cables and/or the detector themselves. A clear picture is still not available. Future GERDA developments will definitely need to individuate and mitigate this noise source in order to improve the PSD in the BEGe detectors, while increasing the detector string length.

The first Phase II data release showed that GERDA is the first background-free experiment in the field, this thanks to the selection of very radio-pure materials and to the use of efficient techniques to actively discriminate the possible $0\nu\beta\beta$ signal from the background: the LAr veto and the PSD. The achieved background in the $Q_{\beta\beta}$ region is of $0.7^{+1.1}_{-0.5} \cdot 10^{-3}$ cts/(keV·kg·yr) for BEGe detectors and $3.5^{+2.5}_{-1.5} \cdot 10^{-3}$ cts/(keV·kg·yr) for $^{\mathrm{enr}}$Ge coaxial detectors. This allowed to set a new limit on the ^{76}Ge $0\nu\beta\beta$ decay half-life of $5.3 \cdot 10^{25}$ yr (90% C.L.) with the new data.

A study of the observed background before the LAr and PSD cuts is however needed to fully determine the residual contaminations and their location, and to understand how to further reduce the background in future developments. An analysis of the background spectrum observed in recent Phase II data has been performed in the thesis: the sources were characterized through the study of the observed α structures and γ-lines. In spite the actual GERDA background is very low hence the individual contaminations are quite difficult to be identified.

The potential background in the region of the $0\nu\beta\beta$ signal may come in equal fraction from α, β and γ events. The α spectrum is mostly coming from the ^{210}Po, hence it decays away with an half-life of 138.4 days. β events can be induced by the ^{214}Bi and ^{208}Tl isotopes, occurring in the natural decay chain of ^{238}U and ^{232}Th, and by the ^{42}K contamination, produced in LAr by the the long-lived ^{42}Ar isotope. The γ events are from ^{214}Bi and ^{208}Tl isotopes: their contribution is lower with respect to Phase I.

A statistical analysis to assess the GERDA Phase II $0\nu\beta\beta$ decay sensitivity in different background scenarios is performed as last part of the thesis. A new statistical model, including a time-dependent background component, has been developed and adopted to simulated Phase II realizations. The results showed that, including a fraction of α events from ^{210}Po, the prediction for the median sensitivity at the Phase II final exposure of ~ 100 kg·yr is $17.6 \cdot 10^{25}$ yr, namely 5–8% larger than expected for a constant background.

On the basis of the GERDA Phase II results, a new world wide $0\nu\beta\beta$ collaboration named LEGEND, including GERDA and MAJORANA, was recently formed. The first goal is the deployment of 150–200 kg of $^{\mathrm{enr}}$Ge detectors in the further upgraded GERDA cryostat, aiming to a sensitivity on the ^{76}Ge $0\nu\beta\beta$ decay of $\sim 10^{27}$ yr in three years of data taking and with a background reduction of factor 5 with respect to Phase II. The final goal of the new collaboration is the realization of a ^{76}Ge ton-scale $0\nu\beta\beta$ experiment in order to reach a sensitivity of $\sim 10^{28}$ yr, corresponding to an upper limit on the effective Majorana neutrino mass of 10–20 meV.

Appendix A

Detector configuration and energy resolution in Phase II

A.1 Detector configuration

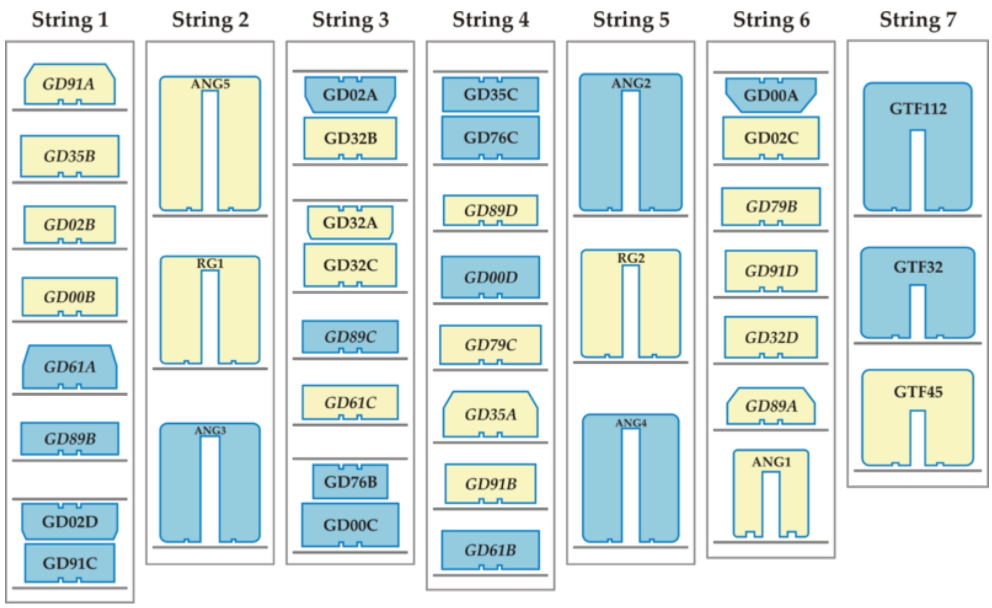

Figure A.1: Schematic view of the GERDA Phase II array: the name of the 40 detectors is indicated. The BEGe detectors are arranged in 4 strings (in string 6 there is also a coaxial), the coaxial in the other 3 strings. In blue are marked the passivated detectors. From [227].

A.2 Resolution in the Phase II super-calibration

Table A.1: FWHM at the 2614.5 keV line for the 40 Phase II detectors in the super-calibration, obtained including all the 31 runs performed during the first six months of the data taking. The progressive number and the detector names are also indicated.

string	number.**det**	FWHM [keV]
STRING 1	0.**GD91A**	2.72 ± 0.01
	1.**GD35B**	2.90 ± 0.01
	2.**GD02B**	3.22 ± 0.01
	3.**GD00B**	3.32 ± 0.01
	4.**GD61A**	3.65 ± 0.01
	5.**GD89B**	4.04 ± 0.01
	6.**GD02D**	4.65 ± 0.02
	7.**GD91C**	3.98 ± 0.01
STRING 2	8.**ANG5**	3.65 ± 0.01
	9.**RG1**	3.88 ± 0.01
	10.**ANG3**	3.56 ± 0.01
STRING 3	11.**GD02A**	2.69 ± 0.01
	12.**GD32B**	3.24 ± 0.01
	13.**GD32A**	3.44 ± 0.01
	14.**GD32C**	3.02 ± 0.01
	15.**GD89C**	3.44 ± 0.01
	16.**GD61C**	3.50 ± 0.01
	17.**GD76B**	3.48 ± 0.01
	18.**GD00C**	2.88 ± 0.01
STRING 4	19.**GD35C**	2.65 ± 0.01
	20.**GD76C**	2.80 ± 0.01
	21.**GD89D**	2.93 ± 0.01
	22.**GD00D**	3.02 ± 0.01
	23.**GD79C**	3.92 ± 0.01
	24.**GD35A**	3.51 ± 0.01
	25.**GD91B**	5.58 ± 0.01
	26.**GD61B**	3.29 ± 0.01
STRING 5	27.**ANG2**	4.34 ± 0.01
	28.**RG2**	4.09 ± 0.01
	29.**ANG4**	3.37 ± 0.01
STRING 6	30.**GD00A**	3.27 ± 0.01
	31.**GD02C**	3.02 ± 0.01
	32.**GD79B**	3.24 ± 0.01
	33.**GD91D**	3.11 ± 0.01
	34.**GD32D**	3.22 ± 0.01
	35.**GD89A**	3.41 ± 0.01
	36.**ANG1**	3.64 ± 0.01
STRING 7	37**GTF112**	3.51 ± 0.01
	38.**GTF32**	3.66 ± 0.01
	39.**GTF45**	4.20 ± 0.01

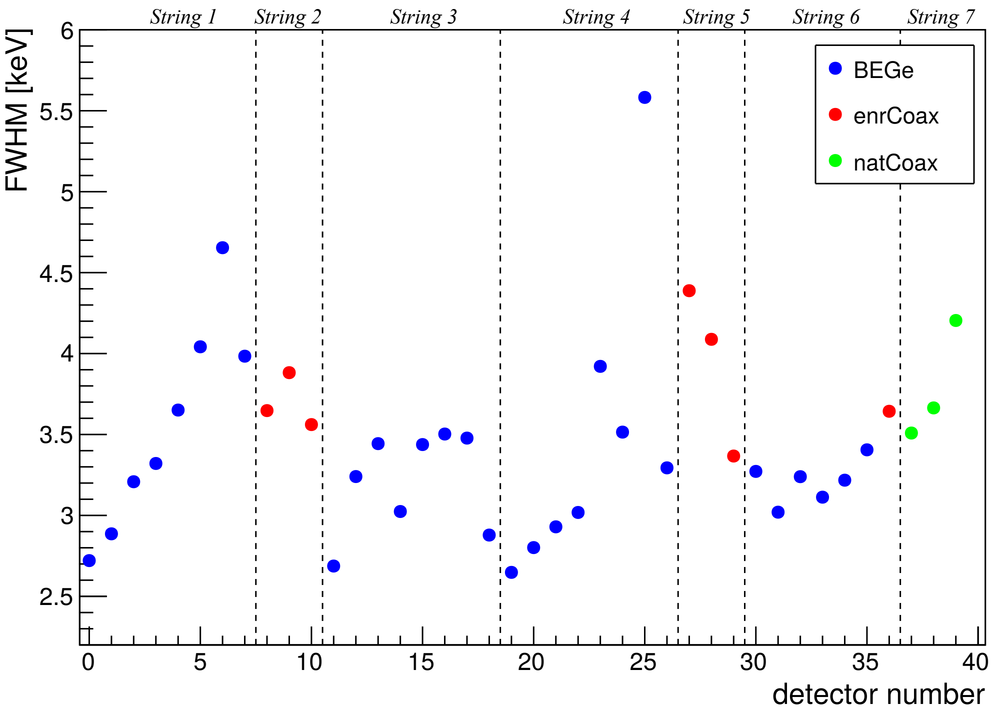

Figure A.2: FWHM at the 2614.5 keV line in the Phase II super-calibration as function of the detector number.

Appendix B

Determination of the Phase II cross-talk matrix

The cross-talk is an undesired effect produced by the transmission of the signal from one channel to the others, e.g. when there is a real waveform in one detector a little signal, usually with opposite polarity, is observed also in the others. In GERDA the cross-talk is evaluated through the GELATIO [136] module that extracts the energy with a pseudo-gaussian shaping (described in Sec. 4.2). A special calibration, where all the detector traces are acquired at each trigger, and the reconstruction also of the waveforms with opposite polarity are needed.

The method adopted to calculate to cross-talk in Phase II consists in selecting good high energy events on channel i (Energy[i] $>$ 2 MeV) and then evaluate the cross-talk between channel i and j as:

$$\text{CrossTalk}[i][j] = \frac{\text{EnergyRevPol}[j] - \text{offset}[j]}{\text{Energy}[i]} \tag{B.1}$$

where EnergyRevPol[j] is the reverse polarity energy in channel j and offset[j] is an offset value needed because of the reconstruction algorithm and evaluated through the average of EnergyRevPol[i] in baseline events.

The distribution of CrossTalk[i][j] for each combination of i and j (in total $40 \times 40 = 1600$ cases) is then fitted with a gaussian function and the mean is extracted. The resulting matrix with all the cross-talk values in % is reported in Fig. B.1: in the row there is the triggering detector (channel i in Eq. B.1), in the column the channel with a cross-talk event (j in Eq. B.1). The higher values are with detectors in the same string, the average cross-talk is -0.15% and -0.41% in BEGe and coaxial strings respectively. In gray are indicated the cross-talk values $\leqslant -0.4\%$ between detectors in different strings. Another method to evaluate the cross-talk using the average pulses has been developed and compared with the one presented here, all the values of Tab. B.1 are well in agreement [228].

	STRING 1								STRING 2			STRING 3							
	0	1	2	3	4	5	6	7	8	9	10	11	12	13	14	15	16	17	18
91A 0		-0,17	-0,10	-0,06	-0,10	-0,09	-0,10	-0,09	-0,07	-0,05	-0,10	-0,01	-0,01	-0,01	-0,01	0,00	-0,02	-0,02	-0,02
35B 1	-0,15		-0,14	-0,09	-0,08	-0,07	-0,09	-0,07	-0,05	-0,05	-0,09	-0,01	-0,03	-0,01	-0,01	-0,02	-0,02	-0,02	-0,01
02B 2	-0,10	-0,20		-0,18	-0,11	-0,07	-0,09	-0,09	-0,06	-0,07	-0,11	-0,01	-0,02	-0,01	-0,01	-0,01	-0,01	-0,02	-0,01
00B 3	-0,09	-0,11	-0,19		-0,15	-0,09	-0,10	-0,09	-0,06	-0,08	-0,12	-0,01	-0,02	-0,01	-0,01	-0,02	-0,01	-0,02	-0,01
61A 4	-0,02	-0,03	-0,05	-0,07		-0,22	-0,09	-0,05	-0,03	-0,04	-0,05	-0,02	-0,01	-0,02	-0,02	-0,03	-0,03	-0,04	-0,03
89B 5	-0,01	-0,03	-0,04	-0,04	-0,27		-0,27	-0,08	-0,03	-0,04	-0,04	-0,01	-0,01	-0,01	0,00	-0,03	-0,02	-0,02	-0,02
02D 6	-0,02	-0,04	-0,04	-0,03	-0,08	-0,31		-0,39	-0,04	-0,04	-0,06	-0,01	-0,02	-0,01	-0,01	-0,02	-0,03	-0,03	-0,02
91C 7	-0,07	-0,04	-0,05	-0,05	-0,11	-0,10	-0,52		-0,08	-0,05	-0,08	-0,01	-0,02	-0,01	-0,01	-0,01	-0,01	-0,03	-0,02
ANG5 8	-0,05	-0,05	-0,07	-0,07	-0,04	-0,04	-0,06	-0,04		-0,44	-0,56	-0,02	-0,03	-0,03	-0,05	-0,02	-0,02	-0,03	-0,05
RG1 9	-0,06	-0,07	-0,09	-0,08	-0,06	-0,06	-0,08	-0,05	-0,32		-0,72	-0,01	-0,02	-0,02	-0,02	-0,03	-0,03	-0,03	-0,05
ANG3 10	-0,09	-0,08	-0,07	-0,06	-0,05	-0,05	-0,07	-0,05	-0,17	-0,37		-0,01	-0,02	-0,01	-0,01	-0,02	-0,02	-0,02	-0,03
02A 11	-0,01	-0,02	-0,03	-0,02	-0,02	-0,01	-0,03	-0,02	-0,11	-0,14	-0,26		-0,15	-0,05	-0,04	-0,03	-0,04	-0,04	-0,05
32B 12	-0,01	-0,02	-0,03	-0,04	-0,02	-0,02	-0,04	-0,02	-0,06	-0,09	-0,32	-0,11		-0,10	-0,05	-0,02	-0,03	-0,04	-0,03
32A 13	-0,02	-0,03	-0,04	-0,05	-0,03	-0,01	-0,05	-0,03	-0,06	-0,07	-0,26	-0,04	-0,09		-0,13	-0,03	-0,03	-0,03	-0,03
32C 14	-0,03	-0,04	-0,05	-0,07	-0,03	-0,04	-0,06	-0,04	-0,07	-0,07	-0,22	-0,03	-0,04	-0,08		-0,05	-0,03	-0,03	-0,03
89C 15	-0,01	-0,02	-0,02	-0,01	-0,02	-0,02	-0,04	-0,03	-0,01	-0,02	-0,02	-0,02	-0,03	-0,02	-0,07		-0,20	-0,08	-0,08
61C 16	0,00	-0,01	-0,02	-0,02	-0,02	-0,02	-0,04	-0,02	-0,03	-0,02	-0,03	-0,02	-0,03	-0,02	-0,03	-0,24		-0,24	-0,14
76B 17	-0,23	-0,19	-0,02	-0,02	0,00	-0,02	-0,06	-0,10	-0,08	-0,05	-0,08	-0,03	-0,05	-0,02	-0,02	-0,05	-0,30		-0,32
00C 18	0,00	-0,02	-0,02	-0,02	-0,01	-0,01	-0,03	-0,02	-0,17	-0,07	-0,06	-0,06	-0,03	-0,03	-0,04	-0,04	-0,10	-0,39	
35C 19	0,00	-0,01	-0,02	-0,02	-0,01	-0,01	-0,05	-0,01	-0,09	-0,08	-0,09	-0,02	-0,03	-0,02	-0,01	-0,01	-0,01	-0,02	-0,02
76C 20	-0,01	-0,02	-0,02	-0,02	-0,01	-0,02	-0,04	-0,03	-0,05	-0,06	-0,17	-0,03	-0,03	-0,02	-0,01	-0,01	-0,01	-0,02	-0,01
89D 21	-0,01	-0,02	-0,03	-0,03	-0,02	-0,01	-0,03	-0,01	-0,04	-0,05	-0,15	-0,02	-0,04	-0,01	-0,02	-0,01	0,00	-0,03	0,00
00D 22	-0,01	-0,02	-0,03	-0,03	-0,02	-0,02	-0,04	-0,03	-0,04	-0,04	-0,11	-0,01	-0,02	-0,02	-0,01	-0,03	-0,01	-0,02	-0,01
79C 23	-0,01	-0,01	-0,02	-0,03	-0,01	-0,03	-0,05	-0,02	-0,02	-0,02	-0,02	-0,05	-0,04	-0,02	-0,01	-0,02	-0,02	-0,02	-0,01
35A 24	-0,03	-0,04	-0,05	-0,04	-0,02	-0,03	-0,04	-0,03	-0,04	-0,04	-0,07	-0,01	-0,02	-0,02	-0,03	-0,01	-0,02	-0,02	-0,01
91B 25	-0,04	-0,05	-0,05	-0,04	-0,03	-0,03	-0,07	-0,04	-0,03	-0,04	-0,07	-0,02	-0,02	-0,01	-0,01	-0,02	-0,02	-0,02	-0,01
61B 26	-0,04	-0,05	-0,05	-0,04	-0,04	-0,04	-0,06	-0,04	-0,03	-0,03	-0,06	-0,06	-0,03	-0,02	-0,01	-0,02	-0,01	-0,03	-0,02
ANG2 27	-0,01	-0,02	-0,03	-0,02	-0,02	-0,02	-0,03	-0,01	-0,01	-0,01	-0,02	-0,02	-0,02	-0,01	-0,02	-0,03	-0,03	-0,04	-0,04
RG2 28	-0,02	-0,02	-0,02	-0,02	-0,02	-0,03	-0,05	-0,02	-0,01	-0,02	-0,02	-0,01	-0,03	-0,02	-0,02	-0,03	-0,03	-0,03	-0,03
ANG4 29	0,00	-0,01	-0,02	-0,02	-0,01	-0,02	-0,03	-0,01	-0,01	-0,01	-0,02	-0,01	-0,02	-0,02	-0,02	-0,02	-0,02	-0,03	-0,02
00A 30	-0,01	-0,02	-0,03	-0,01	-0,03	-0,02	-0,04	-0,02	-0,02	-0,01	-0,01	0,00	-0,02	-0,01	-0,01	-0,02	-0,02	-0,02	-0,01
02C 31	-0,01	-0,02	-0,02	-0,02	-0,01	-0,02	-0,05	-0,02	-0,01	-0,01	-0,02	-0,01	-0,02	-0,01	-0,01	-0,01	-0,01	-0,02	-0,01
79B 32	-0,01	-0,02	-0,02	-0,02	-0,03	-0,02	-0,03	-0,03	0,00	-0,01	-0,03	-0,01	-0,02	-0,01	-0,02	-0,02	-0,02	-0,02	-0,02
91D 33	-0,01	-0,03	-0,03	-0,02	-0,04	-0,02	-0,04	-0,02	-0,02	-0,01	-0,02	-0,01	-0,01	-0,01	-0,01	-0,02	-0,02	-0,02	-0,01
32D 34	-0,01	-0,02	-0,02	-0,03	-0,02	-0,03	-0,04	-0,02	-0,02	-0,02	-0,03	-0,04	-0,02	-0,01	0,00	-0,01	-0,02	-0,02	-0,01
89A 35	-0,01	-0,02	-0,03	-0,04	-0,02	-0,04	-0,03	-0,01	-0,01	-0,02	-0,04	-0,02	-0,04	-0,01	-0,05	-0,01	-0,01	-0,02	-0,01
ANG1 36	-0,01	-0,02	-0,02	-0,02	-0,02	-0,03	-0,05	-0,03	-0,01	-0,02	-0,03	-0,01	-0,03	-0,02	-0,01	-0,02	-0,02	-0,02	-0,01
GTF112 37	-0,02	-0,02	-0,03	-0,02	-0,02	-0,02	-0,04	-0,02	-0,06	-0,03	-0,04	-0,07	-0,03	-0,02	-0,01	-0,01	-0,02	-0,02	-0,02
GTF32 38	-0,01	-0,03	-0,05	-0,04	-0,03	-0,03	-0,06	-0,03	-0,02	-0,03	-0,05	-0,07	-0,06	-0,04	-0,02	-0,02	-0,03	-0,04	-0,02
GTF45 39	-0,02	-0,01	-0,03	-0,02	-0,02	-0,02	-0,03	-0,02	-0,01	-0,01	-0,02	-0,03	-0,03	-0,02	-0,01	-0,03	-0,02	-0,02	-0,02

	STRING 4								STRING 5			STRING 6							STRING 7		
	19	20	21	22	23	24	25	26	27	28	29	30	31	32	33	34	35	36	37	38	39
91A 0	-0,01	-0,01	0,00	0,00	-0,01	0,00	-0,12	-0,02	-0,02	-0,02	-0,03	-0,02	-0,01	-0,04	-0,08	-0,04	-0,02	-0,06	-0,02	-0,01	-0,01
35B 1	0,00	-0,01	0,00	0,00	-0,01	-0,01	-0,12	-0,02	-0,01	-0,01	-0,01	-0,01	-0,02	-0,02	-0,07	-0,08	-0,06	-0,22	-0,01	-0,01	-0,01
02B 2	-0,01	-0,02	-0,01	0,00	-0,02	-0,02	-0,13	-0,01	-0,02	-0,01	-0,01	-0,02	-0,01	-0,02	-0,04	-0,06	-0,12	**-0,61**	-0,02	-0,01	-0,02
00B 3	-0,02	-0,01	-0,01	-0,02	-0,02	-0,01	-0,13	-0,02	-0,01	-0,03	-0,02	-0,01	-0,01	-0,01	-0,02	-0,05	-0,11	**-0,89**	-0,02	-0,02	-0,02
61A 4	-0,06	-0,04	-0,04	-0,04	-0,05	-0,08	-0,16	-0,06	-0,06	-0,03	-0,04	-0,03	-0,02	-0,02	-0,05	-0,02	-0,01	-0,02	-0,08	-0,03	-0,04
89B 5	-0,03	-0,03	-0,03	-0,03	-0,05	-0,05	-0,13	-0,04	-0,12	-0,05	-0,06	-0,02	-0,01	-0,02	-0,02	-0,01	-0,01	-0,02	-0,09	-0,04	-0,05
02D 6	-0,02	-0,02	-0,02	-0,02	-0,03	-0,03	-0,11	-0,03	-0,26	-0,08	-0,08	-0,03	-0,02	-0,02	-0,02	-0,01	-0,01	-0,02	-0,08	-0,04	-0,07
91C 7	-0,02	-0,01	-0,01	-0,01	-0,01	-0,02	-0,14	-0,01	**-0,43**	-0,21	-0,16	-0,05	-0,03	-0,02	-0,02	-0,01	-0,02	-0,03	-0,05	-0,04	-0,08
ANG5 8	-0,01	-0,01	-0,01	-0,01	-0,02	-0,03	-0,13	-0,01	-0,04	-0,02	-0,04	-0,03	-0,01	-0,01	-0,01	-0,01	-0,01	-0,02	-0,04	-0,01	-0,01
RG1 9	-0,01	-0,02	-0,01	-0,01	-0,02	-0,02	-0,15	-0,02	-0,04	-0,02	-0,04	-0,05	-0,02	-0,02	-0,02	-0,02	-0,01	-0,03	-0,02	-0,02	-0,02
ANG3 10	-0,01	-0,01	0,00	0,00	-0,02	-0,01	-0,13	-0,03	-0,02	-0,01	-0,01	-0,09	-0,05	-0,02	-0,02	-0,01	-0,01	-0,03	-0,01	-0,02	-0,01
02A 11	-0,03	-0,03	-0,02	-0,01	-0,01	0,00	-0,12	-0,02	-0,03	-0,09	**-0,58**	-0,01	0,00	-0,01	-0,01	-0,01	-0,01	-0,01	-0,01	-0,01	-0,02
32B 12	-0,01	-0,02	-0,02	-0,02	-0,01	-0,02	-0,11	-0,03	-0,02	-0,08	0,00	-0,02	-0,01	-0,01	-0,01	-0,02	-0,01	-0,02	-0,01	-0,01	-0,03
32A 13	-0,02	-0,02	-0,01	-0,02	-0,01	-0,03	-0,12	-0,03	-0,02	-0,03	0,00	-0,02	-0,01	-0,01	0,00	0,00	0,00	-0,02	0,00	-0,03	-0,02
32C 14	-0,01	-0,02	-0,01	-0,01	-0,04	-0,02	-0,15	-0,02	-0,02	-0,01	-0,04	-0,01	-0,01	-0,01	-0,01	-0,01	-0,02	-0,02	-0,02	-0,01	-0,02
89C 15	-0,08	-0,06	-0,06	-0,07	-0,10	-0,18	-0,20	-0,10	-0,26	-0,02	-0,03	-0,02	-0,01	-0,01	-0,02	-0,01	-0,01	-0,01	-0,19	-0,04	-0,04
61C 16	-0,04	-0,03	-0,03	-0,04	-0,08	-0,08	-0,16	-0,06	-0,24	-0,04	-0,03	-0,01	-0,01	-0,01	-0,01	-0,01	-0,01	-0,01	-0,20	-0,08	-0,07
76B 17	-0,02	-0,02	-0,05	-0,04	-0,05	-0,04	-0,13	-0,03	**-0,53**	0,00	0,00	-0,17	-0,01	0,00	-0,01	-0,01	-0,01	-0,02	-0,16	-0,09	-0,14
00C 18	-0,02	-0,01	-0,01	-0,01	-0,06	-0,02	-0,17	-0,02	**-0,82**	**-0,40**	-0,22	-0,01	-0,01	0,00	-0,01	-0,01	-0,02	-0,02	-0,05	-0,05	-0,13
35C 19		-0,10	-0,05	-0,03	-0,09	-0,04	-0,15	-0,03	-0,07	-0,18	**-0,76**	-0,01	-0,01	0,00	0,00	-0,01	-0,01	-0,01	-0,02	-0,02	-0,03
76C 20	-0,09		-0,09	-0,05	-0,02	-0,04	-0,16	-0,03	-0,04	-0,07	-0,22	-0,01	-0,01	0,00	-0,01	-0,01	0,00	-0,01	-0,02	-0,01	-0,02
89D 21	-0,04	-0,12		-0,10	-0,03	-0,03	-0,12	-0,03	-0,04	-0,04	-0,14	-0,01	-0,01	-0,01	0,00	-0,01	-0,02	-0,03	-0,02	-0,01	-0,02
00D 22	-0,01	-0,03	-0,11		-0,18	-0,04	-0,17	-0,04	-0,03	-0,02	-0,07	-0,02	-0,02	-0,01	-0,01	0,00	-0,02	-0,02	-0,02	-0,01	-0,03
79C 23	-0,02	-0,02	-0,03	-0,17		-0,10	-0,21	-0,06	-0,04	-0,02	-0,03	-0,01	0,00	0,00	-0,01	-0,02	-0,02	-0,02	-0,31	-0,08	-0,06
35A 24	-0,02	-0,02	-0,02	-0,04	-0,11		-0,25	-0,14	-0,04	-0,02	-0,04	-0,02	-0,01	-0,01	-0,02	-0,01	-0,01	-0,03	-0,02	-0,01	-0,02
91B 25	-0,01	-0,02	-0,03	-0,03	-0,12	-0,33		-0,35	-0,03	-0,01	-0,02	-0,04	-0,02	-0,01	-0,01	0,00	-0,01	-0,04	-0,02	-0,01	-0,02
61B 26	-0,05	-0,02	-0,07	-0,05	-0,05	-0,13	-0,49		-0,03	-0,01	-0,02	-0,06	-0,04	-0,02	-0,01	-0,01	-0,01	-0,05	-0,04	-0,02	-0,03
ANG2 27	-0,17	-0,08	-0,06	-0,04	-0,08	-0,09	-0,23	-0,19		-0,53	-0,58	-0,03	-0,06	-0,03	-0,03	-0,02	-0,05	-0,07	-0,30	-0,06	-0,12
RG2 28	-0,20	-0,14	-0,08	-0,04	-0,08	-0,06	-0,20	-0,14	-0,17		-0,44	-0,02	-0,03	-0,01	-0,02	-0,03	-0,04	-0,04	-0,10	-0,04	-0,06
ANG4 29	-0,08	-0,11	-0,15	-0,09	-0,09	-0,04	-0,17	-0,08	-0,08	-0,11		-0,02	-0,02	-0,01	-0,01	-0,01	-0,02	-0,03	-0,08	-0,02	-0,04
00A 30	-0,09	-0,08	-0,07	-0,05	-0,03	-0,05	-0,14	-0,07	-0,07	-0,04	-0,07		-0,19	-0,05	-0,03	-0,04	-0,04	-0,08	-0,06	-0,03	-0,02
02C 31	-0,11	-0,07	-0,05	-0,04	-0,03	-0,05	-0,17	-0,09	-0,08	-0,05	-0,05	-0,10		-0,09	-0,06	-0,03	-0,03	-0,04	-0,06	-0,02	-0,01
79B 32	-0,08	-0,05	-0,05	-0,04	-0,04	-0,07	-0,19	-0,10	-0,07	-0,04	-0,05	-0,04	-0,10		-0,11	-0,03	-0,03	-0,03	-0,07	-0,02	-0,02
91D 33	-0,05	-0,04	-0,04	-0,03	-0,04	-0,08	-0,21	-0,06	-0,07	-0,03	-0,05	-0,03	-0,04	-0,14		-0,05	-0,05	-0,04	-0,09	-0,02	-0,03
32D 34	-0,02	-0,02	-0,02	-0,02	-0,04	-0,02	-0,18	-0,03	-0,05	-0,03	-0,04	-0,03	-0,02	-0,03	-0,10		-0,18	-0,10	-0,07	-0,02	-0,02
89A 35	-0,01	-0,02	-0,02	-0,02	-0,03	-0,03	-0,16	-0,03	-0,04	-0,02	-0,06	-0,02	-0,02	-0,02	-0,04	-0,19		-0,19	-0,06	-0,03	-0,05
ANG1 36	-0,03	-0,03	-0,04	-0,06	-0,03	-0,03	-0,15	-0,04	-0,11	-0,07	-0,09	-0,07	-0,04	-0,04	-0,04	-0,08	-0,27		-0,13	-0,05	-0,08
GTF112 37	-0,02	-0,02	-0,02	-0,02	-0,18	-0,02	-0,15	-0,03	-0,07	-0,03	-0,03	-0,01	-0,01	-0,01	-0,01	-0,03	-0,03	-0,04		-0,13	-0,22
GTF32 38	-0,05	-0,04	-0,05	-0,07	**-1,46**	-0,04	-0,23	-0,05	-0,06	-0,03	-0,05	-0,03	-0,02	-0,01	-0,03	-0,03	-0,04	-0,04	-0,29		-0,37
GTF45 39	-0,06	-0,04	-0,07	-0,11	**-1,49**	-0,04	-0,18	-0,05	-0,05	-0,03	-0,06	-0,01	-0,01	-0,02	-0,02	-0,01	-0,02	-0,03	-0,32	-0,23	

Figure B.1: Phase II cross-talk matrix (value in %). In the rows the triggering detectors, in gray are indicated the cross-talk values $\leqslant -0.4$ %).

Acronyms

$0\nu\beta\beta$	neutrinoless double beta.
$2\nu\beta\beta$	double beta with 2 anti-neutrinos.
$Q_{\beta\beta}$	Q-value of the $\beta\beta$ process.
^{enr}Ge	germanium enriched in ^{76}Ge.
^{nat}Ge	natural germanium.
GERDA	GErmanium Detector Array.
HDM	Heidelberg-Moscow.
IGEX	International Germanium Experiment.
GTF	Genius Test Facility.
AC	anti-coincidence.
ANN	artificial neural network.
BAT	Bayesian Analysis Toolkit.
BCS	Bardeen-Cooper-Schrieffer.
BEGe	Broad Energy Germanium.
BI	background index.
C.I.	credible interval.
C.L.	confidence level.
CKM	Cabibbo-Kobayashi-Maskawa.
CP	charge conjugation parity.
CSP	charge sensitive preamplifier.
DEP	double escape peak.
DSP	Digital Signal Processing.
ENC	Equivalent Noise Charge.
FADC	Flash Analog to Digital Converter.
FEP	full energy peak.
FFT	Fast Fourier Trasform.
FIR	Finite Impulse Response.
FWHM	Full Width at Half Maximum.
GDL	Germanium Detector Laboratory.
GUT	grand unification theories.
HPGe	High Purity Germanium.
HV	high voltage.
IBM	interacting boson model.

ICP-MS	Inductively Coupled Plasma Mass Spectrometers.
IH	inverted hierarchy.
ISM	interacting shell model.
JFET	Junction Field-Effect Transistor.
LAr	liquid argon.
LNGS	Laboratori Nazionali del Gran Sasso.
MA	Moving Average.
MGDO	MAJORANA-GERDA Data Objects.
MS	mini-shroud.
MSE	multi-site event.
MV	muon veto.
NH	normal hierarchy.
NME	nuclear matrix element.
PCB	Printed Circuit Board.
PMNS	Pontecorvo-Maki-Nakagawa-Sakata.
PMT	photomultiplier.
PSD	pulse shape discrimination.
PSF	phase space factor.
QD	quasi-degenerate.
QRPA	quasiparticle random phase approximation.
ROI	region of interest.
SEP	single escape peak.
SiPM	silicon photomultiplier.
SM	Standard Model.
SSE	single site event.
VFE	very front-end.
ZAC	Zero Area Cusp-like.

Bibliography

[1] GERDA collaboration. Background free search for neutrinoless double-β decay of ^{76}Ge with GERDA Phase II. *Nature*, 544(7648):47–52, Apr 2017. URL `http://dx.doi.org/10.1038/nature21717`.

[2] M. Agostini et al. First results from GERDA Phase II. *Talk at the XXVII International Conference on Neutrino Physics and Astrophysics, London*, July 2016.

[3] W. Pauli. Neutrino hypothesis in beta-decay (Addressed to participants of Tubingen conference on radioactivity), 4 December 1930.

[4] C. L. Cowan, F. Reines, F. B. Harrison, H. W. Kruse, and A. D. McGuire. Detection of the Free Neutrino: a Confirmation. *Science*, 124(3212):103–104, 1956. ISSN 0036-8075. URL `http://science.sciencemag.org/content/124/3212/103`.

[5] F. Reines and C. L. Cowan. The Neutrino. *Nature*, 178(4531):446–449, sep 1956. URL `http://www.nature.com/nature/journal/v178/n4531/abs/178446a0.html`.

[6] E. Fermi. Versuch einer Theory der β-Strahlen. *Z. für Phys.*, 88(161–177), 1934.

[7] E. Majorana. Teoria simmetrica dell'elettrone e del positrone. *Il Nuovo Cimento (1924-1942)*, 14(4):171, 1937. ISSN 1827-6121. URL `http://dx.doi.org/10.1007/BF02961314`.

[8] E. J. Konopinski and H. M. Mahmoud. The Universal Fermi Interaction. *Phys. Rev.*, 92:1045–1049, Nov 1953. URL `http://link.aps.org/doi/10.1103/PhysRev.92.1045`.

[9] B. Pontecorvo. Inverse beta processes and nonconservation of lepton charge. *Sov. Phys. JETP*, 71:172–173, 1957.

[10] M. Goldhaber, L. Grodzins, and A. W. Sunyar. Helicity of Neutrinos. *Phys. Rev.*, 109:1015–1017, Feb 1958. URL `http://journals.aps.org/pr/abstract/10.1103/PhysRev.109.1015`.

[11] C. S. Wu, E. Ambler, R. W. Hayward, D. D. Hoppes, and R. P. Hudson. Experimental Test of Parity Conservation in Beta Decay. *Phys. Rev.*, 105:1413–1415, Feb 1957. URL `http://link.aps.org/doi/10.1103/PhysRev.105.1413`.

[12] Donald R. Hamilton, W. Parker Alford, and Leonard Gross. Upper Limits on the Neutrino Mass from the Tritium Beta Spectrum. *Phys. Rev.*, 92:1521–1525, Dec 1953. URL http://link.aps.org/doi/10.1103/PhysRev.92.1521.

[13] S. L. Glashow. Partial Symmetries of Weak Interactions. *Nucl. Phys.*, 22:579–588, 1961. URL http://inspirehep.net/record/4328.

[14] Z. Maki, M.Nakagawa, and S. Sakata. Remarks on the Unified Model of Elementary Particles. *Prog. Theor. Phys.*, 28(5):870–880, 1962.

[15] V. Gribov and B. Pontecorvo. Neutrino astronomy and lepton charge. *Physics Letters B*, 28(7):493–496, 1969. ISSN 0370-2693. URL http://www.sciencedirect.com/science/article/pii/0370269369905255.

[16] C. Patrignani et al. (Particle Data Group). Review of particle physics. *Chinese Physics C*, 40(100001), 2016.

[17] W. Hampel et al. GALLEX solar neutrino observations: Results for GALLEX IV. *Phys. Lett.*, B447:127–133, 1999.

[18] M. Altmann et al. Complete results for five years of GNO solar neutrino observations. *Phys. Lett.*, B616:174–190, 2005. URL https://arxiv.org/abs/hep-ex/0504037.

[19] J. N. Abdurashitov et al. Measurement of the solar neutrino capture rate with gallium metal. III. Results for the 2002–2007 data-taking period. *Phys. Rev. C*, 80:015807, Jul 2009. URL http://link.aps.org/doi/10.1103/PhysRevC.80.015807.

[20] Y. Fukuda et al. Solar Neutrino Data Covering Solar Cycle 22. *Phys. Rev. Lett.*, 77:1683–1686, Aug 1996. URL http://link.aps.org/doi/10.1103/PhysRevLett.77.1683.

[21] S. Fukuda et al. Determination of solar neutrino oscillation parameters using 1496 days of Super-Kamiokande I data. *Phys. Lett.*, B539:179–187, 2002.

[22] Q. R. Ahmad et al. Direct evidence for neutrino flavor transformation from neutral current interactions in the Sudbury Neutrino Observatory. *Phys. Rev. Lett.*, 89:011301, 2002.

[23] T. Araki et al. Measurement of Neutrino Oscillation with KamLAND: Evidence of Spectral Distortion. *Phys. Rev. Lett.*, 94:081801, Mar 2005.

[24] Y. Ashie et al. Evidence for an Oscillatory Signature in Atmospheric Neutrino Oscillations. *Phys. Rev. Lett.*, 93:101801, Sep 2004. URL http://link.aps.org/doi/10.1103/PhysRevLett.93.101801.

[25] M. H. Ahn et al. Measurement of Neutrino Oscillation by the K2K Experiment. *Phys. Rev.*, D74:072003, 2006.

[26] P. Adamson et al. Measurement of the Neutrino Mass Splitting and Flavor Mixing by MINOS. *Phys. Rev. Lett.*, 106:181801, 2011.

[27] K. Abe et al. Measurement of Neutrino Oscillation Parameters from Muon Neutrino Disappearance with an Off-axis Beam. *Phys. Rev. Lett.*, 111(21):211803, 2013.

[28] K. Abe et al. Evidence for the Appearance of Atmospheric Tau Neutrinos in Super-Kamiokande. *Phys. Rev. Lett.*, 110(18):181802, 2013.

[29] A. Pastore. talk at the EPS HEP 2013 Conference, July 18-24, 2013, Stockholm.

[30] K. Abe et al. Indication of Electron Neutrino Appearance from an Accelerator-produced Off-axis Muon Neutrino Beam. *Phys. Rev. Lett.*, 107:041801, 2011.

[31] P. Adamson et al. Improved Search for Muon-Neutrino to Electron-Neutrino Oscillations in MINOS. *Phys. Rev. Lett.*, 107:181802, Oct 2011.

[32] K. Abe. Evidence of electron neutrino appearance in a muon neutrino beam. *Phys. Rev. D*, 88:032002, Aug 2013.

[33] Y. Abe et al. Indication of Reactor $\overline{\nu}_e$ Disappearance in the Double Chooz Experiment. *Phys. Rev. Lett.*, 108:131801, Mar 2012. URL `http://link.aps.org/doi/10.1103/PhysRevLett.108.131801`.

[34] F. P. An et al. New Measurement of Antineutrino Oscillation with the Full Detector Configuration at Daya Bay. *Phys. Rev. Lett.*, 112:061801, 2014.

[35] J. H. Choi et al. Observation of Energy and Baseline Dependent Reactor Antineutrino Disappearance in the RENO Experiment. *Phys. Rev. Lett.*, 116:211801, May 2016.

[36] Y. Abe et al. Reactor electron antineutrino disappearance in the Double Chooz experiment. *Phys. Rev.*, D86:052008, 2012.

[37] F. Capozzi, E. Lisi, A. Marrone, D. Montanino, and A. Palazzo. Neutrino masses and mixings: Status of known and unknown 3ν parameters. *Nucl. Phys.*, B908:218–234, 2016.

[38] E. K. Akhmedov, S. Razzaque, and A. Y. Smirnov. Mass hierarchy, 2-3 mixing and CP-phase with Huge Atmospheric Neutrino Detectors. *JHEP*, 02:082, 2013.

[39] M. S. Athar et al. India-based Neutrino Observatory: Project (INO Collaboration). *Volume I*, 2006.

[40] Ch. Kraus et al. Final results from phase II of the Mainz neutrino mass search in tritium beta decay. *Eur. Phys. J.*, C40:447–468, 2005.

[41] V. N. Aseev, A. I. Belesev, A. I. Berlev, E. V. Geraskin, A. A. Golubev, N. A. Likhovid, V. M. Lobashev, A. A. Nozik, V. S. Pantuev, V. I. Parfenov, A. K. Skasyrskaya, F. V. Tkachov, and S. V. Zadorozhny. Upper limit on the electron antineutrino mass from the Troitsk experiment. *Phys. Rev. D*, 84:112003, Dec 2011.

[42] Florian Priester, Michael Sturm, and Beate Bornschein. Commissioning and detailed results of KATRIN inner loop tritium processing system at Tritium Laboratory Karlsruhe. *Vacuum*, 116:42–47, 2015. ISSN 0042-207X. doi: 10.1016/j.vacuum.2015.02.030. URL `http://www.sciencedirect.com/science/article/pii/S0042207X15000846`.

[43] P. A. M. Dirac. The Quantum Theory of the Electron. *Proceedings of the Royal Society of London A: Mathematical, Physical and Engineering Sciences*, 117(778):610–624, 1928. ISSN 0950-1207. URL `http://rspa.royalsocietypublishing.org/content/117/778/610`.

[44] P. A. M. Dirac. The Quantum Theory of the Electron. Part II. *Proceedings of the Royal Society of London A: Mathematical, Physical and Engineering Sciences*, 118(779):351–361, 1928. ISSN 0950-1207. URL `http://rspa.royalsocietypublishing.org/content/118/779/351`.

[45] P. Minkowski. $\mu \to \gamma$ at a rate of one out of 109 muon decays? *Physics Letters B*, 67(4):421–428, 1977. ISSN 0370-2693. URL `http://www.sciencedirect.com/science/article/pii/037026937790435X`.

[46] R. N. Mohapatra and G. Senjanović. Neutrino Mass and Spontaneous Parity Nonconservation. *Phys. Rev. Lett.*, 44:912–915, Apr 1980.

[47] T. Yanagida. Horizontal symmetry and masses of neutrinos. *Conf. Proc.*, C7902131:95–99, 1979.

[48] S. Dell'Oro, S. Marcocci, M. Viel, and F. Vissani. Neutrinoless double beta decay: 2015 review. *Advances in High Energy Physics*, 2016 (2162659), 2016. URL `https://arxiv.org/abs/1601.07512`.

[49] J.D. Vergados, H. Ejiri, and F Šimkovic. Neutrinoless double beta decay and neutrino mass. *Int. J. Mod. Phys. E*, 25(1630007), 2016. URL `https://arxiv.org/abs/1612.02924`.

[50] J. Engel and J. Menendez. Status and Future of Nuclear Matrix Elements for Neutrinoless Double-Beta Decay: A Review. URL `https://arxiv.org/abs/1610.06548`.

[51] M. Goeppert-Mayer. Double Beta-Disintegration. *Phys. Rev.*, 48(6):512–516, Sep 1935. URL `http://link.aps.org/doi/10.1103/PhysRev.48.512`.

[52] W. H. Furry. On Transition Probabilities in Double Beta-Disintegration. *Phys. Rev.*, 56:1184–1193, Dec 1939.

[53] J. Schechter and J. W. F. Valle. Neutrinoless double-β decay in SU(2)$\times$U(1) theories. *Phys. Rev. D*, 25:2951–2954, Jun 1982.

[54] M. Duerr, M. Lindner, and A. Merle. On the Quantitative Impact of the Schechter-Valle Theorem. *JHEP*, 06:091, 2011.

[55] H. Fritzsch and P. Minkowski. Unified interactions of leptons and hadrons. *Annals of Physics*, 93(1):193–266, 1975. ISSN 0003-4916. doi: 10.1016/0003-4916(75)90211-0. URL `http://www.sciencedirect.com/science/article/pii/0003491675902110`.

[56] M. Doi, T. Kotani, H. Nishiura, K. Okuda, and E. Takasugi. Neutrino Mass, the Right-Handed Interaction and the Double Beta Decay I. *Progress of Theoretical Physics*, 66(5):1739–64, November 1981.

[57] J. Kotila and F. Iachello. Phase-Space factors for double-β decay. *Phys. Rev.*, C 85(034316), 2012. URL `https://arxiv.org/abs/1209.5722`.

[58] F. Bohem and P. Vogel. *Physics of Massive Neutrinos*. Cambridge University Press, June 26, 1992.

[59] J. Menendez, A. Poves, E. Caurier, and F. Nowacki. Disassembling the Nuclear Matrix Elements of the Neutrinoless beta beta Decay. *Nucl. Phys.*, A818:139–151, 2009. URL `https://arxiv.org/abs/0801.3760`.

[60] F. Šimkovic, V. Rodin, A. Faessler, and P. Vogel. $0\nu\beta\beta$ and $2\nu\beta\beta$ nuclear matrix elements, quasiparticle random-phase approximation, and isospin symmetry restoration. *Phys. Rev.*, C87(4):045501, 2013. URL `https://arxiv.org/abs/1302.1509`.

[61] J. Barea, J. Kotila, and F. Iachello. Nuclear matrix elements for double beta decay. *Phys. Rev.*, C 87(014315), 2013. URL `https://arxiv.org/abs/1301.4203`.

[62] J. Barea, J. Kotila, and F. Iachello. $0\nu\beta\beta$ and $2\nu\beta\beta$ nuclear matrix elements in the interacting boson model with isospin restoration. *Phys. Rev. C*, 91(034304), 2015. URL `https://arxiv.org/abs/1506.08530`.

[63] F. Šimkovic, G. Pantis, J. D. Vergados, and A. Faessler. Additional nucleon current contributions to neutrinoless double β decay. *Phys. Rev. C*, 60:055502, Oct 1999. URL `https://arxiv.org/abs/hep-ph/9905509`.

[64] R. G. H. Robertson. Empirical Survey of Neutrinoless Double Beta Decay Matrix Elements. *Mod. Phys. Lett.*, A28:1350021, 2013. URL `https://arxiv.org/abs/1301.1323`.

[65] F. T. Avignone III, G. S. King, and Y. G. Zdesenko. Next generation double-beta decay experiments: metrics for their evaluation. *New J. Phys.*, 7(6), 2005. URL `http://iopscience.iop.org/article/10.1088/1367-2630/7/1/006/meta;jsessionid=58C4BA602B39B175689824A90CB2F856.c1.iopscience.cld.iop.org`.

[66] A. S. Barabash. Double Beta Decay: Historical Review of 75 Years of Research. *Physics of Atomic Nuclei*, 74(4):603–613, apr 2011. URL https://arxiv.org/abs/1104.2714.

[67] H. V. Klapdor-Kleingrothaus. Seventy years of double beta decay: From nuclear physics to beyond-standard- model particle physics. *World Scientific*, 2010. URL http://www.worldscientific.com/worldscibooks/10.1142/6921.

[68] E. L. Fireman. A Measurement of the Half-Life of Double Beta-Decay from ^{124}Sn. *Phys. Rev.*, 75(323), 1949.

[69] M. I. Kalkstein and W. F. Libby. An Investigation of the Double Beta-Decay of ^{124}Sn. *Phys. Rev.*, 85:368–369, Jan 1952. URL http://link.aps.org/doi/10.1103/PhysRev.85.368.

[70] M. G. Inghram and J. H. Reynolds. Double Beta-Decay of ^{130}Te. *Phys. Rev.*, 78:822–823, Jun 1950. URL http://link.aps.org/doi/10.1103/PhysRev.78.822.2.

[71] E. Fiorini, A. Pullia, G. Bertolini, F. Cappellani, and G. Restelli. Neutrinoless double-beta decay of ^{76}Ge. *Nuovo Cimento A*, 137(3): 747–763, 1973. URL http://link.springer.com/article/10.1007/BF02784100.

[72] R. K. Bardin, P. J. Gollon, J. D. Ullman, and C. S. Wu. A search for the double beta decay of ^{48}Ca and lepton conservation. *Nucl. Phys.*, A158: 337–363, 1970. URL http://inspirehep.net/record/1437788.

[73] B. T. Cleveland, W. R. Leo, P. J. Gollon, C. S. Wu, L. R. Kasday, J. D. Ullman, and A. M. Rushton. Lepton Conservation in the Double β Decay of ^{82}Se. *Phys. Rev. Lett.*, 35(757), 1975.

[74] N. Takaoka and K. Ogata. *Z. Naturforsch.*, 21(85), 1966.

[75] T. Kirsten, O. A. Schaeffer, and W. Gentner. *Z. Phys.*, 202(273), 1967.

[76] E. W. Hennecke, O. K. Manuel, and D. D. Sabu. Double beta decay of ^{128}Te. *Phys. Rev. C*, 11(4), 1975. URL http://link.aps.org/doi/10.1103/PhysRevC.11.1378.

[77] E. Bellotti, O. Cremonesi, E. Fiorini, C. Liguori, A. Pullia, P. P. Sverzellati, and L. Zanotti. The milano experiment on lepton number nonconservation in double beta-decay of ^{76}Ge. *Il Nuovo Cimento A*, 95(1):1, 1986. ISSN 1826-9869. URL http://dx.doi.org/10.1007/BF02768738.

[78] D. O. Caldwell. Double beta decay-present and future. *Journal of Physics G: Nuclear and Particle Physics*, 17(S):S137, 1991. URL http://stacks.iop.org/0954-3899/17/i=S/a=014.

[79] M. Günther et al. Heidelberg-Moscow $\beta\beta$ experiment with ^{76}Ge: Full setup with five detectors. *Phys. Rev. D*, 55(54), 1997. URL http://journals.aps.org/prd/abstract/10.1103/PhysRevD.55.54.

[80] H. V. Klapdor-Kleingrothaus et al. Latest results from the Heidelberg-Moscow double beta decay experiment. *Eur. Phys. J.*, A12:147–154, 2001. URL `https://arxiv.org/abs/hep-ph/0103062`.

[81] C.E. Aalseth et al. Recent results from the IGEX double-beta decay experiment. *Nuclear Physics B*, 48(1-3):223–225, 1996. URL `http://www.sciencedirect.com/science/article/pii/0920563296002447`.

[82] C. E. Aalseth et al. IGEX ^{76}Ge neutrinoless double-beta decay experiment: Prospects for next generation experiments. *Phys. Rev. D*, 65 (092007), 2002. URL `https://journals.aps.org/prd/abstract/10.1103/PhysRevD.65.092007`.

[83] R. Luescher et al. Search for $\beta\beta$ decay in ^{136}Xe: new results from the Gotthard experiment. *Physics Letters B*, 434(3–4):407–414, 1998. ISSN 0370-2693. URL `http://www.sciencedirect.com/science/article/pii/S037026939800906X`.

[84] E. Bellotti, O. Cremonesi, E. Fiorini, G. Gervasio, C. Liguori, S. Ragazzi, L. Rossi, J. Szarka, P.P. Sverzellatti, T. Tabarelli, and L. Zanotti. A search for lepton number non-conservation in double beta decay of 136Xe. *Physics Letters B*, 221(2):209–215, 1989. ISSN 0370-2693. URL `http://www.sciencedirect.com/science/article/pii/0370269389915001`.

[85] S. R. Elliott, A. A. Hahn, and M. K. Moe. Direct evidence for two-neutrino double-beta decay in ^{82}Se. *Phys. Rev. Lett.*, 59:2020–2023, Nov 1987. URL `http://link.aps.org/doi/10.1103/PhysRevLett.59.2020`.

[86] H. Ejiri et al. Double beta decays of Mo-100. *Phys. Lett.*, B258:17–23, 1991. doi: 10.1016/0370-2693(91)91201-6.

[87] D. Dassié et al. Two-neutrino double-β decay measurement of ^{100}Mo. *Phys. Rev. D*, 51:2090–2100, Mar 1995. URL `http://link.aps.org/doi/10.1103/PhysRevD.51.2090`.

[88] R. Arnold et al. Double-beta decay of Cd-116. *Z. Phys.*, C72:239–247, 1996. doi: 10.1007/s002880050241.

[89] R. Arnold et al. Double beta decay of Se-82. *Nucl. Phys.*, A636:209–223, 1998. doi: 10.1016/S0375-9474(98)00208-5.

[90] H. V. Klapdor-Kleingrouthaus, A. Dietz, H. L. Harney, and I. V. Krivosheina. Evidence for neutrinoless double beta decay. *Modern Physics Letters A*, 16(37):2409–2420, 2001. URL `http://www.worldscientific.com/doi/abs/10.1142/S0217732301005825`.

[91] H. V. Klapdor-Kleingrothaus et al. Search for neutrinoless double beta decay with enriched ^{76}Ge in Gran Sasso 1990-2003. *Phys. Lett. B*, 586 (198-212), 2004. URL `https://arxiv.org/abs/hep-ph/0404088`.

[92] H. V. Klapdor-Kleingrothaus et al. The evidence for the observation of 0nbb decay: the identification of 0nbb events from the full spectra. *Modern Physics Letters A*, 21(20):1547–1566, March 2006.

[93] B. Schwingenheuer. Status and prospects of searches for neutrinoless double beta decay. *Ann. Phys. (Berlin)*, 525(4):269, 2013.

[94] GERDA collaboration. Results on Neutrinoless Double-β Decay of ^{76}Ge from Phase I of the GERDA Experiment. *Phys. Rev. Lett.*, 111(122503), 2013. URL https://arxiv.org/abs/1307.4720.

[95] NEMO-3 Collaboration. Measurement of the double-beta decay half-life and search for the neutrinoless double-beta decay of ^{48}Ca with the NEMO-3 detector. *Phys. Rev. D*, 93:112008, Jun 2016. URL https://arxiv.org/abs/1604.01710.

[96] GERDA Collaboration. $2\nu\beta\beta$ decay of ^{76}Ge into excited states with GERDA Phase I. *J. Phys. G: Nucl. Part. Phys.*, 42(115201), 2015. URL http://arxiv.org/abs/1506.03120.

[97] NEMO-3 Collaboration. First Results of the Search for Neutrinoless Double-Beta Decay with the NEMO 3 Detector. *Phys. Rev. Lett.*, 95: 182302, Oct 2005. doi: 10.1103/PhysRevLett.95.182302. URL http://link.aps.org/doi/10.1103/PhysRevLett.95.182302.

[98] A. S. Barabash et al. Investigation of double beta decay with the NEMO-3 detector. *Phys. Atom. Nucl.*, 74:312–317, 2011.

[99] NEMO-3 Collaboration. Measurement of the $2\nu\beta\beta$ Decay Half-Life and Search for the $0\nu\beta\beta$ Decay of ^{116}Cd with the NEMO-3 Detector. 2016. URL https://arxiv.org/abs/1610.03226.

[100] F. A. Danevich et al. Search for double beta decay of ^{116}Cd with enriched $^{116}CdWO_4$ crystal scintillators (Aurora experiment). *Journal of Physics: Conference Series*, 718(6):062009, 2016. URL http://iopscience.iop.org/article/10.1088/1742-6596/718/6/062009.

[101] A. S. Barabash. Average and recommended half-life values for two neutrino double beta decay: upgrade-2013. *Nucl. Phys. A*, 935:525–536, 2015. URL https://arxiv.org/abs/1311.2421.

[102] NEMO-3 Collaboration. Measurement of the $\beta\beta$ Decay Half-Life of ^{130}Te with the NEMO-3 Detector. *Phys. Rev. Lett.*, 107:062504, Aug 2011. URL https://arxiv.org/abs/1104.3716.

[103] D. Chiesa et al. CUORE-0 background analysis and evaluation of ^{130}Te $2nu\beta\beta$ decay half-life. *Proceeding of the conference: "28th Rencontres de Blois, Particle Physics and Cosmology", Chateau Royal de Blois*, May 29 - June 03, 2016. URL https://arxiv.org/abs/1610.04518.

[104] KamLAND-Zen Collaboration. Measurement of the double-β decay half-life of ^{136}Xe with the KamLAND-Zen experiment. *Phys. Rev. C*, 85 (045504), 2012. URL https://arxiv.org/abs/1201.4664.

[105] N. Ackerman et al. An improved measurement of the $2\nu\beta\beta$ half-life of ^{136}Xe with EXO-200. *Phys. Rev. C*, 89(015502), 2014. URL https://arxiv.org/abs/1306.6106.

[106] NEMO-3 Collaboration. Measurement of the $2\nu\beta\beta$ decay half-life of ^{150}Nd and a search for $0\nu\beta\beta$ decay processes with the full exposure from the NEMO-3 detector. *Phys. Rev.*, D94(7):072003, 2016. URL https://arxiv.org/abs/1606.08494.

[107] NEMO Collaboration. Technical design and performance of the NEMO 3 detector. *Nucl. Instrum. Meth.*, A536:79–122, 2005. URL https://arxiv.org/abs/physics/0402115.

[108] The EXO-200 Collaboration. Search for Majorana neutrinos with the first two years of EXO-200 data. *Nature*, 510(7504):229–234, jun 2014. ISSN 0028-0836. URL https://arxiv.org/abs/1402.6956.

[109] KamLAND-Zen Collaboration. Search for Majorana Neutrinos Near the Inverted Mass Hierarchy Region with KamLAND-Zen. *Phys. Rev. Lett.*, 117:082503, Aug 2016. URL https://arxiv.org/abs/1605.02889.

[110] CUORE Collaboration. Search for Neutrinoless Double-Beta Decay of ^{130}Te with CUORE-0. *Phys. Rev. Lett.*, 115:102502, Sep 2015. URL https://arxiv.org/abs/1402.6072.

[111] NEMO-3 Collaboration. Results of the search for neutrinoless double-β decay in ^{100}Mo with the NEMO-3 experiment. *Phys. Rev.*, D92(7): 072011, 2015. URL https://arxiv.org/abs/1506.05825.

[112] KamLAND Collaboration. ^{7}Be solar neutrino measurement with KamLAND. *Phys. Rev. C*, 92(055808), Nov 2015. URL http://journals.aps.org/prc/abstract/10.1103/PhysRevC.92.055808.

[113] CUORE Collaboration. CUORE: A Cryogenic Underground Observatory for Rare Events. *Nucl. Instrum. Meth.*, A518:775–798, 2004. URL https://arxiv.org/abs/hep-ex/0212053.

[114] E. Andreotti et al. ^{130}Te neutrinoless double-beta decay with CUORICINO. *Astroparticle Physics*, 34(11):822–831, 2011. ISSN 0927-6505. URL https://arxiv.org/abs/1012.3266.

[115] MAJORANA Collaboration. Status of the MAJORANA DEMONSTRATOR. *AIP Conf. Proc.*, 1686(020005), 2015. URL https://arxiv.org/abs/1507.07612.

[116] Y. Liang. Status and Prospects for the EXO-200 and nEXO Experiments. *XXVII International Conference on Neutrino Physics and Astrophysics. London*, 8 July 2016. URL http://neutrino2016.iopconfs.org/IOP/media/uploaded/EVIOP/event_948/10.05__5__Yang.pdf.

[117] SuperNEMO Collaboration. Probing New Physics Models of Neutrinoless Double Beta Decay with SuperNEMO. *Eur. Phys. J. C*, 70:927–943, 2010. URL https://arxiv.org/abs/1005.1241.

[118] CUPID Collaboration. R&D towards CUPID (CUORE Upgrade with Particle IDentification). 2015. URL https://arxiv.org/abs/1504.03612.

[119] SNO+ Collaboration. Current Status and Future Prospects of the SNO+ Experiment. *Advances in High Energy Physics*, 2016(6194250). URL https://arxiv.org/abs/1508.05759.

[120] NEXT Collaboration. NEXT-100 Technical Design Report (TDR). Executive Summary. *JINST*, 7(T06001), 2012. URL https://arxiv.org/abs/1202.0721.

[121] J. W. Beeman et al. Double-beta decay investigation with highly pure enriched ^{82}Se for the LUCIFER experiment. *Eur. Phys. J. C*, 75(591), 2015. URL https://arxiv.org/abs/1508.01709.

[122] V. Alenkov et al. Technical Design Report for the AMoRE $0\nu\beta\beta$ Decay Search Experiment. 2015. URL https://arxiv.org/abs/1512.05957.

[123] J. Ebert et al. Current Status and Future Perspectives of the COBRA Experiment. *Advances in High Energy Physics*, 2013(70357), 2013. URL https://www.hindawi.com/journals/ahep/2013/703572.

[124] E. Armengaud et al. LUMINEU: a search for neutrinoless double beta decay based on $ZnMoO_4$ scintillating bolometers. *J. Phys. Conf. Ser.*, 718(6):062008, 2016. URL https://arxiv.org/abs/1601.04989.

[125] H. Ejiri et al. MOON for neutrino-less double beta decays. *Eur. Phys. J. ST*, 162:239–250, 2008. URL http://inspirehep.net/record/807971?ln=en.

[126] CANDLES Collaboration. Status and future prospect of ^{48}Ca double beta decay search in CANDLES. *Journal of Physics: Conference Series*, 718(6):062026, 2016. URL http://iopscience.iop.org/article/10.1088/1742-6596/718/6/062026.

[127] GERDA collaboration. The GERDA experiment for the search of $0\nu\beta\beta$ decay in ^{76}Ge. *Eur.Phys. J. C*, 73(2330), March 2013. URL https://arxiv.org/abs/1212.4067.

[128] GERDA. URL http://www.mpi-hd.mpg.de/gerda.

[129] GERDA Collaboration et al. GERDA - Letter of Intent. *tech. rep.*,, 2004.

[130] G. Heusser. Low radioactivity background techniques. *Annu. Rev. Nucl. Part. Sci.*, 45(1):543–590, 1995.

[131] Laboratori Nazionali del Gran Sasso. URL https://www.lngs.infn.it.

[132] L. Baudis et al. GENIUS: a new dark matter project. *Physics Reports*, 307(1-4):301–308, 1998. URL http://www.sciencedirect.com/science/article/pii/S0370157398000659.

[133] H.V. Klapdor-Kleingrothaus et al. GENIUS-TF: a test facility for the GENIUS project. *Nucl. Instrum. Methods A*, 481(1-3):49–159, 2002. URL http://www.sciencedirect.com/science/article/pii/S016890020101258X.

[134] M. Agostini et al. The MGDO software library for data analysis in Ge neutrinoless double-beta decay experiments. *Journal of Physics: Conference Series*, 375(042027), 2012. URL https://arxiv.org/abs/1111.7260.

[135] R. Brun and F. Rademakers. ROOT: An object oriented data analysis framework. *Nucl. Instrum. Meth.*, A389(81-86), 1997.

[136] M. Agostini, L. Pandola, P. Zavarise, and O. Volynets. GELATIO: a general framework for modular digital analysis of high-purity Ge detector signals. *JINST 6 P08013*, October 2011. URL https://arxiv.org/abs/1106.1780.

[137] M. Agostini, L. Pandola, and P. Zavarise. Off-line data processing and analysis for the GERDA experiment. *Jour. Phys. Conf. Ser.*, 368 (012047), 2012. URL https://arxiv.org/abs/1111.3582.

[138] GERDA collaboration. Pulse shape discrimination for GERDA Phase I data. *Eur. Phys. J. C*, 73(2583), 2013. URL https://arxiv.org/abs/1307.2610.

[139] GERDA collaboration. The background in the $0\nu\beta\beta$ experiment GERDA. *Eur. Phys. J. C*, 74(2764), 2014. URL https://arxiv.org/abs/1306.5084.

[140] GERDA collaboration. Limit on neutrinoless double beta decay of ^{76}Ge by GERDA. *Physics Procedia*, 61:828 – 837, 2015. URL http://www.sciencedirect.com/science/article/pii/S187538921500382X.

[141] GERDA collaboration. Results on $\beta\beta$ decay with emission of two neutrinos or Majorons in ^{76}Ge from GERDA Phase I. *Eur. Phys. J. C*, 75(416), 2015. URL https://arxiv.org/abs/1501.02345.

[142] K. T. Knöpfle et al. Upgrade of the GERDA experiment. *PoS*, TIPP2014: 109, 2014.

[143] GERDA collaboration. Production, characterization and operation of ^{76}Ge enriched BEGe detectors in GERDA. *Eur. Phys. J. C*, 75(39), 2015. URL https://arxiv.org/abs/1410.0853.

[144] Broad Energy Germanium Detectors from Canberra. URL http://www.canberra.com/products/detectors/germanium-detectors.asp?Accordion1=1.

[145] Z. He. Review of the Shockley–Ramo theorem and its application in semiconductor gamma-ray detectors. *Nucl. Instrum. Meth. A*, 463(1-2):250–267, 2001. URL http://www.sciencedirect.com/science/article/pii/S0168900201002236.

[146] D. Budjas et al. Pulse shape discrimination studies with a Broad-Energy Germanium detector for signal identification and background suppression in the GERDA double beta decay experiment. *JINST 4 P10007*, 2009.

[147] M. Agostini et al. Signal modeling of high purity Ge detectors with a small read-out electrode and application to neutrinoless double beta decay search in 76Ge. *JINST 6 P03005*, 2011.

[148] V. Wagner. *Pulse Shape Analysis for the* GERDA *Experiment to Set a New Limit on the Half-life of* $0\nu\beta\beta$ *Decay of* ^{76}*Ge, MPI-K and Univ. Heidelberg (2016).* PhD thesis, . URL http://www.ub.uni-heidelberg.de/archiv/22621.

[149] M. Agostini et al. LArGe - Active background suppression using argon scintillation for the GERDA $0\nu\beta\beta$-experiment. *Eur. Phys. J. C*, 75(506), 2015. URL https://arxiv.org/abs/1501.05762.

[150] M. Di Marco, P. Peiffer, and S. Schönert. LArGe: Background suppression using liquid argon (LAr) scintillation for $0\nu\beta\beta$ decay search with enriched germanium (Ge) detectors. *Nucl.Phys.Proc.Suppl.*, 172(45-48), 2007. URL https://arxiv.org/abs/physics/0701001.

[151] Janicsko-Csathy J. et al. Development of an anti-Compton veto for HPGe detectors operated in liquid argon using Silicon Photo-Multipliers. *Nucl.Instrum.Meth.*, A654(225-232), 2011. URL https://arxiv.org/abs/1011.2748.

[152] Janicsko-Csathy J. et al. Optical fiber read-out for liquid argon scintillation light. URL https://arxiv.org/abs/1606.04254.

[153] A. Lubashevskiy et al. Nylon mini-shroud coated with wavelengh shifter for the GERDA Phase II detectors array. GERDA *Scientific/Technical Report*, 2015.

[154] A. Lazzaro et al. Quality Cuts concept, efficiency, application, GERDA Collaboration Meeting, Ringberg, June 2016.

[155] A Kirsch. *Search for the Neutrinoless Double* β*-decay in* GERDA *Phase I Using a Pulse Shape Discrimination Technique, MPI-K and Univ. Heidelberg (2014).* PhD thesis. URL http://www.ub.uni-heidelberg.de/archiv/17149.

[156] Glenn F. Knoll. *Radiation Detection and Measurement.* John Wiley & Sons, 2010.

[157] Hamamatsu. Characteristics and use of Charge amplifier. Technical report, Solid State Division, 2001.

[158] A. Pullia et al. A Cryogenic Low-Noise JFET-CMOS Preamplifier for the HPGe Detectors of GERDA. *IEEE Nuclear Science Symposium and Medical Imaging Conference (NSS/MIC)*, 2008.

[159] A. D'Andragora et al. Spectroscopy Performances of the GERDA Cryogenic Charge Sensitive Amplifier Based on JFET-CMOS ASIC Coupled to Germanium Detectors. *IEEE Nuclear Science Symposium and Medical Imaging Conference (NSS/MIC)*, 2009.

[160] S. Riboldi et al. A low-noise charge premplifier for Ge spectroscopy operating at cryogenic temperature in the GERDA experiment. *IEEE Nuclear Science Symposium and Medical Imaging Conference (NSS/MIC)*, 2010. URL http://ieeexplore.ieee.org/document/5873998.

[161] Polyflon a Crane Co. Company. URL http://www.polyflon.com.

[162] C. M. Cattadori, B. Gallese, A. Giachero, C. Gotti, M. Maino, and G. Pessina. A new approach to the readout of cryogenic ionization detectors: GeFRO. *IOP Science*, 2011. URL https://arxiv.org/abs/1102.4143.

[163] C. M. Cattadori, A. Giachero, C. Gotti, M. Maino, and G. Pessina. GeFRO, a new front-end approach for the phase II of the GERDA experiment. *IEEE Nuclear Science Symposium and Medical Imaging Conference (NSS/MIC)*, 2011. URL http://ieeexplore.ieee.org/abstract/document/6154349.

[164] S. Riboldi et al. Improvement of the "CC2" Charge Sensitive Preamplifier for the GERDA Phase II Experiment. *IEEE Nuclear Science Sym- posium and Medical Imaging Conference (NSS/MIC)*, 2012. URL http://ieeexplore.ieee.org/abstract/document/6551209.

[165] S. Riboldi, C. M. Cattadori, E. Ferri, F. Salamida, V. D'Andrea, A. Di Vacri, C. Macolino, and G. Benato. Cryogenic Readout Techniques for Germanium Detectors. *IEEE Advancements in Nuclear Instrumentation Measurement Methods and their Applications (ANIMMA)*, 2015. URL http://ieeexplore.ieee.org/document/7465549.

[166] V. D'Andrea. Analisi delle prestazioni di rivelatori Broad Energy Germanium (BEGe) nei tests della fase II dell'esperimento GERDA ai LNGS, Università degli Studi dell'Aquila. Master's thesis, 2013.

[167] Tecnomec s.r.l. URL http://www.pcb-tecnomec.com.

[168] Semefab. URL http://www.semefab.com.

[169] C. M. Cattadori. Selected Topics on FE Electronics for the GERDA Phase II Ge detector readout, Conference on Low Radiation Techniques, Seattle, March 2015. URL https://www.mpi-hd.mpg.de/gerda/public/2015/t15_lrt_FE_development_cc.pdf.

[170] C. M. Cattadori et al. Status of FE: FE cables and CC3, Talk at the GERDA Collaboration Meeting, LNGS, November 2014.

[171] TPT Wire Bonder. URL http://www.tpt-wirebonder.com.

[172] Texas Instruments. URL http://www.ti.com.

[173] V. D'Andrea et al. Performances of BEGe detectors in GDL and MiB integration tests, Talk at the GERDA Collaboration Meeting, Heidelberg, June 2014, .

[174] V. D'Andrea et al. JFET preparation for last GERDA Integration Tests, Talk at the GERDA Collaboration Meeting, February 2015.

[175] B. Schwingenheuer. Availability of holder components & flex cable fixation, Talk at the GERDA Collaboration Meeting, Tubingen, June 2015.

[176] Häfele GmbH & Co KG. URL https://www.hafele.com/com.

[177] V. D'Andrea et al. ZAC optimization in Integration Tests 20150726 and 20150930, Talk at the GERDA Collaboration Meeting, LNGS, November 2015, .

[178] V. Wagner. Preliminary Results of GERDA Integration Tests Run 20150726 and 20150930, Talk at the GERDA Collaboration Meeting, LNGS, November 2015, .

[179] S. Riboldi et al. Noise Investigations and Actions, Talk at the GERDA Collaboration Meeting, LNGS, November 2015.

[180] GERDA collaboration. Improvement of the energy resolution via an optimized digital signal processing in GERDA Phase I. *Eur. Phys. J. C*, 75 (255), 2015. URL https://arxiv.org/abs/1502.04392.

[181] G. Benato, V. D'Andrea, C. M. Cattadori, and S. Riboldi. Improvement of the GERDA Ge Detectors Energy Resolution by an Optimized Digital Signal Processing. *Physics Procedia*, 61:673–682, 2015. URL http://www.sciencedirect.com/science/article/pii/S1875389214006828.

[182] G. Benato. *Data Reconstruction and Analysis for the* GERDA *Experiment, University of Zurich*. PhD thesis, 2015. URL https://www.mpi-hd.mpg.de/gerda/public/2015/phd2015_giovanniBenato.pdf.

[183] E. Gatti and P. F. Manfredi. Processing the Signals of Solid State Detectors. *Riv. Nuovo Cimento*, 9(1), 1986.

[184] V. Radeka. Low-Noise Techniques in Detectors. *Annual Review of Nuclear and Particle Science*, 38(217-77), 1988.

[185] B.G. Lowe. Measurements of Fano factors in silicon and germanium in the low-energy X-ray region. *Nucl. Instrum. Methods A*, 399(2-3):354–364, 1997.

[186] M. O. Deighton. Minimum-Noise Filters with Good Low-Frequency Rejection. *IEEE Transactions on Nuclear Science*, 16(5):68–75, 1969.

[187] E. Gatti, P. F. Manfredi, M. Sampietro, and V. Speziali. Suboptimal filtering of 1/f-noise in detector charge measurements. *Nucl. Instrum. Methods A*, 297(3):467–478, 1990.

[188] Cambridge University. Optimal (Wiener) Filtering with the FFT. In *Numerical Recipies in C: the Art of Scientific Computing*. Numerical Recipies Software, 1988-1992.

[189] A. Geraci and E. Gatti. Optimum filters for charge measurements in the presence of 1f current noise. *Nucl. Instrum. Methods A*, 361(1-2): 277–289, 1995.

[190] A. Geraci, I. Rech, E. Gatti, and G. Ripamonti. Shared baseline restoration at minimum noise for high resolution spectroscopy. *Nucl. Instrum. Methods A*, 482(1-2):441–448, 2002.

[191] V. Radeka. Trapezoidal filtering of signals from large germanium detectors at high rates. *Nucl. Instrum. Methods*, 99(3):525–539, 1972.

[192] F. S. Goulding and D. A. Landis. Ballistic deficit correction in semiconductor detector spectrometers. *IEEE Transactions on Nuclear Science*, 35(1), 1988.

[193] G. W. Phillips and K. W. Marlow. Automatic analysis of gamma-ray spectra from germanium detectors. *Nucl. Instrum. Methods*, 137(3):525–536, 1976.

[194] V. D'Andrea et al. Update on ZAC energy in GERDA Phase II, Talk at the GERDA Collaboration Meeting, Ringberg, June 2016.

[195] F. Salamida et al. Energy resolution and Calibration Linearity, Talk at the GERDA Collaboration Meeting, Tubingen, June 2015.

[196] Recommended data, Laboratoire National Henri Becquerel. URL `http://www.nucleide.org/DDEP_WG/DDEPdata.htm`.

[197] R. L. Coldwell and G. P. Lasche. Experimental measurements of Doppler broadening of escape peaks in HPGe detectors. *Journal of Radioanalytical and Nuclear Chemistry*, 307(3):2509–2512, 2016. URL `http://link.springer.com/article/10.1007/s10967-015-4463-0`.

[198] F. Salamida and C. M. Cattadori. Private communication and talk at the GERDA Analysis Phone Call in March 2016.

[199] V. Wagner. Update on A/E Analysis, Private communication and talk at the GERDA Collaboration Meeting, LNGS, November 2015.

[200] C. M. Cattadori et al. Status of Electronics, noise and stability, Talk at the GERDA Collaboration Meeting, LNGS, February 2016.

[201] V. D'Andrea et al. Alternative PSDs for BEGe, Talk at the GERDA Collaboration Meeting, LNGS, November 2015, .

[202] N. Becerici-Schmidt. Background modeling for the GERDA experiment. *AIP Conf. Proc.*, 1549(156), 2013. URL `https://arxiv.org/abs/1306.2302`.

[203] V. D'Andrea et al. Study of the GERDA Phase II background spectrum. *Poster at the XXVII International Conference on Neutrino Physics and Astrophysics, London*, July 2016.

[204] C. Wiesinger et al. Data selection, Talk at the GERDA Collaboration Meeting, Ringberg, June 2016.

[205] C. Wiesinger et al. Data selection, Talk at the GERDA Collaboration Meeting, LNGS, November 2016.

[206] H. Neder, G. Heusser, and M. Laubenstein. *53*, 191, 2000.

[207] M. Laubenstein. Screening measurements, Talk at the GERDA Collaboration Meeting, LNGS, February 2016.

[208] J. Hakenmüller. Monte Carlo Simulations for GERDA Phase II, Private communication and talk at the GERDA Collaboration Meeting, Ringberg, June 2016.

[209] S. Nisi et al. Determination of K, Th and U in an optical fiber sample, LNGS chemistry laboratory, 2011.

[210] WARP Collaboration. Measurement of the specific activity of ^{39}Ar in natural argon. *Nucl.Instrum.Meth.*, A574(83–88), 2007. URL http://xxx.lanl.gov/abs/astro-ph/0603131.

[211] K. von Sturm et al. Background Modeling Phase II - Alpha Fit, Talk at the GERDA Collaboration Meeting, Ringberg, June 2016.

[212] A.-K. Schütz et al. Background Modeling Phase II, Talk at the GERDA Collaboration Meeting, Ringberg, June 2016.

[213] A. Caldwell, D. Kollar, and K. Kröninger. BAT - The Bayesian Analysis Toolkit. *Comput. Phys. Commun.*, 180(2197-2209), 2009. URL https://arxiv.org/abs/0808.2552.

[214] S. E. Hemmer. *Study of Lepton Number Conserving and Non-Conserving Processes Using* GERDA *Phase I Data, Università degli Studi di Padova.* PhD thesis. URL https://www.mpi-hd.mpg.de/gerda/public/2014/phd2014_SabineHemmer.pdf.

[215] J. Neyman and E. S. Pearson. On the Problem of the Most Efficient Tests of Statistical Hypotheses. *Philosophical Transactions of the Royal Society of London A: Mathematical, Physical and Engineering Sciences*, 231(694-706):289–337, 1933. ISSN 0264-3952. doi: 10.1098/rsta.1933.0009. URL http://rsta.royalsocietypublishing.org/content/231/694-706/289.

[216] C. M. Cattadori. GERDA Status Report: Results from Commissioning. *Journal of Physics: Conference Series*, 375(042008), 2012. URL http://iopscience.iop.org/article/10.1088/1742-6596/375/1/042008.

[217] V. D. Ashitkov et al. Liquid Argon Ionization Detector for Double Beta Decay Studies. *Inst. Exp. Tech.*, 46(153), 2003. URL `http://xxx.lanl.gov/abs/nucl-ex/0309001`.

[218] A. S. Barabash et al. On concentration of ^{42}Ar in the Earth's atmosphere. *Preprint*, 2016. URL `https://arxiv.org/abs/1609.08890`.

[219] A. W. Nelson et al. Understanding the Radioactive Ingrowth and Decay of Naturally Occurring Radioactive Materials in the Environment: An Analysis of Produced Fluids from the Marcellus Shale. *Environmental Health Perspectives*, 123(7), July 2015. URL `http://ehp.niehs.nih.gov/1408855`.

[220] I. Barabanov et al. Cosmogenic activation of Germanium and its reduction for low background experiments. *Nucl. Instrum. Meth.*, B251 (115-120), 2006. URL `https://arxiv.org/abs/nucl-ex/0511049`.

[221] A.-K. Schutz et al. Investigation of dead layer parameters by studies of the ^{39}Ar spectrum, Talk at the GERDA Collaboration Meeting, LNGS, November 2016.

[222] Cowan G. et al. Asymptotic formulae for likelihood-based tests of new physics. *Eur. Phys. J. C*, 71(1554), 2011. URL `https://arxiv.org/abs/1007.1727`.

[223] A. Caldwell and K. Kröninger. Signal discovery in sparse spectra: A Bayesian analysis. *Physical Review D*, 74(092003), 2006. URL `http://journals.aps.org/prd/abstract/10.1103/PhysRevD.74.092003`.

[224] TRandom3 Class Reference. URL `https://root.cern.ch/doc/master/classTRandom3.html`.

[225] M. Matsumoto and T. Nishimura. Mersenne twister: a 623-dimensionally equidistributed uniform pseudo-random number generator. *ACM Transactions on Modeling and Computer Simulation (TOMACS)*, 8(1):3–30, January 1998. URL `http://dl.acm.org/citation.cfm?doid=272991.272995`.

[226] TUUID Class Reference. URL `https://root.cern.ch/doc/master/classTUUID.html`.

[227] K. Gusev et al. Integration in December 2015, Talk at the GERDA Collaboration Meeting, LNGS, February 2016.

[228] T. Wester. Crosstalk evaluation, Private communication and talk at the GERDA Collaboration Meeting, Ringberg, June 2016.